

Moscow Institute of Electronic Technology
(Technical University)
Bauman Moscow State Technical University
Technical University Munich
Friedrich-Alexander-University Erlangen-Nurnberg

Robert Bauernschmitt, Yuri Chaplygin, Hubertus Feussner,
Yuri Gulyaev, Joachim Hornegger, Ernst Mayr, Nassir Navab,
Sergey Schookin, Sergey Selishchev, Sergei Umnyashkin (Eds.)

**4th
Russian-Bavarian
Conference on
Bio-Medical Engineering
Proceedings**

Proceedings of the
4th Russian-Bavarian Conference on Biomedical Engineering
at Moscow Institute of Electronic Technology (Technical University)
Zelenograd, Moscow, Russia, July 8/9, 2008

Moscow 2008

UDK 61:57; 615.47

B63

Robert Bauernschmitt, Yuri Chaplygin, Hubertus Feussner, Yuri Gulyaev, Joachim Hornegger, Ernst Mayr, Nassir Navab, Sergey Schookin, Sergey Selishchev, Sergei Umnyashkin (Eds.)

B63 Proceedings of the 4th Russian-Bavarian Conference on Biomedical Engineering. - Moscow.: MIET, 2008. - 378 p.

ISBN 978-5-7256-0506-8

Proceedings of the 4th Russian-Bavarian Conference on Biomedical Engineering are presented. Papers are grouped on three basic topics: biomedical imaging and signal processing; instrumentation for surgery, implants and artificial organs; therapeutic and diagnostic systems.

The book will be useful to researchers and engineers, students specializing in the field of biomedical engineering.

ISBN 978-5-7256-0506-8

© Authors, 2008

© MIET, 2008

Preface

Biomedical Engineering (BME) is an interdisciplinary field which scope is exceptionally wide and ranges from molecular imaging to tomography of the whole body, from patch-clamp instruments to EGG and EEG machines, from molecular and cellular engineering to robotics applied in surgery and from artificial molecular complex to mechanical heart pumps and artificial lung.

It is well-known that BME success depends upon many disciplines coming together, such as: biology, medicine, physics, chemistry, engineering, electronics, computer science and so on. No less important is integration of science, engineering, technology and education with industrial need.

BME is an interdisciplinary bridge which is erected by people. Italian anatomist and physician Luigi Galvani, studying what was called “animal electricity,” initiated a line of research known as electrophysiology. When Luigi Galvani's experiments with "animal electricity" were published (1791), Italian physicist Alessandro Volta began experiments which led him to theorize that animal tissue was not necessary for conduction of electricity. Proof of this theory was the battery, which Volta invented in 1800. This is the basis of all modern wet-cell batteries, and it was a tremendously important scientific discovery, because it was the first method found for the generation of a sustained electrical current. X-ray imaging, invented by German physicist Wilhelm Roentgen from Munich University in 1895, had enormous impact on medicine; already in 1896 Siemens and General Electric began selling X-ray equipment.

BME is an interdisciplinary bridge for international collaboration. Russian-born U.S. electronic engineer Vladimir Zworykin (1889 – 1982) was a television pioneer and a founder and president of the International Federation for Medical Electronics and Biological Engineering. Russian physician Naum Gurvich (1905 – 1981), who was a pioneer in defibrillation, introduced a biphasic waveform for electrical pulses of all modern defibrillators. German physicist Max Schaldach (1936 – 2001), pioneer in pacemaker engineering, founded the Department of Medical and Engineering Physics at the Technical University of Nuremberg/Erlangen and Biotronic Co. in 1963 with subsidiaries established in the United States and Switzerland. He became a partner and a consultant to worldwide technological enterprises and medical centers, including Russia. Russian surgeon Valery Shumakov (1931 – 2008), a pioneer in organ transplantation

and artificial organs, was a coordinator of international collaboration on developing artificial hearts and mechanical circulation. His numerous inventions include a mitral valve prosthesis and several types of artificial heart.

All over the world electronic research and education centers are most suitable places for BME activities. Fraunhofer Institute for Integrated Circuits IIS, Erlangen hosted the 3rd Russian-Bavarian Conference on Biomedical Engineering 2007. Moscow Institute of Electronic Technology (Technical University) hosts the 4th Russian-Bavarian Conference on Biomedical Engineering 2008.

A lot of thanks to sponsors of the conference: Prefecture of Zelenograd, Moscow; Innovative Technological Centre of Zelenograd, Moscow; Siemens Ltd, Moscow; Deutsche Forschungsgemeinschaft, Germany.

Professor Sergey Selishchev,
Head of Biomedical Systems Department
of Moscow Institute of Electronic Technology
(Technical University)

Organization

4th Russian-Bavarian Conference on Biomedical Engineering 2008 is organized by the partners:

Moscow Institute of Electronic Technology (Technical University),
Bauman Moscow State Technical University,
Lomonosov Moscow State University,
Munich Technical University ,
Friedrich-Alexander University Erlangen-Nuremberg.

Sponsors:

Prefecture of Zelenograd, Moscow
Innovative Technological Centre of Zelenograd, Moscow
Siemens Ltd, Moscow
Deutsche Forschungsgemeinschaft, Germany.

Conference Scientific Committee:

Robert Bauernschmitt, Germany
Vladimir Beshpalov, Russia
Yuri Chaplygin, Russia
Hans-Henning Eckstein, Germany
Igor Fedorov, Russia
Hibertus Feussner, Germany
Helmut Friess, Germany
Reza Ghotby, Germany
Peter Guggenbicher, Germany
Yuri Gulyaev, Russia
Joachim Hornegger, Germany
Arkady Karyakin, Russia
Stefan Kramer, Germany
Rudiger Lange, Germany
Ernst Mayr, Germany
Oleg Naraykin, Russia
Nassir Navab, Germany
Maximillian Reiser, Germany
Sergey Schookin, Russia

Sergey Selishchev, Russia
Igor Spiridonov, Russia
Sergei Tereshchenko, Russia
Sergei Umnyashkin, Russia
Alexander Zasedatelev, Russia

Organizing Chairs:

Sergei Umnyashkin, Russia
Nassir Navab, Germany
Sergey Selishchev, Russia
Victor Ganzha, Germany

Section 1

Biomedical imaging and signal processing

3D-Reconstruction in the Presence of Motion

Marcus Prümmer¹ and Joachim Hornegger¹

Chair for Pattern Recognition (LME), Friedrich-Alexander-University
Erlangen-Nürnberg, Martensstrasse 3, 91058 Erlangen, Germany.
{pruemmer, Joachim.Hornegger}@informatik.uni-erlangen.de

Abstract. 3D reconstruction of a moving object using X-ray cine-angiograms from monoplane c-arm systems is still a challenging problem. Non-model based state of the art reconstruction methods are still not able to deal with object motion. The new proposed iterative reconstruction and motion correction approach allows a 3d reconstruction in the presence of motion. One of the main clinical applications is a reconstruction of coronary vessels. The advanced reconstruction method is an iterative scheme of EM-type. First an initial algebraic reconstruction with few projections of a specific heart phase is performed applying new relaxation techniques. Then the projection information of other heart states is added to the initial reconstruction by maximizing the amount of usable projection data for the reconstruction via registration of the object motion. This approach provides a data-driven fully automatic method for 3d reconstruction in the presence of motion.

Index Terms Component averaging; Iterative techniques; Motion correction; Coronary reconstruction; Bootstrap relaxation; Correlation-based component averaging.

1 Introduction

Coronary angiography is performed to detect obstruction in the coronary arteries. A 3d-quantification of obstructed vessels (stenosis) as well as a blood flow analysis is advantageous for physicians.

1.1 Clinical Motivation

Cone-beam reconstruction for ECG-gated multislice spiral CT of the heart is state-of-the-art in coronary reconstruction. But a disadvantage is the lower spatial resolution compared to reconstructions using c-arm systems. Furthermore a cardiac catheterization, that is performed to examine stenosis using CT-scanners, is not possible.

1.2 State Of The Art

C. Blondel et. al. [1] perform 3D reconstruction using precomputation of the coronary artery motion, modelled as a parametric 4D motion field. J. Chen and J. Carroll [2] reconstruct based on two cine-angiograms by extracting feature points and computing a global and local transformation that describes the coronary vessel motion. An image based technique for automatic gating depending on the coronary vessel segment is done in [3].

2 Contributions

The outline of this paper is the following:

ECG-Gating Using ECG-gated X-ray angiogram projections, we select few X-ray images of a specific heart phase T , where we expect less motion, and perform an initial reconstruction using only this sparse number of X-ray images.

Sparse Projection Reconstruction The reconstruction result is improved by a new relaxation technique for the component averaging (CAV) algebraic reconstruction technique [4] that improves image quality and is able to deal with highly inconsistent linear equation systems (ES). The new relaxation scheme is applied on the reconstruction in the presence of motion, especially coronary angiography.

EM-type Reconstruction Then we apply a new iterative EM-type combination (fig. 1) of reconstruction using CAV and motion correction by registering observed X-ray images, where the heart phase is similar but different to T , with their corresponding Digitally Reconstructed Radiographs (DRR) [5] that we compute from the initial reconstruction and add the motion corrected X-ray images to the reconstruction process. This new approach improves the reconstruction quality of a moving object and provides an approximate solution in some sense.

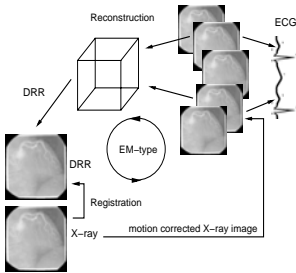


Fig. 1. Reconstruction in the presence of motion.

In the following sections we will deal with the following real world problems for cardiac reconstruction: Heart motion leads to poor reconstruction results and limits the number of usable X-ray images. Intensity inhomogeneities, caused by fast flow-variations of contrast agent between X-ray images, make the equation system for ART inconsistent. The I_0 intensity correction of X-ray images, determined by the c-arm calibration and the truncation problem makes the ES also inconsistent. During a coronary angiography the X-ray intersection length through the human's body undergoes high variations depending on the angle of the thorax intersection and leads therefore to data truncations.

3 Methods

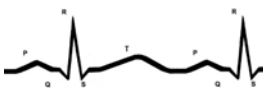


Fig. 2. PQRST-wave of the ECG signal.

ECG Gating The cyclic heart beating is divided into several time frames, defined by the PQRST-wave (fig. 2). During the coronary angiography using a c-arm system the ECG signal is recorded. The duration of a heart beat cycle, which is the time between two RR peaks, is about 0.5 to 1.0 seconds. In the quiescent phase of the cardiac cycle, i.e. the diastole phase, the heart is in rest for about 0.1-0.2 seconds.

The relative position t that we call heart state of an acquired X-ray image between the RR-peak is known. We select X-ray images of the diastole phase $T = [t - \delta_1, t + \delta_1]$, defined by a tolerance δ_1 and call them valid projections. B^T denotes the set of X-rays provided by these valid projections.

3.1 Sparse Projection Reconstruction (SPR)

As considered above is for a specific heart phase T only a limited number of projections available. We use an algebraic reconstruction technique because it is shown that for a sparse projection number a better image quality is given compared to the filtered backprojection technique.

Algebraic Image Reconstruction Algebraic image reconstruction [6] means solving the equation system $\mathbf{A}\mathbf{x} = \mathbf{b}$ where the observed X-ray data is stored in the vector $\mathbf{b} = (b_1, \dots, b_{M^T})^\top \in \mathbb{R}^{M^T}$. M^T is the number of observed intensities caused by an attenuated X-ray after casting through the human's body. The projection geometry of a c-arm system with oblique projections is defined by $\mathbf{A} = (a_{i,j})$ a nonzero $(M^T \times N)$ -matrix and $\mathbf{x} \in \mathbb{R}^N$ contains N unknown voxel intensities.

Extended Component Averaging (ECAV) An efficient algorithm (CAV) for large and sparse unstructured problems was introduced by Censor, Gordon et al. [4]. We use an extended version of CAV introduced in [7]. Both techniques are iterative and parallel especially for oblique projections and converge even in the inconsistent case and unit relaxation. Here we refer for a more detailed description of relaxation strategies to [6]. To solve for $\mathbf{x}^{(k),T}$ we initialize $\mathbf{x}^{(0),T}$ with zero. (k) is the iteration number of the iterative formula

$$x_j^{(k+1),T} = x_j^{(k),T} + \lambda^{(k)} r_j^{(k),T,p} \quad \text{and} \quad r_j^{(k),T,p} := \sum_{i \in B_p^T} \frac{b_i - \mathbf{a}^i \mathbf{x}^{(k),T}}{\sum_{l=1}^N \frac{(a_{i,l})^2}{g_{i,l}}} a_{i,j} \quad (1)$$

and $\mathbf{a}^i = (a_{i,1}, a_{i,2}, \dots, a_{i,N})$ denotes the i th row of \mathbf{A} . As introduced in [6] we apply an iterative subset B_p^T relaxation on $\mathbf{x}^{(k),T}$, where $B^T = \{1, \dots, M^T\} = \bigcup_{p=1}^{P^T} B_p^T$ and P^T is the number of subsets available for heart phase T to compute $\mathbf{x}^{(k+1),T}$. In our case one subset B_p^T includes the X-rays of one X-ray image. We apply a sequential subset-iterative relaxation scheme because as classified and shown in [6], it converges faster than a simultaneous relaxation scheme. For simplicity we define one ECAV iteration by iterating over all P^T subsets. The diagonal weighting is as introduced in [7] defined as

$$g_{i,l} := \frac{a_{i,l}}{\sum_{k \in B_p^T} a_{k,l}}, \quad (2)$$

where also the weight of the rays that intersect the l th voxel and not only the number is considered.

Now we will focus again on the before mentioned real world reconstruction problems. First we have to deal with the subset ordering dependency of the sequential relaxation scheme. Furthermore in the presence of motion, as discussed in section two, arise additional problems using standard ECAV.

Data Scaling It is shown in [8] that data normalization is essential to the numerical solution. Therefore we do some pre-conditioning by data scaling, depending on the observed X-ray data \mathbf{b} . Let ρ be the mean intensity value of \mathbf{b} . Then we

multiply both sides of the ES with $\mu := \sqrt{2} \left(\frac{1}{M^T} \sum_{i=1}^{M^T} |b_i - \rho| \right)^{-1}$.

Bootstrap Relaxation Let us now consider the relaxation more deeply using a subset of hyperplanes [4] $\mathbf{a}^i \mathbf{x} = b_i$ and $i \in B_p^T$. In a consistent ES all hyperplanes intersect in one point, the unique solution (fig. 3, left). But in real world we will have an inconsistent problem caused by the above mentioned facts. Therefore there will be several hyperplane intersections (fig. 3, right). It is a difficult task to determine which intersection points does have in the solution space a smaller euclidean distance to each other and which intersection points are in this sense outliers (fig. 3, hyperplane four and five in the right figure). Using real data, there is a distribution of such intersection points. To deal with the statistical

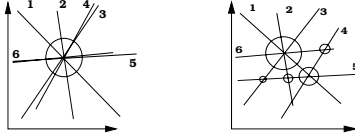


Fig. 3. Intersection of hyperplanes in the 2d case. Consistent ES (left) and inconsistent ES (right) where hyperplane four and five is shifted parallel by scaling of it's b_i .

distribution of such intersection points, we apply bootstrapping [9] which is a known technique for assigning measures of accuracy to statistical estimates. We first introduce a new relaxation scheme for CAV and second compute an average solution, based on bootstrapping.

For one CAV iteration we use a subset index set $w = \{p_1, \dots, p_{pT}\}$. Let W be the number of subsets ($W \ll |w|$) used for one bootstrap relaxation, a robust and smoothed average relaxation is then given with algorithm 1.

Algorithm 1 Bootstrap relaxation

Input: w , subsets B_p^T and $p = 1, \dots, |w|$.
while $w \neq \emptyset$ do
 for $f = 1$ to W do
 Select randomly an index element $w_f \in w$
 Compute relaxation $r_j^{(k),T,w_f}$ according to (1) $\forall j = 1, \dots, N$.
 $w \leftarrow w \setminus \{w_f\}$
 end for
 Compute relaxation mean: $\bar{r}_j^{(k),T} := \frac{1}{W} \sum_{f=1}^W r_j^{(k),T,w_f} \quad \forall j = 1, \dots, N$.
 for $f = 1$ to W do
 Relaxation variance: $\sigma_j^{(k),T,w_f} := (r_j^{(k),T,w_f} - \bar{r}_j^{(k),T})^2 \quad \forall j = 1, \dots, N$.
 end for
 Order the W relaxations such that: $\sigma_j^{(k),T,w_1} \leq \sigma_j^{(k),T,w_2} \leq \dots \leq \sigma_j^{(k),T,w_W}$.
 Compute κ_1 -trimmed mean: $\tilde{r}_j^{(k),T} := \frac{1}{W - \kappa_1} \sum_{f=1}^{W - \kappa_1} r_j^{(k),T,w_f} \quad \forall j = 1, \dots, N$.
 Relax $x_j^{(k+1),T} \leftarrow x_j^{(k),T} + \lambda^{(k)} \tilde{r}_j^{(k),T} \quad \forall j = 1, \dots, N$.
 $k \leftarrow k + 1$
end while
Output: $\mathbf{x}^{(k),T}$

Accuracy Estimation - Bootstrapping To estimate the accuracy of a solution $\mathbf{x}^{(k),T}$ a random sampling on B^T is applied (see algorithm 2). In the following

Algorithm 2 CAV with bootstrap extension (BECAV)

Input: Size of random sample: P_S^T and $P_S^T < P^T$, number of samples: D
 for $d = 1$ to D do
 Select randomly bootstrap sample $B^{T,d} \subset B^T$ and $B^{T,d} = \bigcup_{p=1}^{P_S^T} B_p^{T,d}$
 Solve $\mathbf{x}^{(k),T,d}$ using (1), algorithm 1 and all subsets $B_p^{T,d}$ and $p = 1, \dots, P_S^T$.
 end for
 Compute mean: $\bar{\mathbf{x}}^{(k),T} := \frac{1}{D} \sum_{d=1}^D \mathbf{x}^{(k),T,d}$
 for $d = 1$ to D do
 Compute variance: $\sigma^{T,d} := \frac{1}{N} \sum_{j=1}^N (\mathbf{x}_j^{(k),T,d} - \bar{\mathbf{x}}_j^{(k),T})^2$.
 end for
 Ensure: Order the solutions $\mathbf{x}^{(k),T,d}$ such that $\sigma^{T,1} \leq \sigma^{T,2} \leq \dots \leq \sigma^{T,D}$.
 Apply κ_2 -trimmed mean: $\bar{\mathbf{x}}^{(k),T} := \frac{1}{D-\kappa} \sum_{d=1}^{D-\kappa_2} \mathbf{x}^{(k),T,d}$.
 Output: $\bar{\mathbf{x}}^{(k),T}$

sections we call this bootstrap extension BECAV.

3.2 Maximization of Projection Information

For the SPR we use approximately ten percent of the acquired X-ray images. The next step is to add additional projection data from a similar heart phase to the SPR. Therefore we define a second tolerance δ_2 and expand the valid data frame to $\hat{T} = [t - \delta_2, t + \delta_2]$ and $\delta_2 > \delta_1$ and define $\tilde{T} := \hat{T}/T$. But before the additional subsets $B_p^{\hat{T}}$ are useable for the reconstruction, a correction of the heart motion is crucial. On the subsets B_p^T is no motion correction done.

Correlation Weighted Component Averaging (CCA) After the motion correction is applied on the additional subsets $B_p^{\hat{T}}$ we add them to the set of valid data subsets used for the previously performed SPR and execute further CAV iterations starting with $\bar{\mathbf{x}}^{(k),T}$ from the SPR. During the CAV is the residuum $h_i := b_i - \mathbf{a}^i \mathbf{x}^{(k)}$ of each hyperplane multiplied by a similarity weight $|d_i|$. The similarity is computed between a corresponding $DRR_p^{\hat{T}}$ and motion corrected subset $B_p^{\hat{T}}$ for each hyperplane using the Normalized Cross Correlation (NCC) [10] of a $ne \times ne$ pixel neighborhood. $|d_i|$ regularizes the amount of influence of each hyperplane to the ES. The weight d_i for a hyperplane $i \in B_p^T$ is set to one. If we change the influence of hyperplanes during CAV, we have to reconsider the diagonal weighting (2). Therefore we define

$$\tilde{g}_{i,l} := \frac{a_{i,l}}{\sum_{k \in B_p^{\hat{T}}} |d_k| a_{k,l}}. \quad (3)$$

The CCAV is then defined as

$$x_j^{(k+1),\hat{T}} = x_j^{(k),\hat{T}} + \lambda^{(k)} \sum_{i \in B_p^{\hat{T}}} \frac{|d_i| (b_i - \mathbf{a}^i \mathbf{x}^{(k),\hat{T}})}{\sum_{l=1}^n \frac{(a_{i,l})^2}{\tilde{g}_{i,l}}} a_{i,j}. \quad (4)$$

Motion Correction To estimate the object motion in the observed X-ray images we register each subset $B_p^{\hat{T}}$ with its corresponding $DRR_p^{\hat{T}}$ and correct the motion. The system provides curvature registration by maximization of the mutual information [11] and block-matching techniques extensively studied for digital subtraction angiography (DSA) in [10] that are state-of-the-art techniques. The motion correction and CCAV is applied iteratively and therefore is the algorithm of EM-type. The final approach, that we call EM-CCAV, is then described in algorithm 3.

Algorithm 3 EM-CCAV

Input: ri iterations of the registration algorithm, annealing factor af .

Compute SPR as described in section 3.1.

Initialize volume $\mathbf{x}^{(k),\hat{T}}$ with solution of SPR.

while $k < \text{iteration limit}$ do

 Compute all $DRR_p^{\hat{T}}$ from $\mathbf{x}^{(k),\hat{T}}$.

 Perform motion correction (ri iterations) as described in section 3.2.

 Compute similarities d_i , $\forall i \in B_p^{\hat{T}}$ as described in section 3.2.

 Solve $\mathbf{x}^{(k+1),\hat{T}}$ using (4) and algorithm 1.

 Optional: Random reordering of the X-ray images $B_p^{\hat{T}}$.

 Annealing $ri \leftarrow \lfloor \frac{ri}{af} \rfloor$

$k \leftarrow k + 1$

end while

Output: 3d-reconstruction $\mathbf{x}^{(k),\hat{T}}$.

4 Results

All experiments were elaborated on a Intel Pentium 3GHz with 1 GB RAM. The reconstructed phantom volumes are of size $64 \times 64 \times 64$ and the X-ray images are 128×128 . All experiments were performed with a real c-arm calibration that is given for each acquired X-ray image. Commercially available c-arm systems do not provide an ECG signal, but in our experimental clinical setup the c-arm was equipped afterwards. We proof our concept on a synthetic phantom and an ECG signal from a real data set.

Clock Phantom The phantom \mathbf{x}^{Ph} consists of smoothed background noise and sphere objects that are aligned along a helix where the radius of both the helix and the spheres is getting smaller. The phantom data provide 248 projections including seven RR-ECG intervals.

Reconstruction Accuracy and Convergence We define the relative error $\epsilon^{(k)}$ and the absolute relaxation r_e^p of a subset $B_p^{\hat{T}}$ as

$$\epsilon^{(k)} := \frac{1}{\sum_{j=1}^N |x_j^{Ph}|} \sum_{j=1}^N |x_j^{(k)} - x_j^{Ph}|, \quad r_e^p := \sum_{j=1}^N \left| \sum_{i \in B_p^{\hat{T}}} \frac{b_i - \langle \mathbf{a}_i, \mathbf{x}^{(k)} \rangle}{\sum_{l=1}^n s_l (a_l^i)^2} \right| a_j^i. \quad (5)$$

4.1 Experimental Results

Accuracy Consideration of Sparse Projection Reconstruction We compare the ECAV and BECAV for accuracy and convergence. To simulate an inconsistent ES we scale all hyperplanes of one X-ray image by a random factor $IC \in [1 - ICS, 1 + ICS]$. In our experiments we use the same initialization of the subset $B_{p_i}^{\hat{T}}$ order $w = \{p_1 = 1, p_2 = \lceil \frac{P^{\hat{T}}}{2} \rceil + 1, p_3 = 2, p_4 = \lceil \frac{P^{\hat{T}}}{2} \rceil + 2, \dots\}$ for the ECAV and BECAV. The experimental setup is shown in table 1.

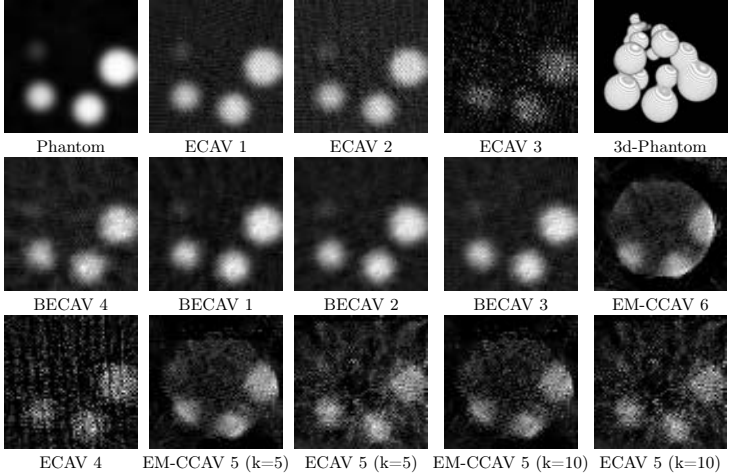


Fig. 4. Volume slice 16. The parameters of the experiments are given in table 1. With increasing ICS the BECAV shows better results compared to ECAV (exp. 1,2,3 and 4). The EM-CCAV reconstruction shows stronger object edges and less artifacts. But there are small object deformations caused by the motion correction (exp. 5,6: an identical SPR is used for EM-CCAV and ECAV reconstruction).

Motion Correction and Correlation Weighted Component Averaging In our experiments we set $t = 75$, $\delta_1 = 5$ and get $P^T = 25$ X-ray images used for the SPR. For $\delta_2 = 9$ we get 25 additional X-ray images B_p^T where we add a sinusoidal motion of maximum eight pixel. Acceptable motion correction results were achieved using curvature registration with maximization of the mutual information [11] performing ri iterations. Figure 4 and table 1 show the results comparing ECAV and EM-CCAV.

5 Discussion and Conclusion

In conclusion we can say that depending on the data the BECAV at least improves the image quality. For inconsistent ES it provides a better approximative solution with a higher image quality. The EM-CCAV reconstruction returns an approximative solution in the sense of the motion corrected X-ray images and the SPR. The registration does obviously have a high influence on the EM-CCAV reconstruction. Poor registration results may introduce artificial vessel obstructions. For the EM-CCAV is an acceptable SPR crucial, otherwise the motion correction will fail. Therefore contrast enhancing techniques, that do not make the ES inconsistent, are essential to make the EM-CCAV applicable for cardiac images. Another application for the EM-CCAV could be a motion artifact reduction in Digital Subtraction Angiography [10].

	BECAV				ECAV					EM-CCA		
Exp.	1	2	3	4	1	2	3	4	5		5	6
P^T	25	25	25	15	25	25	25	15	45	P^T	25+20	25+20
d	20	20	20	12	-	-	-	-	-	af	20	10
ICS	0.001	0.01	0.1	0.1	0.001	0.01	0.1	0.1	0.0	ri	500	300
K	3	3	3	5	24	24	24	40	15	K	15	5
$\epsilon^{(k)}$	0.67	0.67	0.70	0.67	0.83	0.83	0.85	0.84	0.98		0.99	0.98

Table 1. Parameter setup of the experiments. In all experiments is $\lambda = 2$, κ_1 -trim = 1, κ_2 -trim = 1, $D=8$, $t = 75$, $W = 3$, $ne = 15$ and K specifies the number of iterations.

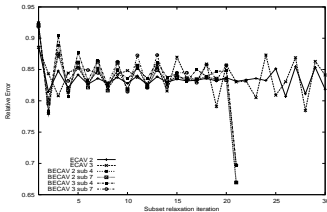


Fig. 5. $\epsilon^{(k)}$ of exp. two and three of ECAV and BECAV. The caption BECAV 2 sub 4 defines the $\epsilon^{(k)}$ of exp. 2, sample $d = 4$ of solution $\mathbf{z}^{(k),T,4}$ that averages to $\bar{\epsilon}^{(k)}$ of the average smoother. solution $\bar{\mathbf{x}}^{(k),T}$.

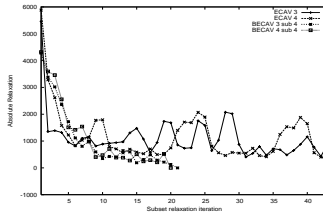


Fig. 6. Absolute relaxation τ_e^p of ECAV and BECAV of experiment three and four. The bootstrap relaxation of BECAV converges

References

- Blondel, C., Vaillant, R., Malandain, G., Ayache, N.: 3-D tomographic reconstruction of coronary arteries using a precomputed 4-D motion field. *Physics in Medicine and Biology* 49 (2004) 2197–2208
- Chen, S.Y.J., Carroll, J.D.: Kinematic and deformation analysis of 4-d coronary arterial trees reconstructed from cine angiograms. *IEEE Trans. Med. Imaging* 22 (2003) 710–721
- Movassaghi, B., Istel, T., Rasche, V.: Automatic gating window positioning for 3D rotational coronary angiography (3DRCA). In: *Medical Imaging 2004: Image Processing*, Edited by Fitzpatrick, J. Michael; Sonka, Milan. Proceedings of the SPIE, Volume 5370, pp. 1932–1942 (2004). (2004) 1932–1942
- Censor, Y., Gordon, D., Gordon, R.: Component averaging: An efficient iterative parallel algorithm for large and sparse unstructured problems, *Parallel Computing* (2001) Volume 27, 777–808
- Russakoff, D.B., Rohlfing, T., Rueckert, D., Shahidi, R., Kim, D., Maurer, C.R.: Fast calculation of digitally reconstructed radiographs using light fields. In: *Medical Imaging 2003: Image Processing*, Edited by Sonka, Milan; Fitzpatrick, J. Michael. Proceedings of the SPIE, Volume 5032, pp. 684–695 (2003). (2003) 684–695
- Jiang, M., Wang, G.: Convergence studies on iterative algorithms for image reconstruction. *IEEE Trans. Med. Imaging* 22 (May, 2003) 569–79
- Popa, C., Zdunek, R.: New Generalized Oblique Projections in DW Algorithm with Application to Borehole Tomography. Editura Academiei Romane (2004)
- Hartley, R., Zisserman, A.: Multiple view geometry. In: *Multiple View Geometry in computer vision*. (2003) 107–109
- Efron, B., Tibshirani, R.J.: *An Introduction to the Bootstrap*, Bradley Efron, Robert J. Tibshirani. Volume 57. Chapman Hall CRC (1998)
- Meijering, E.: Image enhancement in digital x-ray angiography. PhD thesis, Utrecht University, The Netherlands (2000)
- D’Agostino, E., Modersitzki, J., Maes, F., Vandermeulen, D., Fischer, B., Suetens, P.: Free-form registration using mutual information and curvature regularization. *Biomedical Image Registration, Workshop WBIR* (2003) 11–20

Interpreting PET Scans by Structured Patient Data: A Data Mining Case Study in Dementia Research

*J. Schmidt¹, A. Hapfelmeier¹, M. Mueller¹, A. Drzezga²,
R. Perneczky³, A. Kurz³, S. Kramer¹*

¹ *Technische Universität München, Institut für Informatik,
email: {jana.schmidt, andreas.hapfelmeier,
marianne.mueller, stefan.kramer}@in.tum.de*

² *Technische Universität München, Nuklearmedizinische Klinik,
email: a.drzezga@lrz.tum.de*

³ *Technische Universität München, Klinik u. Poliklinik für Psychiatrie u.
Psychotherapie,
email: {robert.perneczky, alexander.kurz}@lrz.tum.de*

Abstract

One of the goals of medical research in the area of dementia is to correlate images of the brain with other variables, for instance, demographic information or outcomes of clinical tests. The usual approach is to select a subset of patients based on such variables and analyze the images associated with those patients. In this paper, we apply data mining techniques to take the opposite approach: We start with the images and explain the differences and commonalities in terms of the other variables. In the first step, we cluster PET scans of patients to form groups sharing similar features in brain metabolism with k-Medoids. In the second step, we explain the clusters by relating them to non-image variables. To do so, we employ RSD, an algorithm for relational subgroup discovery, with the cluster membership of patients as target variable. Our results enable interesting interpretations of differences in brain metabolism in terms of demographic and neuropsychological variables.

1. Introduction

Every year 200,000 people are diagnosed with some type of dementia in Germany, 40% of which with Alzheimer's disease. Therefore, there is great interest in expanding our knowledge of various forms of dementia, including Alzheimer's disease. Generally speaking, the symptoms of Alzheimer's disease are caused by deposition of pathological proteins in the form of intracellular tangles and extracellular plaques. This deposition is followed by neuron

death and deficits in neurotransmitter systems. Furthermore, deficits in glucose metabolism occur, which can be assessed in-vivo by [18]F-FDG Positron-Emission-Tomography (FDG-PET) to detect regional functional pathology.

Given the results from such neuroimaging studies, one of the major goals of medical research is to correlate them with other non-image based variables (e.g., demographic information or neuropsychological data). The usual approach is to select a subset of patients fulfilling specific predefined criteria (e.g., the level of cognitive impairment) and to compare the images associated with those patients to data from healthy controls in a group analysis. However, it is clear that such an approach can never be guaranteed to be complete: If the first step misses an important subset, it is not possible to recover from this omission in subsequent steps. Therefore, we propose to apply data mining techniques to take the opposite approach: to start with the images and explain the differences and commonalities in terms of non-image variables. The approach allowed the detection of differences in cognitive performance in presence of comparable brain pathology, thus potentially helping to identify factors supporting compensation (e.g., age, gender, education).

2. Data

The data was provided by the psychiatry and nuclear medicine departments of Klinikum rechts der Isar of Technische Universität München. It consists of demographic information, clinical data, including neuropsychological (42 variables) test results of 4,037 patient visits and 454 PET scans (10GB) that have been collected between 1995 and 2006.

PET The recorded PETs in this study indicate the metabolism of the brain, i.e., the transformation of glucose. This reflects the activity of the neural cells. The brain of patients suffering from dementia contains regions where the metabolism is clearly lowered. At the end of the preprocessing, each file consists of 69 matrices of 79 rows and 96 columns, summing up to 523,296 voxels. Each of the 69 layers reflects a horizontal cut through the brain, presenting a two dimensional image of the layer with voxels displaying the intensity of metabolism of the corresponding region. In order to visualize a group of scans, we computed a *mean image* using SPM5. In a mean image, each voxel contains the mean voxel value at that position.

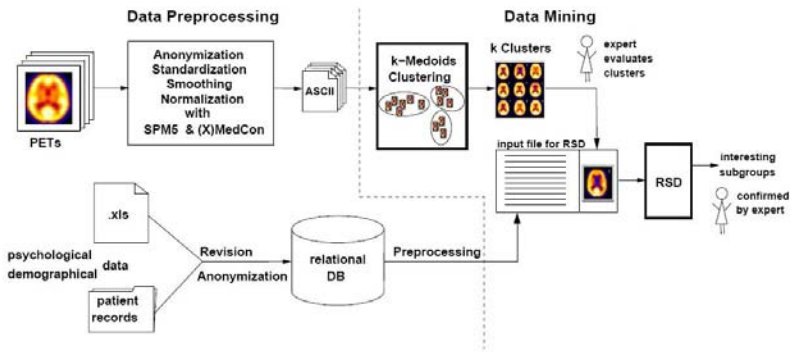


Figure 1: Workflow of our approach. The upper part shows the processing of image data, the lower part the processing of the structured non-image data. Preprocessing steps are on the left side, data mining and interpretation of results on the right.

Demographic and clinical data We had access to demographic data of 4,037 patients. The clinical data for each patient consists of psychological test results that were completed during their hospital visit. Additionally, the diagnosis for each visit is provided in the form of ICD-10 codes [7]. The assessment instruments are the standard to diagnose dementia: *CERAD test*, *CDR test*, and the *clock drawing* [1].

3. Method

The data mining part of our approach is illustrated on the right-hand side of Figure 1. In the first step, we apply k-Medoids clustering [3] with variance-weighted distance measure to the image data. The clusters of the best clusterings according to clustering quality and expert evaluation are further interpreted by the corresponding non-image data. For the interpretation of image clusters, we employ RSD (relational subgroup discovery) [4, 6], an algorithm for finding interesting subgroups in data. In subgroup discovery, the goal is to find subgroup descriptions (typically conjunctions of attribute values as in

rule learning) for which the distribution of examples with respect to a specified target variable is “unusual” compared to the overall target distribution and statistically relevant [2]. In our case, clinical and demographic variables form the subgroup descriptions, and the cluster membership is chosen as the target variable. Before applying RSD, we still remove images with incomplete corresponding non-image data as well as all clusters below a certain size. Interesting subgroups were identified by checking their p -value and by expert validation.

4. Results of the Subgroup Discovery on Clustering

We computed clusterings for several values of k and chose that with appropriate silhouette coefficient [3] for discussion here. It has 16 clusters and is denoted as \mathcal{C}_{16}^* . We kept seven clusters for the further subgroup analysis. Clusters 1, 4, 5, 6, 7, 11, and 14, containing (22, 69, 58, 17, 13, 37, 29) images were large enough for further subgroup mining (more than five images). Figure 2 shows those clusters and those having more than five images before the filtering steps (Cluster 3 and Cluster 8). In this clustering we find that cluster 4 strongly resembles the mean image of the healthy controls and owns subgroups that also indicate high mental health. Cluster 7 shows a group of patients suffering from a frontotemporal dementia, which was supported by the subgroups found as well as from the experts. The mean image of Cluster 11 is the prototype of a patient with Alzheimer’s disease, which is confirmed by the subgroups. 78.4% of the patients in this cluster have the disease, which is visible in the mean image through the reduction of metabolism in the temporoparietal cortex. Regarding the subgroups found for Cluster 14 it seems that this cluster describes elderly women with weak test results and therefore show a similar state of dementia. Surprisingly, there is a group of men with high psychological scores. Although this subgroup is not significant, it is highly interesting. It indicates that men with the same metabolic patterns as women have a less impaired cognitive ability. This could be interpreted by the hypothesis of “cognitive reserve” that says that certain factors (higher education, gender) may compensate the progress of dementia [5].

Even though all subgroups found are statistically significant, certain clusterings (\mathcal{C}_{16}^*) differentiate more accurately between the neuropsychological properties of the clusters compared to other clusterings e.g. \mathcal{C}_{10}^* . For example, it detects an “Alzheimer cluster” (Cluster 11), whereas the distribution of Alzheimer

patients in e.g. \mathcal{C}_{10}^* is not that focused. Therefore, none of the clusters in \mathcal{C}_{10}^* shows a preference of being a definite “Alzheimer cluster”.

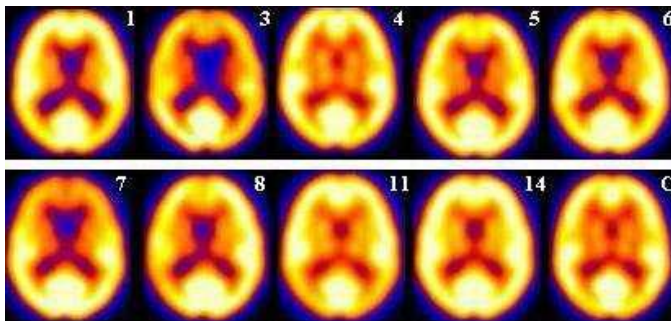


Figure 2: Mean images of the nine largest clusters of the clustering with $k = 16$. Cluster C represents healthy controls.

5. Summary

We showed that it is possible to obtain meaningful clusters of PET scan images. Medical experts could clearly identify different patterns of disease. Furthermore, the clustering was able to determine outliers. A standard subgroup discovery algorithm, RSD, was applied to identify interesting subgroup descriptions of the clusters. From the application point of view, the presented approach groups patients according to the features of PET scans, which represent the different patterns of dementia. In a second step, it finds similarities and differences in the psychological data of the corresponding patients. The overall approach is new in this area of research, as the standard approach is, the other way round, to first group the patients by their psychological features and then compare their PET scan images.

References

- [1] M. J. Chandler, L. H. Lacritz, L. S. Hynan, H. D. Barnard, G. Allen, M. Dechener, M. F. Weiner, and C. M. Cullum. A total score for the CERAD neuropsychological battery. *Neurology*, 65(1):102–6, 2005.

- [2] J. Kalbfleisch. *Probability and Statistical Inference: Vol. 2: Statistical Inference*. Springer, 1985.
- [3] L. Kaufman and P. J. Rousseeuw. *Finding Groups in Data. An introduction to cluster analysis*. Wiley, 1990.
- [4] N. Lavrač, F. Železný, and P. A. Flach. RSD: Relational subgroup discovery through first-order feature construction. In S. Matwin and C. Sammut, editors, *Proceedings of the 12th International Conference on Inductive Logic Programming*, volume 2583 of *Lecture Notes in Artificial Intelligence*, pages 149–165. Springer, 2003.
- [5] R. Perneczky, A. Drzezga, J. Diehl-Schmid, G. Schmid, A. Wohlschläger, S. Kars, T. Grimmer, S. Wagenpfeil, A. Monsch, and A. Kurz. Schooling mediates brain reserve in Alzheimer’s disease: findings of FDG PET. *Journal of Neurology, Neurosurgery and Psychiatry (JNNP)*, 77:1060–1063, 2006.
- [6] F. Železný and N. Lavrač. Propositionalization-based relational subgroup discovery with RSD. *Machine Learning*, 62(1-2):33–63, 2006.
- [7] World Health Organization. *ICD-10 : International Statistical Classification of Diseases and Related Health Problems (Tenth Revision)*. World Health Organization, Geneva, Switzerland, 2 edition, 2005.

Correction of Intensity Inhomogeneities Utilizing Histogram-based Regularization

F. Jäger, M. Balda, and J. Hornegger

*Chair of Pattern Recognition, University of Erlangen, Germany,
{jaeger,michael.balda,hornegger}@informatik.uni-erlangen.de*

Abstract. Magnetic resonance imaging is one of the most important imaging modalities. However, local magnetic inhomogeneities of the coils system and susceptibility effects can cause severe problems for post-processing of the data sets and medical diagnostics. In literature, these artifacts are called signal inhomogeneities caused by a bias field. The approach proposed in this article presents a new regularizer for an entropy based method to correct these signal intensity artifacts. In contrast to most state-of-the-art methods, our approach introduces a-priori knowledge about the used data sets. The additional knowledge about the images is stored in histograms. It can be computed from either an atlas or previously acquired images. Furthermore, it can be automatically approximated from the histogram of the given image. The bias field is modeled by bi-cubic splines. In order to estimate a bias field approximation, each node defining the bias field model, is iteratively optimized. As distance measure a combination of the entropy within the images and to regularize the computation of the bias fields, the Kullback Leibler distance to the reference histogram is used. First, the proposed approach was evaluated using simulated brain images. Furthermore, the algorithm was tested on real T1 weighted data sets acquired in clinical routine; thus, the volumes included lesions and other pathologies. The results show, that using a-priori knowledge as additional regularization can enhance the robustness of bias field correction algorithms. Compared to Homomorphic Unsharp Masking, our approach increased the SNR by up to 3.7 db.

1 Introduction

MRI is the preferred imaging modality of the brain due its excellent soft tissue contrast. Susceptibility effects and local inhomogeneities of the coils system on the other hand can influence signal intensity values. This means, that a single tissue class might have different intensities within a single volume. In general, intensity inhomogeneities have no significant influence on medical diagnostics, but automatic segmentation and quantification methods will fail as these heavily depend on the observed image intensities. In the last decade several algorithms to correct these inhomogeneities (bias field, gain field) in MRI images have been developed [1]. In the following the most widely used approaches are summarized. Basically there are two types of methods: classifying and non-classifying approaches. For each pixel all methods assume a multiplicative bias

field $y_i = x_i \cdot b_i + n_i$, where y_i is the observed image intensity, x_i is the ideal image intensity and b_i is the bias field value. The additive noise n_i is neglected in general.

The quality of the correction of classifying methods is highly related to the segmentation results they provide. If a reliable segmentation was possible, the resulting bias fields are estimated very accurately. A drawback of these methods is, that they cannot be generalized to other body regions or sometimes even to different pulse sequences. Ahmed et al. [2] present a bias field correction method based on a segmentation using a modified fuzzy c-means approach. In [3] the bias field is estimated by modeling the brain intensities by a mixture of Gaussians. The mixing parameters as well as the bias field are approximated using the expectation maximization algorithm.

Non-classifying methods are more general and usually faster. However, the resulting bias field is not as precise as the estimated bias field of classifying approaches. In general non-classifying bias field correction methods require additional assumptions about the shape of the bias field, like smoothly varying intensity inhomogeneities. Furthermore, most approaches rely on the assumption that all tissue classes are homogeneously distributed in the MRI image. Simple methods for intensity correction are fitting a polynomial surface to the image intensities and frequency domain filtering. These approaches are directly derived from the mentioned assumptions. Based on this Axel et al. propose a method called Homomorphic Unsharp Masking (HUM)[4]. Sled et al. propose a nonparametric method for automatic bias field correction (N3) that relies on image statistics [5] only. The histograms of images affected by bias fields are smoothed, as intensities of a single tissue class are spread. Consequently, the entropy of the images is increased. In [6] Salvado et al. a method is introduced that relies on the minimization of the entropy of the images. In this article we introduce an extension to Salvado's method [6] that utilizes prior knowledge about the shape of the probability density functions of the data sets to increase the robustness of the algorithm.

2 Methods

2.1 Entropy Minimization

Salvado's method [6] bases on the assumption that the observed images are composed by an ideal image corrupted by signal inhomogeneities, that can be approximated using a bi-cubic spline model. As the observed image contains information of both signal components, the entropy of the corrected image has to be smaller than that of the observed image. The correction approach iteratively estimates a bi-cubic spline model that minimizes the entropy in the corrected image. A regularizer has to be introduced into the optimization process, as otherwise a trivial solution will be found.

The initial bias field estimation is based on a least-squares approximation with a two-dimensional polynomial. A fourth order polynomial was used. After that a bi-cubic spline interpolator is set up with a node spacing of d . The initial

bias field is used to initialize the nodes of the interpolator by evaluating the polynomial B at the node locations of the interpolator.

The optimization itself is performed by a golden section search and parabolic interpolation. The entropy is computed using

$$E_{\Omega} = - \sum_{l=g_{\min}}^{g_{\max}} h_{\Omega}[l] \log(h_{\Omega}[l]), \quad (1)$$

where h_{Ω} is the histogram of the active region Ω of the image Y . The histogram has a binning resolution of half a gray level value and serves as an estimate of the real probability density function (pdf). g_{\min} and g_{\max} are the minimal/maximal possible gray values of the image. The bias field is obtained by evaluating the estimated bi-cubic spline at each image position.

2.2 Histogram-based Regularization

In order to increase the robustness a histogram-based distance measure that rates the similarity of the corrected histogram to a previously computed reference histogram is introduced. We chose the Symmetric KL-Divergence

$$\hat{D}_{\text{KL}}(p_Y, p_R) = \int_t p_R(t) \log \frac{p_R(t)}{p_{\hat{X}}(t)p_R(t)} dt + \int_t p_{\hat{X}}(t) \log \frac{p_{\hat{X}}(t)}{p_R(t)p_{\hat{X}}(t)} dt \quad (2)$$

as similarity measure with $p_R(x)$ being the reference pdf and $p_{\hat{X}}(x)$ being the pdf of the corrected image.

The objective function is a combination of both measures with a parameter α that defines the influence of the measures:

$$O_{\text{EH}} = (1 - \alpha)E_{\Omega} + \alpha D_{\text{KL}}, \quad (3)$$

where E_{Ω} is the entropy, D_{KL} the approximated KL-Distance.

Note that these two measures still have to be computed on their own histograms: The entropy is calculated on the local histogram of region Ω whereas D_{KL} is always based on the global histogram.

The parameter α has to be chosen carefully, as the two measures cover different ranges which depend on parameters like the binning resolution for the histograms or the input image size. In general the KL-Divergence yields larger values than the entropy.

Combining both measures allows us to get rid of the regularizer proposed by Salvado [6] and replaces it with a robust histogram-based distance measure. However, an additional parameter α is introduced which has to be chosen carefully. Since the measures work on different histograms, there are little synergies that can be used for optimization. This makes the computation time considerably worse compared to the "single-measure" approaches. A further problem of this approach is how to acquire a reference histogram. There are three possibilities:

1. From reference data (e. g. an atlas)
2. From an image with a similar tissue distribution which is known to be bias field free
3. Generated from the histogram of the disturbed image

3 Results

3.1 Simulated MR Brain data sets

Data: First, the proposed method was evaluated using simulated MR brain images provided by the McConnell Brain Imaging Centre (BIC) of the Montreal Neurological Institute, McGill University [7]. All used volumes had a slice thickness of 1mm and a resolution of 181×217 pixels. The reference images are taken from undisturbed data without noise and bias field but inheriting partial volume effects. The distorted T1 and T2 images show 3% noise and signal intensity inhomogeneities of 40%. The PD images have 3% noise and a linear bias field with a strength of 50%.

Evaluation Method: As a quality measure we use the *signal-to-noise ratio (SNR)* and *peak signal-to-noise ratio (PSNR)* between the true bias field and the approximated bias field. The measures are defined as

$$\text{SNR} = 10 \log_{10} \left(\frac{\sum_{i=1}^N b_i^2}{\sum_{i=1}^N (b_i - \hat{b}_i)^2} \right) \quad \text{and} \quad \text{PSNR} = 10 \log_{10} \left(\frac{N b_{\max}^2}{\sum_{i=1}^N (b_i - \hat{b}_i)^2} \right).$$

The signal to noise ratio is based on the ratio between noise energy and signal energy. The values b_i denote the reference bias field intensities and \hat{b}_i are the values of the approximated bias field. Negative values indicate that the noise power exceeds the signal power. PSNR is based on the ratio between the maximal image power b_{\max}^2 and the *mean square error (MSE)*. For evaluation all bias fields were scaled, such that the mean intensity value of the estimated fields corresponds to the mean value of the true bias field.

Results: The correction results of the proposed method were compared to Homomorphic Unsharp Masking (HUM). As only one image was available for each acquisition protocol, the reference histogram had to be estimated from the observed image. Using HUM a SNR value of $s_{\text{HUM},\text{T1}} = 14.88$ db, $s_{\text{HUM},\text{T2}} = 17.27$ db and $s_{\text{HUM},\text{PD}} = 19.07$ db and a PSNR value of $p_{\text{HUM},\text{T1}} = 17.42$ db, $p_{\text{HUM},\text{T2}} = 19.70$ db and $p_{\text{HUM},\text{PD}} = 22.78$ db. The results for the proposed histogram-based entropy optimization are $s_{\text{HR},\text{T1}} = 17.79$ db, $s_{\text{HR},\text{T2}} = 19.63$ db and $s_{\text{HR},\text{PD}} = 19.29$ db and a PSNR value of $p_{\text{HR},\text{T1}} = 20.34$ db, $p_{\text{HR},\text{T2}} = 22.06$ db and $p_{\text{HR},\text{PD}} = 23.01$ db.

3.2 MR data sets from clinical routine

Data: The T1-weighted volume had a resolution of $208 \times 256 \times 19$ with an isotropic in-plane resolution of 0.86 mm^2 , 7.2 mm slice thickness and $\text{TE} = 14$ and $\text{TR} = 510$ ms. The images were acquired during clinical routine on a Siemens Symphony 1.5 T MR scanner at the clinics for diagnostic radiology at the University of Erlangen.

Evaluation Method: As the bias fields of the data sets were not known, the results were presented to several experts in order to judge the quality of the correction result. This was done by presenting the images pairwise. The expert had to evaluate which of the presented image he prefers. At this the evaluator

did not know which image was the original and which was corrected by HUM, the entropy optimization approach introduced by Salvado [6] and the proposed extension.

Results: In total all methods for bias correction increased the image quality. However, the difference between the different evaluated algorithms was not as big as for the artificial images. There are several reasons for this. First, many physicians are used to the intensity distorted images; thus, they prefer images with slight intensity inhomogeneities. Moreover, only clearly visible differences can be judged by the experts. Using the SNR and PSNR measures, small differences, that can affect segmentation algorithms for instance, can be measured as well.

4 Summary

In this article we presented an extension to Salvado's method [6] for bias correction basing on entropy optimization. The new regularizer increases the robustness and the applicability of the method. Hence, it is possible to use the method on a broad variety of problems. The experiments on simulated MR brain images show, that the proposed method outperforms other state-of-the-art methods like HUM. How to compute the reference images is still an open research topic. In this article we used filtering techniques to generate the references from the histograms of the disturbed images.

References

1. Vovk, U., Pernus, F., Likar, B.: A review of methods for correction of intensity inhomogeneity in MRI. *IEEE Transactions on Medical Imaging* **26**(3) (2007) 405–421
2. Ahmed, M.N., Yamany, S.M., Mohamed, N., Farag, A.A., Moriarty, T.: A modified fuzzy c-means algorithm for bias field estimation and segmentation of MRI data. *IEEE Transactions on Medical Imaging* **21**(3) (2002) 193–199
3. Van Leemput, K., Maes, F., Vandermeulen, D., Suetens, P.: Automated model-based bias field correction of MR images of the brain. *IEEE Transactions on Medical Imaging* **18**(10) (1999) 885–896
4. Axel, L., Constantini, J., Listerud, J.: Intensity correction in surface coil MR imaging. *American Journal of Roentgenology* **148**(2) (1987) 418–420
5. Sled, J.G., Zijdenbos, A.P., Evans, A.C.: A nonparametric method for automatic correction of intensity nonuniformity in MRI data. *IEEE Transactions on Medical Imaging* **17**(1) (1998) 87–97
6. Salvado, O., Hillenbrand, C., Zhang, S., Wilson, D.L.: Method to correct intensity inhomogeneity in MR images for atherosclerosis characterization. *IEEE Transactions on Medical Imaging* **25**(5) (2006) 539–552
7. Collins, D., Zijdenbos, A., Kollokian, V., Sled, J., Kabani, N., Holmes, C., Evans, A.: Design and construction of a realistic digital brain phantom. *IEEE Transactions on Medical Imaging* **17**(3) (1998) 463–468

2D-3D Nonrigid Registration of Vascular Structures for Liver Chemoembolizations

M. Groher¹, D. Zikic¹, N. Navab¹

¹Technische Universität München, CAMP, {groher,zikic,navab}@cs.tum.edu

In this work, we introduce a method capable of deformably registering 3D vessel structures to a respective single projection of the scene. Our approach addresses the inherent ill-posedness of the problem by incorporating a priori knowledge about the vessel structures into the formulation. We minimize the distance between the 2D points and corresponding projected 3D points together with regularization terms encoding the properties of length preservation of vessel structures and smoothness of deformation. We demonstrate the performance and accuracy of the proposed method by quantitative tests on synthetic examples as well as real angiographic scenes.

1. Introduction

Angiographic imaging is a widely used technique for visualization of vessel anatomy in diagnosis and treatment. During most abdominal catheterizations, contrasted 2D projections from one view are acquired by a C-arm for catheter guidance and treatment monitoring. A 3D angiographic scan is usually acquired preoperatively to assess the region of interest and identify possible complications for the treatment. In clinical practice, the available 3D information is currently not brought to the interventional room. Only guided by images from one view, it is often very difficult for the physician to find a path through the patient's vessel system mainly due to overlay of vessel structures and breathing deformation. An accurate registration of 3D to 2D vasculature would yield one-to-one vessel feature correspondences, which can be used for intraoperative 3D roadmapping or catheter tip backprojection. With this 3D enhancement of angiographic interventions, both increase in depth perception and decrease in injected contrast agent can be achieved. In abdominal or thoracic regions that are subject to deformation, these correspondences cannot be established by a mere rigid or affine transformation model. Instead, it is necessary to create a 3D deformation field that locally deforms the 3D vasculature such that its projection matches the

2D vasculature. For 3D-3D registration of vascular images, methods have been developed to compute the deformation field from sparse correspondences that are determined manually or through rigid pre-alignment [1]. However, the computation of a dense 3D deformation field from sparse 2D-3D feature correspondences is in general an ill-posed problem: The displacement of a point along the projection ray cannot be computed without additional constraints, compare Fig. 1. Currently, methods for 2D-3D alignment of vascular images use a rigid transformation model discarding local motion.[2] Such algorithms tend to be robust against deformation changes of vessel structures but do not solve for these changes, leaving a considerable amount of misalignment, which can be, as reported for e.g. liver, up to 2 cm [3]. In order to overcome the shortcomings of the rigid approach, we propose a method for computing a meaningful deformation of a 3D structure from a single 2D projection, which minimizes an energy consisting of a difference measure and regularization terms, which incorporate the a priori knowledge about the problem, see Fig. 2. The difference term used in our approach penalizes the distance between the projection of 3D points from the input vasculature, represented as nodes of a centerline graph, and the corresponding points from the 2D projection image. Minimizing only the difference term results in what we refer to as the Naive approach, which is not able of recovering the deformation in the projection direction and thus leads to unnatural results. In order to overcome this problem we employ a combination of two regularization terms, which model assumptions about vessel structures and thus yield realistic deformations. The first term describes the assumption that the length of vessels does not change heavily inside the human body and penalizes large changes of the vessel length. Since this term models a soft constraint, the assumption is valid from a medical point of view in a soft tissue environment like liver. Although the length preservation itself is successful, in these cases the property that the nearest solution to the initial position is computed introduces unnatural bends in the vessels, thus leading to unwanted results. In order to counteract this effect, we impose a smoothness condition on the resulting displacement field. This is done by using the standard diffusion regularization term.

2. Method

As input for our method we use an extracted model of 2D and 3D vasculature, as well as a feature-based rigid pre-alignment in a calibrated setting yielding a projection matrix and correspondence information between

2D and 3D feature points. All of these steps have been previously presented in the literature and are not within the scope of this paper. A graph model is created in both 2D and 3D from a region growing step yielding vessel segmentations, followed by topological thinning and bifurcation detection as described in [4]. A rigid 2D-3D registration is computed by distance minimization of 2D and projected 3D centerline curves as has been successfully applied to vessels (see e.g. [2]) solving for both a projection matrix and correspondences of centerline points. If corresponding information is not available at each centerline point, a closest point operator can be incorporated after the rigid registration to assign one-to-one correspondences to all curve points. If ambiguities arise in this assignment due to projection overlay of vessel structures, these features can be left out of the correspondence set, which does not influence the proposed method.

The Model:

The deformable registration process is described as a minimization of the energy function E with respect to the displacements ϕ of the vessel nodes in order to get the estimate ϕ' of ϕ , that is $\phi' = \arg \min_{\phi} D + \alpha S_L + \beta S_D$. We use the standard gradient descent optimization scheme to minimize the energy term.

Difference Measure The difference measure D which drives the registration process penalizes the distance between the projection of 3D points from the input graph and the corresponding 2D points from the input projection image. Given point correspondences $\{X_i \leftrightarrow x_i\}$ and a projection function $f : \mathbb{R}^3 \rightarrow \mathbb{R}^2$, we can define the distance measure

$$D = 1/n \sum_n \|x_i - f(X_i + \phi)\|^2.$$

Length Preservation Constraint We define the terms $d_i^-(\phi)$ and $d_i^+(\phi)$, which measure the length of the edges connected to the sampling node X_i for a given set of displacements ϕ by $d_i^-(\phi) = \|Y_i - Y_i\|^2$, and $d_i^+(\phi) = \|Y_i - Y_i\|^2$, where $Y_i = X_i + \phi$. Now we can define the length preserving cost function as

$$S_L = 1/n \sum_n |d_i^-(0) - d_i^-(\phi)|^2 + |d_i^+(0) - d_i^+(\phi)|^2,$$

which penalizes the deviation from the initial length of the two edges which are directly influenced by the i -th node.

Diffusion Regularization This term is often used in order to impose a smoothness constraint onto the displacement field and is defined as

$$S_D = 1/n \sum_n \|\hat{\varphi}_i^{(x)}\|^2 + \|\hat{\varphi}_i^{(y)}\|^2 + \|\hat{\varphi}_i^{(z)}\|^2,$$

where $\hat{\varphi}^{(d)}$ is defined by using the dense version of the displacement field, which is computed using the 3D TPS.

3. Results and Evaluation

In order to validate our results, besides visual inspection, we compute two different quantitative error measures. The first is the 3D euclidean distance between the nodes of the ground truth (GT) structure and a given graph. Since this first measure does not take topology into account we also introduce a second measure, which does not penalize the position, but only evaluates the shape. At every node, the angle between the two adjacent edges is computed. The error evaluation is summed up in Tab. 1. We perform the tests on synthetic graphs with artificial deformations in order to test various aspects of the method (compare Synth 1, 2, 3). To demonstrate the applicability for real applications, we apply our method to two real vessel data sets, segmented from angiographic images. In the first test with real data, we use a liver data set (Liver 1) from a patient who suffers from hepatocellular carcinoma compare Tab. 1. Since the natural deformation field is not available, the vessel structures are deformed by an artificial field in order to be able to perform quantitative measurements. In order to verify our method on possibly natural deformations we employ the results presented by [3]. The displacement fields provided by this work are computed from a series of contrasted 4D MR images of the liver. We segment the vessel structures from the contrasted MR images, and generate the input 3D graph for our method. A projection matrix yielding an anterior-posterior image was used for 2D input creation. In the same way as for the synthetic data sets, the 3D ground truth together with initial and deformed 3D input graph is used to quantitatively assess the performance of our method. Despite the small deformation observable in the data set (Liver 2), a clear improvement is achieved. Compare Tab. 1.

4. Conclusion

In this paper, we present a method for deformable registration of 3D vessel structures to a single 2D projection image. By combining a difference measure with constraints resulting from valid assumptions, we improve the

rigid spatial alignment of the 3D vessel, which up to now presents the state of the art for this problem. The improvement in the spatial alignment is important for 3D depth perception and navigation during interventions. Quantitative and qualitative tests on medical and synthetic data sets demonstrate the improvement achieved by our method.

References

- [1] A. Charnoz, V. Agnus, G. Malandain, C. Forest, M. Tajine, and L. Soler, "Liver registration for the follow-up of hepatic tumors," in MICCAI, Lecture Notes in Computer Science 3750, pp. 155–162, Springer, 2005.
- [2] M. Groher, N. Padoy, T. Jakobs, and N. Navab, "New CTA protocol and 2D-3D registration method for liver catheterization," in MICCAI, Lecture Notes in Computer Science 4190, pp. 873–882, 2006.
- [3] von Siebenthal, M., Szekely, G., Gamper, U., Boesiger, P., Lomax, A., Cattin, and Ph., "4d mr imaging of respiratory organ motion and its variability," *Phys. Med. Biol.* 52, pp. 1547–1564, February 2007.
- [4] D. Selle, B. Preim, A. Schenk, and H.-O. Peitgen, "Analysis of vasculature for liver surgery planning," *IEEE Trans. on Medical Imaging (TMI)* 21(8), pp. 1344–1357, 2002.
- [5] S. J. Weickert and C. Schnörr, "A theoretical framework for convex regularizers in pde-based computation of image motion," *International Journal of Computer Vision* 45(3), pp. 245–264, 2001.

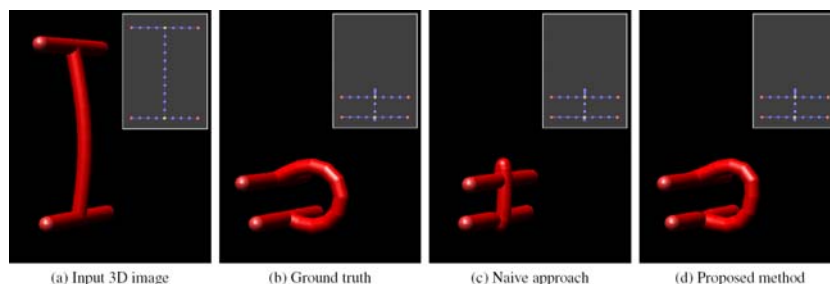


Fig 1.

Test Type	Data	Position Error [mm]		Shape Error [rad]	
		μ	σ	μ	σ
Synth 1	Input	4.46	3.58	0.5847	0.7769
	Result	0.19 (95.8%)	0.05	0.0723 (87.6%)	0.0583
Synth 2	Input	1.36	1.09	0.3224	0.3628
	Result	0.22 (83.5%)	0.11	0.0254 (92.1%)	0.0192
Synth 3	Input	1.42	0.80	0.3463	0.1990
	Result	0.56 (60.3%)	0.37	0.1503 (56.6%)	0.1317
Liver 1	Input	7.38	2.23	0.1675	0.1676
	Result	3.25 (56.0%)	2.89	0.1106 (33.9%)	0.1277
Liver 2	Input	1.20	0.65	0.0082	0.0093
	Result	0.96 (19.7%)	0.74	0.0057 (30.3%)	0.0075

Tab 1.

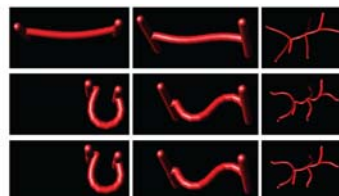


Fig 2.

Taking endoscopy to a higher dimension: Computer Aided 3-D NOTES

*K. Höller¹, M. Petrunina², J. Penne², A. Schneider³,
D. Wilhelm³, H. Feußner³, J. Hornegger¹*

¹*Chair of Pattern Recognition (LME), Friedrich-Alexander-University Erlangen-Nuremberg, {hoeller,hornegger}@informatik.uni-erlangen.de*

²*Department of Medicine I (MEDI),
Friedrich-Alexander-University Erlangen-Nuremberg,*

³*Workgroup for Minimal Invasive Surgery (MITI),
Klinikum r. d. Isar, Technical University Munich*

With a novel approach, abdominal surgery can be performed through the natural orifices with a following incision in stomach or colon. "Natural Orifice Translumenal Endoscopic Surgery" (NOTES) is assumed to offer significant benefits to patients such as less pain, faster recovery, and better cosmesis than current laparoscopic techniques. The potential advantages can be only achieved through secure and standardized operation methods. Several barriers identified for the clinical practicability in flexible intra-abdominal endoscopy can be solved with computer-assisted surgical systems. For some of them additional 3-D information is useful, for some it is mandatory. At our institute a 3-D endoscope called Multisensor-Time-Of-Flight (MUSTOF) endoscope is in development. In this paper some MUSTOF based solutions for NOTES will be pointed out: The so obtained 3-D information can be registered with preoperative CT or MR data. These enhanced volumes can be used to find the transgastric or transcolonic entry point or to provide better orientation. It also will enable intra-operative collision prevention and an optimized field of off-axis view. With such a progressive endoscopic system, translumenal surgery will be able to be performed in a safe and feasible manner.

1. Introduction

In medical applications 3-D information can be acquired by endoscopic ultrasound [1], magnetically anchored instruments [2] or active optical approaches like a modulated light source. The last one is used with our MUSTOF system [3] and measures distance by its dependency on time of flight (TOF) which causes a detectable phase shift, so it is called TOF technology [4]. With a precondition of real-time ability and an accuracy of 1mm, existing problems with NOTES can be solved. Especially registered with preoperative CT or MR volumes there will be great improvements possible.

2. NOTES

In 2003 and 2004, the first documented human NOTES procedures were performed in India. In March 2007, first hybrid transvaginal cholecystectomies were reported in the USA and France [5]. NOTES offers a great area of active research in experimental endoscopy and has the potential to significantly advance the field of minimally invasive surgery [6]. So in July 2005 leading surgeons and gastroenterologists met together in New York City to coordinate further research activities in NOTES. They founded the Natural Orifice Surgery Consortium for Assessment and Research (NOSCAR). In a White Paper they addressed fundamental challenges to the safe introduction of NOTES and discussed potential barriers [7]. Three points seem to be solvable with additional 3-D data.

2.1. Peritoneal access

Transluminal surgery offers challenging possibilities for trauma reduction. Current investigations are mainly focused upon optimization of the access routes and its safe closure [8]. Not also the route, but above all the optimal location of the secure introduction of the instrument into the abdominal cavity is hard to find. To visualize the vessels on the reverse side of the hollow organ and so to reduce the risk of lacerations would be a great improvement.

2.2. Maintaining spatial orientation

In contrast to gastroenterologists, who are accustomed to working in line with their camera and light source, laparoscopic surgeons normally use multiple instruments and access ports. According to the white paper many NOTES procedures will be performed with the endoscope in a retroflexed position where the image is upside down and an off-axis manipulation is required. Potential solutions to perform advanced procedures with two or more instru-

ments and assistants include incorporating visualization systems and electronic image stabilization/ inversion. If the principles learned in advanced laparoscopic operations are applicable to NOTES, then orientation, as well as triangulation, will be fundamental requirements for any NOTES surgical system [7].

2.3. Development of a multitasking platform

Because some procedures will require a team to manipulate instruments, devices with multiple ports are likely to be important. The role of robotics in this area seems promising, though a great deal of development work remains to be done. Development should focus on manual tools that ultimately can be modified for robotic control [7]. Several approaches with computer-assisted surgical systems [9] require additional 3-D information to prevent injury or navigation errors.

3. 3-D endoscopy contributions

3.1. Orientation

To provide more information on position and orientation of the robotic device or the endoscope intraoperative 3-D data could be registered with preoperative CT or MR data. With the aid of the calculated transformation parameters, position and orientation can be represented, corrected and visualized.

3.2. Augmented Reality

Registration with preoperative volumes opens up lots of additional possibilities. The most promising one is to show hidden organs or vessels by augmented reality. They have to be segmented in the preoperative volumes and to be transformed by iteratively computed transformation parameters. Then these organs and vessels can be displayed by Augmented Reality (AR). This additional information is needed to avoid injuries, e.g. while finding the entry point to the peritoneal cavity which requires a wall incision in stomach or colon without knowledge of structures behind the visible wall.

3.3. Enhanced field of view

Endoscopic axis in-line view and loss of spatial orientation is especially for surgeons quite uncomfortable. To compensate this disadvantage, 3-D surface knowledge can be used to extend and virtually rotate the field of view (fig. 1).

Using a 3-D mosaicking technique, field of view can be extended by reconstruction of the operation area.

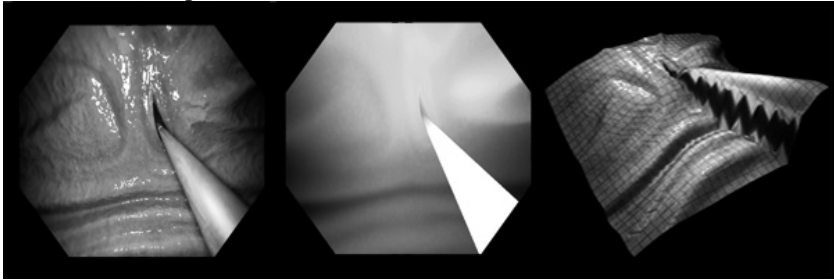


Fig. 1. l.: conventional color image, c.: depth values, r.: off-axis view

3.4. Collision Prevention

The increasing demand of robotic devices to control multiple instruments through only one flexible endoscope needs additional control mechanisms to avoid unintentional injuries. To enable efficient collision prevention, real-time distance information is needed. Avoidance of impending tissue injury or collision with other instruments can be realized as well as auto-positioning depending on respiration or other patient movements. For the spectrum of endoscopic surgery there is an urgent demand for a stable platform for secure movement and stabilization of the tissue during the operation in the peritoneal cavity.

4. Conclusion

Having additional 3-D data will not be an unalterable precondition for performing NOTES. But it will help especially a safer introduction of robotic devices and surgeons who are not used to flexible endoscopy with in-line-view and loss of orientation. Since gastroenterologists and surgeons are still not absolutely familiar with this new NOTES approach, they both will accept new technologies more likely than with established procedures.

References

- [1] A. Fritscher-Ravens, C. A. Mosse, K. Ikeda, and P. Swain, "Endoscopic transgastric lymphadenectomy using EUS for selection and guidance," *Gastrointest Endosc*, vol. 63, no. 2, pp. 302–306, Feb 2006.

- [2] D. J. Scott, S. J. Tang, R. Fernandez, R. Bergs, M. T. Goova, et al., “Completely transvaginal NOTES cholecystectomy using magnetically anchored instruments,” *Surg Endosc*, vol. 21, no. 12, pp. 2308–2316, Dec 2007.
- [3] J. Penne, K. Höller, S. Krüger, and H. Feussner, “NOTES 3D: Endoscopes learn to see 3D; basic algorithms for a novel endoscope,” in A. H. Arajo, H. Vitri, J. (Eds.): *Proceedings of VISAPP 2007*, 2007, pp. 134–139.
- [4] R. Lange, 3D Time-of-flight distance measurement with custom solidstate image sensors in CMOS/CCD-technology, Ph.D. thesis, Department of Electrical Engineering and Computer Science at University of Siegen, 2000.
- [5] J. Hochberger, K. Matthes, P. Köhler, et al., “NOTES a perspective for gastrointestinal medicine,” *Endosk. heute*, vol. 21, no. 1, pp. 2–5, Mar 2008.
- [6] S. von Delius, S. Gillen, E. Doundoulakis, et al., “Evaluation of different transgastric access techniques for NOTES,” *Endoscopy*, vol. 39, no. 10, pp. 854– 859, Oct 2007.
- [7] D. Rattner and A. Kalloo, “ASGE/SAGES working group on natural orifice transluminal endoscopic surgery october 2005,” *Surg Endosc*, vol. 20, no. 2, pp. 329–333, Feb. 2006.
- [8] D. Wilhelm, A. Meining, S. von Delius, M. Burian, S. Can, A. Fiolka, et al., “Second generation sigmoid access for NOTES using the ISSA-system,” *Endoskopie heute*, vol. 21, no. 1, pp. 70, Mar 2008.
- [9] F. Härtl, K. Höller, S. Beller, and H. Feußner, “Current status of the use of medical robots in Germany, Austria and Switzerland,” in 3rd Russian- Bavarian Conference on Biomedical Engineering, J. Hornegger, E. W. Mayr, S. Schookin, H. Feußner, N. Navab, Y. V. Gulyaev, K. Höller, and V. Ganzha, Eds., Erlangen, 2007

Bolus Detection in Colon MRI

A. Keil¹, C. Harrer¹, S. Kirchhoff², C. Kirchhoff², T. Mussack³,
A. Lienemann², M. Reiser², N. Navab¹

¹*Technische Universität München, CAMP, Germany, keila@cs.tum.edu*

²*Institute of Clinical Radiology, University Hospital Munich, Germany*

³*Department of Surgery, University Hospital Munich, Germany*

Although an exact differentiation of the causing pathologies causing functional gastrointestinal disorders is essential for adequate therapy, diagnosis is still only based on a clinical evaluation [1]. Regarding quantification of constipation only the ingestion of radio-opaque markers or radioactive isotopes and the consecutive assessment of colonic transit time using X-ray or scintigraphy, respectively, has been feasible in clinical settings [2]. Most recently a new technique for the assessment of colonic transit time using MRI and MR-contrast media filled capsules has been introduced [3], avoiding the exposure of the patient to ionizing radiation. The aim of our work was to develop a computer tool to facilitate the detection of the capsules in T1-weighted MRI datasets and thus to shorten the evaluation time which is rather high for the multiple data sets to be examined per patient. We present a semi-automatic tool which provides an intensity, size [4], and shape-based [5,6] detection of ingested contrasted capsules. After an automatic pre-classification, radiologists may easily correct the results using the user interface, therefore decreasing the evaluation time significantly. A longer version of this paper can be found in [7].

1. Introduction

Different forms of chronic constipation have to be differentiated: a) normal-transit constipation and b) slow-transit constipation with pathological, prolonged transit times. The differentiation of the causing pathologies is essential for adequate therapy. Recently, a new technique for the assessment of colonic transit time using MRI and Gd-DTPA-saline-filled capsules (see Figure 1, left) was introduced in the literature [3]. Due to numerous examinations and images/examination, data-evaluation is time-consuming.

Therefore, the aim was to develop a computer-aided detection tool prototype to facilitate the finding of the capsules in MR-datasets, thus to shorten the evaluation time of the colonic transit.



Fig. 1: Left: Enlarged image and model of the capsule being ingested after filled with contrast agent and saline. Right: User interface with automatic classification and correction possibilities.

2. Methods

An interactive slice browser (see Figure 1, right) was developed providing a quick overview of the image data. The user selects a region of interest, where an automated screening for the capsules is performed. After screening, the detected objects are shown colored in the corresponding slices. False negative and false positive findings can be added or removed, respectively, by the radiologist. Several image processing methods like signal intensity thresholding, connected component analysis, and principal component analysis were applied enabling the combination of several criteria for an automatic capsule detection.

2.1. Thresholding

For better visibility in MRI volumes, the capsules ingested by the patients were filled with Gd-DTPA-saline-mixture yielding a fairly high signal intensity. Thus, intensity thresholding [4] was applied as a first segmentation step. A suitable threshold value was selected by manually looking for capsule-images in a certain number of volumes.

However, selecting a threshold value for segmenting the contrast agent filled capsules is rather difficult because the cross section of the capsule and thus the visible signal of contrast agent may vary. Since other classification criteria will be applied in the following stages of the capsule detection, the threshold value is chosen so that usually all capsules are segmented, leading to many false positives but no false negative findings at this stage (see Figure 2).

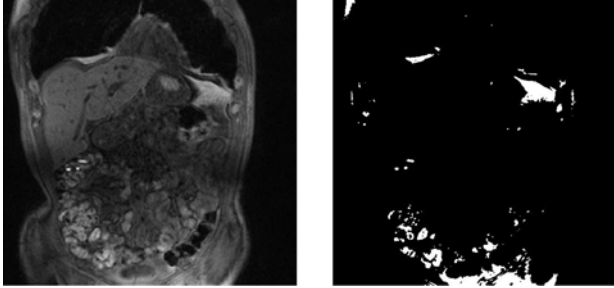


Fig. 2: Original and thresholded T1-weighted MR-image. Three capsules are located in the middle-left area of the slice. They are properly segmented but a lot of high-intensity artifacts (= false positives) are remaining when using the current threshold value.

Intensity thresholding is a very useful and computationally inexpensive first step because it preprocesses the data so that more elaborate classification criteria based on shape- and volume-analysis can be applied thereafter.

2.2. *Connected Component Analysis for Volume Discrimination*

After having segmented voxels with high intensity, a connected components analysis [4] has to be performed in order to extract separate objects. The resulting objects can then be analyzed with respect to their volume as well as their shape. The exact dimensions of the real capsules are known and are used to compute their volume (approx. 520mm^3). An extracted object's volume can then be used as a criterion of discrimination. However, due to anisotropic image resolution ($0.78\text{mm} : 0.78\text{mm} : 2\text{mm}$ in first tests), the voxel count of one capsule may strongly vary, depending on the capsule's position and orientation w.r.t. the coordinate axes of the imaging system (see Figure 3, left) and the range of acceptable object voxel counts has to be set rather wide.

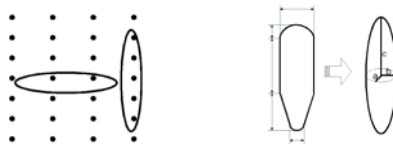


Fig. 3: Left: Dependence of the voxel count on position and orientation for highly anisotropic data sets. Right: Approximation of capsule shape by ellipsoid with three principal components.

2.3. *Principal Component Analysis for Shape Analysis*

Since the intensity as well as the volume tests performed up to this stage can only use weak conditions due to the highly varying image representation of the capsules, a last, shape-based criterion is added to the analysis. The capsules are modeled as ellipsoids with a ratio of the three main axes (= principal components) $a:b:c = 1:1:4$ derived from the actual measurements of the capsules (see Figure 3, right).

The principal axes of one segmented object are computed using principal components analysis (PCA) and then compared to the ratios mentioned above. Principal components analysis [5,6], in the literature also referred to as proper orthogonal decomposition (POD) or Karhunen-Loève transformation is a method used in many scientific fields such as statistical data analysis and image processing. In our case, where the data represents a scatter plot in 3D-space, PCA tries to treat this point cloud as a representation of an ellipsoid which can be exactly described by the directions and lengths of its main axes, the principal components.

If the analyzed object is the image of a colon capsule, the ratio of its main axes $a:b:c$ should be roughly $1:1:4$, enabling us to introduce an additional shape based classification criterion for capsule detection. As error measure, we use $E = |a/b - 1| + |c/a - 4|$, penalizing deviations from the assumed ellipsoid's axes ratios. Only objects with E not exceeding a certain threshold were accepted as possible capsules.

3. Results

As mentioned before, all of the three criteria used (intensity, volume, and shape) are subject to high variance. However, the shape-based measure turned out to be quite accurate. This was the reason for pursuing a multi-stage approach of sorting out object candidates based on weak conditions for intensity and volume and then using the (computationally most expensive but also most accurate) shape criterion in the last step.

In an evaluation experiment on seven datasets more than 50% of the visible capsules were automatically detected by our algorithm, leaving only the false positive findings to the radiologist to be removed (Figure 4). The inhomogeneous resolution of the available image data turned out to be the greatest challenge for the segmentation task. Since we designed our software tool with a function providing the opportunity to delete obvious false positives by simply clicking on them, a relatively high number of false positives is tolerable.

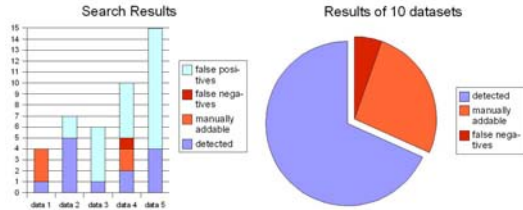


Fig. 4: Results of the study used to evaluate the detection results.

4. Conclusion

The implemented user interface presents a great improvement compared to a manual evaluation performed by the radiologist in terms of scrolling through all images of one dataset looking for the capsules. Capsule candidates are extracted automatically and false positive findings can be removed by the radiologist in very fast and effective way. The average time needed to correctly locate all capsules in one dataset was considerably decreased with a resulting approximate time effectiveness of 2-3 minutes per dataset. The faster and more comfortable evaluation provided by the computer-aided detection tool presented in this work offers the possibility of using the new MR-based transit time assessment in clinical routine.

References

- [1] Lembo and Camilleri. Chronic constipation. *N. Engl. J. Med.* 349, 1360-1368 (2003)
- [2] Hinton, Lennard-Jones, and Young. A new method of studying gut transit times using radiopaque markers. *Gut* 10, 842-847 (1969)
- [3] S. Buhmann(=Kirchhoff), C. Kirchhoff, Ladurner, Mussack, Reiser, and Lienemann. Assessment of colonic transit time using MRI: A feasibility study. *Eur. Radiol.* (Epub ahead of print), (2006)
- [4] Gonzalez and Woods. *Digital Image Processing*. Prentice Hall (2002)
- [5] Chatterjee. An introduction to the proper orthogonal decomposition. *Current Science* 78(7), 808-817 (2000)
- [6] Pearson. On lines and planes of closest fit to systems of points in space. *Philosophical Mag.* (1901)
- [7] Harrer, S. Kirchhoff, Keil, C. Kirchhoff, Mussack, Lienemann, Reiser, Navab. Semi-automatic detection of Gd-DTPA-saline filled capsules for colonic transit time assessment in MRI. *SPIE Med. Imag.* 2008

Analysis of artificial heart period series for time domain convergence

A. Maistrou^{1,2}

¹*Technische Universität München, maistrov@in.tum.de*

²*Bauman Moscow State Technical University*

In this paper a motivation for analysis and development of synthetic heart period signals is discussed. An overview of existing models for artificial heart period signals is presented. The most appropriate model for spectral analysis methods standardization is selected and extended. For time domain convergence analysis direct comparison of time domain heart rate variability measures between real signals and artificial signals with the same spectral measures is performed.

1. Introduction

The variation in the timing between beat occurrences of the cardiac activity, known as heart rate variability (HRV), has been shown to be vital noninvasive indicator of cardiovascular, autonomic system function and overall health condition [1-2]. Usually HRV is analyzed from the heart period (HP) or corresponding heart rate (HR) series that is formed by a sequence of heart period length values at time instants of heart beat occurrence. Quantification of HRV is mathematically derived from HP signal, and results are generally classified to time domain, frequency domain and nonlinear dynamics indexes. While nonlinear dynamics analysis of HRV is comparatively young, spectral analysis has been shown to have the best balance between amount of recovered information and length of HP records.

In spite of shown HRV indexes analysis efficiently in diagnostics [1], there is still no consensus on the applicability of HRV in literature. Variety of mathematical methods, its formulations and assumptions for particular HRV analysis causes serious bias in the outcomes of different authors implementing the same tests [3]. Further direct comparison of these results stimulates spurious conclusions and common distrust to the HRV method. Especially this problem affects spectral analysis of HRV since there are a lot of mathematical methods for spectrum recovery (for stochastic signals,

including HP signal, spectral analysis imply power spectral density (PSD) function estimation), and their results can vary considerably [4].

Fundamental problem that confuses HRV spectral measures is a lack of complete understanding of real underlying HRV dynamics and its physiological origins. At this conjecture it is problematic to do direct validation and build up standardization of methods for spectral analysis of HRV, since “golden standard” method is not chosen. Comparison of methods using synthetic signals is a possible way out, since their characteristics are known and thus, it is possible to compare efficiency of the spectral analysis methods. But then, synthetic signals should be realistic enough to take into account all most important features of real signals during standardization process, what was a motivation for this work.

1.1. Existing models for generation artificial heart period series

There is comparatively a little number of works focusing on analysis and improvements of ordinary HP series to make it more realistic. Modeling heart rate variability during special physiological events (vaso-vagal syncope, sleep apneas) is more popular. However, there are different approaches to model HRV:

Integral Pulse Frequency Modulator (IPFM) model, which is widely used for a generation of normal sinus beats, representing HRV through integrated modulation function;

Time domain modeling using a set of sinusoidal components, corresponding to HP signal oscillations;

Creation of HP signal by transforming its PSD function, which is directly set up [5].

Idea of modeling directly in frequency domain was used for the current research, because it provides the best accuracy for spectral domain error estimation, since true model spectra is given. While this model is already used for analysis of different HRV phenomenas (analysis of artifacts, missing data [8]), there is still no intensive studies on proving correctness of resulting artificial HP dynamics.

2. Modeling of heart period series through frequency domain

Direct modeling of PSD components was introduced in [6] and then extended in [7], where PSD function is represented as a sum of three Gaussian distributions in VLF (0.0033 – 0.04 Hz), LF (0.04-0.15 Hz) and HF (0.15-0.4 Hz) diapasons. Additional extension presented in this work, linked

to investigation of realistic spectrum magnitude irregularity. Irregular spectral components are formed by multiplication of initial Gaussian distributions with Beta distribution. Normalization of spectrum components is applied to preserve cumulative signal power content. Original and distorted PSDs are shown in Fig.1(a-b). Indeed, artifacts and noise cause distortions in the true spectra, and for short 5 minutes records of the HP signal it is impossible to get sufficient frequency components' averaging (especially in VLF region).

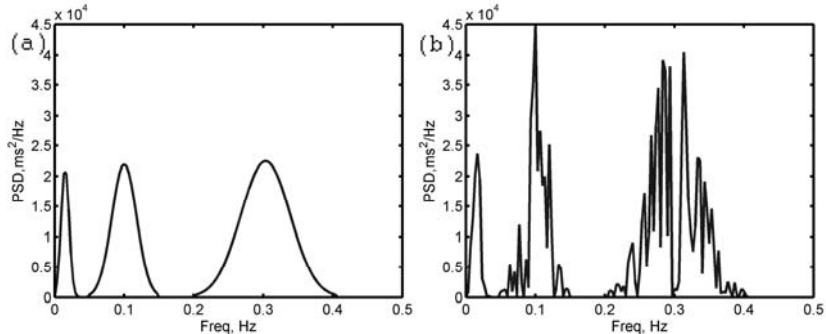


Fig. 1: Power spectral density function of artificial heart period signal before (a) and after (b) distortion

Before transformation to time domain can be executed, corresponding phase function should be initialized. Phase content of the signal is set randomly. It ensures uniqueness of the HP signal in time domain at each generation. Magnitude and phase functions are transformed to the time domain HP function using inverse fast Fourier transform (IFFT). Realistic irregular sampling peculiar to HP signals also introduced using the algorithm presented in [8].

2.1. Time domain convergence analysis of the artificial signals

Time and frequency domain measures of HRV [1] represent dominant part of available HRV indexes. While frequency domain convergence of the described artificial HP series is ensured by definition, it is important to analyze accuracy of corresponding time domain parameters, as well as its stability in case of spectral distortions presence. Disparity measures between time domain parameters of real HP series and artificial HP series are used as indexes of time domain convergence of artificial HP series.

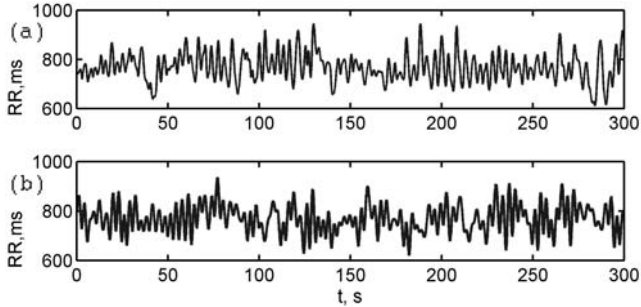


Fig. 2: Interpolated real heart period signal (a) and corresponding artificial heart period signal (b) with identical spectra

ECG records of 20 young volunteers (21-34 years) in supine resting, without cardiovascular diseases, 120 minutes in length, 250 Hz sampling rate were used for experiment. Analysis of data was performed on 5 minutes window with 30 seconds shift between windows resulting in 4500 analyzed fragments. For each interval time domain and frequency domain measures were calculated. For spectral analysis cubic spline interpolation, 10 Hz resampling and Welch's fast Fourier transform (FFT) were used. Example of original real HP signal and its artificial exemplar is presented at Fig.2(a-b). After estimation of HRV spectral measures, artificial time series was built using introduced algorithm and time domain parameters for the modeled signal were calculated. Table 1 keeps a list of means (M) and standard deviations (SD) of error in measures recovery using artificial time series with using beta distortion and without (for time domain measures notation see [1], Table 1).

Table 1. Analysis of errors in frequency domain

Measure	Without β -distrib.		$\alpha=0.5, \beta=0.5$		$\alpha=1, \beta=3$	
	M,%	SD,%	M,%	SD,%	M,%	SD,%
SDNN	-0.83	14.35	-0.87	14.43	-0.78	13.22
SDSD	-1.79	10.21	-1.69	12.12	-1.63	10.71
RMSSD	5.53	10.27	5.43	10.32	5.42	10.19
pNN50	19.15	27.39	18.35	30.13	18.26	29.88
Triang.ind	-5.44	15.36	-7.12	16.03	-5.49	14.32
TINN	2.23	14.98	2.08	14.88	2.33	14.49

3. Discussion and Conclusions

Results presented in Table 1 demonstrates that presented method for artificial time series generation can represent significant part of time domain information with a good accuracy and thus, potentially can support standardization of frequency domain methods process. Severely biased parameters (like PNN50) definitely represent nonlinear components of HRV dynamics and additional modifications in the modeling process should be applied for their correct recovery. Spectral distortion through beta distribution function has shown to have almost no influence on time domain parameters. In the current work, time domain convergence of signal modeled in frequency domain is presented, implying incremental step in the way of HRV spectral domain methods standardization.

References

- [1] M. Malik, "Heart rate variability: Standards of measurement, physiological interpretation, and clinical use," *Circulation*, vol. 93, pp. 1043–1065, 1996. M. Malik and A. J. Camm, *Heart Rate Variability*. New York: Futura, 1995.
- [2] M. Malik and A. J. Camm, *Heart Rate Variability*. New York: Futura, 1995.
- [3] G. Sandercock, C. Shelton, P. Bromley and D. "Brodie Agreement between three commercially available instruments for measuring short-term heart rate variability," *Physiol. Meas.*, 2004, 25: 1115–1124.
- [4] A. Pichon et al. "Spectral analysis of heart rate variability: interchangeability between autoregressive analysis and fast Fourier transform," *Journal of Electrocardiology*, 2006, 39: 31– 37.
- [5] Point:Counterpoint: Cardiovascular variability is/is not an index of autonomic control of circulation," *J Appl Physiol* 2006, 101: 676–682.
- [6] P. E. McSharry, G. D. Clifford, L. Tarassenko, and L. A. Smith, "Method for generating an artificial RR tachogram of a typical healthy human over 24-hours," *Comput. Cardiol.*, pp. 225–228, 2002.
- [7] D.C. McLernon et al, "New Nonlinear Model for Generating RR Tachogram," *Comp. in Card.* 2004, 31:481-484.
- [8] G.D. Clifford, L. Tarassenko, "Quantifying Errors in Spectral Estimates of HRV Due to Beat Replacement and Resampling," *IEEE Trans. on Biomed. Eng.*, 2005, 52: 630-638.

Embedded QRS Detection for Noisy ECG Sensor Data Using a Matched Filter and Directed Graph Search

B. Eskofier¹, J. Kornhuber² and J. Hornegger¹

*¹University of Erlangen-Nuremberg, Chair of Pattern Recognition
Martensstraße 3, Erlangen, Germany, {eskofier,hornegger}@cs.fau.de*

*²University of Erlangen-Nuremberg, Department of Psychiatry
Schwabachanlage 6, Erlangen, Germany, johannes.kornhuber@uk-erlangen.de*

Abstract

In a lot of medical as well as sports applications, the precise recognition of heart beat (HB) events in electrocardiogram (ECG) sensor signals is mandatory to facilitate subsequent diagnosis and analysis of the data. However, especially in the presence of motion, e.g. in sports or sleep monitoring, the signal-to-noise ratio of such signals can become very low. This paper discusses the accurate detection of the QRS complexes corresponding to heart beats in this noisy environment. The noise cannot be completely eliminated by traditional bandpass filtering because the signal bandwidth often has considerable overlap with the bandwidth of the artifact. We describe a novel method using a simple Matched Filter (MF) and subsequent directed graph search to accurately detect the QRS complexes in the ECG signal. When using the MF, a clean QRS template is correlated with the noisy signal. This procedure is optimal in the case of white noise. However, false detection of QRS complexes can occur because of the extraneous peaks added by motion artifacts. To circumvent this, we additionally perform a directed graph search, eliminating these extraneous peaks. The method can easily be implemented on the restricted hardware environment of customary embedded microprocessors. We demonstrate the effectiveness of our method by application to real ECG sensor data.

1 Introduction

Accurate QRS complex [1] detection in a mobile environment offers new opportunities for analysis and monitoring applications, e.g. in sports or homecare. We will show a reliable method for this detection that is implementable on mobile hardware, i.e. does not pose too many computational requirements.

2 Materials and Methods

Figure 1 shows two ECG example signals. While the heart beats can clearly be identified in Fig. 1(a), the presence of motion artifacts as exemplified in Fig. 1(b) severely complicates the recognition. Still, humans can identify the QRS complexes corresponding to heart beats. The most straightforward approach first selects likely events in the signal, then removes those

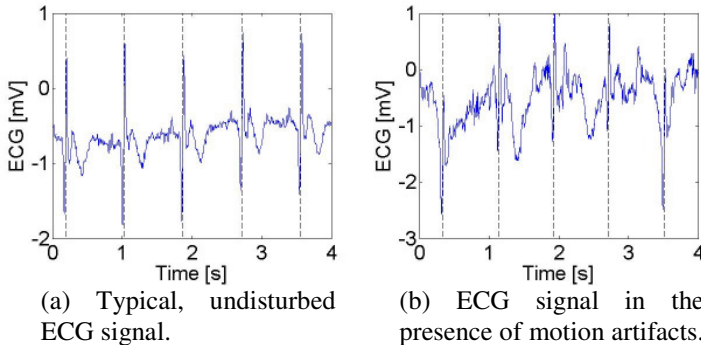


Fig. 1: ECG example signals. The dashed lines represent beat locations as identified by medical expert annotators [2].

event time points that can not represent HB because they would signify unnatural beat times.

Our proposed recognition procedure closely follows the human approach. We first detect likely heart beat events by applying a Matched Filter (MF) [3]. MFs are an established concept used in information transmission where the waveform of the original signal is known, see Figure 2. The coefficients of the filter are the time-reversed values of the sought signal. It can be shown that the MF maximizes the output SNR.

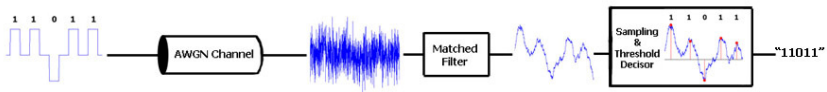


Fig. 2: MF application. Source: http://en.wikipedia.org/wiki/Matched_Filter.

In our case, the original waveform is also known from clear reference signals. We thus build a waveform prototype by averaging over $N = 100$ QRS complexes. The application of the MF to the noisy signal then gives us likely

HB time points, which is illustrated in Figure 3. The output shows some incorrect detected events that are due to the motion artifacts.

To remove these, we perform a graph search, eliminating these extraneous peaks. We interpret all peaks as vertices of a directed graph with weights, and iteratively add the most likely vertices. The algorithm is depicted in Figure 4 and works as follows: First, the mean distance d_m of the currently

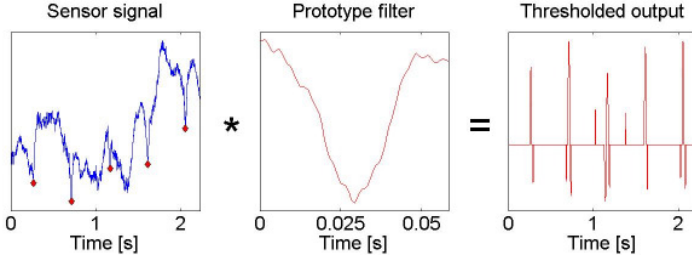


Fig. 3: Application of the MF prototype filter to the noisy signal. Correct heart beat locations are marked with diamonds in the leftmost plot.

examined $k = 5$ vertices is calculated and propagated to the next candidate heart beat locations, see Fig. 4, left. The next vertex is then set by taking the one that leads to the lowest distance of the current subset, which is depicted in Fig. 4, right. This process is then iterated. In the case that no likely candidate can be found, a maximum of one vertex at a time is inserted.

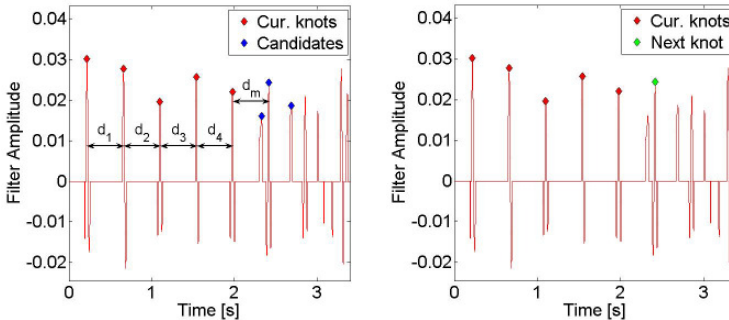


Fig. 4: Candidate search (left) and establishment of next vertex (right).

3 Experiments

We conducted our experiments using the MIT-BIH Noise Stress Test Database which is part of the PhysioBank signal archives [2]. In this database, half hour records of electrode motion artifacts have been added to clean half hour ECG recordings. Artifacts from electrode motion are considered the most troublesome, since they can mimic ectopic beats and cannot be removed easily by simple filters. By adding the noise in a controlled way, the SNR of the generated signal is known. The process is further described in [4]. The correct beat locations are known from the clean signal and have been annotated by experts. Two different subjects $S1$ and $S2$ are contained in the database with different SNR of noise added to the clean signal.

The performance of our algorithm is summarized in Table 1. For the different subjects, the half hour recordings were examined for decreasing SNRs. The percentages shown are those HB that do not differ more than $t_{max}=0.01s$ from the annotated time HB time points. Our algorithm proved to work reliably at all investigated levels of noise. The small number of misdetections can easily be smoothed out by a simple lowpass filter.

Subject	Nr. HB	SNR=24dB	SNR=18dB	SNR=12dB	SNR=6dB
$S1$	2166	99,6%	99,6%	99,4%	98,4%
$S2$	1543	99,7%	99,7%	99,6%	98,4%

Tab. 1: Summary of the algorithm performance for different SNRs.

All our algorithm components can easily be implemented on a microprocessor for mobile use. Matched Filters have already successfully implemented on such devices [5], the graph search and an additional lowpass filter do not demand too much computational power either.

4 Conclusions

We presented an algorithm for the detection of heart beats in ECG signals that exhibit artifacts due to the presence of motion. We first applied a MF to identify likely events in the signal; to remove erroneous HB we additionally performed a directed graph search. All presented algorithm components can be implemented on a microprocessor for mobile usage. We demonstrated the effectiveness of our method by application to real ECG sensor data and substantiated that our method works reliable. Even when the SNR decreases to 6dB, well over 98% of HB are detected correctly.

References

- [1] Mark, J.B., "Atlas of cardiovascular monitoring", Churchill Livingstone, New York; 1998.
- [2] Goldberger, A.L., Amaral, L.A.N., et. al., "PhysioBank, PhysioToolkit, and PhysioNet: Components of a New Research Resource for Complex Physiologic Signals", *Circulation* 101(23): e215-e220; June 2000.
- [3] Turin, G., "An introduction to matched filters", *IEEE Transactions on Information Theory*, 6(3): 311-329; June 1960.
- [4] Moody, G.B., Muldrow, W.E. and Mark, R.G., "A noise stress test for arrhythmia detectors", *Computers in Cardiology*, 11: 381-384; 1984.
- [5] Hahn, M.D., Friedman, E.G. and Titlebaum, E.L., "A comparison of analog and digital circuit implementations of low power matched filters for use in portable wireless communication terminals", *IEEE Transactions on Circuits and Systems II: Analog and Digital Signal Processing*, 44(6): 498-506; June 1997.

Hypertension Causes Lack of Recovery of Baroreflex Function After Heart Surgery

B Retzlaff^d, N Wessel², H Malberg³, G Brockmann¹, R Lange¹, R Bauernschmitt¹

¹German Heart Center Munich, ²University of Potsdam, ³University of Karlsruhe

1 Introduction

While the pathogenesis of essential hypertension is still widely unclear, data from the Framingham study suggest a correlation of decreased HRV and the development of hypertension [1]. Likewise, an association of BRS and hypertension was described in the older population [2]. From earlier studies we know, that cardiovascular autonomic function declines following heart surgery with a tendency to recover within 3-6 months [3]. The following prospective study was performed to analyse differences in the autonomic response to heart surgery between hypertensive and normotensive patients.

2 Methods

66 consecutive patients undergoing various types of open heart surgery were prospectively enrolled; 102 of them were hypertensive according to the WHO-criteria (systolic blood pressure above 140 mmHg, diastolic above 90 mmHg, or antihypertensive medication for more than 6 months). The mean age of our patients was 68 +/- 13 years. Patients with arrhythmias were excluded.

After 10-min equilibrations to the environment, non-invasive blood pressure signals were collected from the radial artery by a tonometer (Colin Medical Instruments) at 1000 Hz. Data were channelled into a bed-side laptop after A/D-conversion and stored for analysis. Simultaneously, breathing

excursions and a standard ECG were monitored. Data were sampled for a 30-min period the day before surgery at the hemodynamic laboratory and 24 hours after surgery on the ICU. Care was taken to perform the measurements during the same time of the day in each patient. From the recorded data the beat-to-beat intervals as well as the beat-to-beat systolic and diastolic values were extracted; premature beats, artifacts and noise were excluded using an adaptive filter considering the instantaneous variability .

3 Results

Time and frequency domain parameters of heart rate variability showed comparable dynamics in normotensive and hypertensive patients there was a pronounced decline 24h after surgery and partial recovery seven days after surgery (data not shown).

Baroreflex sensitivity showed a different behaviour throughout the postoperative course. Regarding the number of bradycardic regulations, there was a marked reduction in both groups 24h after surgery. After 7d partial recovery was observed in normotensive patients, while the values

remained unchanged in hypertensives (Fig. 1).

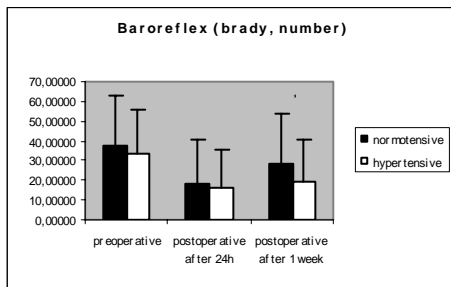


Fig. 1: BRS, number of bradycardic regulations

For the tachycardic regulation, values for number and strength of regulation were more or less unchanged one day after surgery, but were significantly decreased one week after the operation; this drop was more pronounced in the hypertensive group (Fig. 2).

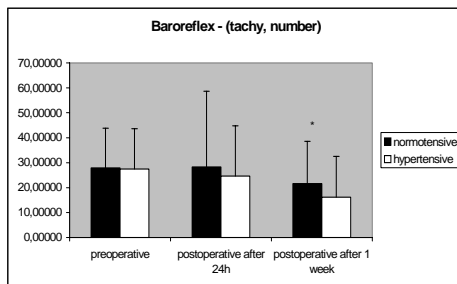


Fig.2: BRS, number of tachycardic regulations

4 Discussion and Conclusions

Although there still is a lack of knowledge concerning the pathogenesis of essential hypertension, a correlation to reduced baroreflex sensitivity and heart rate variability seems possible [1,2]. The analysis of BRS and HRV provides information about the individual risk in cardiac patients and is significantly altered in these patients as compared to healthy volunteers [3,4]. Therefore the aim of our study was to assess differences of autonomic regulation among normotensive and hypertensive patients in response to cardiac surgery.

We did not find major differences in the preoperative values, and we did not expect that, because our “control” group also suffered from cardiovascular diseases and therefore altered regulation can be assumed. The analysis of HRV-parameters did not disclose any major variations among the groups during the postoperative course.

Baroreflex sensitivity, however, was markedly reduced in hypertensives one week after surgery. This may explain the increased risk of patients with hypertension after cardiac surgery. Ongoing research is required for further clarification of the

pathophysiology of this phenomenon and to establish strategies to restore autonomic function.

Acknowledgements

This study was supported by grants from the Deutsche Forschungsgemeinschaft (DFG BA 1581/4-1, BR 1303/8-1, KU 837/20-1).

References

- [1] Liao D, Cai J, Barnes RW, Tyroler HA, Rautaharju P, Holme I, Heiss G. Association of cardiac autonomic function and the development of hypertension: the ARIC study. *Am J Hypertens.* 1996;9:1147-56
- [2] Harrington F, Murray A, Ford GA. Relationship of baroreflex sensitivity and blood pressure in an older population. *J Hypertens* 2000;18:1629-33
- [3] Bauernschmitt R, Malberg H, Wessel N, Kopp B, Schirmbeck EU, Lange R. Impairment of cardiovascular autonomic control in patients early after cardiac surgery. *Eur J Cardiothorac Surg* 2004;25(3):320-6.

Machine learning based prediction of compound behavior in CYP 3A4, CYP 2D6 and CYP 2C9

T. Girschick¹, T. Herz² and S. Kramer¹

¹Technische Universität München,

email: {tobias.girschick, stefan.kramer}@in.tum.de

²4SC AG, Martinsried, email: Thomas.Herz@4sc.com

Discovering and developing a new drug with as few side effects and drug-drug interactions as possible is known to be very time consuming and expensive. One family of metabolic relevant proteins responsible for side effects and drug-drug interactions are cytochrome P450 enzymes. They chemically interact with a broad spectrum of xenobiotics, and their inhibition can have serious consequences for a patient. In this work we achieved good results using the RUMBLE machine learning software for predicting if a certain chemical compound is an inhibitor, a substrate or none of both for each of the three cytochrome P450 isoforms, 3A4, 2D6 and 2C9. We also compared different machine learning algorithms like decision trees and support vector machines with respect to their ability to predict the behavior of a chemical compound.

Introduction

The development cost of a new drug is currently, on average, 802 million US \$ [4]. According to Kennedy [8], approximately 60% of all drug failures during clinical phases are due to poor pharmacokinetics (39%) or unacceptable toxicity (21%). With the advent of *in silico* methods it is now possible to shorten this long and expensive path. However, it is still an enormous challenge to predict the metabolic fate of a drug due to the vast complexity of the metabolic system responsible for the detoxification of xenobiotics in humans. A variety of enzymes is involved in the detoxification process. For the oxidation reactions in phase I metabolism the cytochrome P450 enzymes (CYPs) are the most important family. They play a significant role in the disposition of drugs, and their coherence with drug-drug interactions and negative side effects has led to an increased number of computer-based approaches in the past few years [2, 6, 7, 12]. But those approaches are hard to compare and often the data or part of it is proprietary.

In this paper we only consider the cytochrome P450 isoforms 3A4, 2D6 and 2C9, since they metabolize more than 64% of all drugs relevant for this enzyme family in man and as only for them a sufficient amount of data is available. RUMBLE and various other machine learning schemes are compared regarding their applicability and performance on the stated problem using the same data and test protocol.

Methods

All the data in this work is taken from the supplementary information of Yap and Chen [12]. There are six datasets, two for the three cytochrome P450 isoforms of interest each. The first set per isoform consists of compounds representing inhibitors and noninhibitors (I/NI), and the second one consists of compounds representing substrates and non-substrates (S/NS). As the supplementary information only contains the names of the structures, the structural information was gathered from the PubChem compound database (<http://pubchem.ncbi.nlm.nih.gov/>) and converted into 3D using the Corina software (version 2.4; [5]). The structures were then checked by a chemist, to avoid obviously corrupt structures. The compound Colestyramine (Cholestyramine) which occurs in all 6 datasets was not taken into account, as it is a polymere with variable size. All data sets were split into training and validation sets according to molecule similarity. For details of the partitioning procedure we have to refer the interested reader to the paper by Yap and Chen [12].

For using the molecular information with machine learning algorithms, we chose two different representations for the molecules. Firstly, 215 numeric descriptors based on MOE (Molecular Operating Environment from Chemical Computing Group; version 2006.8) calculated molecule properties. Secondly, frequent occurring substructures that were generated using the free tree miner (FTM) software [9].

We compare several standard classifiers as implemented in the Weka Data Mining Software (version 3.5.6) [11]: Naive Bayes (NB), k -Nearest Neighbor (k NN), C4.5 decision tree (J48), SVM (SMO), PART rule learner (PART) and bagged C4.5 (BJ48). The k NN classifier is run with $k = 7$, SMO with the complexity parameter $C = 0.01$, epsilon for round-off error to 10^{-12} and a linear kernel. NB, J48 and BJ48 with default Weka parameters. Furthermore, the 3D-decomposition kernel (3DDK)

[3] using a plugin for *SVM Dlight* [1] and RUMBLE [10].

We trained all our models using 10-fold cross validation (CV) on the training sets. The models then were evaluated using the validation sets. We tested the performance of every standard classifier on three descriptor sets: MOE numerical descriptors (moe), FTM binary feature vectors with a minimum frequency cut-off of 0.07 (ftm007) and a combination of both (moeFtm007).

Results and Discussion

Due to space limitations we only present and discuss the results for isoform CYP 3A4 in table 1. At first we compare the Weka calculated classifiers on basis of the AUC values. Regardless with which descriptor set or for which of the two models predictions are made, the BJ48 classifier always performs better than the single J48 decision tree classifier. This is consistent with our expectations as bagging is applied to improve an individual prediction algorithm. Looking at the remaining Weka results, we can say that the support vector machine is the best single classifier following behind the BJ48 meta classifier.

The 3D-decomposition kernel performs nearly equally well combined with either the quadratic or the cubic kernel, with a slight advantage for the cubic kernel. We now compare the performance (sensitivity and specificity) of the 3DDK combined with the cubic kernel with the BJ48 classifier. For the I/NI model, the 3DDK outperforms the BJ48. For the S/NS model, the sensitivity is always higher and the specificity always lower than that of the BJ48, but overall the 3DDK performs better. Those findings can be explained easily, as the linear SVM performed second best looking only at the performances of Weka classifiers, and 3DDK is a problem-specific kernel used in an SVM classifier. This structural 2- and 3-dimensional information implied in the 3D-decomposition kernel seems to be sufficient to outperform the BJ48 meta classifier.

RUMBLE overall performs better than the SVM and slightly worse than the BJ48. Furthermore it has to be noted that there was no time for intensive tests with RUMBLE that offers many more possibilities than used here, so we expect that RUMBLE performs better or at least equal compared to the 3DDK if the plugins and refinement operators are applied to the full extent of their possibilities.

Setup		inhibitors/noninhibitors			substrates/nonsubstrates		
		Sensitivity	Specificity	AUC	Sensitivity	Specificity	AUC
ftm007	Bj48 ^a	0.360	0.947	0.833	0.464	0.818	0.702
	J48	0.520	0.853	0.665	0.446	0.773	0.573
	NB	0.280	0.853	0.649	0.214	0.932	0.715
	PART	0.400	0.800	0.583	0.536	0.568	0.553
	SMO	0.360	0.987	0.796	0.214	0.955	0.719
	kNN	0.160	0.987	0.691	0.357	0.818	0.598
moe	Bj48 ^a	0.640	0.893	0.816	0.857	0.705	0.859
	J48	0.600	0.800	0.710	0.750	0.659	0.656
	NB	0.480	0.973	0.753	0.446	0.841	0.782
	PART	0.560	0.840	0.750	0.696	0.523	0.593
	SMO	0.320	0.973	0.803	0.875	0.659	0.793
	kNN	0.560	0.920	0.813	0.911	0.818	0.898
moeFtm007	Bj48 ^a	0.520	0.933	0.839	0.661	0.773	0.802
	J48	0.120	0.840	0.477	0.500	0.455	0.533
	NB	0.720	0.600	0.649	0.375	0.795	0.667
	PART	0.480	0.507	0.459	0.393	0.591	0.443
	SMO	0.480	0.987	0.844	0.232	0.932	0.781
	kNN	0.080	0.987	0.575	0.161	0.955	0.508
3DDK	poly ²	0.760	0.933	- ^c	0.889	0.698	- ^c
	poly ³	0.760	0.920	- ^c	0.926	0.698	- ^c
RUMBLE	FTM ^b	-	-	0.795	-	-	0.830

^a bagged J48 decision tree (implementation of C4.5)

^b Free Tree Miner plugin used for rule generation.

^c The AUC measure is not given by the software.

Table 1: Results for CYP 3A4 on the external validation set

Conclusion

The goal of this work was to find out which of the applied machine learning algorithms is suited best for predicting the behavior of a chemical compound with respect to the three main metabolizing cytochrome P450 isoforms. Despite the fact that there are large differences in performance in the single classification methods, we found that meta classifiers (BJ48) give improved and stabilized results. This has also been reported by Yap and Chen [12]. Of the non-meta classification methods, the three best performing are the 3DDK [3], RUMBLE [10] and a simple linear SVM. We also observed that the way a chemical compound is represented, either with numerical molecular descriptors, structural features or a combina-

tion of both, influences the classifiers' performance significantly. The two best performing single classification methods, the 3DDK and RUMBLE, both use structural features. For the remaining classifiers the numeric molecular descriptors show a better performance. A reason for this may be that the structural features contain more or better information, but not all classification algorithms can use this information to their advantage.

References

- [1] *Machine learning and neural networks group, universita degli studi di firenze*; <http://www.dsi.unifi.it/neural/src/svm-dlight/>.
- [2] R. Arimoto, *Computational models for predicting interactions with cytochrome p450 enzyme*, *Curr Top Med Chem* **6** (2006), 1609–1618.
- [3] A. Ceroni, F. Costa, and P. Frasconi, *Classification of small molecules by two- and three-dimensional decomposition kernels*, *Bioinformatics* **23** (2007August), no. 16, 2038–2045.
- [4] J.A. Dimasi, R.W. Hansen, and H.G. Grabowski, *The price of innovation: new estimates of drug development costs*, *Journal of Health Economics* **22** (2003March), no. 2, 151–185.
- [5] J. Gasteiger, C. Rudolph, and J. Sadowski, *Automatic generation of 3d-atomic coordinates for organic molecules*, *Tetrahedron Computational Methods* (1990), no. 3, 537–547.
- [6] C. de Graaf, N.P.E. Vermeulen, and A.K. Feenstra, *Cytochrome p450 in silico: an integrative modeling approach*, *J Med Chem* **48** (2005), 2725–2755.
- [7] B.F. Jensen, C. Vind, S.B. Padkjaer, P.B. Brockhoff, and H.H.F. Refsgaard, *In silico prediction of cytochrome P450 2D6 and 3A4 inhibition using Gaussian kernel weighted k-nearest neighbor and extended connectivity fingerprints, including structural fragment analysis of inhibitors versus noninhibitors*, *J Med Chem* **50** (2007), 501–511.
- [8] T. Kennedy, *Managing the drug discovery/development interface*, *Drug Discovery Today* **2** (1997October), no. 10, 436–444.
- [9] U. Rückert and S. Kramer, *Frequent free tree discovery in graph data*, SAC '04: Proceedings of the 2004 ACM Symposium on Applied computing, 2004, pp. 564–570.
- [10] U. Rückert and S. Kramer, *Margin-based first-order rule learning*, *Machine Learning* **70** (2008), no. 2-3, 189–206.
- [11] I.H. Witten and E. Frank, *Data mining: Practical machine learning tools and techniques with java implementations*, Morgan Kaufmann, 1999.
- [12] C. W. Yap and Y. Z. Chen, *Prediction of cytochrome P450 3A4, 2D6, and 2C9 inhibitors and substrates by using support vector machines*, *J Chem Inf Model* **45** (2005), 982–992.

Structure and form measurement of medical and biologic images

I.N. Spiridonov

*Bauman Moscow State Technical University (BMSTU),
inspiridonov@yandex.ru*

Medical-biological images (MBI) are optical or registered pictures of tissues and organs, assigned for analysis of morphological and functional features of biological object. For the medical technique engineer these images are signals with physical, structural and semantic properties. So the image processing system has to be designed as technical means, hardware-software complex and system of decoding, providing information in accordance to medical-biological image nature.

The main object shape features are distribution and extreme values of curvature, insularity and contour length, and the structure object features are properties of size and element order distribution. Physical characteristics of structure and shape properties are linear dimensions, contrast and resolution.

There are a number of optical, digital and optical-digital devices for image generation and processing. All of them realize visualization, generation, registration and transformation of physical image properties but do not provide automation of processes of detection, recognition, classification and interpretation of information important for decision-making.

Visual scanning is described by laws of contrasting light perception, contrasting visual perception, visual perception of subject image and extreme visual information perception. It is known that light perceiving is provided with maximum amount of information by Shannon and correspond to maximal structure and shape changes.

It was experimentally established that probability P of object recognition on an image depends on parameters of axiological information – factor of the form of object – B , physical characteristics: the object size – d , the scale – m , average optical density of an image D_{avr} , contrast of an image – C and structural characteristics: image resolution – N .

$$P = \exp \left[- \left(Bm / 2N, d \sqrt{CD - c_p} \right)^2 \right]$$

Thus the increase of probability of object recognition on an image can be achieved by transformation of structural or physical properties – increasing of image resolution N or increasing of optical object and background densities difference. First operation is impossible for single picture, and the second can be done with the help of linear and non-linear image transformations.

Inasmuch as MBI represent individual realization of the random process, their correct description is possible only under the condition of stationarity and ergodicity of analyzed process. The experience of the image analysis in a medical and biological practice allows to consider that this condition is valid in most cases. Therefore the power spectrum (PS) should be used for the description of the form and the structure of biological objects as characteristics of random process which single realization is MBI.

Measured sample PS of analyzed image $S_{tt}^B(v_x, v_y)$ is a random variable. The $S_{tt}^B(v_x, v_y)$ convolution with a spectral window $W(v_x, v_y)$ is used to get stable estimations. This gives smoothed evaluation of $S_{tt}^B(v_x, v_y)$ by the following equation:

$$S_{tt}^{W,B}(v_x, v_y) = \int_{-\infty-\infty}^{\infty} \int_{-\infty-\infty}^{\infty} S_{tt}^B(\xi - v_x, \zeta - v_y) W(\xi, \zeta) d\xi d\zeta.$$

Window scale extension increases reliability and decreases stability of estimation. At that the effective width of main lobe $W(v_x, v_y)$ should not recover the area of uncorrelated values of $S_{tt}(v_x, v_y)$.

The object structure analysis consists of extraction of harmonic components from random process SP, detection of its polar direction φ , frequencies (v_x, v_y) and amplitudes of spectral components $A(v_x, v_y)$.

It is appropriate to use integral spatial J_i^n and frequency J_i and differential spatial $D_{n,v_{r1}}^n$ and frequency $D_{n,\varphi_1} D_{N,\varphi_1}^u$ characteristics to form these parameters. The integral characteristics describe distribution of PS evaluations by polar angle and frequency and the differential ones – position and intensity of separate components (fig.1,2).

PS distribution measurement by frequency and angle allows not only to smooth but also to eliminate bias of estimator. The interconnection of above characteristics with generalized and local structure features is defined by the

following equations:

$$J_N^n(\varphi_i) = \frac{\int_{\varphi_i}^{\varphi_i + \Delta\varphi} \int_{v_{r\min}}^{v_{r\max}} S_{it}^{W,B}(v_r, \varphi) v_r dv_r d\varphi}{\sum_{i=1}^N \int_{\varphi_i}^{\varphi_i + \Delta\varphi} \int_{v_{r\min}}^{v_{r\max}} S_{it}^{W,B}(v_r, \varphi) v_r dv_r d\varphi}, N = 2\pi / \Delta\varphi, \varphi_i \in [0; 2\pi], i = 1, \dots, N$$

$$J_N(v_{r_i}) = \frac{\int_0^{2\pi v_{r_i} + \Delta v_r} \int_{v_{r\min}}^{v_{r\max}} S_{it}^{W,B}(v_r, \varphi) v_r dv_r d\varphi}{\sum_{i=1}^N \int_0^{2\pi v_{r_i} + \Delta v_r} \int_{v_{r\min}}^{v_{r\max}} S_{it}^{W,B}(v_r, \varphi) v_r dv_r d\varphi}, N = (v_{r\max} - v_{r\min}) \Delta v_r, v_{r_i} \in [v_{r\max}; v_{r\min}], i = 1, \dots, N$$

$$D_{n, v_{r1}}^n = \frac{\int_{\varphi_i}^{\varphi_i + \Delta\varphi} \int_{v_{r1}}^{v_{r1} + \Delta v_r} S_{it}^{W,B}(v_r, \varphi) v_r dv_r d\varphi}{\sum_{i=1}^n \int_{\varphi_i}^{\varphi_i + \Delta\varphi} \int_{v_{r1}}^{v_{r1} + \Delta v_r} S_{it}^{W,B}(v_r, \varphi) v_r dv_r d\varphi}, n = (\varphi_{\max} - \varphi_{\min}) \Delta\varphi, \varphi_i \in [\varphi_{\max}; \varphi_{\min}], i = 1, \dots, n$$

$$D_{n, \varphi_1} = \frac{\int_{\varphi_1}^{\varphi_1 + \Delta\varphi} \int_{v_{r1}}^{v_{r1} + \Delta v_r} S_{it}^{W,B}(v_r, \varphi) v_r dv_r d\varphi}{\sum_{i=1}^n \int_{\varphi_1}^{\varphi_1 + \Delta\varphi} \int_{v_{r1}}^{v_{r1} + \Delta v_r} S_{it}^{W,B}(v_r, \varphi) v_r dv_r d\varphi}, n = (v_{r\max} - v_{r\min}) / \Delta v_r, v_r \in [v_{r\max}; v_{r\min}], i = 1, \dots, n$$

The number of quantization levels, ranges of variables $(v_{r\max}, v_{r\min})$, $(\varphi_{\min}, \varphi_{\max})$ and measuring results $\Delta J_N^n(\varphi_i)$, $\Delta J_N(v_{r_i})$, $\Delta D_{n, v_{r1}}^n$, $\Delta D_{n, \varphi_1}$ can be determined from the requirements to measurement accuracy and speed or empirically.

The description and measurement of geometric features of flat objects shape is provided by analysis of integral spatial object characteristics distribution $J_N^n(\varphi_i)$. This provides the information compression and extraction of semantic information about contour features.

At present decoding systems and medical-technical information technologies of different complexity is created using methods of MBI morphometry.

The dermatoglyphic observation system uses above presented and more complicated algorithms and provides complex of dermatoglyphic parameters measurement. These parameters allow determining heritable diseases presence, particularities of behavior in extreme cases, choosing individual education strategy, etc.

The measurements of iris properties are the base for conclusions about functional status and human adapt ability. Analysis results are used in practice of genetic consultation, criminalistical examination and occupational selections.

The designed software-hardware complex for face and head image analysis measures feature points coordinates. These allow personal identification, determining presence of different syndromes, symptoms and forming biometrical sample for passport.

The complex "Granat" was designed for automated blood smears and other biological preparations quality estimation and for automated recognition of atypical cells, blood corpuscles, etc.

Conclusion

MBI morphometry methods provide possibility to measure structure and shape properties of biological objects. On the base of these methods devices, automated systems and complexes for dermatoglyphic and iridoglyphic parameters of human functional status measurements, blood smears analysis, etc. were developed.

Medical technique designed is destined for scientific investigations and clinical application. It provides the opportunity for human tissues and organs morphology measurements, medical observations automation and effective using of telemedicine methods, broadening and systemizing of psychosomatic disorders knowledge, creating methodology for safety human vital activity.

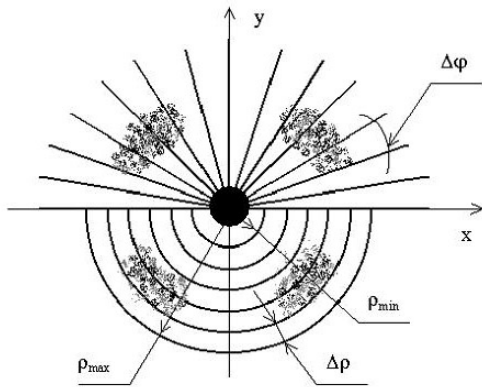


Fig.1 – To the calculation of integral spatial and frequency characteristics

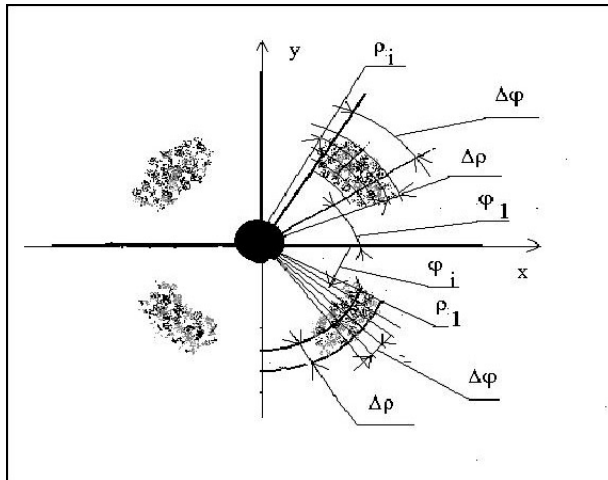


Fig.2 – To the calculation of differential spatial and frequency characteristics

Quantitative Morphometry of Medical and Biologic Preparations

A.V. Samorodov, M.G. Polyanskaya, I.N. Spiridonov

*Bauman Moscow State Technical University (BMSTU),
avsbmstu@yandex.ru*

Morphometric research of images of medical and biologic preparations (MBP), including hematological, cytological, histological, crystallographic and other images, is widely spread in the laboratory analysis practice. However until recently the unified approach to the evaluation of the structure and form of images has not been elaborated, requirements on accuracy for these analyses have not been defined, and there are no corresponding standards.

The main subject of the morphological analysis are plane preparations, such as fixed on object-plate blood smears, cytological preparations, preparations of sediments and dehydrated biologic fluids, histological preparations.

Automated morphological analysis of images of MBP shell include the stages of estimation of the quality of its preparing, the evaluation of integral (structural) parameters, estimation of differential parameters of microobjects on MBP image and shell solve classification tasks.

For the quality of MBP preparing estimation different criteria should be used, which are calculated from MBP image and corresponded to the features of MBP preparing procedure. For example, the main criterion for preparing quality of cytological preparations is the presence of monolayer region, i.e. the region, where cells are stationary distributed over the image and do not overlap.

The investigations of standardly prepared blood smears have allowed to reveal their characteristic structure formed during smear preparing and consisting of five zones statistically distinguishing from each other. The third zone is the monolayer, which is the area of stationarity and in which the morphological analysis should be carried out (Fig. 1).

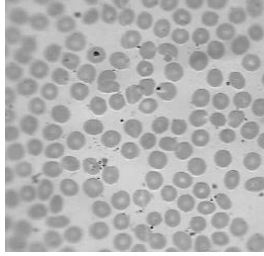


Fig. 1. A monolayer of blood smear. Blood smears were provided by Scientific Center of Child Health, RAMS

As a result of the researches carried out the method for the estimation of quality of preparing of blood smears has been elaborated, allowing to localize in an automatic mode the area of monolayer. The method includes the scanning of blood smear, registration the series of images and the calculation of the factor of the quality K_q , characterizing the degree of stationarity of the image. If K_q exceeds the threshold value, then the corresponding image contains monolayer, which manifests that blood smear has good quality and could be automatically analyzed. Typical dependence of factor of quality versus the distance from an edge of blood smear is showed on Fig. 2.

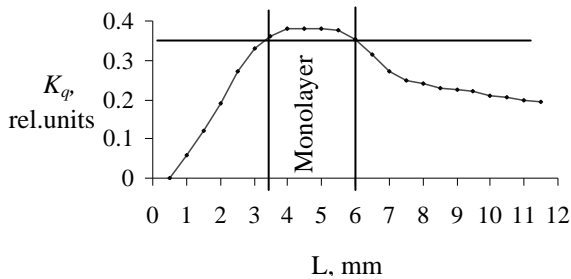


Fig. 2. Typical dependence of factor of quality versus the distance L from an edge of blood smear

The created criterion and method will allow to increase the reliability of results of the analysis of blood smears by the automated systems, to minimize errors of the analysis, to use for the analysis smears, prepared on a standard

technique, and also provides an approach to the creation of reference materials for this type of the laboratory analysis.

In contrast to the widespread methods of elementwise analysis, the method based on performance of various integral transformations of images for the integral parameters estimation, is more perspective. The research carried out in BMSTU has shown that the method of spatial-frequency analysis (SFA) allows to formalize the description of the structure and form of MBP images, characterized by the essential variability of these parameters. The spatial-frequency analysis includes the calculation of spatial-frequency spectrum (SFS) $I(\nu, \varphi)$ of the image, its one-dimensional characteristics: radial SFS (1) and angular SFS (2), and then the complex of characteristics, which allows to estimate quantitative and qualitative parameters of images.

$$I_R(\nu) = \int_0^\pi I(\nu, \psi) d\psi \Big/ \int_0^\pi \int_{\nu_{\min}}^{\nu_{\max}} I(\rho, \psi) \rho d\rho d\psi, \quad (1)$$

$$I_A(\varphi) = \int_{\nu_{\min}}^{\nu_{\max}} I(\rho, \varphi) \rho d\rho \Big/ \int_0^\pi \int_{\nu_{\min}}^{\nu_{\max}} I(\rho, \psi) \rho d\rho d\psi, \quad (2)$$

ν_{\max}, ν_{\min} – boundary values of spatial frequencies.

In the result of theoretical and experimental researches, carried out in BMSTU, the method for quantitative estimation of the degree of anisocytosis and the degree of poikilocytosis of erythrocytes in blood smears, based on SFA, the method for the degree of radial asymmetry of dehydrated biological fluids estimation (Fig.3) and others were proposed.

For the classification of biological microobjects on MBP images it is expedient to use different texture features, calculated on SFS, co-occurrence matrix, run-length matrix, geometrical invariants and others. For particular type of MBP optimal features are different.

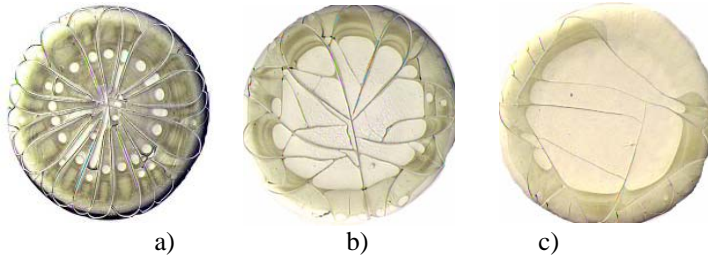


Fig. 3. Dehydrated biological fluids and their degree of radial asymmetry k : a) $k=3,1$ (radial type); b) $k=7,2$ (partly radial type); c) $k=24,4$ (unradial type). Images were provided by Russian R&D Institute of Gerontology

For example, researches of various methods of formation of attribute vectors and different decision rules for classification of leukocytes have shown essential dependence of classification results on the chosen algorithm. Analysis carried out has showed that the use of the SFS characteristics as a vector of data of the leukocyte image, and the combination of different classification methods provide the increase of the probability of correct classification up to required values. The steps of leukocyte analysis are the registration of images of blood smear, the detection and segmentation of leukocytes, calculation of SFS characteristics and classification (Fig. 4).

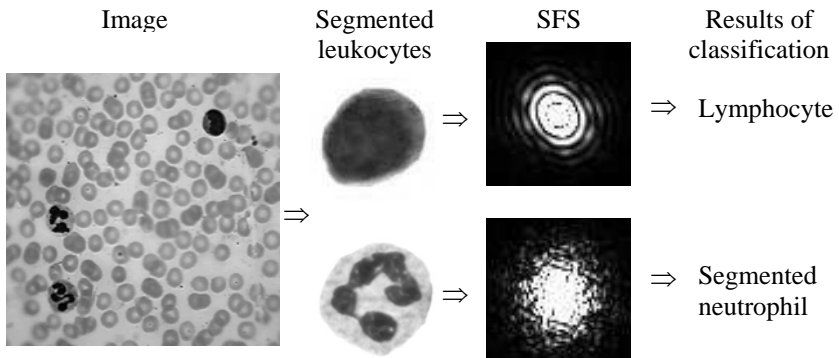


Fig. 4. The steps of leukocytes analysis in blood smears

Conclusions

In BMSTU methods of medical and biological preparations (MBP) morphometry were developed. Systems for the morphological analysis of MBP should be constructed on the base of formation and processing of different texture characteristics of MBP images. This allows to create criteria for the quality of MBP preparing and for the localization of stationary areas on the MBP, to develop methods which takes into account the aprioristic information on the MBP features, to create on their basis methods of formation of complexes of the measured characteristics adequate to morphological parameters of micro-objects, to construct optimal attribute spaces for classification. The specified methods are realized in a hardware-software complex "GRANAT" and demonstrate high efficiency for different types of MBP.

Morphometry of Dermatoglyphic Images

A.A. Khrulev, E.V. Burlay, I.N. Spiridonov

*Bauman Moscow State Technical University (BMSTU),
Andrei.Khrulev@gmail.com*

It is known that the main properties of a complex self-organizing system are its stability and mobility. In human biology these properties are called homeostasis and homeorhesis. These terms characterize an ability of adaptation and compensatory mechanisms and vital organism functions. So, functional conditions of a person should be described by parameters of functional status (connected with human genotype) and functional liability.

The correlation of human genotype features and informative morphogenetic variants of a head, a neck, the iris of an eye, palms, and fingers has been shown by Russian scientists [V.G. Solonichenko, N.L. Delone, 1999]. Among these variants the morphological features of finger patterns (called dermatoglyphic phenotype) are the most important ones because of their polygenic heritability.

The correlation of the finger's morphological features with individual physical, physiological and behavioural features is used in sports medicine for sportsmen's selection, for career-guidance, for problems of forensic medicine and biometric identification.

It is possible to use dermatoglyphic research in medical genetic consultation for diagnostics and prediction of some inherited illnesses and inborn abnormal development. An application of dermatoglyphic research in psychiatry is connected with the objective estimation of inherited component parts of mental disorders (especially schizophrenia).

At present a complex of dermatoglyphic parameters (CDP) includes localization, a pattern type (such as an arch, loop, and a whorl), orientation (ulnar, radial, or symmetric) and ridge count is used in the manual method. Ridge count is defined by a number of ridges in the central area of a pattern.

However, until recently wide application of dermatoglyphic research has been complicated by subjective estimation of basic dermatoglyphic parameters. Therefore, the objectivity of this research is certainly crucial. To provide this objectification the quantitative estimation of the structure and form of fingerprint images should be developed.

Dermatoglyphic images have a complex semantic structure, which makes it difficult for manual classification. The theory of optical and digital images processing demands a hierarchic examination of these images. It is considered that complex images should be described by properties' groups – physical properties (spatial characteristics, frame size etc.), structure properties (spatial resolution) and semantic properties (direction's distribution, characteristic point's position etc.).

According to this approach the system architecture includes a set of equipment (capture device, processor and output device), a hardware and software system and an encoding subsystem. So fingerprint image's requirements should be developed according to this approach.

The capture device (or so-called live-scan fingerprint) allows to obtain a fingerprint image directly from the finger without the intermediate step of getting an impression on paper. The capture device of a dermatoglyphic system should be based on the optical frustrated total internal reflection (FTIR) concept. When a finger is placed on one side of a glass prism, the ridges of the finger are in contact with the platen, while the valleys of the finger are not in contact with the platen. This approach allows reducing the noise rate on fingerprint images and provides a sufficient spatial resolution (500 dpi, according to ISO/IEC 19794-4).

Development of a hardware and software system should be carried out in concordance with biological and technical parts of a biotechnical system. It means that the frame size of a sensing area ($a \times b$) and sufficient spatial resolution (δ) should be granted.

It is important that a dermatoglyphic image depicts not only the central part of a pattern but also the deltas of a fingerprint during enrollment. On the other hand, the large frame size of a sensing area results in extremely high cost of hardware. Our research has shown that the minimal frame size of a sensing area should be equal to 30x40 mm.

Given a minimal frame size of the sensing area, the spatial resolution of dermatoglyphics images should be estimated by means of boundary spatial frequencies of the energy spatial-frequency spectrum of a fingerprint image.

The ridge profile $f(x)$ of a finger print image at direction φ could be approximated by cosine-profile functions (Fig. 1):

$$f(x) = \text{rect}(x/T) \times \left\{ \frac{A_{\max} - A_{\min}}{2} g(x/l) \otimes \text{comb}(x/l) + \frac{A_{\max} + A_{\min}}{2} - \frac{A_{\max} - A_{\min}}{2} g(x/(L-l)) \otimes \text{comb}\left(\frac{x-L/2}{L-l}\right) \right\}$$

$$g(x) = \cos(\pi x) \text{rect}(x),$$

$$\text{comb}(x) = \sum_{k=-\infty}^{\infty} \delta[x - kL],$$

where A_{\min} , A_{\max} – minimal and maximal brightness value; l – ridge's width; L – ridge's period; T – segment's length.

Spatial-frequency analysis and numeric calculations of boundary spatial frequencies values according to the above model allow us to determine spatial resolution. Given five percent error rate, the boundary spatial frequency of a fingerprint image is equal to 6 cycle/mm. So, the spatial resolution should be at least 300 dpi.

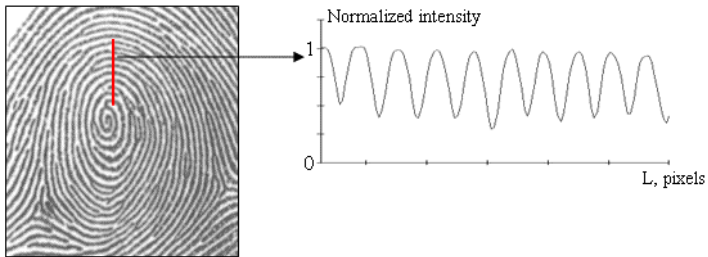


Fig. 1. The ridge profile of a fingerprint image

It is necessary to provide quantitative description of dermatoglyphic parameters and classification of pattern's types and create formalized techniques for the interpretation of research results.

A necessary condition of the measurement automation is quality control of dermatoglyphic images. The analysis of dermatoglyphic image's distortion (including blur, void, and double lines) has allowed to generate a quantitative criterion of its quality. Proposed criterion includes the estimation of local dispersion of image's intensity, the analysis of textured features (minutiae

points, ridge lines etc.) and the estimation of eigen values of local covariation matrix.

At the next step values of partial criterions are used to score quality level by classification or combination (e.g. weighted average of all partial values). So, this criterion allows to estimate the pattern's quality, to localize areas of fingerprint's distortion, to discard non-informative regions with irrelevant information and to locate the region of interest.

Two methods providing extraction of the encoded information are used for fingerprint's data vector forming in this work: a method of a direction's field and a method of spatial – frequency analysis.

The spatial – frequency analysis based on the two dimensional Fourier-transform provides for the definition of an average spatial angle, an average spatial frequency and some differential characteristics of finger patterns.

The direction's field method allows to describe the image by the distribution of directions of papillary lines, their variability, and to define the position of characteristic points: tops and deltas of a pattern. Examples of direction's fields for fingerprints are shown at Fig. 2.

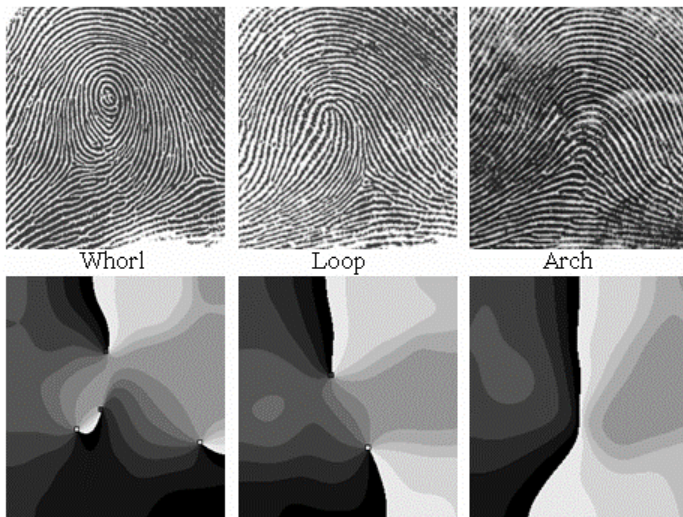


Fig. 2. Direction's fields and characteristic point of fingerprints (whorl, loop, arch)

These data are used for the classification of patterns and estimation of a set of dermatoglyphic parameters. The main advantage of this combined approach is that it considers dermatoglyphic images as a realization of a random stationary ergodic process, and takes into account the a priori information of the patterns. It increases considerably the accuracy of evaluating quantitative parameters and probability of correct classification and gives statistically reliable results.

The experimental verification of developed algorithms was carried out on a set of 200 fingerprint samples with different pattern types (arch, loop and whorl). The results of this experimental verification are shown in Table 1.

Table 1. Results of the fingerprint's pattern classification

Probability of correct classification	Arch	Loop	Whorl
Finger's type, %	90	94	93
Finger's orientation, %	—*	95	—*

Note: * – could not be estimated

Conclusion

The described algorithms are used in an automated complex for dermatoglyphic research named "Malachite", which was developed at BMSTU. The complex provides for the registration of fingerprints, their automated processing, systematization and storage. The software allows solving effectively scientific and practical problems of dermatoglyphics.

The approbation of the complex was carried out on the basis of Russian leading research and development organizations and was aimed at solving several problems such as:

- the measurement of informative morphogenetic variants,
- forming individual educational trajectories,
- occupational selection of personnel working under extreme conditions,
- biometric individual identification.

Development of Numerical Methods of Iris Integral Parameters Assessment

A.V. Khrustalev, Y.V. Krylov, V.A. Potapov, I.N. Spiridonov

*Bauman Moscow State Technical University (BMSTU),
d1821@yandex.ru*

The range of environmental aspects variations exceeds the human adaptive capabilities. It leads to that the functional state of human working in extreme environmental conditions can appear unequal to his mission, that ascertains by increasing in number of man-made disasters resulting, in turn, to change of environmental conditions. So necessity of professional selection (evaluation of human adaptive and reparative abilities) becomes more and more actual and important.

It is established that inherited features of human adaptive and reparative abilities are shown on phenotypic level and represented in a lesser maldevelopments of single organs, among that the most informative lesser maldevelopments are characteristics of a human iris. The embryonic origin community of the central nervous system and the iris determines the relation of human adaptive and reparative abilities with iris parameters, but visual evaluation of iris color and morphological parameters makes numerous iridoglyphic investigation results essentially subjective.

The purpose of this work is development of numerical methods of iris color and morphological parameters assessment.

Existing complexes for iridoglyphic investigations don't have a wide distribution because of the high intraindividual biological variability of iris parameters caused by exogenous factors: registration of iris images in unregulated conditions doesn't provide convergence of iridoglyphic investigation results. To obtain the reliable and stationary results of iridoglyphic investigation it is necessary to define conditions of iris images registration.

As a result of the analysis of 954 iris images received at illuminance from 10 to 1000 lux by light source with the correlated color temperature of 6500K and angular size of 10 degrees, it is established that the variation factor of the reduced pupil diameter doesn't exceed an admissible analytical variation of 6,6 % at iris illuminance more than 200 lux. Also it is shown that changes of color parameters at illuminance more than 100 lux statistically are not significant (figure 1).

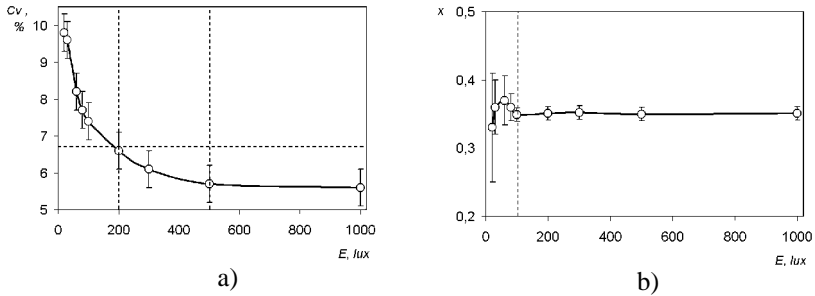


Figure 1 – a) dependence of the variation factor of the reduced pupil diameter C_v on illuminance E ; b) Dependence of chromaticity coordinate x of iris image elements on illuminance E

It is established that iris illuminance more than 500 lux causes discomfort in the majority of the examined. Thus, stationary and reliability of iridoglyphic investigation results is provided at iris illuminance in a range from 200 to 500 lux.

On the basis of approaches to medical and biologic images processing and axiological information extraction, originated on chair «Biomedical technical systems» by I.N. Spiridonov, I.A. Apollonova, L.P. Safonova, I.V. Karasev, A.V. Samorodov, the numerical methods of iris color and morphological parameters assessment are offered.

Iris color is determined by ciliary and papillary zones colors, each of that is characterised by a maximum of the histogram of chromaticity coordinates distribution in colour space x, y . On learning sample of 176 iris images the borders of classes of ciliary and papillary zones colors are determined and a procedure of automatic classification is developed. Results are presented in figure 2.

Instability of color temperature of the light source and difference between spectral response of photodetector's elements and spectral response of observer's cones brings in uncertainty of color measuring results. For ensuring of reliability of iris color parameters measuring results a set of color test-objects is developed for iris capture system calibration.

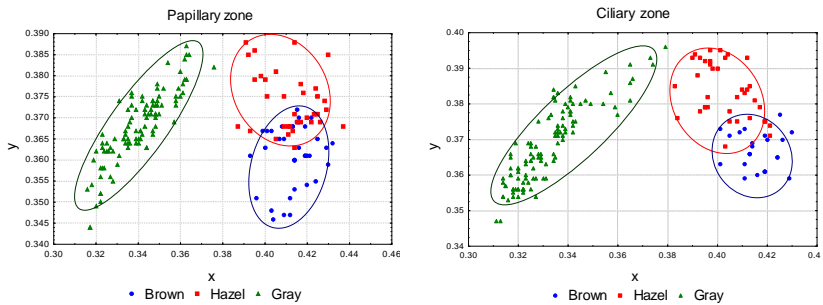


Figure 2 – Chromaticity coordinates for various iris colors

Iris stroma density indicates the individual reparative abilities characterising its resistibility and ability of tissues to regeneration. The iris stroma is considered from the point of view of a texture which characteristics are a measure of such properties of iris structure as a smoothness, a roughness, a regularity etc. Within this approach the method for evaluation of iris stroma density by means of Laws's power textural characteristics is used.

As a result of the analysis of 15 power textural characteristics five characteristics were chose. Further algorithm functioning is a statistical classification. Presentation of irises with various stroma density in attribute space E1-E4 are shown on figure 3.

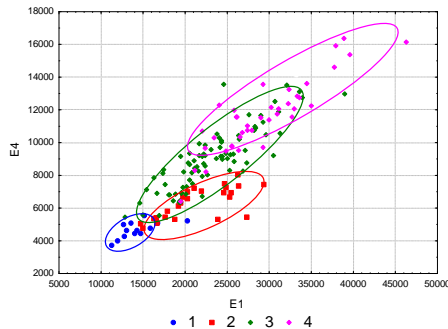


Figure 3 – Presentation of irises with various stroma density in attribute space E1-E4

For approbation of iris color assessment algorithm the check sample of 33 iris images was used. Approbation of iris color assessment algorithm shows 100% rate for gray iris classification, 3% rate for ciliary zone and 12% for papillary zone for brown and hazel iris classification. Classification errors for brown and hazel irises caused by expert judgement subjectivity for these irises.

For approbation of iris stroma density assessment algorithm the learning sample of 115 iris images with various density and the check sample of 50 iris images were used. Densities of 4, 5 and 6 were united. Classification errors are 0% for density of 1, 37% for density of 2, 16% for density of 4. Obtaining results show perceptivity of using proposed algorithm for iris stroma density assessment.

Using additional textural characteristics (for example, histograms of distribution of gradient magnitude and gradient direction) allows to boost the accuracy of iris stroma density assessment. So, conditions of iris images registration are defined, ensuring reliable and stationary results of iridoglyphic investigation. Numerical methods of iris color and morphological parameters evaluation are developed, as well as calibration method for iris capture system.

The Developing of Cytological Image Segmentation Method

Maria G. Polyanskaya, Andrey V. Samorodov
*Bauman Moscow State Technical University, masha.pol@gmail.com,
avsbmstu@yandex.ru*

Cytological analysis is an effective diagnostic technique in detecting malignant and benignant tumors because it allows to fix character of changes, cell differentiation and to determine oncological process of any stage without regard to a tumor node size. The credibility of cytological analysis is 91% at least.

Since cytologists conduct the analysis visually, the main drawback is its subjectivity because of absence of objective quantitative measurements. Thus, the result of cytological investigation is highly dependent on the professional skill of a physician conducting the analysis. The problem of analysis subjectivity can be solved by process automation and the expert support system development.

The procedure of image processing should be designed in accordance with the strategy of visual cytological analysis conducted by a physician. The process of automated cytological image analysis contains the following steps:

- image segmentation - extracting the separate nuclei from the whole image,
- object (nucleus) feature extraction,
- each nucleus classification - the presenting nuclear changes determination,
- giving final conclusion by integration the results of separate nuclei classification.

Each step of the processing has it's own particularities and complexities but this paper is emphasized at segmentation step. There are a lot of various approaches to image segmentation, which can be grouped in such a way:

- pixel-based methods. This group is represented by thresholding methods. Their main drawback is that space information is not included into the segmentation process so it is significantly sensitive to noise and intensity heterogeneity through object area;
- region-based methods, such as region growing, morphological methods, watershed. Previous investigations of applying of this group of methods to cytological image segmentation gave not satisfactory results;

- contour-based methods – different kinds of methods using gradient information. The segmentation with a method of such a kind often fails because of fuzzy boundaries of objects on cytological images;
- model methods: active contours, deformable models, snakes. This methods demonstrate the most desirable results but need some previous information about the objects to be segmented.

The segmentation meets with the problem caused by features of cytological preparation – high variability of stain degree, floating, artifacts, noise and, as well, merged objects and fuzzy boundaries of objects. This forces to abandon of such segmentation methods as thresholding, edge-based methods, etc. and to pass to more sophisticated model methods. In this work the results of the application of active contour method are introduced.

The active contour is a curve that evolves from initial position towards object boundary in a way to minimize some function, called energy functional. This functional is represented by two parts – the image energy, which is responsible for moving snake towards the boundaries of interest, and the internal energy, which provides the smoothness of the segmented object boundaries. The final contour position is determined by the minimum of energy functional, so the segmentation process is solving the optimization task. The concrete type of energy functional and the algorithm of optimization depend on the kind of segmenting image.



Figure 1. The results of active contour segmentation

Testing of the considered active contour method approach was conducted with the images of the kidney epithelium preparations stained by AgNO_3 for nuclear-organizer regions (images were given by Moscow Herten Oncological Research Institute). The results of proposed model application to cytological image segmentation are represented in Figure 1.

The energy functional consists, as it was already mentioned, of image and internal energy parts, represented by image edge information and curve properties respectively. The image energy at each step of optimization is evaluated by summarizing gradient values along the active contour curve. For this purpose the image gradient is calculated and smoothed by Gaussian filter. The internal energy part of functional is linear combination of length

and curvature of the contour. Quasi-Newton gradient method is used to solve the optimization problem.

As it is seen in Fig.1 the algorithm shows rather good and important to further logical designing results. It deals with substantially heterogeneous background of image and especially it should be underlined that the method has high capability to extracting merged objects separately what is important because such cases are rather frequent.

In conclusion it should be pointed out that the proposed approach of active contour method strongly depends on the initial contour position and is still sensitive to noise since image energy part of functional contains only gradient information which in the case of heterogeneous background is insufficient for object boundary detection. Including the part of so called region energy will help to avoid the above mentioned drawbacks. It is responsible for differentiation between the object and background areas and can be represented as, for instance, the average intensity of the region inside the contour.

So conducted research shows that active contour method is very efficient in application to segmentation of cytological images and can be used in the devising of automated cytological image processing system.

A Modification of Image Compression Algorithm Based on Encoding of Tree-Arranged Wavelet Coefficients

Sergei V. Umnyashkin, Dmitri M. Koplovich, Andrei S. Pokrovskiy

Moscow Institute of Electronic Technology (Technical University)

E-mail: vrinf@miee.ru

Abstract — A modification of image compression algorithm is proposed, which includes context model initialization and multi-model sign encoding of wavelet coefficients. The modification performs 0.2...0.6 dB higher than JPEG 2000 and adds 0.1...0.35 dB to the PSNR of the original algorithm.

1 Problem overview

In [1], a computationally effective image compression algorithm was proposed, which applied multi-model arithmetic encoding for RD-optimized zerotree structured wavelet coefficients. This algorithm (referred as “basic algorithm” in this paper) outperformed JPEG 2000, but some opportunities for further improvement were still open.

The basic algorithm relies on a special prognosis value calculated for each quantized coefficient $\hat{w}_i = q\tilde{w}_i$, where $\tilde{w}_i = \text{Round}(w_i/q)$ and w_i is an original wavelet decomposition coefficient. The value is composed as a weighted sum of its parent and neighbor coefficients absolute values [1]. Based on this prognosis value, a decision is made (via simple thresholding) which statistical model will be used for adaptive arithmetic encoding of the coefficient w_i . Such multi-model approach exploits non-linear dependencies between each coefficient and its neighbors and parent, making lossless compression ratio of quantized coefficients substantially higher.

There are ten statistical models in the arithmetic coder applied for the basic algorithm: 6 for wavelet coefficients \tilde{w}_i (one of them for the LL subband) and 4 for zerotree map indices N_i . This solution is obviously not optimal in terms of coding efficiency. First, using lots of models reduces data volume each of them encodes. The more models are used, the more sensitive they are to initial model statistics distribution, which is uniform by default in the basic algorithm, but the actual data distribution is certainly *not*

uniform. Hence, model initialization is significant for the overall performance of the compression algorithm.

Second, encoding positive and negative coefficients together is simplest in the sense of implementation, but not the best for getting good compression. Separate encoding of each coefficient's sign and absolute value is preferable because wavelet coefficient signs are themselves correlated [2], and this correlation should be exploited.

2 Modifications description

First of all, signs were separated from the coefficients; absolute values and signs were encoded independently.

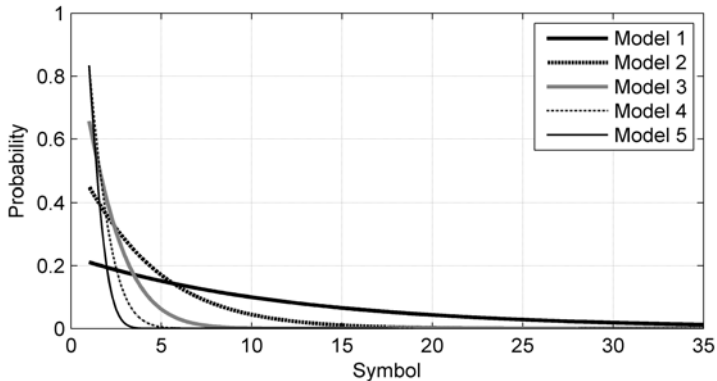


Figure 1: Initialized models for the Goldhill test image at 0.5 bpp

To model initial statistics of the absolute values of wavelet coefficients we applied exponential distribution (Fig. 1):

$$f(x) = \begin{cases} \lambda e^{-\lambda x}, & x \geq 0 \\ 0, & x < 0 \end{cases}$$

and maximum likelihood estimation for the λ parameter in each model:

$$\lambda = \left(\frac{1}{n} \sum_{k=1}^N x_i \right)^{-1}$$

where $\{x_i\}_{i=1}^N$ is the data to be encoded by the particular model. Prognosis value calculation and model selection rules used for absolute values encoding

remain virtually the same as in the basic algorithm excepting zero coefficients which are encoded by sign models (see below).

Coefficient signs were encoded separately using $3^3 = 27$ models with three symbols available for each model: z_{-1} (coefficient is negative), z_0 (coefficient is zero), z_{+1} (coefficient is positive). The symbol z_0 was introduced here to encode zero coefficients thus excluding zeros from the models for absolute values.

Dependencies between signs were taken into account by context encoding. Instead of prognosis calculation and thresholding we used simpler approach similar to JPEG 2000 [3]: model choice for each sign symbol z_i was strictly determined by its three neighbor sign values (upper, left and upper left), which results in 27 different combinations. There is no need to initialize sign models as three-symbol alphabet statistics can adapt pretty fast.

3 Experimental results and conclusion

Results for *Lena*, *Barbara* and *Goldhill* standard test images are shown in Fig. 2. ACDSSee Pro utility (version 8.1) was applied to measure JPEG 2000 characteristics.

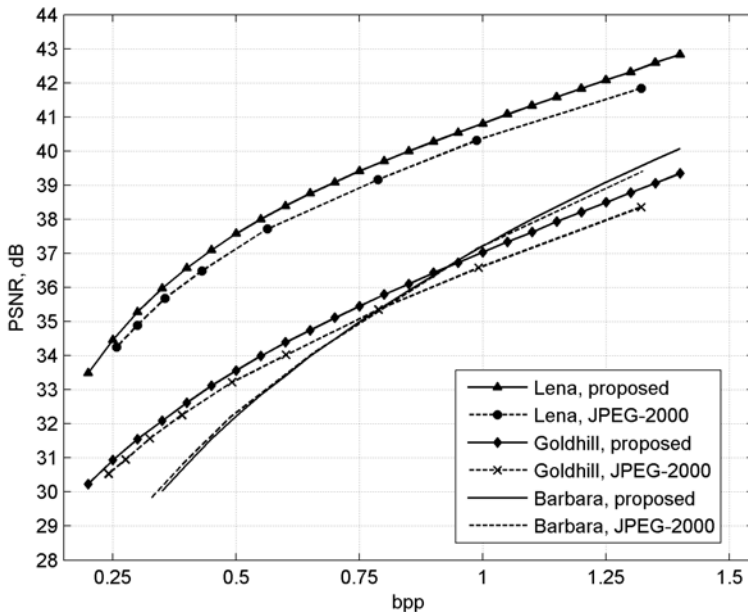


Figure 2: Comparative performance of the modified algorithm (9/7 filters) and JPEG 2000.

Proposed modification performs 0.2...0.5 dB higher than JPEG 2000 on all test images excepting *Barbara* and 0.1...0.35 dB higher than the basic algorithm on all images with common 9/7 filter bank.

We also conducted experiments using advanced filters [4], which resulted in additional performance gain of 0.1 dB for *Lena* and 0.4 dB for *Barbara* as shown in Table 1 and Table 2. In this case, total increase relative to JPEG 2000 is 0.2...0.6 dB.

Table 1: Modified algorithm PSNR performance with common 9/7 filters

BPP	Lena	Barbara	Goldhill
0.25	34.46	28.36	30.89
0.50	37.58	32.22	33.57
1.00	40.81	37.21	37.03

Table 2: Modified algorithm PSNR performance with advanced filters [4]

BPP	Lena	Barbara	Goldhill
0.25	34.61	28.67	30.88
0.50	37.71	32.65	33.57
1.00	40.88	37.67	37.05

4 References

1. S. Umnyashkin, D. Koplovich, A. Pokrovskiy, A. Alexandrov. Image Compression Algorithm Based on Encoding of Tree-Arranged Wavelet Coefficients // Proc. of 3rd Russian-Bavarian Conference on Biomedical Engineering. Erlangen, July 2/3, 2007, pp.121-126.
2. A. Deever, S. S. Hemami. What's Your Sign?: Efficient Sign Coding for Embedded Wavelet Image Coding // Proceedings of the 2000 IEEE Data Compression Conference, 2000, pp. 273-282
3. Marcellin M., Gormish M., Bilgin A., Boliek M. An Overview of JPEG-2000 // Proceedings of the 2000 IEEE Data Compression Conference, Snowbird, Utah, March 2000, pp. 523-541.
4. D. Wei, H.-T. Pai, and A. C. Bovik. Antisymmetric Biorthogonal Coiflets for Image Coding // Proceedings of IEEE International Conference on Image Processing, Chicago, IL, Oct. 1998, vol. 2, pp. 282-286.

About digital image structure

A.S. Pospelov

Moscow Institute of Electronic Technology (Technical University)

e-mail: hml@miee.ru

We consider a discrete image as a square matrix $A = (a_{pq})$,
 $p, q = 0, 1, \dots, 2^s - 1$, s – fixed natural number, which satisfies the additional condition

$$\sum_{p,q=0}^{2^s-1} a_{pq} = 0. \quad (1)$$

Though this definition is differing from generally accepted [1], where all matrix elements have to be non-negative, condition (1) is not onerous and comes to addition constant value to all the matrix elements.

At the same time these matrices belong to 4^s - dimensional Euclidean space and according to condition (1) lie at $4^s - 1$ - dimensional hyper plane passing through the point of origin. Hereinafter the common Euclidean norm being used.

In our digital image structure investigation we used its decomposition by orthonormalized basis which elements are direct products of one-dimensional discrete Walsh's system vectors [2, 3]:

$$w_{n,k}(p, q) = 2^{-s} w_n(p) w_k(q), \quad n, k = 0, 1, \dots, 2^s - 1, \quad (2)$$

where for $n = n_0 + 2n_1 + \dots + 2^{s-1} n_{s-1}$, $p = p_0 + 2p_1 + \dots + 2^{s-1} p_{s-1}$

$$w_n(p) = \exp \left\{ \pi i \sum_{v=0}^{s-1} p_v n_{s-1-v} \right\}. \quad (3)$$

Discrete image decomposition by two-dimensional Walsh's system (2), (3) looks like:

$$c_{n,k} = \sum_{p,q=0}^{2^s-1} a_{pq} w_{nk}(p,q), \quad n,k = 0,1,\dots,2^s-1, \quad (4)$$

$$a_{p,q} = \sum_{n,k=0}^{2^s-1} c_{n,k} w_{n,k}(p,q), \quad p,q = 0,1,\dots,2^s-1. \quad (5)$$

Formulas (4) and (5) called forward and inverse two-dimensional Walsh transforms [2].

It's not difficult to make sure that conditions (1) and $c_{0,0} = 0$ are equivalent.

Let's review special partial sums for right part of decomposition (5). For any r and t , $0 \leq r, t \leq s$ we assume

$$u_{r,t}(p,q) = \sum_{n=0}^{2^r-1} \sum_{k=0}^{2^t-1} c_{n,k} w_{n,k}(p,q). \quad (6)$$

Digital image analysis basis consists in characteristic property of sums (6) which determines in the next assertion.

Lemma. Let r and t are integer numbers, $0 \leq r, t \leq s$. If $p = p^{(1)} + p^{(2)} 2^{s-r}$ and $q = q^{(1)} + q^{(2)} 2^{s-t}$, then

$$u_{r,t}(p,q) = 2^{(r+t)-2s} \sum_{n=0}^{2^{s-r}-1} \sum_{k=0}^{2^{s-t}-1} a_{n+p^{(2)} 2^{s-r}, k+q^{(2)} 2^{s-t}}. \quad (7)$$

It's not difficult to see that $U_{r,t} = (u_{r,t}(p,q))$ represents averaging of elements $a_{p,q}$ by index rectangles $(p,q): \nu 2^{s-r} \leq p \leq (\nu+1) 2^{s-r} - 1,$

$$\mu 2^{s-t} \leq q \leq (\mu+1) 2^{s-t} - 1, \quad \nu = 0,1,\dots,2^r-1, \quad \mu = 0,1,\dots,2^t-1.$$

We introduce and study two new concepts called image skeleton and image component which are very important characteristics of the digital image structure.

Image skeleton and image stability.

Our next subject of inquiry are elementary blocks sum of which may represent discrete image A . In [4, 5] they were examined as a basis of some image compression methods.

For any $r = 1, 2, \dots, s$ assume

$$l_r(p, q) = u_{r,r}(p, q) - u_{r-1,r-1}(p, q), \quad p, q = 0, 1, \dots, 2^s - 1. \quad (8)$$

L_r matrix we identify as image layer number r . It follows from (7) that for any $r = 1, 2, \dots, s$ elements $l_r(p, q)$ of layer L_r look like

$$l_r(p, q) = \frac{1}{4} \sum_{\alpha, \beta=0}^1 \left(u_{r,r} \left(p \dot{+} \alpha 2^{s-r}, q \dot{+} \beta 2^{s-r} \right) \right),$$

where $\dot{+}$ is coordinate-wise binary addition operation [3].

Two-dimensional matrix $b_{v,\mu}^{(r)}$,

$$\begin{aligned} b_{v,\mu}^{(r)}(0,0) &= l_r \left(v 2^{s-r+1}, \mu 2^{s-r+1} \right), \\ b_{v,\mu}^{(r)}(0,1) &= l_r \left(v 2^{s-r+1}, \mu 2^{s-r+1} + 2^{s-r} \right), \\ b_{v,\mu}^{(r)}(1,0) &= l_r \left(v 2^{s-r+1} + 2^{s-r}, \mu 2^{s-r+1} \right), \\ b_{v,\mu}^{(r)}(1,1) &= l_r \left(v 2^{s-r+1} + 2^{s-r}, \mu 2^{s-r+1} + 2^{s-r} \right) \end{aligned} \quad (9)$$

where $v, \mu = 0, 1, \dots, 2^{r-1} - 1$, is termed elementary block of layer number r .

Thus image layer number r consists of 4^{r-1} elementary blocks like (9). Therefore the total number of elementary blocks in discrete image A equals

$$\text{to } \frac{1}{3} \left(4^r - 1 \right).$$

Let $b_{v,\mu}^{(r)} = (b(i, j), i, j = 0, 1)$ is any elementary block like (9). Signature $\sigma_{v,\mu}^{(r)}$ of this block is two-dimensional matrix which consists of elements $\{-1, 0, 1\}$ and determined as

$$\sigma_{v,\mu}^{(r)}(i, j) = \text{sign } b(i, j), \quad i, j = 0, 1, \quad (10)$$

where $\text{sign } a = -1$, if $a < 0$; 0 , if $a = 0$ and 1 , if $a > 0$.

All the set of elementary block signatures $K(A) = \left\{ \sigma_{v,\mu}^{(r)}, v, \mu = 0, 1, \dots, 2^{r-1} - 1, r = 1, 2, \dots, s \right\}$ we termed as skeleton of digital image A .

Digital image skeleton may be splitted into non intersected subsets $K(A) = K_0 + K_n$. Elementary block signature is a member of K_0 if one of its element equals to zero. In all other cases signature belongs to K_n . We indicate image skeleton $K(A)$ as non-degenerate if $K_0 = \emptyset$.

Finally, if there is such a number $\varepsilon > 0$ exists, that any image \tilde{A} with condition $\|A - \tilde{A}\| < \varepsilon$ has the same skeleton with A , then image A considered to be stable.

Theorem 1. Discrete image is stable if and only if its skeleton is non-degenerate.

This theorem hallmarks small pixel values changing tolerance. Next theorem determines some numerical bounds of this tolerance.

Theorem 2. Let A is non-degenerate image,

$$\rho_r = \frac{2}{\sqrt{3}} \min_{v,\mu=0,1,\dots,2^{r-1}-1} \min_{i,j=0,1} \left| b_{v,\mu}^{(r)}(i, j) \right|$$

and $\rho(a) = \min_{r=1,\dots,s} \rho_r$. Then

1°. For any image \tilde{A} such, that $\|A - \tilde{A}\| < \rho(A)$, $K(A) = K(\tilde{A})$.

2°. If $\rho(A) = \rho_s$ then there is such degenerate image B exists, that $\|A - B\| = \rho(A)$.

Discrete image components.

For each fixed $r = 1, 2, \dots, s$ let's determine partial components in each digital image layer.

$$\begin{aligned} c_r^{(1)}(p, q) &= u_{r,r-1}(p, q) - u_{r-1,r-1}(p, q), \\ c_r^{(2)}(p, q) &= u_{r-1,r}(p, q) - u_{r-1,r-1}(p, q), \\ c_r^{(3)}(p, q) &= u_{r,r}(p, q) - u_{r,r-1}(p, q) - u_{r-1,r}(p, q) + u_{r-1,r-1}(p, q). \end{aligned} \quad (11)$$

If $C_r^{(1)} = \left(c_r^{(1)}(p, q) \right)$, $C_r^{(2)} = \left(c_r^{(2)}(p, q) \right)$ and $C_r^{(3)} = \left(c_r^{(3)}(p, q) \right)$ are corresponding matrices, then each image layer may be represented as sum of three orthogonal items $L_r = C_r^{(1)} + C_r^{(2)} + C_r^{(3)}$. Summing all these decompositions we obtaining next assertion:

Theorem 3. For each discrete image A orthogonal decomposition exists:

$$A = C^{(1)} + C^{(2)} + C^{(3)}, \quad (12)$$

where $C^{(v)} = \sum_{r=1}^s C_r^{(v)}$, $v = 1, 2, 3$.

It make sense to call these items as vertical, horizontal and diagonal components since for their elements the following equalities are correct:

$$\begin{aligned} c_r^{(1)}(p, q \dot{+} 2^{s-r}) &= c_r^{(1)}(p, q), \quad c_r^{(2)}(p \dot{+} 2^{s-r}, q) = c_r^{(2)}(p, q), \\ c_r^{(3)}(p \dot{+} 2^{s-r}, q \dot{+} 2^{s-r}) &= c_r^{(3)}(p, q), \quad r = 1, 2, \dots, s. \end{aligned}$$

Literature

1. **R.C.Gonzales, R.E.Woods.** Digital Image Processing, –2nd edition, Prentice Hall, –2002.
2. **N.Ahmed, K.R.Rao.** Orthogonal Transforms for Digital Signal Processing, –Springer Verlag, –1975.
3. **B.I.Golubov, A.V.Efimov, V.A.Scvortsov.** Walsh`s serieses and transforms: theory and applications // –Moscow, –1987 (in Russian).
4. **A.S.Pospelov.** Using averaging operators for digital signal compression // Electronics, –Moscow: MIEE, –2005. –№ 2. –p.11-18 (in Russian).
5. **A.S.Pospelov.** Discrete image compression method using multiplicative transforms // III International symposium «Fourier serieses and theirs applications», –2005. –p.29 (in Russian).

Image compression method using layer decomposition and elementary layer block prediction

S.A. Bolotov

*Moscow Institute of Electronic Technology (Technical University)
e-mail: bolotovsa@gmail.com*

Let $A = \left\| a_{ij} \right\|_{i,j=0}^{2^s-1}$, $a_{i,j} = 0, 1, \dots, 255$ is a digital image. Let's examine the set of averaging operators in $2^s \times 2^s$ dimensional Euclidean space.

$$\Psi_n(A, m, k) = \frac{1}{4^{s-n}} \sum_{i=0}^{2^{s-n}-1} \sum_{j=0}^{2^{s-n}-1} a_{m \dot{+} i, k \dot{+} j}, \quad n = 0, 1, \dots, s,$$

where $\dot{+}$ is coordinate-wise binary addition operation [1]. We named $\Psi_n(A)$ as n -rank image.

Image layer we determine as $L_0(A) = \Psi_0(A)$,
 $L_n(A) = \Psi_n(A) - \Psi_{n-1}(A)$, $n = 1, \dots, s$.

It was shown in [2] that any digital image may be represented as orthogonal layer decomposition:

$$A = \sum_{k=0}^s L_k(A).$$

It is significant that we obtain n -rank image by averaging initial image pixel groups. Therefore only $2^n \times 2^n$ dimension matrix is enough for its representation: $\Psi^{(n)} = \left\| d_{ij}^{(n)} \right\|_{i,j=0}^{2^n-1}$. And the same situation with layer number

$$r: L^{(r)} = \left\| l_{ij}^{(r)} \right\|_{i,j=0}^{2^r-1}.$$

The next subject of inquiry is the elementary layer blocks. Elementary layer block is 2×2 matrix

$$b_{k,m}^{(r)} = \left\| \begin{array}{cc} I_{2k,2m}^{(r)} & I_{2k+1,2m}^{(r)} \\ I_{2k,2m+1}^{(r)} & I_{2k+1,2m+1}^{(r)} \end{array} \right\|, \quad r = 1, 2, \dots, s.$$

It is obvious that sum of block elements equals to zero, since they were obtained by subtraction average value of corresponding r -rank image elements.

We introduce image compression method based on construction predicted block $\tilde{b}_{k,m}^{(r-1)}$ for each elementary block $b_{k,m}^{(r-1)}$. This prediction is a function of context C and its parameters $W(C)$, where context $C = (c_0, c_1, \dots, c_7)$ is a vector of neighbors from previous rank image (fig. a).

$c_0 = d_{k-1,m-1}^{(r-1)}$	$c_1 = d_{k-1,m}^{(r-1)}$	$c_2 = d_{k-1,m+1}^{(r-1)}$	
$c_7 = d_{k,m-1}^{(r-1)}$	$I_{2k,2m}^{(r)}$	$I_{2k,2m+1}^{(r)}$	$c_3 = d_{k,m+1}^{(r-1)}$
	$I_{2k+1,2m}^{(r)}$	$I_{2k+1,2m+1}^{(r)}$	
$c_6 = d_{k+1,m-1}^{(r-1)}$	$c_5 = d_{k+1,m}^{(r-1)}$	$c_4 = d_{k+1,m+1}^{(r-1)}$	

Fig. a. $r = 2, \dots, s$; $k, m = 1, \dots, 2^{r-1} - 1$.

Let's see on simple example. Prediction of r -rank image elements we obtain as weighted sums:

$$p(d_0) = p(d_{2k,2m}^{(r)}) = w_0 c_0 + w_1 c_1 + w_2 c_7$$

$$p(d_1) = p(d_{2k,2m+1}^{(r)}) = w_0 c_2 + w_1 c_3 + w_2 c_1$$

$$p(d_2) = p(d_{2k+1,2m+1}^{(r)}) = w_0 c_4 + w_1 c_5 + w_2 c_3$$

$$p(d_3) = p(d_{2k+1,2m}^{(r)}) = w_0 c_6 + w_1 c_7 + w_2 c_5$$

Prediction for block itself obtained by subtracting average:

$$\begin{aligned} \bar{p} &= \frac{1}{4} (p(d_0) + p(d_1) + p(d_2) + p(d_3)) = \\ &= w_0 \frac{c_0 + c_2 + c_4 + c_6}{4} + w_1 \frac{c_1 + c_3 + c_5 + c_7}{4} + w_2 \frac{c_7 + c_1 + c_3 + c_5}{4}. \end{aligned}$$

Finally:

$$\begin{aligned} p(a_0) &= p(l_{2k,2m}^{(r)}) = p(d_0) - \bar{p} = \\ &= w_0 \frac{3c_0 - c_2 - c_4 - c_6}{4} + w_1 \frac{3c_1 - c_3 - c_5 - c_7}{4} + w_2 \frac{3c_7 - c_1 - c_3 - c_5}{4} \\ p(a_1) &= p(l_{2k,2m+1}^{(r)}) = p(d_1) - \bar{p} = \\ &= w_0 \frac{3c_2 - c_0 - c_4 - c_6}{4} + w_1 \frac{3c_3 - c_1 - c_5 - c_7}{4} + w_2 \frac{3c_1 - c_7 - c_3 - c_5}{4} \\ p(a_2) &= p(l_{2k+1,2m+1}^{(r)}) = p(d_2) - \bar{p} = \\ &= w_0 \frac{3c_4 - c_2 - c_0 - c_6}{4} + w_1 \frac{3c_5 - c_3 - c_1 - c_7}{4} + w_2 \frac{3c_3 - c_1 - c_7 - c_5}{4} \\ p(a_3) &= p(l_{2k+1,2m}^{(r)}) = p(d_3) - \bar{p} = \\ &= w_0 \frac{3c_6 - c_2 - c_4 - c_0}{4} + w_1 \frac{3c_7 - c_3 - c_5 - c_1}{4} + w_2 \frac{3c_5 - c_1 - c_3 - c_7}{4} \end{aligned} \tag{1}$$

The set of weight $W = (w_0, w_1, w_2)$ we find as solution of the optimization problem:

$$F(W) = \sum_{i=0}^3 (a_i - p(a_i, W))^2 \rightarrow \min_{\mathbb{R}^3}.$$

As a result we obtain weights vector $W^* = (w_0^*, w_1^*, w_2^*)$, which values are determined by prediction context and block values themselves.

We propose to analyze a several images for coder/decoder construction and split all the set of contexts $\{C_i\}_{i=0}^{N-1}$ into several groups $\{G_0, G_1, \dots, G_{M-1}\}$ using clustering. Then we assign weight vector $W(G_n) = (w_0^{(n)}, w_1^{(n)}, w_2^{(n)})$ to each group G_n . Coder and decoder have to know this distribution.

Block encoding procedure consists of three steps. During the first step coder determines prediction context group. Then block prediction $\tilde{b}_{k,m}^{(r)}$ is constructed using (1) and corresponding coefficients. On the last step we encode difference between exact and predicted blocks using one of well known lossless compression algorithm.

Prior result shows advisability for working along this line. At the moment we are working on increasing prediction quality.

Literature

1. **B.I. Golubov, A.V. Efimov, V.A. Scvortsov.** Walsh's serieses and transforms: theory and applications // –Moscow, –1987 (in Russian).
2. **S.A. Bolotov, A.S. Pospelov.** Some properties of digital image averaging operators. System analysis and informing-controlling systems. Collected scientific articles, Moscow, MIEE, -2007, p. 35 (in Russian).

Layered Motion Compensation for a Low Bit Rate Embedded Wavelet Video Coder

Sergei V. Umnyashkin, Eugenia A. Koplovich, Andrei A. Alexandrov

*Moscow Institute of Electronic Technology (Technical University),
E-mail: vrinf@miee.ru*

Abstract — In this paper we propose a framework of scalable motion estimation and coding for a wavelet based video coder. The proposed motion compensation technique includes three layers: one base layer, which corresponds to a coarse motion field, and two sequentially enhancing layers. Experiments are conducted to demonstrate the performance of the embedded video coder with the proposed scheme at various bitrates.

1 Introduction

In image sequences coding temporal redundancy is usually reduced by predicting subsequent frames from a reference frame. Most of practical video coders are based on motion estimation by a block matching in the spatial domain. The block matching compensation (BMC) is also widely employed for wavelet video coders due to its relatively low computational complexity. However, several wavelet domain motion estimation schemes were proposed. The predicted frame is used to calculate a residual image, which is then encoded together with the field of image block motion vectors (MVs) defining the predicted frame.

Wavelet video coders usually produce fully scalable bit streams for residual images since they use bit plane coding. Reordering wavelet coefficients according to their significance enables to achieve the best performance for a given bit rate. While residual image supposed to be coded with a lossy compression scheme, MVs of image blocks have to be coded losslessly. The main problem here is how to make estimated MVs coding scalable and allocate bits between the motion field and the residual image. It is particularly significant for low bit rates where the motion field coding requires most of the strongly limited bandwidth. To achieve better trade-off between motion and texture coding a scalable encoding of image blocks MVs is desirable.

The proposed approach to motion coding generates an embedded bit stream, which consists of three layers representing progressive refinement of the motion field. The encoder decides how many layers to use counting on

the available bandwidth. To estimate coding efficiency, rate-distortion (RD) criterion is applied both for the motion estimation (ME) and the residual image coding.

2 Layered Motion Coding

Figure 1 illustrates image blocks assignment for three motion layers. While processing the first layer MVs are estimated for a quarter of all frame blocks only. Next quarter is processed at the second layer, and the rest 2/4 of the blocks are used for motion estimation at the third layer processing. Each block in the layer is associated with a MV, founded by RD-optimized ME which minimizes Lagrangian function

$$J = D_{MV} + \lambda \cdot R_{MV}, \quad (1)$$

where D_{MV} is the distortion caused by block prediction error, R_{MV} is the bit rate required to encode the MV and λ is the Lagrangian factor setting the balance between the desired rate and distortion characteristics of the compression algorithm used.

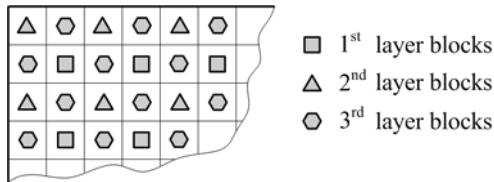


Figure 1: Image blocks layer assignment

At each layer a MV for a current block is coded as a difference between the estimated and a predicted vector. Previously determined MVs are used to build the predicted MV for the block. If \mathbf{m}_A , \mathbf{m}_B , \mathbf{m}_C , \mathbf{m}_D are neighboring MVs, then the motion prediction is calculated as follows:

$$\mathbf{m}_{pred} = \text{median}(\mathbf{m}_A, \mathbf{m}_B, \mathbf{m}_C, \mathbf{m}_D) \quad (2)$$

MVs at the first layer are predicted using previously estimated vectors, as shown in Figure 2a. The prediction for the second layer blocks is based on the estimated MVs from the first layer (Figure 2b). MVs at the third layer are predicted basing on two MVs from the first layer and two MVs from the third layer (Figure 2c).

After each layer MV differences between predicted and real values are coded. If the bit budget for motion compensation is not exceeded the next

motion layer is processed. Otherwise missing MVs are calculated by linear interpolation of neighboring MVs. The decoder performs the same interpolation, so no side information is transmitted.

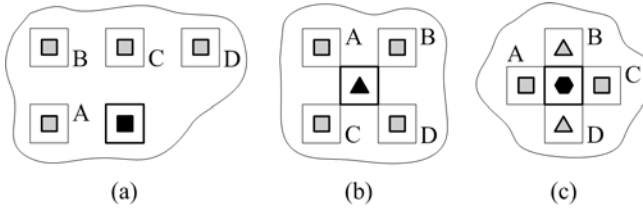


Figure 2: Blocks used for prediction of a current block motion vector at first (a), second (b) and third (c) layers

3 Implementation in Wavelet Video Coder

The layered ME scheme described above is implemented in a wavelet video coder. MV differences are mapped to indices and then coded by a range coder [1] with different quasistatic probability models for each layer. Estimated and interpolated (if less than three layers were processed) MVs are used to form forward predicted frames by means of overlapped BMC technique [2].

Residual images are transformed to a wavelet domain and encoded by SPIHT algorithm [3]. After each bit plane is coded, Lagrangian RD-function similar to (1) with the same parameter λ is calculated to find an optimal number of bit planes to encode wavelet coefficients.

4 Experimental Results

Extensive experiments have been carried out on several videos including standard test sequences to show the performance of the proposed scheme. The RD curves for the Flower Garden sequence with various number of used motion layers are shown in Figure 3. The Flower Garden sequence frame size is 352×224 and it consists of 150 frames (30 fps). Only the very first frame is coded as key I-frame.

Though MVs were estimated for 8×8 blocks with a pixel accuracy, which is rather coarse for such resolution, obtained results confirm that using layered ME can improve coding efficiency particularly at low bit rates. A number of motion layers to use can be chosen depending on channel bandwidth available.

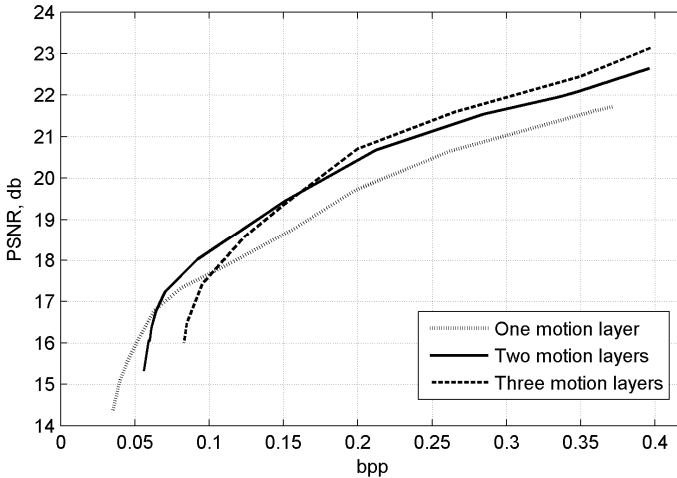


Figure 3: Rate-distortion performance for the Flower Garden sequence with various used layers number

5 Conclusion

A new scalable motion coding scheme with layered structure is proposed in this paper. The simulation results show that it allows to improve coder RD-performance especially at low bit rates. Proposed layered ME method is computationally effective and can be implemented in various real-time video coders.

6 References

- [1] G.N.N. Martin. Range encoding: an algorithm for removing redundancy from a digitised message. Presented to the Video & Data Recording Conference, Southampton, July 24–27, 1979.
- [2] M.T. Orchard, G.J. Sullivan. Overlapped block motion compensation: an estimation-theoretic approach Image Processing, IEEE Transactions on, Volume 3, Issue 5, Sept. 1994 Page(s):693–699.
- [3] A. Said, W.A. Pearlman. A New Fast and Efficient Image Codec Based on Set Partitioning in Hierarchical Trees. IEEE Transactions on Circuits and Systems for Video Technology, vol. 6, pp. 243–250, June 1996.

Tissue modeling for the impedance imaging of the heart

Y.E. Kirpichenko¹, D.P. Timohin¹

¹ *Department of Biomedical Techniques, Bauman Moscow State Technical University, Moscow, Russia*

Introduction

Nowadays noninvasive instrumental methods are to be used in medicine. There is an opportunity to study cardiac electrical activity in conjunction with hemodynamics when a method of tetrapolar frequency-division of rheocardiographic and electrocardiographic signals is used. Addition to the traditional transthoracic rheocardiographic technique precardiac rheographic signals processing allows to analyze not only comprehensive indicators of hemodynamics, but also all the processes of individual sites of heart (valves, ventricles, cardiac apex). Thus, the precardiac rheocardiogram technique can be considered as an additional tool for ultrasound or even as an independent procedure for heart functionality determination. In precardiac rheography method development it is essential to solve several tasks, one of them is modelling of the distribution of electric potentials in the precardiac area (direct problem) and the other one is the determination of model parameters by means of these distributions (inverse problem).

Thereby, solving direct and inverse problems in the precardiac rheocardiography (preRCG) and calculating parameters of the heart model, we can estimate the location of the heart and also determine its biomechanical parameters, such as stroke volume, heart-rate etc.

Precardiac rheocardiography technique

Examinations carried out are connected with tool elaboration to determine functioning parameters of the cardiovascular system by using impedance methods. At the same time measurements are realized in the precardiac area, since such allocation of current and measuring electrodes allows increasing of method precision.

The essence of this technique is that for measurement purposes 4 electrodes usually have to be applied to the body surface. Two electrodes (usually called current electrodes) are used to pass a constant alternating current with a high frequency (60 - 100 kHz) and very low amplitude (1 mA).

The current is imperceptible to the patient and does not cause any physiological reactions. The other two electrodes (usually called measuring electrodes) are placed between the current electrodes and they measure the voltage which is caused by the current flowing through the body segment. This voltage corresponds to the impedance of the body segment and changes in blood volume variations. On this basis the blood flow can be measured and analyzed.

For our modeling for solving direct and inverse problems in the precardiac rheography method we use two biological tissue models: two-layered model and three-layered model.

Direct problem

Under the poly-layer model we consider tissue compound, which contains muscle tissue ($\rho_{\text{muscle}} = 5 \text{ Ohm}\cdot\text{m}$), pulmonary tissue ($\rho_{\text{pulm}} = 8 \text{ Ohm}\cdot\text{m}$), myocardium ($\rho_{\text{myo}} = 5 \text{ Ohm}\cdot\text{m}$, $h_{\text{myo}} = 0.02 \text{ m}$) and bone tissue ($\rho_{\text{bone}} = 10 \text{ Ohm}\cdot\text{m}$). In case of the two-layered model this compound is replaced by effective specific resistance ρ_1 , upper layer's thickness is determined by occurrence depth of the heart, $h_1 = 0.1 \text{ m}$, and specific resistance of the lower layer corresponds to specific resistance of blood ($\rho_{\text{blood}} = 1.0\text{-}1.5 \text{ Ohm}\cdot\text{m}$). In case of the three-layered model we consider a myocardium layer as a separate layer.

The major mathematical modeling of the preRCG involves calculation of direct and inverse problems. In the direct problem governing equations in the preRCG field are derivable from Laplace's Equation (electrostatic approximation for low frequency).

In this section the three-layered model will be considered. The model imitates precardiac area properties very well. The three-layered heart model is shown in Fig.1. There are current electrodes at points A and B and measuring electrodes at points M and N, respectively.

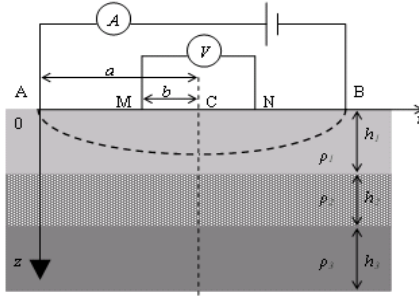


Fig.1. Three-layered heart model

To solve Laplace's equation we can make use of boundary conditions, i.e. continuity of potential and continuity of the normal component of the current density at the bedding interface. Besides, we take into consideration that air is not a good electrical conductor and the potential must be equal to 0 at infinity

Under these boundary conditions the expression for impedance on the body surface is:

$$R(a, b) = \frac{\rho_1}{\pi} \left[\frac{1}{a^2 - b^2} + \int A_1(m) \cdot J_0[m \cdot (a - b)] dm - \int A_1(m) \cdot J_0[m \cdot (a + b)] dm \right]$$

$$A_1(m) = \frac{N}{D_1 + D_2}$$

$$N = (\rho_2 - \rho_1) \cdot (\rho_3 + \rho_2) \cdot e^{-4 \cdot m \cdot h_1} + (\rho_2 + \rho_1) \cdot (\rho_3 - \rho_2) \cdot e^{-4 \cdot m \cdot h_1 - 2 \cdot m \cdot h_2}$$

$$D_1 = (\rho_1 + \rho_2) \cdot (\rho_3 + \rho_2) \cdot e^{-2 \cdot m \cdot h_1} + (\rho_2 - \rho_1) \cdot (\rho_3 - \rho_2) \cdot e^{-2 \cdot m \cdot h_1 - 2 \cdot m \cdot h_2}$$

$$D_2 = (\rho_1 - \rho_2) \cdot (\rho_3 + \rho_2) \cdot e^{-4 \cdot m \cdot h_1} + (\rho_1 + \rho_2) \cdot (\rho_2 - \rho_3) \cdot e^{-4 \cdot m \cdot h_1 - 2 \cdot m \cdot h_2}$$

Final impedance vs. distance between current electrodes is shown in Fig.2 (the distance between measuring electrodes is 0.05 m).

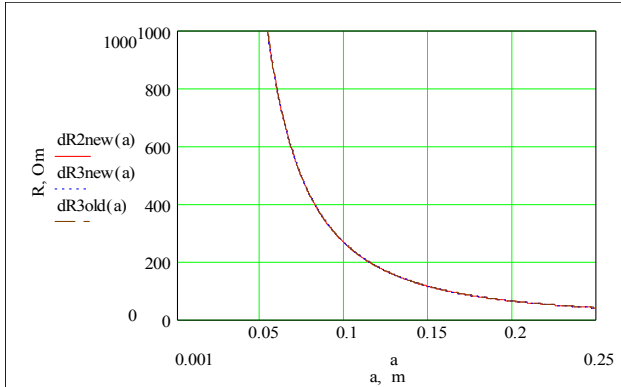


Fig.2 Impedance distance between current electrodes (the distance between measuring electrodes is equal to 5 cm)

Inverse problem. Apparent resistivity conception.

In a homogeneous half-space with specific resistance $\rho(r)$ the relationship has the following form:

$$\rho(r) = \frac{2 \cdot \pi \cdot r^2}{I} \cdot \frac{\partial \varphi_1(r, 0)}{\partial r}$$

In case of tetra polar gradient electrode system (Fig.1) and under the condition that $MN \ll AC$:

$$\rho \approx \frac{\pi \cdot AM \cdot AN}{MN} = \frac{\pi \cdot (a-b) \cdot (a+b)}{2b} \cdot R_{MN}$$

If the medium is not homogeneous ρ is called apparent resistivity. It is denoted as ρ_k . For the two-layered model:

$$\rho_k = \rho_1 \cdot \left[1 + 2 \sum \frac{K^n \cdot r^3}{[r^2 + 2 \cdot n \cdot h_1^2]^{3/2}} \right]$$

If $r \ll h_1$ $\rho_k \approx \rho_1$, and so if $r \rightarrow \infty$ $\rho_k \rightarrow \rho_2$.

Curves of apparent resistivity as a function of the semidistance between current electrodes are shown in Fig.3 (h_1 is a variable).

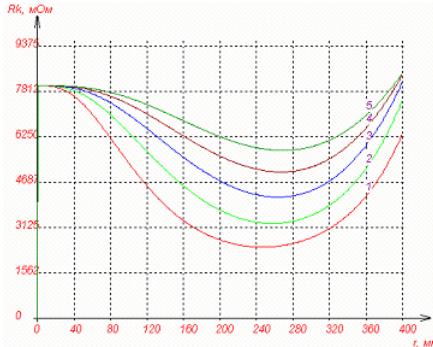


Fig. 3. Apparent resistivity vs. semidistance between current electrodes (the three-layered model, $\rho_1 = 8 \text{ Ohm}\cdot\text{m}$, $\rho_2 = 500 \text{ Ohm}\cdot\text{m}$, $\rho_3 = 1.35 \text{ Ohm}\cdot\text{m}$, $h_1 = 0.03\text{-}0.12 \text{ m}$, $h_2 = 0.02 \text{ m}$).

Thus, the inverse problem is the determination of model parameters by means of impedance distributions. In order to determine the model parameters by using impedance distribution we make use of an apparent resistivity conception. We need to determine 3 parameters (ρ_1, ρ_2, h_1) of the two-layered model and 5 parameters ($\rho_1, \rho_2, \rho_3, h_1, h_2$) of the three-layered model. Having measured the apparent resistance we can determine electrical specific resistance of one of the layers. Also, sorting out all the possible parameters-combinations it is possible to define other unknown parameters by using technique of least squares.

Application

In order to automatize determination of parameters we have developed an application. It allows us to calculate impedance distributions by using model parameters and vice versa: it calculates model parameters by using set of impedance values (a screen shot is shown in Fig. 4).

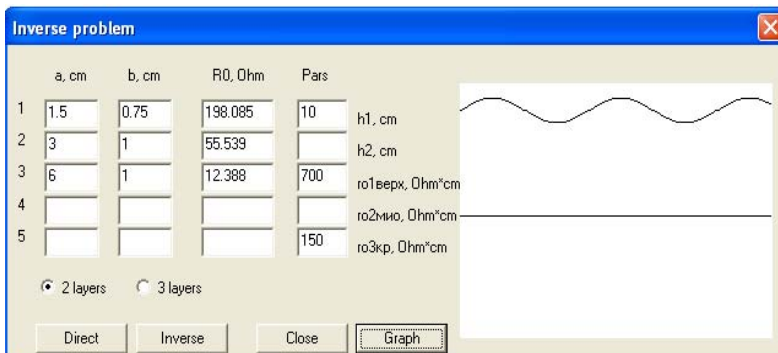


Fig.4. Application for solving direct and inverse problems.

Conclusion

In this paper we analyzed main features of the precardiac rheography technique and examined general poly-layer models to simulate the precardiac area tissues. Solutions for the direct problem (by solving Laplace's equation with the boundary conditions) and determination of model parameters by solving the inverse problem (using the apparent resistivity method) are presented.

The following goals have been reached:

- Estimation of the influence of the electrode system onto impedance distribution
- Estimation of the influence of the electrode system onto the inverse problem (model parameters determination having used different impedance values)
- Algorithm for solving the inverse problem for the two-layered model by means of processing acquired impedance values
- Parameters determination of a biological tissue in the precardiac area. (Determination of such parameters as resistivity and thickness of the upper layer for the two-layered model)

According to the solution of the inverse problem for the two-layered model and using the developed algorithm for solving the inverse problem and total impedance measurement accuracy of 10mOhm for the multichannel system model parameters determination accuracy: upper layer resistivity error less than 1%, thickness of the upper layer error less than 2% and second layer resistivity error less than 5%.

Impedance imaging in human's precardiac area

Y.E. Kirpichenko¹, D.P. Timohin¹

¹ *Department of Biomedical Techniques, Bauman Moscow State Technical University, Moscow, Russia*

Introduction

For a last ten years developed countries have been expressing an interest in tools for non-invasive monitoring of pumping ability of the heart. One of these tools is a transthoracic rheography method. It is based on the impedance measurement which is caused by changes in blood volume of the body segment. In order to increase the determination cardiovascular system's functioning parameters we can place the electrode system in the precardiac area, but for all that we have to develop algorithms and experimental techniques. It is advisable to make use of the precardiac rheography (preRCG) technique for solving these problems. Y.T. Pushkar' pioneered the use of this method in 1959.

The essence of this technique is that for measurement purposes 4 electrodes usually have to be applied to the body surface. Two electrodes (usually called current electrodes) are used to pass a constant alternating current with a high frequency (60 - 100 kHz) and very low amplitude (1 mA). The current is imperceptible to the patient and does not cause any physiological reactions. The other two electrodes (usually called measuring electrodes) are placed between the current electrodes and measure the voltage which is caused by the current flowing through the body segment. This voltage corresponds to the impedance of the body segment and changes in blood volume variations. On this basis the blood flow can be measured and analyzed.

Precardiac rheocardiography perspectives

In precardiac rheography method's development it is essential to solve a number of general theoretical and practical tasks. The following tasks are chosen among theoretical tasks:

- Interpretation of the mechanism of precardiac rheography signal's generation
- Requirements for electrodes positioning

- Layered mediums modelling in order to determine geometrical and electrical characteristics of each of the layers, real-time estimation of these characteristics
- Phase analysis of precordial signals, data acquisition for heart localization and visualization processes in the heart
- Determination heart parameters (stroke volume, heart-rate etc.)

Heart's boundary localization by using precordial signals analysis

Realized research have shown that basic impedance increases in the area of heart projection on the thorax and decreases outside. This feature allows us to determine heart projection on the thorax and to perform heart imaging. (Fig.1). This property allows using imaging as the tomographic technique in the precordial area.

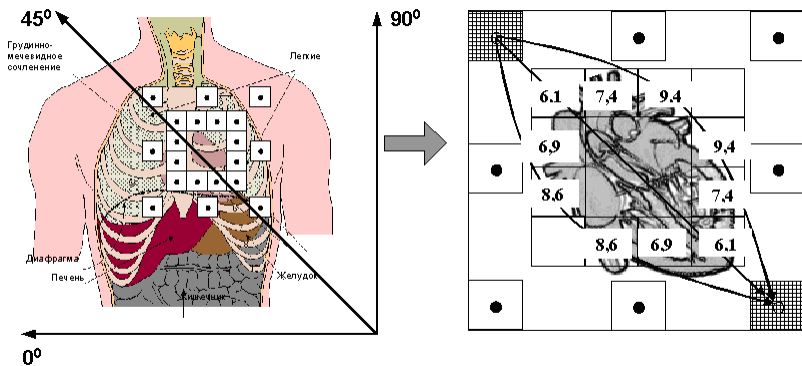


Fig. 1. Basic impedance distribution in the precordial area

The heart's boundary determination by using basic impedance values in different leads is the primary task. It is possible to examine this task as the indirect task. In the area of the heart projection on the thorax basic impedance value Z_{base} essentially less than in other parts of the thorax. It is possible to choose an area $10 \times 10 \text{ cm}^2$ on the thorax surface. Inside this area basic impedance is less than outside it. Having marked this area by using basic impedance data, we determine heart projection on the thorax and estimate it dimensions. It is possible to approximate heart by means of ellipsoid of rotation. It is characterized by 2 parameters: big and small axes. Thus, for

the heart's boundary determination by using the precordial signal analysis it is necessary to solve the following tasks:

- Electrode system creation.
- Algorithms development, which could plot heart projections images, approximation function choice.
- Impedance imaging
- Algorithms development, which could determine heart's boundaries by means of impedance distribution.

Application

In order to obtain heart image it is necessary to develop a multichannel system and an application for data acquisition and perform impedance heart imaging. The multichannel system during its work process is shown in Fig. 2.

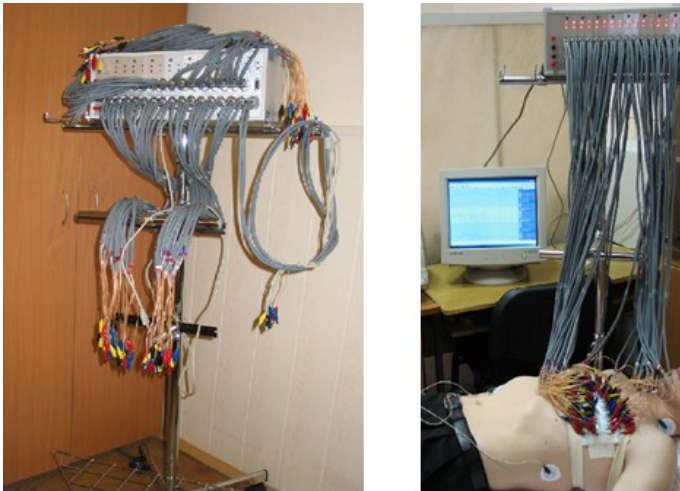


Fig.2. Multichannel system for rheocardiography applications.

Software for the multichannel system has been developed under Win32 OS. It provides the following features:

- data acquisition
- calibration of the multichannel system with a built-in calibrator
- visualization of physiological signals
- online digital signal processing (noise filtration, removing unnecessary biological signals such as respiratory pattern)

- on-line contour analysis of ECG and transthoracic RCG signals
- separation of respiratory pattern from rheocardiographic signals for further analysis
- heart imaging having used the solution of the inverse problem in real-time.

Conclusion

In this paper we analyzed main features of the precardiac rheography technique and investigated the features of real-time impedance heart imaging. The following goals have been reached:

- The principles of electrode system creation were recognized.
- Multichannel system to perform impedance heart imaging was developed. This system includes 30 precardiac rheographic channels, a transthoracic rheographic channel and an electrocardiographic channel. Also, it allows imaging of impedance determination in the precardiac area.
- Software for data acquisition and rheographic signal processing was developed. Software performs connection with multichannel system via USB, includes calibrator functions, digital signal filtering, data bank functions.
- Heart images from precardiac area were recorded and analyzed. Data were obtained from healthy volunteers at the age of 20-25.

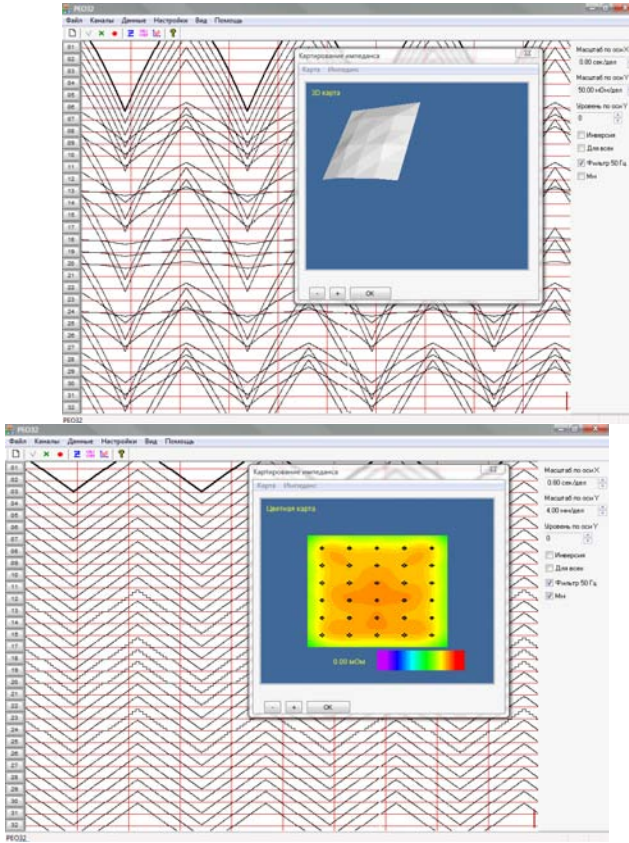


Fig.3. PC-based application for the multi-channel system.

The developed algorithm allows to determine a heart location. It is also possible to estimate heart volumetrical characteristics. Due to system measured data a movement amplitude of the right ventricle wall has been calculated. Calculated values were ranged from 5 to 7 mm.

Ill-posedness in electric impedance tomography forward problem

Anna G. Mikhaylova

Moscow State University of Instrumental Building and Computer Science

e-mail: mikhaylova_anna@list.ru

Electrical impedance tomography method

By electrical impedance tomography (EIT) we mean the process of estimation internal admittivity (complex conductivity) changes from low frequency current and voltage measurements through a system of electrodes at the surface.

The impedance problem is described with Laplace equation at the low frequency:

$$\nabla \cdot (\gamma(x, w) \nabla \varphi(x, w)) = 0,$$

where x – point in Ω , $\varphi(x, w)$ – measured voltages on the surface, $\gamma(x, w) = \sigma(x, w) + iw\varepsilon(x, w)$ – admittivity, $\sigma(x, w)$ – conductivity, $\varepsilon(x, w)$ – permittivity.

and Helmholtz equation at all frequencies:

$$\nabla^2 \varphi(x, w) + k^2 \varphi(x, w) = -\frac{\rho}{\varepsilon},$$

where $k^2 \equiv -i\omega\mu\gamma$, μ – magnetic conductivity

It is necessary to consider discrete nature and high conductivity of electrodes, electrical-chemical effects on the electrode-skin boundary (which is high resistivity) and inner current source absence. These effects add some more equations to the govern equation and produce complete electrode model:

$$\begin{aligned} \gamma(x, w) \frac{\partial \varphi(x, w)}{\partial n} &= j \quad \text{on } \partial\Omega, \\ \int_{e_l} \gamma(x, w) \frac{\partial \varphi(x, w)}{\partial n} ds &= I_l(w) \quad l = 1, 2, \dots, L, \\ \gamma(x, w) \frac{\partial \varphi(x, w)}{\partial n} &= 0, \quad \text{on the gaps between electrodes} \end{aligned}$$

$$u + z_l \gamma(x, w) \frac{\partial \varphi(x, w)}{\partial n} = \varphi_l(x, w) \quad \text{on } e_l, \quad l = 1, 2, \dots, L$$

$$\sum_{l=1}^L I_l = 0$$

This model has an unique solution and predicts the measurement result with 1% accuracy.

Numerical solution of impedance tomography problem

To numerical solution the continuous problem is changed with discrete problem and we use finite element method to do it. So matrix equation $Au=f$ should be solved, where f – applied current, u – measured voltages on the surface, A – operator of electrical properties of biological object (conductivity and permittivity).

Triangulation

Numerical solution of continuous impedance tomography problem is based on transformation to discrete formulation (the whole object is divided into a finite number of simple elements with constant properties within each element). The real biological objects need a fine triangulation with huge amount of elements (for example, Bayford and colleagues [1] model human head with 23219 elements for skin, 63982 - for skull, 47140 - for cerebral fluid, 21574 - for brain, totally – more than 155 thousand elements). Implementation of such a mesh manually is practically impossible, so additionally forward algorithms should be completed with mesh generation algorithms.

Theory of mesh implementation is studied by computational geometry and greatly developed in the last decades [3].

Mesh can give accurate numerical solution, if its elements satisfy the following:

- sharp angles are not allowed (they give the accuracy decreasing) and the minimal permissible angle value is determined
- mesh should be finer in inhomogeneity boundaries (the decreasing mesh quality in homogeneous parts leads to time and resource reduction)

Ill-posedness due to triangulation

Forward solver divergence is strictly depends on system matrix properties – the more similar the matrix eigenvalues are, the faster the divergence is. Measure of matrix eigenvalue range is the ratio between maximum and minimum eigenvalues $k = \frac{\lambda_{\max}}{\lambda_{\min}}$. The range of minimax

eigenvalues limits with minimal and maximal volumes of triangulation elements (triangle in 2D and tetrahedron in 3D). At the same time, it depends slightly on shape elements itself. More important, that maximum eigenvalue is increased dramatically in presence of even single “bed-shaped” element.

Geometry of real biological objects apply a lot of restrictions to get a regular mesh. Also real biological objects contain a lot of conclusions with different shapes and properties.

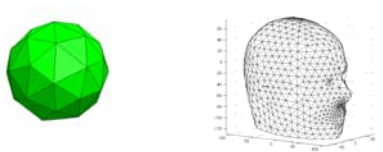
So the typical impedance matrix is ill-posed.

Experimental results – degree of ill-posedness due to different triangulation

Several triangulations were implemented and degree of ill-posedness based on element volumes was investigated (using netgen mesh generator, v.4.3 - J.Schöberl, Johannes Kepler University, Austria).

Several objects were investigated – simple sphere (as the simplest object), spheres with one and several inclusions (with finer mesh near boundaries), human head model ([2]) (as the most sophisticated object, much more similar to the real biological object). The coarse and fine simulation were implemented for each kind of objects. Picture shows the triangulation samples.

Picture. Triangulation of different objects.



Simulations show the object complexity and inhomogeneity as a main reason of ill-posedness in impedance tomography. Considering the maximal eigenvalue as not depended on element volumes, it is possible to see the

minimal eigenvalue range. It expands with structure and shape complexity increasing and runs up to 3rd – 4th order to complicated objects compared with simple objects.

Table. Condition number estimation for different meshes

	nodes and tetrahedrons	max and min tetrahon volume	condition number estimation
single sphere with different mesh quality			
coarse	44 nodes	0.0457	7.9506
	112 tetrahedrons	0.3632	
fine	546 nodes	0.0024	6.9441
	2146 tetrahedrons	0.0164	
cube with one and several inclusions			
single inclusions	276 nodes	0.00027	820.36
	1320 tetrahedrons	0.2187	
several inclusions	323 nodes	0.00004	707.54
	1655 tetrahedrons	0.0281	
human head model with different mesh quality			
coarse	5226 nodes	0.1195	14775.7
	27684 tetrahedrons	1765.7	
fine	48394 nodes	0.1039	1767.3
	262368 tetrahedrons	183.5647	

Special algorithms should be developed to solve impedance problem. They should be stressed with resource-consuming and algorithm stability (because of noises in measured data). More often, they are several steps algorithms with preliminary conditioning and regularization.

1. Bayford R.H., Gibson A., Tizzard A., Tidswell T., Holder D.S. “Solving the forward problem in electrical impedance tomography for the human head using IDEAS (integrated design engineering analysis software). A finite element model tool”, *Physiol. Meas.*, #22, 2001. – pp. 55-64.
2. Tizzard, A. and Bayford, R.H. (2007). Improving the Finite Element Forward Model of the Human Head by Warping using Elastic Deformation. *Physiol.Meas.*, #28, 2007. – pp.S163-S182.
3. Sheymos M., Preparata F. Computational geometry. Introduction. M., «Nayka», 1989. (in Russian)

The experimental setup for obtaining an optical tomograms

I.V. Pyanov

*Moscow Institute of Electronic Technology (Technical University),
e-mail: ivan-pyanov@yandex.ru*

A transmission optical tomography (TOT) is a perspective method of medical diagnostics of biological tissues and organs. Fundamental advantages of TOT are a nonionizing optical radiation, compact and low cost of necessary devices.

However optical radiation is attenuated through biological tissues significantly due to high scattering, which leads also to complication of mathematical processing of the experimental data and difficult registering. The most promising targets for TOT are neonatal brain and woman breast.

The fundamental equation for description of the radiation propagation in the scattering medium is the radiation transport equation (RTE). But this equation can not be solved in general terms. Therefore, the various methods have been used to simplify RTE under certain conditions.

This work is based on the non-axial model of radiation transport [1] and aims to the tomographic reconstruction of the spatial distribution of radial symmetric phantoms' extinction coefficient (the sum of scattering and absorption coefficients). In this case the approximation of proportional medium has been used additionally. This approximation postulated that scattering coefficient is directly proportional to the absorption coefficient.

The special experimental setup and scattering phantoms are required for obtaining an optical tomograms.

The experimental setup (Figure 1) consists of:

1) the source of optical radiation (continuous wave semiconductor laser with 650 nm wavelength);

2) the object of investigation (the phantom of high scattering medium): an emulsion of the intralipid particles in the flax oil (the refractive index $n_1=1.483$) filled in a cylindrical deepening with diameter 28 mm in polymethylmetacrylate (PMMA) parallelepiped $60\times 40\times 45$ mm with $n_2 = 1.491$;

3) the object linear displacement system – computerized motorized mechanical system Standa 8MT175-200;

4) the photodetector for registration radiation passed through the phantom of high scattering medium – a silicon photodiode, which is connected to personal computer using external ADC with RS-232 interface.

The control of a linear movement, the collection and processing of experimental data were carried out using a PC.

In the tomographical experiment the laser beam (diameter of 1 mm) scans the object in the horizontal plane to normal for the central part of object. The laser beam moving with 0.5 mm step in the plane.

The special light-protective module (600×600×300 mm) used in the experimental setup to minimize influence of the outside light.

The optical characteristics of high scattering medium, which used in experiments, are close to the corresponding values of biological tissue. For example the refractive index of the woman breast was 1.45.

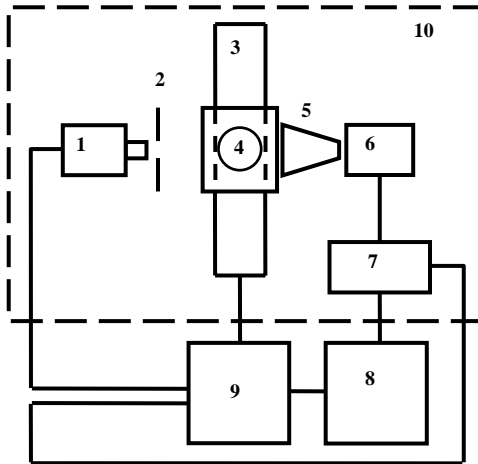


Fig. 1. The experimental setup block-scheme: 1 – semiconductor laser, 2 – iris diaphragm Ø2 mm, 3 – motorized mechanical system, 4 – phantom of high scattering media, 5 – focusing cone, 6 – photodiode, 7 – ADC, 8 – personal computer, 9 – motorized system control and power supply unit, 10 – light-protective module

PMMA-cylindrical mould core (diameter 15 mm) or PMMA-pipe (outer diameter 12 mm and inner diameter 6 mm) was placed in the middle of cylindrical deepening for formation of the the heterogeneity. Such model object represents medium which has homogeneous of refraction index and heterogeneous absorbing and scattering coefficients.

An example of reconstruction of the homogeneous radial symmetric phantom is shown in Fig. 2.

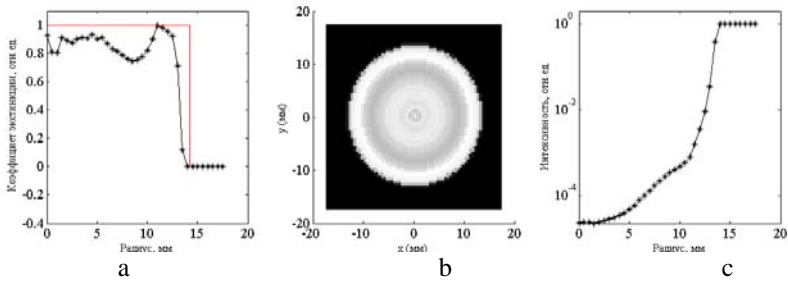


Fig. 2. The result of reconstruction of 28 mm diameter homogeneous radial symmetric object: the reconstructed 1-D extinction coefficient spatial distribution (a), the restored 2-D image of extinction coefficient spatial distribution (b), the registered projection (c)

An example of reconstruction of the radial symmetric phantom with heterogeneity in the form of cylindrical mould core (diameter 15 mm) is shown in Fig. 3.

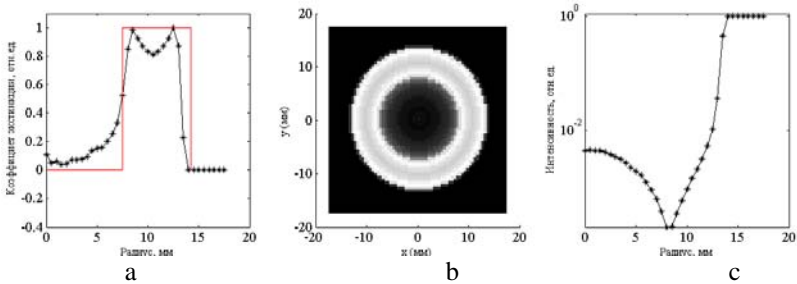


Fig. 3. The result of reconstruction of radial symmetric object with heterogeneity as a cylindrical mould core (diameter 15 mm): the reconstructed 1-D extinction coefficient spatial distribution (a line with points – a real structure of distribution, a continuous line – geometrically set) (a), the restored 2-D image of extinction coefficient spatial distribution (b), the registered projection (c)

An example of reconstruction of the radial symmetric phantom with heterogeneity in the form of pipe (outer diameter 12 mm and inner diameter 6 mm) is shown in Fig. 4.

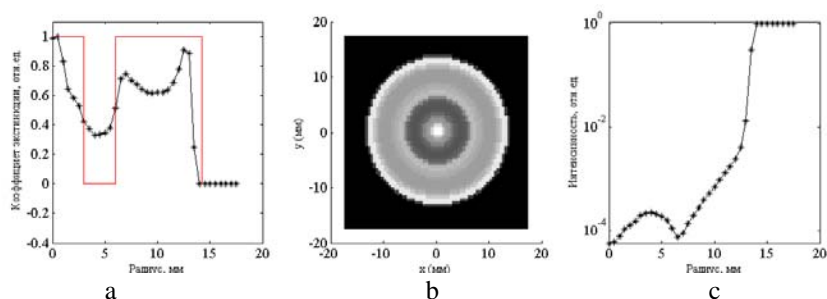


Fig. 4. The result of reconstruction of radial symmetric object with heterogeneity as a pipe (outer diameter 12 mm and inner diameter 6 mm): the reconstructed 1-D extinction coefficient spatial distribution (a line with points – a real structure of distribution, a continuous line – geometrically set) (a), the restored 2-D image of extinction coefficient spatial distribution (b), the registered projection (c)

The results of radial symmetric phantoms reconstruction corresponds to the expected results. There are some reconstruction artifacts due to an effects of light refraction and reflection at the surface of medium and PMMA-parallelepiped. The instrumental and program correction methods used to minimize the artifacts. This correction methods can improved the quality of reconstruction.

Literature:

1. Tereschenko S.A. The methods of computed tomography. – M.: Fizmatlit, 2004, 320 p.

A method for the investigation of psychophysiological status of individuals working under extreme conditions

N.S. Gogulina, I.N. Spiridonov

*Bauman Moscow State Technical University (BMSTU)
natalya.gogulina@gmail.com, inspiridonov@yandex.ru*

Introduction

Staff recruitment for working under extreme conditions calls for a special approach to choice criteria of professional aptitude. As a rule, first of all genotype-determinate behavioral responses become apparent under stress, under excessive load, in case of need to make a responsible decision. At the same time, genotype is responsible for heredity and its adaptation ability. So, it is necessary to develop a method of psychophysiological status (PPS) research, which will permit to get genotype-determinate features.

Recently, parameters of papillary patterns have been used as an original genetic marker of brain morphological constitution. It is well known that the development of skin ridges and nervous system comes from the ectoderm of an embryo; they develop simultaneously during pregnancy under the same conditions. Consequently, the interconnection between fingerprints and the features of nervous system can exist. A lot of Russian and foreign scientists have been doing research in this field, as a result of which correlation between fingerprints and hereditary diseases of nervous system, for example, schizophrenia and Down's syndrome, has been found. Besides, correlation between fingerprints and physiological features of professional sportsmen has been discovered.

A complex of dermatoglyphic parameters (CDP) used for PPS research has some advantages, i.e. skin ridges are readily available for research, dermatoglyphic parameters can be expressed by both qualitative and quantitative attributes, which can have diagnostic value, papillary patterns appear during pre-natal development and don't change in time.

There are a lot of methods of psychophysiological status research, for example, testing light and sound reactions, testing attention, memory, temperament and ability, using questionnaires.

The most common techniques of testing are Minnesota Multiphasic Personality Inventory (MMPI), the 16 Personality Factors of R.Cattell, the tests of Hans. J. Eysenck, Test Anxiety Inventory of C. D. Spielberger. There

are a lot of hardware and software complexes for the measurement of motorial and other reactions of a person and also polygraph detectors.

All these methods have a common drawback: a research process takes too much time.

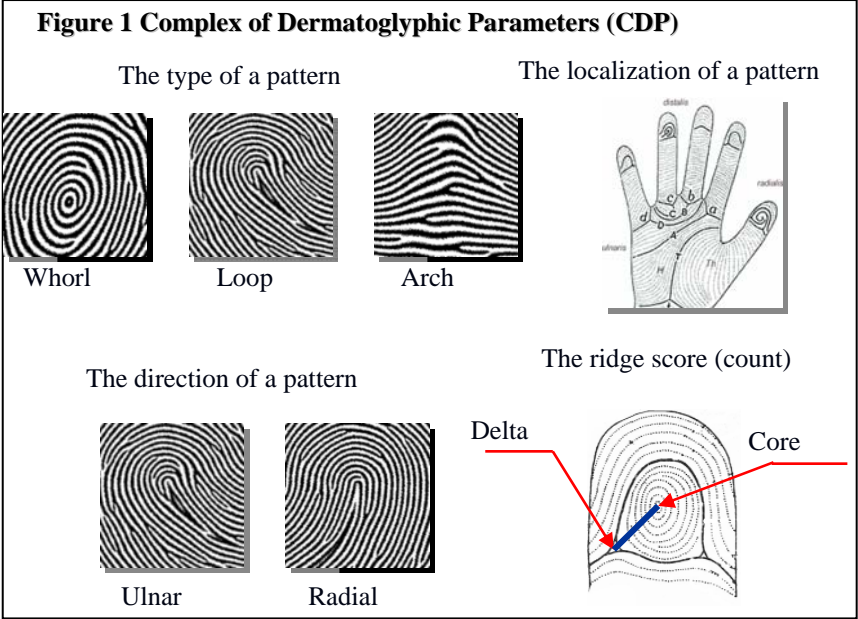
Materials and methods of research

Cattell's test technique (or The Cattell 16PF (16 Personality Factor)) has been chosen for the investigation of the interrelation of fingerprints and PPS. Research has been carried out in cooperation with a psychologist from the Institute of Medical and Biologic Problems.

This technique is also frequently applied for vocational guidance by many businesses where work is connected with extreme conditions, for example, GASPROM (natural gas industry).

The technique represents a test questionnaire consisting of 187 questions with 3 variants of answers to each. The test resulted in determining 16 main personal factors.

For the research of the interrelation of CDP parameters and PPS the results of psychological testing and the following dermatoglyphic parameters have been compared: the type of a pattern, its localization and direction, a deltoid index and the ridge score. (Figure 1)



Dermatoglyphic parameters and the results of psychological testing of 60 BMSTU students born between 1982 and 1985 were used as the initial material for research.

Data gathering was carried out on forms without indicating personal data; the results were identified by numbers using double coding, which provided both confidentiality of the received information and the objectivity of the obtained PPS estimations.

Results

The results of comparing CDP and PPS have shown the interrelation of psychological features and the following dermatoglyphic parameters (Table 1)

Table 1. Conformity between PPS and CDP

Parameter	A component of a dermatoglyphic phenotype
Leader abilities	The type, localization of a pattern, and the ridge count (W)
Skill to communicate	The type, localization of a pattern, and the ridge count (W)
Extroversion	The type, localization of a pattern, and the ridge count (A)
Conflicting character	The type, localization of a pattern, and the ridge count (Lr)
Extremeness	Patterned asymmetry of hands
Estimation of I.Q.	The type, localization of a pattern, and the ridge count (W)

The results of interrelation research of PPS characteristics' estimation using Cattell's tests and the estimations of similar PPS characteristics obtained by dermatoglyphic research are presented in Table 2. Mark "+" designates complete correspondence of the estimation obtained in dermatoglyphic research and Cattell's tests while "0" marks the impossibility of defining PPS parameters ("average value") and "-" - discrepancy of results.

Table 2. Results of research of interrelation between CDP and PPS

Presence of interrelation	Leader abilities	Skill to communicate	Extroversion	Conflicting character	Extremeness	Estimation of I.Q.	Total
+	71%	63%	48%	78%	81%	54%	65.5%
0	0%	29%	30%	0%	19%	42%	20.1%
-	29%	8%	22%	22%	0%	4%	14.4%

Conclusion

Thus the research has shown the existence of interrelation between psychological and dermatoglyphic features. Discrepancies observed in some cases between the results of Cattell's test and dermatoglyphic research could be explained by situational variability and correction of personal genotype features in the course of education and under the influence of social environment. The features of person's genotype manifests above all under extreme conditions, therefore the developed technique could be more reliable in comparison with the methods of psychometric testing.

The developed method will allow to create a new tool for the psychologist's work. The scope of the developed technique includes

- Medicogenetic consultation
- Occupational selection
- Sports medicine
- Ethnic anthropology
- Forensic medical examination
- Biometrical research

Experimental Investigation of Optical Characteristics of Homogeneous High-Scattering Biological Medium

*A. A. Danilov, Yu. P. Masloboev, D.A.Potapov, S. V. Selishchev
and S. A. Tereshchenko*

Moscow Institute of Electronic Technology (MIET)
Department of BioMedical Systems, Moscow, Russia
E-mail: tsa@miee.ru

Transmission optical tomography (TOT) is a promising method for medical diagnosis. However, in spite of significant effort, no commercial TOT tomograph model is presently available, and so this method has not yet been introduced into medical practice. This is primarily due to the difficulty of mathematical description of the interaction of laser radiation with high-scattering biological medium (HSM). The interaction of laser radiation with HSM is more complicated than the interaction of laser radiation with optically pure absorbing medium. In the case of HSM, it is impossible to neglect the scattering properties of biological tissue. Therefore, mathematical algorithms used in conventional tomography cannot be directly applied to TOT. Efficient TOT algorithms cannot be developed without first solving the problem of adequate mathematical description of the interaction of laser radiation with HSM. The goal of this work was to describe the results of measurement of temporal distribution of laser pulse propagating through a homogeneous layer of model HSM (milk dissolved in water) and to determine of the optical characteristics of the medium at various concentrations of the scatterers (milk). Two approximate models were used for the theoretical description of laser radiation interaction with HSM: diffusion approximation [1] and non-stationary axial model [2]. Both models were used to determine physical characteristics of the scattering medium on the basis of experimental data.

The non-stationary radiation transmission equation (RTE) is the main approach to description of interaction of laser radiation with HSM [1,2]:

$$\frac{1}{v} \frac{\partial}{\partial t} \Phi(\vec{r}, \vec{\Omega}, t) + \vec{\Omega} \text{grad}(\Phi(\vec{r}, \vec{\Omega}, t)) + \mu(\vec{r}) \Phi(\vec{r}, \vec{\Omega}, t) - \iint_{4\pi} \Phi(\vec{r}, \vec{\Omega}', t) \mu_s(\vec{r}, \vec{\Omega}' \rightarrow \vec{\Omega}) d\Omega' = S(\vec{r}, \vec{\Omega}, t) \quad , \quad (1)$$

where $\Phi(\vec{r}, \vec{\Omega}, t)$ is the density of photon flow at point \vec{r} in time moment t propagating in direction $\vec{\Omega}$; $\mu_s(\vec{r}, \vec{\Omega} \rightarrow \vec{\Omega}')$ is the angular differential scattering coefficient (scattering indicatrix); $\mu(\vec{r}) = \mu_a(\vec{r}) + \mu_s(\vec{r})$ is the extinction coefficient; $\mu_a(\vec{r})$ is the radiation absorption coefficient; $\mu_s(\vec{r}) = \iint_{4\pi} \mu_s(\vec{r}, \vec{\Omega}' \rightarrow \vec{\Omega}) d\Omega' = \iint_{4\pi} \mu_s(\vec{r}, \vec{\Omega}' \rightarrow \vec{\Omega}) d\Omega$ is the scattering coefficient; $S(\vec{r}, \vec{\Omega}, t)$ is the density of photon sources at point \vec{r} in time moment t propagating in direction $\vec{\Omega}$; v is the modulus of radiation propagation speed in the medium.

Equation (1) has no general analytical solution. Some additional assumptions allow the expression for temporal distribution of ultrashort pulse passed through an HSM layer to be derived. According to the diffusion approximation, the following expression describes the temporal distribution of intensity of photons scattered with a homogeneous HSM layer at the axis of a monodirectional point source (axis z) in the semi-infinite medium [1]:

$$R(z, t) = \frac{U_0 \left| (z - z_0) \exp\left(-\frac{(z - z_0)^2}{4Dvt}\right) - (z + z_0) \exp\left(-\frac{(z + z_0)^2}{4Dvt}\right) \right|}{2(4\pi Dv)^{3/2} t^{5/2} \exp(\mu_a vt)} \quad (2)$$

where $z_0 = (\mu'_s)^{-1} = (\mu_s - \mu_1)^{-1} = [(1 - g)\mu_s]^{-1}$; μ'_s is the reduced scattering coefficient; g is mean cosine of scattering angle; U_0 is the initial pulse energy, $D = (3(\mu - \mu_1))^{-1}$ is the diffusion coefficient.

The nonstationary axial approximation RTE is based on the assumption of "scattering straight back" in HSM [2]. In this case, the resulting temporal distribution of relative intensity of scattered photons at the axis of a monodirectional point source in the semi-infinite medium can be described as [7]:

$$R(z, t) = U_0 \eta (\mu vt - \mu z) \frac{v \mu_s z}{\sqrt{(vt)^2 - z^2}} I_1 \left(\mu_s \sqrt{(vt)^2 - z^2} \right) \exp(-\mu vt) \quad (3)$$

where $\eta(\bullet)$ is the Heaviside function (unit step function); $I_1(\bullet)$ is the modified Bessel function of the first order; μ_a is absorption coefficient; μ_s is scattering coefficient; $\mu = \mu_s + \mu_a$ is extinction coefficient.

It is assumed that Eqs. (2) and (3) describe the radiation passed through an HSM layer with thickness z . It should be also noted that in the axial and diffusion models, the absorption coefficient and scattering coefficient have different physical meanings. Therefore, numerical values of the coefficient may differ from each other.

The ideal temporal distribution of the intensity of a laser pulse passed through an HSM layer is shown in Fig. 1. The most important parameters of distribution are shift of scattering maximum with respect to ballistic peak τ , full width at the half maximum (FWHM) d , and scattering peak maximum f_m . Such bimodal distribution usually is not observed in experiment because of considerable duration of the initial laser pulse. In the absence of scatterers, only the ballistic peak is observed. As the scatterers concentration increases, the width of the peak (superposition of ballistic and scattering peaks) also increases. Upon further increase in the scatterers concentration, the ballistic peak amplitude tends to zero, so that the observed peak coincides with the scattering peak.

A block diagram of the experimental setup used in this work is shown in Fig. 2. A Becker and Hickl BHL700 IR semiconductor laser (Germany) (wavelength, 782 nm; pulse duration, 75 psec; pulse repetition frequency, 50 MHz; mean power, 2 mW) was used as a radiation source. A Hamamatsu HAM_H5783_2 photomultiplier (Japan) and a Becker and Hickl SPC_130 data board (Germany) were used in the detector channel. The time resolution of the system in photon counting mode was 200-230 ps. Milk dissolved in water was used as a model HSM (milk concentration, 0-0.05). The use of calibrated light filters allowed the radiation intensity to be measured in 10 orders of magnitude range. Transmitted radiation intensity was measured in the presence and in the absence of water to determine the water absorption coefficient. At the radiation wavelength used in the experiment, the water absorption coefficient was found to be 0.003 mm^{-1} .

Temporal dependences of the intensity of radiation transmitted through a 400 mm layer of pure water and milk solution with concentration $n = 0.01$ are shown in Fig. 3 (curves 1 and 2, respectively). Curve 1 can be considered as the ballistic peak or instrument function of the measuring system. This curve was obtained using additional attenuating light filters.

Curve 2 represents the scattering peak. It is shifted relative to curve 1 and has considerably greater half_width.

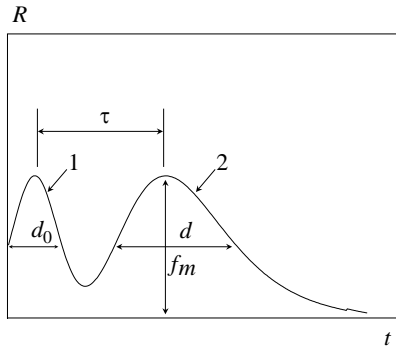


Fig. 1. Ideal temporal distribution of intensity of laser pulse passed through scattering medium: 1) ballistic photons; 2) scattered photons; d_0 is duration of initial pulse; τ is the shift of scattering maximum relative to ballistic peak; d is FWHM

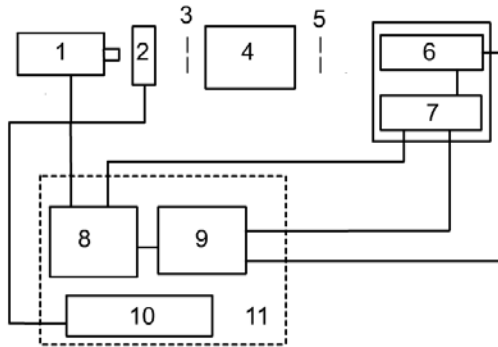


Fig. 2. Block diagram of experimental setup: 1) laser; 2) motorized step attenuator; 3) aperture $d_1=1$ mm; 4) scattering medium; 5) aperture $d_2=12$ mm; 6) photomultiplier; 7) preamplifier; 8) data board; 9) control board; 10) motorized step attenuator control board; 11) computer.

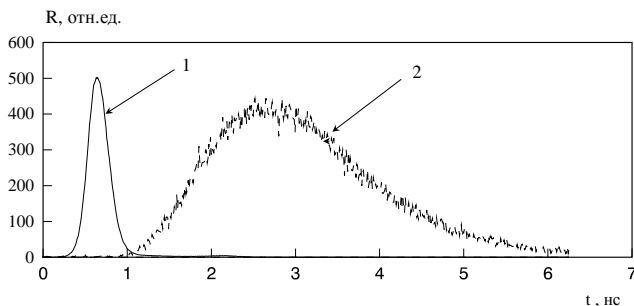


Fig. 3. Temporal dependences of the intensity of radiation transmitted through pure water (1) and milk solution at concentration $n=0.01$ (2)

The dependence of the intensity of transmitted radiation on milk concentration is shown in Fig. 4 (I_0 is the intensity of radiation transmitted through pure water). It should be noted that the curve in Fig. 4 can be divided into an exponential stage (within concentration range from 0 to $1.5 \cdot 10^{-3}$) and a stage of gradual intensity drop (at greater concentrations). This shows the different mechanisms of radiation transmission through the medium. In the exponential stage the detected photons are mainly non-scattered and obey the Bouguer-Lambert-Beer law (ballistic photons). Transmission of ballistic photons at higher concentrations of milk (i.e., when the number of ballistic photons is negligibly small compared to the number of scattered photons) was studied experimentally.

Experimental and theoretical dependences of shift and FWHM of scattering peak on milk concentration are shown in Fig. 5 (scattering layer thickness, 200 mm; absorption coefficient 0.003 mm^{-1}). It is assumed that the scattering coefficient in the axial model and the reduced scattering coefficient in the diffusion model are proportional to milk concentration. In the case of low concentrations, the semi-infinite medium models do not provide adequate description of radiation transmission through scattering medium.

Scattering and absorption coefficients for the axial and diffusion models calculated from experimental data were used to determine the factors of proportionality between milk concentration and the scattering coefficients for the two models (Fig. 6). Dependences shown in Fig. 6 were obtained for 200 mm scattering layer. It can be seen that the absorption coefficient is constant, while the scattering coefficient is directly proportional to milk concentration. At zero concentration (pure water) the scattering coefficient

curve should pass through point (0, 0), which indicates the absence of scattering in pure water.

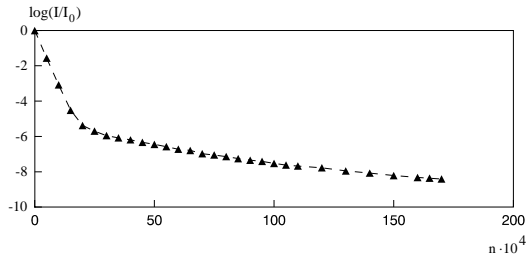


Fig. 4. Dependence of relative intensity of radiation transmitted through a 400 mm layer of milk solution on milk concentration n .

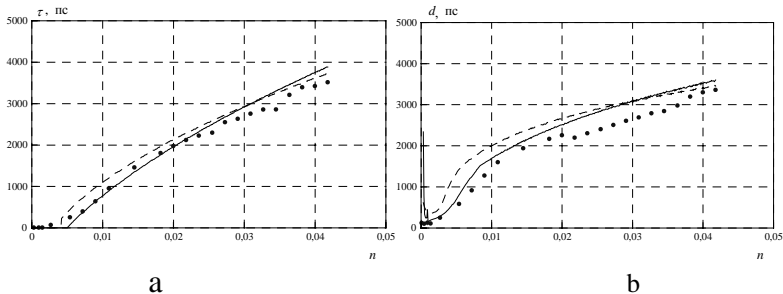


Fig. 5. Dependences of shift (a) and FWHM (b) of scattering peak on milk concentration: experimental dependence (dotted line), theoretical dependence based on axial model (dashed line), theoretical dependence based on diffusion model (solid line). Scattering layer thickness is equal to 200 mm; absorption coefficient is equal to 0.003 mm^{-1}

It should be noted that the scattering coefficient values obtained using the axial model are close to the reduced scattering coefficient for the axial model. Both models gave expectable results: linear dependence of the scattering coefficient on milk concentration was observed; scattering coefficient tends to zero at low milk concentration. It was shown that the theoretical dependences of temporal distribution parameters (FWHM, shift) on the scattering coefficient correspond qualitatively to the experimental curves. Dependences of optical characteristics of HSM on the concentration

of milk in water obtained for the two models are qualitatively similar. Thus, the axial and diffusion models provide adequate description of interaction of laser radiation with HSM.

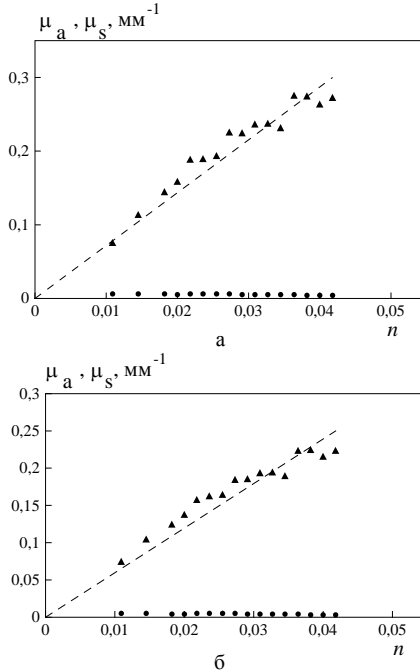


Fig. 6. Dependences of absorption and scattering coefficients (solid circles and triangles, respectively) in axial (a) and diffusion (b) models on milk concentration n (scattering layer thickness is equal to 200 mm)

REFERENCES

1. M. S. Patterson, B. Chance, and B. C. Wilson, *Appl. Optics.*, **28**, No. 12, 2331-2336 (1989).
2. S. A. Tereshchenko, *Methods of Computed Tomography* [in Russian], Moscow, Fizmatlit (2004).

The Investigation of Tomographical Characteristics of Coded Multi-pinhole Apertures Constructed on the Base of Extended Pseudorandom Sequences

G.A.Fedorov¹, S. A. Tereshchenko² and M.A.Antakov²

¹Moscow Engineering Physics Institute (MEPhI)

²Moscow Institute of Electronic Technology (MIET)

E-mail: tsa@miee.ru

The multiplexed measurements systems (MMS) are one of perspective developing directions in the single-photon emission computed tomography. MMS allow to carry out the visualization of spatial distributions of radiation sources without a rotation around of an object, that do not is always possible. With focusing properties of MMS there is possible to receive tomographical (layer-by-layer) focused images of a three-dimensional radiation source. The exception of the contribution of out-of-focus radiation sources with the use of iterative algorithms provides the complete reconstruction of three-dimensional distribution of radionuclides. MMS were covered by the cycle of papers [1-7].

The main part of the coding device of MMS is 2-D multipinhole coding collimator (coded aperture). The arrangement of pinholes is described by positions of units in the 2-D coding table (TDCT), consisting of zeros and units. Practically there are most interesting the TDCT constructed on the basis of the one-dimensional pseudorandom sequences (PRS) of zeros and units, which have the 2-level autocorrelation function [8]. Any PRS is the row in (v, k, λ) -circulant-matrix [9]. The special importance is that for (v, k, λ) -matrix the convenient analytical expression for the inverse matrix exists. Three ways of construction TDCT from one-dimensional PRS are known. These are line-by-line [10], diagonal [8] and selfsupporting [11] methods. First two methods construct the TDCT of dimension $m \times n$ on the base of one of PRS with the length $v = m \times n$. The third method constructs the TDCT of dimension $m \times n$ on the base of two PRS with lengths $v_1 = m$ and $v_2 = n$.

The main defect of the use of MMS is the small number of known PRS. This circumstance stimulates the search of new classes of TDCT. The new class of extended pseudorandom sequences (EPRS) and TDCT on their

base constructed with line-by-line, diagonal and selfsupporting methods [12] was recently offered. Thus the number of possible coding collimators on the base of EPRS with dimensions from 7 up to 99 grows from 379 up to 164679.

For the analysis of tomographical properties of MMS with coding multipinhole collimators of a different type the idealized point spread function (PSF) is offered, which represents the decoded (focused) image in the point (x, y, z) of point radiation source located in the point (x_0, y_0, z_0) [3]. PSF can serve by a criterion of tomographical properties of MMS. Whereas the arbitrary position of the point source tomographical properties of MMS can be characterized with the help of the top and bottom boundary PSF and also with the help of the average PSF. At the fixed distance from a detector plane up to a plane of reconstruction, for example, in the method of focal planes [6], the PSF actually will depend only on a difference $\Delta z = z - z_0$.

There were investigated 6474 tables, which have dimensions not exceeding of 45 and have the maximum difference of dimensions no more than 3. The value of the depth resolution of PSF exceeds the theoretical one more than in 1.5 times for 65% of the investigated coding collimators, and the amplitude of the false peak exceeds 1 for 78%. Among remained tables there were chosen that for which the deviation of the relative depth resolution of PSF from theoretical one does not exceed 20% and which have the amplitude of false peak less than 0,7. The number of such tables is found 215. There was established, that the majority (197 of 215) of coding collimators with good PSF is constructed with the line-by-line method. Others are constructed with the diagonal method. Collimators with good PSF constructed with self-supporting method are not found.

References

1. Fedorov G.A., Tereshchenko S.A.// Izmeritel'naya Tehnika, 1995, No.11, p.49. (In Russian).
2. Fedorov G.A., Tereshchenko S.A.// Izmeritel'naya Tehnika, 1996, No.9, p.50. (In Russian).
3. Fedorov G.A., Tereshchenko S.A.// Izmeritel'naya Tehnika, 1997, No.2, p.44. (In Russian).
4. Fedorov G.A., Tereshchenko S.A.// Izmeritel'naya Tehnika, 1998, No.12, p.50. (In Russian).

5. Fedorov G.A., Tereshchenko S.A.// Izmeritel'naya Tehnika, 1999, No.5, p.48. (In Russian).
6. Fedorov G.A., Tereshchenko S.A.// Izmeritel'naya Tehnika, 2001, No.4, p.57. (In Russian).
7. Fedorov G.A., Tereshchenko S.A.// Izmeritel'naya Tehnika, 2005, No.6, p.58. (In Russian).
8. MacWilliams F. J. and Sloane N. J. A.// TIHER (Proceedings of the IEEE), 1976, V.64, No.12, p.80. (In Russian).
9. Markus M., Mink H. Survey of Matrix Theory and Theory of Matrix Inequalities: Moscow, Nauka, 1972. (In Russian).
10. Spann R.// TIHER (Proceedings of the IEEE), 1965, V.53, No12, p.2363. (In Russian).
11. Gottesman S.R., Schneid E.J.// IEEE Trans. Nucl. Sci., 1986, V.NS-33, No.1, p.745.
12. Fedorov G.A., Tereshchenko S.A.// Izmeritel'naya Tehnika, 2007, No.6, p.66. (In Russian).

Section 2

Instrumentation for surgery, implants and artificial organs

IMPROVING THE QUALITY OF ROBOTIC HEART SURGERY: EVALUATION IN A NEW EXPERIMENTAL SYSTEM

*Robert Bauernschmitt¹, Christian Gaertner¹, Eva U. Braun¹,
Hermann Mayer², Alois Knoll²,
Ulrich Schreiber¹, Rüdiger Lange¹*

*¹German Heart Centre Munich, Clinic for Cardiovascular
Surgery, 80636 Munich, Germany*

*²Robotics and Embedded Systems, Technische Universität
München, 85748 Garching, Germany*

INTRODUCTION

Despite promising initial reports, robotic heart surgery has not been integrated into clinical routine. Various technical improvements of the system are considered to be necessary to achieve that goal.

Currently available robotic surgical systems do not provide haptic or tactile feedback. The lack of haptic (force or tactile) feedback causes damage of tissue and bending or breaking of suture material [MacFarlane1999], [Bholat1999]. In earlier studies we were able to demonstrate the superiority of force-feedback in an experimental setup using three

Kuka-robots [Braun2008]. To come closer to the clinical situation, we established an entirely new system with four Mitsubishi-robots (Fig. 1,2) and evaluated haptic feedback during surgical tasks on heart specimens.



Fig. 1: Experimental robotic platform with integrated haptic feedback: old system



Fig. 2: Experimental robotic platform with integrated haptic feedback (new system)

MATERIALS AND METHODS

Three of the robots were wearing surgical instruments as manufactured by Intuitive Surgical for the DaVinci – telemanipulator, one robot controlled a 3-D-endoscopic camera. Forces were fed back by Phantom-devices.

The human subjects of this study included 15 heart surgeons in different levels of surgical training and age, and 15 medical students. The following tasks on isolated pig hearts obtained from the local slaughterhouse were performed: direct suturing of a cut in the ventricle (Cut), direct ASD-closure (ASD) and artificial

chorda implantation on the mitral valve (AC), with the basic surgical tasks being sewing and knot-tying (see Fig. 2) in all applications. Forces during sewing and knot tying were continuously registered, the overall quality of surgical work and the operators' attitude was assessed by independent observers.

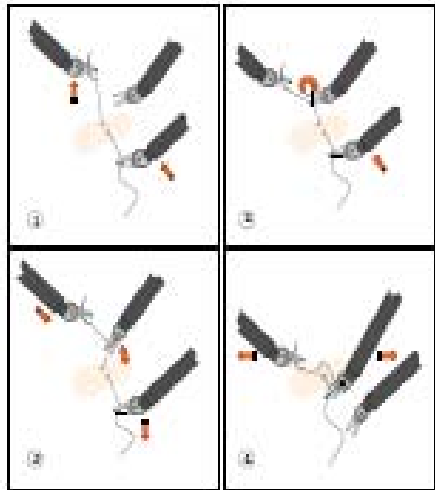


Fig. 3: Surgical knot-tying with endoscopic instruments

RESULTS

No marked differences were noted between students and cardiac surgeons, neither with nor without force-feedback. Force-feedback did not increase or

decrease the speed of actions significantly.

There were, however, marked differences in the forces applied during the procedures.

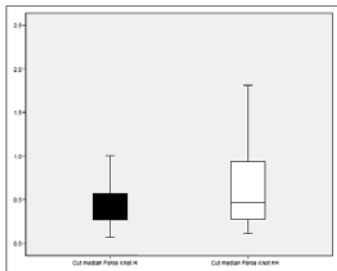


Fig. 4: Median forces during knot tying (“Cut”).
Black: With force-feedback,
white: without force-feedback,
 $p < 0.004$

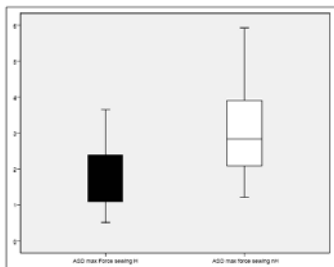


Fig. 5: Maximum forces during sewing (“ASD”)
Black: With force-feedback,
white: without force-feedback,
 $p < 0.0001$

Forces used both during sewing and knot-tying were significantly less in all three experiments (Fig.

3-5). This resulted in less tissue trauma as judged by independent observers: while there were 10 of 30 cases of damage to the specimens without haptics (33%), there were only 3/27 damages with haptics (11%), resulting in a significant difference ($p < 0.02$).

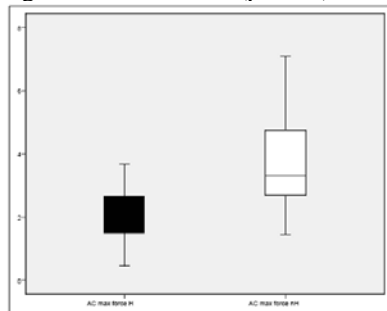


Fig. 6: Maximum forces during sewing (“AC”)
Black: With force-feedback,
white: without force-feedback,
 $p < 0.001$

DISCUSSION

Haptic feedback is currently limited to interact with rigid structures, such as tool-on-tool collisions, not soft tissues. This requires the surgeon to rely on visual feedback in tasks such as suturing. The basic consideration is to offer the heart surgeon an accessory sensory channel in addition to the visual channel not

only to avoid damage of surgical suture material and tissue, but also to decrease fatigue.

In earlier studies [Braun2008] we were able to demonstrate higher forces and increased fatigue without force-feedback, but no difference in tissue damage. This could have been in part due to the artificial nature of the system used, with Kuka-robots and synthetic tissue model.

In our present model, we performed a step closer to everyday's clinical routine. The Mitsubishi-robots could theoretically be used in a clinical setup, and real organs are more suitable for the analysis of tissue damage. This time we found increased tissue damage without haptic information, well fitting to the increased forces used. This study corroborates our hypothesis, that force-feedback improves the quality of endoscopic heart surgery.

ACKNOWLEDGEMENT

This work was supported by the German Research Foundation (DFG) within the Collaborative Research Centre SFB 453 on "High-Fidelity Telepresence and Teleaction".

REFERENCES

- [Bholat1999]
O.S. Bholat, R.S. Haluck, W.B. Murray, P.J. Gorman, T.M. Krummel, „Tactile feedback is present during minimally invasive surgery”, *J Am Coll Surgeons* Vol 189, p 349-355, 1999
- [Braun et al2008]
Eva U. Braun, Hermann Mayer, Alois Knoll, Ruediger Lange, Robert Bauernschmitt. The must-have in robotic heart surgery: haptic feedback. In: V. Bozovic (Editor): *Medical Robotics*. ISBN 978-3-902613-18-9, Vienna, Austria. I-Tech Education and Publishing 2008; 9-20.
- [Falk2003]
V. Falk, S. Jacobs, J. Gummert, T. Walther, F.W. Mohr, „Computer-enhanced endoscopic coronary artery bypass grafting: the da Vinci experience”, *Semin Thorac Cardiovasc Surg*. Vol 15(2), p 104-11, 2003
- [MacFarlane1999]
M. MacFarlane, J. Rosen, B. Hannaford, C. Pellegrini, M. Sinanan, „Force-feedback grasper helps restore sense of touch in minimally invasive surgery”, *J Gastrointest Surg*. Vol 3, p 278-285, 1999

Towards an Computer Assisted Intervention System for Endovascular Abdominal Aortic Repair

S. Demirci¹, O. Kutter¹, F. Manstad-Hulaas², N. Navab¹

*¹ Technische Universität München, CAMP,
email: {demirci,kutter,navab}@cs.tum.de*

*² Norwegian Technical University, St. Olavs Hospital,
email: {manstad-hulaas}@ntnu.no*

The implantation of an endovascular stent-graft, inside the aorta is a minimally-invasive procedure for the treatment of aortic aneurysms. In the current clinical workflow there is no technical guidance during the intervention except for X-Ray images. However, exact placement of the stent-graft is crucial for the success of the procedure. Thus, there is a need for methods and tools aiding in the implantation of the stent-graft. Our system aims at supporting the surgeons during the intervention by visualizing registered pre-operative CTA images and intra-operative X-Ray images. Thereby a roadmap for the catheter navigation can be displayed and the physician has access to all spatial 3D information necessary for the exact graft placement. By this method, we hope to enhance the accuracy of the surgeon's actions and reduce the amount of contrast agent.

1. Introduction

The implantation of an endovascular prosthesis, also referred to as stent-graft, inside the aorta is a minimally-invasive procedure for the treatment of aortic aneurysms. The stent graft remodels the structure of the aorta and excludes the aneurysm from the blood flow, removing the pressure from the inner aortic wall, to prevent further dilation or rupture of the aorta. In the current clinical workflow, the entire interventional catheter navigation is done under 2D angiography imaging where the physician is missing the important 3D information. As the catheter and stent position is only visualized in plane, more image acquisitions are needed during fine positioning of the stent graft

before unfolding. This means an increase in radiation dose and used contrast agent at the same time.

With the implementation of systems providing three dimensional angiography reconstructions during endovascular aortic repairs [3], the image information available for the interventionalist has been improved. However, such acquisitions produce an intense radiation exposure and are too time-consuming for constant application throughout the entire procedure. Normal size detectors of such systems generally cover a field of 30 x 40 cm; a region that doesn't include enough information for navigation tasks during abdominal aortic interventions. Thus, there is a need for enhancing the intraoperative visualization with three dimensional image information.

In [1], [4] and [7], the authors explored the possible prospects of a system that aids the implantation of stent-grafts by preoperatively segmenting the aorta in the CTA¹ data set and registering the pre-operative CTA data of the patient with the intraoperative X-Ray images. Thereby, the position of the stent graft can be visualized in the 3D CTA data set, likewise the contour of the segmented aorta can be displayed in the 2D X-Ray images without having to administer contrast agent to the patient. The registration task was performed via external fiducials placed on the patient's skin. In our present work, we focus on developing and implementing image-based solutions, which in combination with the initial C-arm position information currently available within interventional angiography suites, makes no use of fiducials.

2. Methods

2.1. Preoperative Segmentation

We segment the contrasted vessel tree out of the preoperative volume using a region growing approach. The result of the preoperative segmentation is used intraoperatively as a roadmap for catheter navigation and stent placement.

2.2. Intraoperative Registration

For the intraoperative visualization of the stent in the CTA data set and the display of the contour lines of the segmented aorta in the intraoperative

¹ Computer Tomography Angiography

images a 2D-3D registration of the CTA image and the X-Ray image is required.

For image-based 2D-3D registration of X-Ray and CT images several approaches exist in the literature (for a general overview see [6]). As all intrinsic parameters are stored within interventional angiography suites, we opted for an DRR²-based approach. We use GPU³-accelerated raycasting employing just one single render pass to compute the X-Ray attenuation along each ray. Then, an intensity-based 2D-2D registration is performed using normalized cross-correlation [8] as similarity measure and Powell-Brent's direction search method for optimization.

A problem for image-based registration for aortic interventions is the presence of contrast in the preoperative CTA dataset and the presence of surgical instruments in the intraoperative X-Ray images. To address this problem we implemented a method to remove the contrast inside the aorta during DRR generation. To address the second problem of medical instruments that are inside the detector's field of view at acquisition time, we developed an adapted similarity measure that doesn't consider pixels showing medical instruments.

Image-based 3D-3D registration methods have been studied extensively in the literature (for a general overview see [7]). Here, we opted for an approach using normalized gradient correlation within a Best-Neighbour (also hill climbing) optimization scheme. However, medical instruments that are displayed inside the interventional 3D images prove to be disadvantageous for existing registration algorithms, as the image dissimilarities are too severe for general similarity measures. To overcome these difficulties, we propose the following new registration scheme. First, the instruments are segmented in the interventional image by cropping the volume and applying a threshold filter. Each segmented voxel is then interpolated by three B-Splines [3] for each of the three directions. The mean of all interpolation results is then set as the voxel's intensity.

2.3. Intraoperative Visualization

During the intervention, the previously extracted abdominal vessel tree is projected onto the intraoperative images. Additionally, the position of the catheter or the stent graft is backprojected and visualized within the 3D CTA scan.

² Digitally Reconstructed Radiograph

³ Graphics Processing Unit

3. Experiments and Results

We evaluated our proposed system offline after an EVAR⁴ using the actual patient data acquired during the intervention. Patient data sets were provided by St. Olavs Hospital in Trondheim (Norway). CTA images were acquired by Siemens Somatom Sensation 64 and Siemens Somatom Definition, interventional 2D and 3D X-Ray images were taken by Siemens AXIOM Artis dTA angiography suite equipped with dynaCT software. All computations were performed on an Intel Core 2 PC containing 2.66 GHz CPU and 4096 MB of main memory. For the DRR computation we used GeForce 8800 GTX (NVIDIA Corp.) GPU with 768 MB dedicated GDDR3 memory. The evaluations of the proposed registration algorithms requires a selection of 2D and 3D datasets with varying presence of contrast agent and medical instruments. Each of them is then registered to the preoperative CTA volume by applying the appropriate registration algorithm.



Figure 1: Intraoperative visualization of 2D-3D registration; (left) intraoperative fluoroscopy image; (middle) generated DRR; (right) volume rendered segmentation of abdominal aorta.

Fig. 1 shows the intraoperative visualization of the computer assisted intervention system that was used for visual evaluation by experts of our partner medical center. In order to track the current position of the catheter, the physician clicks on a certain position within the catheter. The selected point is transferred to the registered DRR image and then, backprojected in the preoperative volume. All experts were very impressed and found such a

⁴ EndoVascular Aortic Repairs

system as highly advantageous for difficult catheter navigation and stent placement tasks.

4. Conclusion

In this paper we present the structure of a computer assisted intervention system for endovascular abdominal aortic repairs. It includes methods for aligning a preoperatively acquired 3D volume to interventional 2D and 3D angiography and fluoroscopy images. All methods were evaluated offline after an EVAR using the actual patient data acquired during the intervention. The results were visually inspected by experts from our partner medical center. It turned out that until the insertion of the stiff stent catheter, our system In future work, we aim at integrating our system into EVAR interventions and evaluating the methods online. We further plan to investigate non-rigid registration methods in order to take deformation of the aorta and its branching vessels into account.

References

- [1] Demirci S, Kutter O, Manstad-Hulaas F, Bauernschmitt R, Navab N. Advanced 2D-3D registration of Endovascular Aortic Interventions: Addressing Dissimilarity in Images. Proc. SPIE Medical Imaging 2008; 6918: pages 69182S-69182S-8.
- [2] Eide K, Odegard A, Myhre H, Haraldseth O. Initial Observations of Endovascular Aneurysm Repair Using Dyna-CT. J Endo Ther, 2007; 14: pages 65-68.
- [3] Eiho S, Imamura H, Sugimoto N. Preoperative and Intraoperative Image Processing for Assisting Endovascular Stent Grafting. Proc. IEEE ICKS, 2004; pages 81-88.
- [4] Goshtasby AA. 2D and 3D Image Registration; Wiley, 2005.
- [5] Hill D, Batchelor P, Holden M, Hawkes D. Medical Image Registration Phys. Med. Biol., 2001; 46 (3): pages 1-45.
- [6] Kutter O, Kettner S, Braun E., Navab N, Lange R, Bauernschmitt R. Towards an Integrated Planning and Navigation System for Aortic Stent Graft Placement. Proc. CARS 2007.
- [7] Penney G, Weese J, Little J, Desmedt P, Hill D, Hawkes D. A comparison of similarity measures for use in 2-d-3-d medical image registration, IEEE Trans. Med. Imag., 1998; 17(4): pages 586-595.

A new systems solution to make scarless surgery feasible

A. Schneider¹, A. Meining², D. Wilhelm^{1,3}, S. v. Delius², S. Can¹, A. Fiolka¹,
H. Schlicht⁴, E. Wintermantel⁴, H. Feussner^{1,3}

¹ *Research Group MITI, Technische Universität München*

² *2nd Medical Department, Technische Universität München*

³ *Department of surgery, Technische Universität München*

⁴ *Department for Medical Engineering, Technische Universität München*

A special instrument set and surgical technique was developed and evaluated to allow the placement of a new biocompatible antireflux prosthesis via natural orifice transluminal endoscopic surgery (NOTES). In an animal trial, in 10/12 cases the ring-like structure could successfully be placed around the gastroesophageal junction. This new technique could simplify the surgical therapy of gastroesophageal reflux disease (GERD) without the specific drawbacks of previous extra- and endoluminal procedures.

Introduction:

Fundoplication is the gold standard of surgical treatment for GERD (7). However, the trend is to develop less invasive therapies. In recent years, different endoluminal techniques were developed (2,4,8). Nevertheless, up to now, none of these promising techniques could show convincing, long-lasting results (5,6).

On the other hand, techniques like the “Angelchik scarf” (1) or the resorbable vicryl-scarf (3), which, similar to the surgical fundoplication, strengthen the gastroesophageal junction, showed significant improvements (3). However, these techniques showed severe disadvantages. The “Angelchik scarf” sometimes perforated and migrated, whereas the vicryl-scarf lost the antirefluxive effect after resorption.

Based on these previous results, we developed a biocompatible, porous ring-like structure to overcome migration and perforation. Additionally, a

new system solution including specific instruments and devices for application and navigation to implant the ring-like structure via natural orifice transluminal surgery (NOTES) was designed.

Material and Methods

A new porous ring like structure with an outer diameter of 34,0mm and an inner diameter of 25,0mm of thermoplastic polyurethane (TPU) was developed (Figure 1). The special design allows stretching for transportation through the abdomen; the porosity induces a cell ingrowth, thus a reliable fixation, without the risk of migration and perforation.

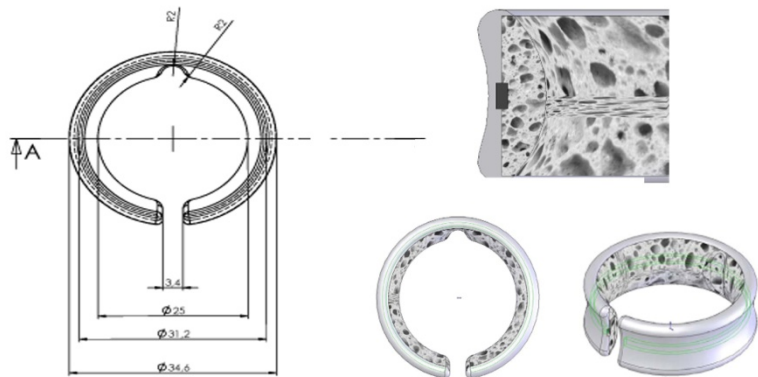


Figure 1: Dimensions, design and porosity of the new biocompatible antireflux prosthesis. On the closed side a small notch was left for the N. vagus.

The main access to the peritoneal cavity was established by a transgmoidal approach with a new trocar prototype especially designed for NOTES interventions. After instillation of 1l decontaminating fluid (Taurolin®, Böhringer Ingelheim, Ingelheim Germany) and 2,5l Ringer

solution in the abdominal cavity (Figure 2a), the pig is positioned in anti-trendelenburg position (head raised up 30°). The fluid leads to an internal excavation of the rectosigmoid (rectocele), which serves as the entry point later on. Then the rectosigmoid is entered using a modified device for transanal endoscopic microsurgery (TEM; Storz, Tuttlingen, Germany). A purse string suture is then placed around the future entry point to seal the bowel wall after the procedure (Figure 2b). Via the TEM tube, a specially designed, sterilized endoscopic guide is introduced. Using the sharp tip, the entry point is perforated, giving entry into the abdominal cavity (Figure 2c). The outer end of the guide tube is connected to an airtight valve unit, and a gas-sterilized flexible endoscope (Olympus CF 1401, Olympus GmbH, Hamburg, Germany) is inserted via the guide tube into the abdomen to perform the preparation of the cardia with the IT- (insulated tip) and TT- (triangle tip) knife (Olympus, Tokyo, Japan) .

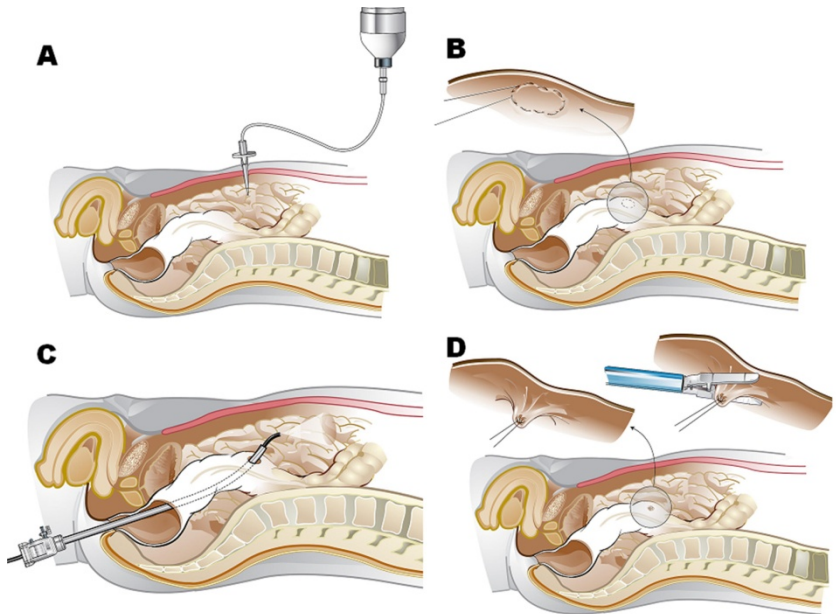


Figure 2: Access to the peritoneal cavity. A Instillation of decontaminating fluid. B Entry point with purse string suture. C Introduction of the sterilizable endoscopic guide. D Closure of the entry point.

A transcutaneously introduced hook was used to create a retroesophageal tunnel and to elevate the esophagogastric junction.

As soon as the cardia was prepared, the prosthesis delivering system was mounted to the endoscope using a muzzle-loading technique. After reentering the esophagocardiac region the ring was positioned in the vicinity of the tip of the hook. As soon as the ring was attached to the hook, it could be pulled back, whereby the prosthesis was placed (Figure 3).



Figure 3: Anti-reflux prosthesis placed around the esophagocardiac area

During the whole intervention, a purpose-built endoscopic magnetic tracking system was used to show the configuration of the endoscope.

Results:

Twelve pigs underwent the new procedure. In ten cases the ring could be successfully placed around the gastroesophageal junction. One animal had to be sacrificed because of a major bleeding.

Reaching of the cardia after introducing the endoscope was possible in less than 10 minutes in all cases. Preparation of the gastroesophageal junction

and introducing the hook lasts $36,4 \pm 17,7$ minutes. Final placing of the ring around the esophagus took $16,9 \pm 8,9$ minutes.

The correctness of the position of the ring was proved after euthanasia and found to be correct in all ten cases.

The use of the endoscope tracking system was found helpful from all team members; however the more experienced endoscopists, the lower the use of the configuration view.

Conclusion

Providing adequate systems solutions make scarless procedures feasible, which were not feasible up to now using conventional instruments.

The porous ring-like structure for antireflux therapy is a promising method, which directly supports the sphincter function. In combination with NOTES, the benefit for the patient could be greater than the short lasting endoluminal techniques.

References

1. Angelchik JP, Cohen R. A new surgical procedure for the treatment of gastroesophageal reflux and hiatal hernia. *Surg Gynecol Obstet* 148: 246-8, 1979.
2. Caca K. [GERD: endoscopic antireflux therapies]. *Schweiz Rundsch Med Prax* 95: 1185-7, 2006.
3. Feussner H, Bonavina L, Collard JM, Holste J, Freys S, Horvath OP, Rudiger T, Stein HJ, Fuchs KH. Experimental evaluation of the safety and biocompatibility of a new antireflux prosthesis. *Dis Esophagus* 13: 234-9, 2000.
4. Filipi CJ, Lehman GA, Rothstein RI, Rajjman I, Stiegmann GV, Waring JP, Hunter JG, Gostout CJ, Edmundowicz SA, Dunne DP. Transoral, flexible endoscopic suturing for treatment of GERD: A multicenter trial. *Gastrointestinal Endoscopy* 53: 416-22, 2001.

5. Schwartz MP, Smout AJ. Review article: The endoscopic treatment of gastro-oesophageal reflux disease. *Aliment Pharmacol Ther* 26 Suppl 2:1-6.: 1-6, 2007.
6. Torquati A, Richards WO. Endoluminal GERD treatments: critical appraisal of current literature with evidence-based medicine instruments. *Surg Endosc* 21: 697-706, 2007.
7. Vidal O, Lacy AM, Pera M, Valentini M, Bollo J, Lacima G, Grande L. Long-term Control of Gastroesophageal Reflux Disease Symptoms After Laparoscopic Nissen-Rosetti Fundoplication. *Journal of Gastrointestinal Surgery* 10: 863-9, 2006.
8. Yeh RW, Triadafilopoulos G. Endoscopic antireflux therapy: the Stretta procedure. *Thorac Surg Clin* 15: 395-403, 2005.

First cholecystectomy with the new, highly versatile single port system for minimally invasive surgery

Salman Can¹, Hermann Mayer³, Alois Knoll³, Adam Fiolka¹, Armin Schneider¹, Johannes Maifeld¹, Dirk Wilhelm^{1,2}, Hubertus Feussner^{1,2}

¹Workgroup MITI, Klinikum r. d. Isar,

Technische Universität München (TUM), Germany

²Department of Surgery, Klinikum r. d. Isar, TUM, Germany

³Chair of Robotics and Embedded Systems, TUM, Germany

In laparoscopic surgery, the demand for a versatile and highly flexible support system is inevitable. The systems proposed so far do not meet these requirements. We developed the “Highly Versatile Single Port System” (HVSPS), a two armed device with an additional semi-flexible telescope, to overcome these drawbacks. The flexible manipulators are inserted independently through an insert with three lumens and this ensemble is guided over a four degree of freedom (DOF) telemanipulator. In a survival animal experiment, the first gallbladder could be successfully resected with the HVSPS. After the ligation of the cystic duct and artery with coagulation current, in an opposite configuration, the gallbladder could be hold with a grasper and dissected using a TT knife. The complete surgical intervention, without technical set-up, could be accomplished in 110 minutes. Laparoscopic cholecystectomy using the HVSPS is feasible. It is expected that the integration of an adequate man-machine interface (MMI) and a simulation environment can significantly ameliorate the procedure.

1. Introduction

In minimally invasive surgery (MIS), trauma to the patient can be reduced by diminishing the number of entry ports (“single port surgery”). Accordingly, the need for a multifunctional single port operation system is growing. [4] Furthermore, “high flexibility” is an inevitable issue investigated by different research groups. [1, 3, 5] The intra-abdominal flexibility limited due to the entry port is augmented with additional articulations.

Another stimulus for single port surgery was the introduction of “Natural Orifice Transluminal Endoscopic Surgery” (NOTES). This type of surgery depends even more upon a suitable single lumen universal tool. The first approach devoted to this problem is the endoscope-based Octopus system as developed by Swanstrom et al. [4] However, this system has a small working range, limited flexibility and the opposite or retroflective working is not possible. Thus a new support system is required to increased penetration of minimally invasive surgery and NOTES.

We developed the “Highly Versatile Single Port System” to overcome these drawbacks. The idea is, literally spoken, to bring surgeon’s head, shoulders and arms into the abdominal cavity to regain the same flexibility as in open surgery. Compared to other systems, only one 4 DOF telemanipulator is required to guide the HVSP system. The surgeon controls the manipulators in an intuitive manner through a master console. Our aim was to prove the maturity for an in vivo surgical operation.

2. Material and Methods

Using the know-how and partially the hardware of flexible endoscopes we designed a two armed device with two manipulators and a semi-flexible telescope. Figure 1 shows the kinematic structure of the complete HVSPS. The flexible manipulators and the telescope are inserted independently through an insert with three lumens. This combination is implemented gas-tightly in a 33 mm trocar and guided over a 4 DOF telemanipulator. An additional restraint system is used to retract the liver out of operating field. Compared to the existing systems the footprint of the HVSPS and the occupied space around the patient is by far smaller.

The hollow manipulators with five DOF have an outer diameter of 12 mm. Flexible instruments are introduced through the central channels which are controlled and changed manually. The bendable section of the manipulator with two DOF, resembling to the human wrist, has a length of 75 mm followed by a 50 mm length hollow tube and an elbow articulation with one DOF. A rotation of 360 degrees and 50 mm linear movement into the abdominal cavity is possible with additional 2 DOF. The conceived semi-flexible telescope with 10 mm diameter consists of a commercial endoscope with 6 mm diameter which is inserted trough a 10 mm tube with an additional articulation. With this ensemble, providing 4 DOF, the telescope can be moved in an S-form so that the instruments can be observed over the complete working range.

Both manipulators are partially automated and controlled over a real-time Matlab-Simulink application. Accordingly, the complete system had to be operated by a team composed of physician and engineers. One surgeon controls the manipulators over two Joysticks, a second one controls manually the flexible instruments guided through the manipulators, a gastroenterologist guides manually the semi-flexible telescope and an engineer operates the manipulators remaining, not automated degrees of freedom.

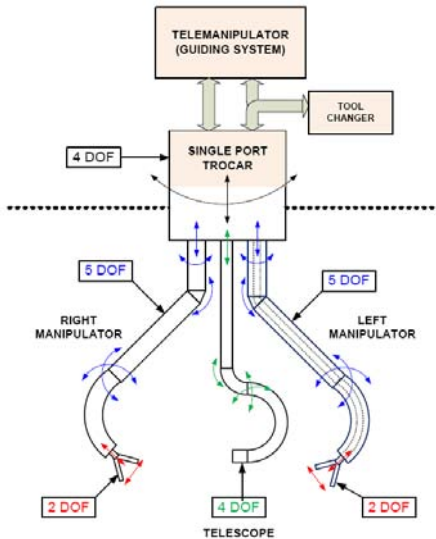


Figure 1: Schematically drawing of the "Highly Versatile Single Port System"

The HVSPS could be integrated into the ARAMIS platform, which comprises a telemanipulator to guide minimally invasive instruments. [2] This platform uses two Sensable PHANToms as input devices and can be ideally used to steer the HVSPS manipulators by Cartesian control (i.e. intuitive control of x, y, z translations and rotations). An integrated simulation and planning interface is provided for virtual training and case studies of such new interventions.

In a first step, the complete system was tested on a human "mock-up" allowing the physicians to practice and get familiar with the control and kinematic of the HVSPS. After this training period the first laparoscopic in-vivo cholecystectomy could be performed in an animal experiment.

3. Results

We could successfully resect the first gallbladder with the HVSPS in a survival swine experiment. The complete surgical intervention, without technical set-up, could be accomplished in 110 minutes. Through one incision the HVSPS was introduced into the abdominal cavity. The manipulators were in a straight position during the introduction and expand afterwards in the peritoneum. A second incision was required to introduce a retractor for retain the liver out of the operating field. Two flexible, endoscopic instruments (grasper, scissors, etc.) were introduced afterwards through the manipulators. Within seconds, the instruments could be exchanged for different tasks.



Figure 2: First cholecystectomy with the HVSPS in an animal experiment

After the ligation of the cystic duct and cystic artery with coagulation current, dissection of the gallbladder was achieved by grasping and cutting instruments. Figure 2 shows how the gallbladder is hold with a grasper through the left manipulator and dissected by using a TT knife introduced through the right. The opposition of the manipulators was essential for an intuitive working. The gallbladder was recovered through the main incision after a last check up for bleeding. Finally, the manipulators were steered to a straight position so that the HVSPS could be pulled out of the abdomen.

The complete surgical intervention was managed by commands of the surgeon who controlled the manipulators. Coordination of the physicians and engineers was essential for the performance and quality of the intervention. We have realized the indispensability of previous interdisciplinary training for an effective teamwork. We suppose that the planning and coordination can be improved by integration of an adequate simulation environment.

4. Conclusion

This study demonstrated the applicability of the HVSPS for laparoscopic surgeries such as the cholecystectomy. The complete operation time can be reduced by optimizing the fully automated HVSPS and introducing an intuitive man-machine interface and a simulation and planning environment.

The kinematic structure of the HVSPS will also be evaluated with slight changes for natural orifice transgastric endoscopic surgery. It is also possible to use the HVSPS for retroflexive interventions which were not possible yet. However, a new control design should be developed, since it was impossible to work in a head over position.

References

- [1] Ikuta,K., Sasaki,K., Yamamoto,K., Shimada,T. Remote Microsurgery System for Deep and Narrow Space-Development of New Surgical Procedure and Micro-robotic Tool, Proc. of 5th International Conference on Medical Image Computing and Computer-Assisted Intervention(2002) 163-172.
- [2] Mayer,H., Nagy,I., Knoll,A., Braun,E.U., Bauernschmitt,R. Human Computer Interfaces of a System for Robotic Heart Surgery. Proceedings of the Second IASTED International Conference on Human-Computer Interaction , 31-36. 2007. Chamonix, France.
- [3] Nakamura,R., Kobayashi,E., Masamune,K., Sakuma,I., Dohi,T., Yahagi,N., Tsuji,T., Hashimoto,D., Shimada,M., Hashizume,M. Multi-DOF Forceps Manipulator System for Laparoscopic Surgery, Proc. Third International Conf. on Medical Image Computing and Computer assisted Interventions, Pittsburgh, PA, USA, October(2000) 11-14.
- [4] Raman,J.D., Bensalah,K., Bagrodia,A., Stern,J.M., Cadeddu,J.A. Laboratory and Clinical Development of Single Keyhole Umbilical Nephrectomy, Urology(2007).
- [5] Song,H., Chung,J., Kim,K., Lee,J. The Development of human-arm like manipulator for Laparoscopic Surgery with Force sensing, Industrial Technology, 2006. ICIT 2006. IEEE International Conference on(2006) 1258-1262.
- [6] Swanstrom,L.L., Kozarek,R., Pasricha,P.J., Gross,S., Birkett,D., Park,P.O., Saadat,V., Ewers,R., Swain,P. Development of a new access device for transgastric surgery, Journal of Gastrointestinal Surgery 9 (2005) 1129-1137.

Evaluation of CT guided upper GI endoscopy using an electromagnetic navigation system

D. Wilhelm²#, M. Doundoulakis#, M. Burian², H. Friess², H. Feussner²#

² Chirurgische Abteilung, Klinikum r.d.Isar, Technische Universität München

Arbeitsgruppe Minimalinvasive Therapie und Intervention (MITI), Klinikum r.d.Isar, München

1.0 Introduction:

Endoscopy is seen as crucial in medical diagnostics for gastrointestinal malignancies. Unfortunately, it only enables evaluation of endoluminal processes, but fails in assigning a lesion to topographic-anatomical landmarks. Even the additional use of endoscopic ultrasound provides only limited information concerning surrounding structures. However, multimodal treatment regimes specifically require referencing of particular medical imaging and comprehensive diagnostic tools.

Therefore we developed an electromagnetically guided endoscopy system, which allows real time CT navigation.

1.1 Material and Methods:

AURORA, a commercially available tracking system was applied for navigation [Aurora (Northern Digital, Waterloo, Ontario)]. The system consists of a miniaturized sensor which is detected inside an electromagnetic field of 60cm in diameter. The pulsed electromagnetic field itself is established by a transmitter to be freely positioned beside the patient. Both components are cable-connected to the system control unit, which on the other hand is connected to a working station. Finally a multiplanar rendered CT scan is navigated by the help of gained navigation data. Due to the small size of the probe, less than 2mm, the system could be integrated inside the working channel of any endoscope used at our department.

Accuracy of the system was evaluated in vitro using a specially constructed box model. The model consists of a 530mm square plate perforated at various accurately defined points. Hereby the correctness of navigation results and the influence of ambient factors could be investigated. Furthermore the ELITE (endoscopic-laparoscopic intervention training module) model mainly contributed for in-vitro evaluation of the system, as it allows for repeated fluoroscopic examinations during endoscopy to exactly assess the position of the endoscopes tip in correlation to radiopaque markers and topographic landmarks.

In 25 patients suffering from esophageal and gastric cancer in vivo examination was performed. Under well defined preconditions the cancerous lesion itself and anatomical landmarks, such as the cardia or esophageal sphincter were endoscopically localized and the correctness of navigation evaluated in direct comparison to the correlating CT slide.

Additionally the accuracy of several referencing modalities was subject of the study.

1.2 Results:

The system worked stable and without technical malfunctions during all evaluation steps. System setup took 5 minutes for registration of the ambient position of the model or patient, but could be decreased during the course of our investigations. Due to unavoidable movements of the patient, a custom-built mounting device had to be constructed to fix the electromagnetic emitter safely to the patients back.

5 measurement circles were performed, each with complete sampling of the perforated plate, resulting in 605 reading points. Accuracy of the system averaged 1,3 mm (0-5mm) in the coronary, 0,5mm (0-2,2mm) in the axial and 0,64 mm (0-5mm) in the sagittal layer. Highest accuracy was achieved at the centre and top part of the perforated plate almost reaching an aberration of 0mm and was relevantly higher at the bottom and close to the metallic examination couch, as well as at both sides of the plate.

Further in-vitro investigations were based on the ELITE model after 5 point registration using surface radiopaque markers. Again 5 cycles were performed. In this considerably larger model, accuracy proved to be marginally lower with an aberration of 4,1mm (2,8-6,4) in the coronary, 2,6mm (1,2-5,7) in the axial and 3,9mm (1,6-8,3) in the sagittal layer, respectively. Nevertheless, the sensor was correctly graphical represented on the computer screen, located within the gastrointestinal lumen during all sequences.



Picture 1: In-vitro evaluation of navigated endoscopy with the ELITE phantom. After adjusting the anatomical cardia with the endoscope, which is done only by virtual-orientation on the navigated CT, fluoroscopy was used to detect the resulting aberration.

24 of 25 investigations could successfully be completed in the in-vivo group. In one patient the fixation device for the electromagnetic emitter turned out to be too small and could not be attached. For the residual 24 patients, a 5 point registration was applied in 16 patients and a 4 point registration in 8 patients. The costal arch, the spinal process or the jugular fossa, therefore, served as superficial anatomical landmarks and could be easily identified in all patients. With this experimental setup, the test results were as follows: 5,0mm (1,9-8,8) in the coronary layer, 5,3mm (1,3-10,5) in the axial layer and 5,0mm (0,9-9,0) in the sagittal layer. Accuracy measurements resulted from distance recordings between the anatomical cardia angled with the endoscope and its position on the registered CT scan.



Picture 2: With the electromagnetic emitter fixed to the patients back, navigated endoscopy enables real-time visualization and control of existing CT scans, resulting in an augmented endoscopic examination.

2.0 Conclusion

Medical decision making is mainly based on examination results, and as surgery is concerned on medical imaging. Each problem has its most suitable imaging modality, or from another point of view, no currently available imaging modality serves for all needs. In numerous cases doctors even have to consult several completely different techniques; consequently a recombination and summary of all gained image information is necessary to choose the optimal pathway of treatment. Referencing of data records allows to establish a topographic relation and furthermore the generation of completely new, merged imaging modalities. Currently, most important imaging modalities in surgery are computed tomography and even more endoluminal endoscopy. We attempted to combine both techniques via electromagnetic referencing and navigation.

The results of the performed in-vitro and in-vivo evaluation demonstrate on one hand, that this new modality is feasible and can be applied in daily routine for real time CT navigation during endoscopy. The system was easy to set up and worked without major complications or any malfunction. Additionally, accuracy proved to be at a sufficient level, even in this early development phase. The

surrounding anatomical structures. If therapeutic interventions are concerned, like CT guided endoscopic fine needle puncture, further improvements are necessary to increase the accuracy and reliability of the data.

On the other hand, we recognized several parameters having a negative influence on the navigation results. First of all, and well known, is the influence of ferromagnetic elements to disturb the electromagnetic field, which would explain the reduced accuracy of our measurements close to the bottom of the experimental setup and close to the examination bed. Secondly, different positioning of the patient during acquisition of the CT data and during endoscopy causes problems. While CT scans are mainly performed in supine position of the patient, endoscopy has to be performed in a left lateral position with elevation of the upper part of the body to avoid aspiration. This dislocation of the patient body causes shifting of internal organs and hereby reduces accuracy. Lastly we recognized variations of anatomical conditions due to breathing movements and due to the extend of insufflation of gastrointestinal organs by the scope. All these aspects demand compensation mechanisms to be implemented into the complete systems and therefore require further investigations to be undertaken.

An Electromagnetic Camera Control System for Minimally Invasive Surgery

A. Fiolka¹, M. Polski², S. Can¹, A. Schneider¹, H. Feußner³

¹ *Research Group MITI, Klinikum r.d. Isar, TU-München
{adam.fiolka, salman.can, armin.schneider@mitigroup.de}*

² *The Institute of Radioelectronics, Warsaw University of Technology,
marcinpolski@gmail.com*

³ *Department of Surgery, Klinikum r. d. Isar, TU-München,
feussner@chir.med.tu-muenchen.de*

In laparoscopic surgery, the surgeon needs permanently an assistant, who guides the camera and makes the field of surgery visible. This task is very stressful and needs full concentration especially during long interventions. This article describes a new semi-autonomous camera control system based on an electromagnetic tracking unit. Two sensors are fixed to the handhold of the instruments and to the camera. The tracking system captures the position of the sensors continuously and almost in real time. This information is used to calculate in real time the positions of the tips of both objects and focuses continuously the telescope. The newly developed system works stable. Various experiments have shown that the size of the generated electromagnetic field and the accuracy of the tracking system are sufficient for this application.

1. Introduction

In minimally access surgery (MAS) an assistant guides the camera and makes the field of surgery visible. This task is stressful and needs full concentration especially during long interventions. Different systems were presented, offering positioning assistance and control of the laparoscope. These support systems are controlled with a joystick or voice control [1]. In clinical practice, however, these controls failed to acquire a relevant role because of various drawbacks.

To improve the handling, research groups automated some of these camera control systems. Different vision-based control methods [2-5] are used to obtain the 3D position information. In all these cases the position and orientation of the camera is semi autonomously corrected by the position of the instrument in the dominating hand of the surgeon. However, the availability of these optical-based systems is not always guaranteed, for example, the markers are covered by adjacent organs or stained by blood and cannot be recognize any longer.

We built a new clinically suitable semi-autonomous camera control system based on an electromagnetic tracking system. This system should avoid the disadvantages of the former systems.

2. Material and Methods

For measurement of orientation and position, the DC magnetic tracker miniBIRD (Ascension, Burlington, VT, USA) was used. Camera control was provided by the new manipulator device SOLOASSIST (AKTORmed, Barbing, Germany) (Fig.1). This mechatronic device is driven by fluid actuators and has no electric drives or sensors in the arm. The intraoperative situs was simulated with a wooden rack with the field generator positioned at the distance of about 200mm (Fig. 2).

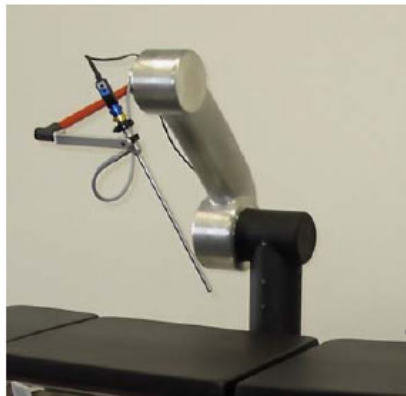


Figure 1 - SOLOASSIST is a mechatronic system providing camera guidance during minimally invasive surgical intervention. This system allows a 360° circle range in conjunction with an 80° inclination of the endoscope.

Measurements errors were analyzed in several test setups. First, one sensor was fixed to the handhold of the instrument and defined points were aimed with the tip of the instrument. Afterwards, the position and orientation was captured and the position of the tip was calculated. Second, the experiments were repeated with two sensors per object. With the results of these experiments the camera control was put into practice.

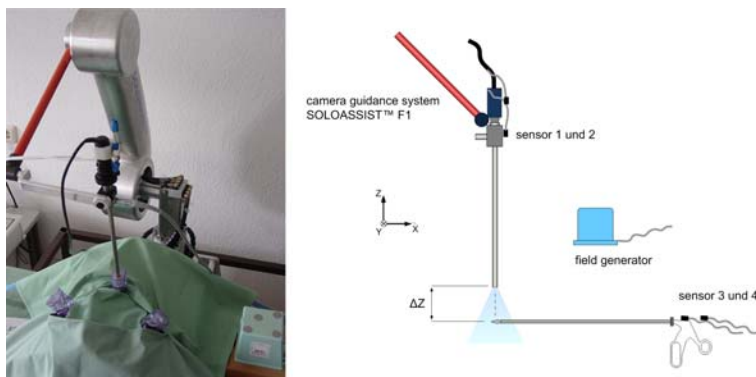


Figure 2 – The test setup for the laparoscopic camera control based on electromagnetic tracking

All functions were implemented directly into the IConnect software (Micro-Epsilon, Ortenburg, Germany) of the SOLOASSIST control unit, running on a standard industrial-PC.

Finally, the new semi-autonomous camera control was tested in an experimental study. The test person had to thread a needle in 2mm eyes mounted on a plate.

3. Results

The autonomous camera control system could be successfully realized. The newly developed system achieves the position and orientation of the tip of the instrument and uses this information to focus continuously the telescope. The size of the generated magnetic field was sufficient for this application.

In the experiments with only one sensor we recognize that the inaccuracy of the orientation falsifies strongly the calculated results. They deviated up to 60 mm on the tip, because of the transformation. The accuracy was increased significantly by using two sensors per object. Capturing only the position of both sensors, the position of the tip could be calculated with an accuracy of +/- 10mm. This precision was found sufficient for camera control in minor access surgery.

The camera speed was made proportional to the distance between the instrument and the camera tip. The user had to define manually the distance between instrument and the camera tip.

The final experimental studies show, that the every test person could finish the exercise twice as fast with the semi autonomous system compared to the manual control. Each person confirmed that the task could be completed more simply with the automated system. One person found the sensor cables disturbing.

4. Conclusion

The experiments confirmed that an electromagnetic tracking system is a potential alternative to other positioning techniques concerning precision, handling and reliability. With this technology it is possible to control mechatronic camera control precisely according to clinical requirements. The sensors are small enough for unproblematic integration into the instrument; however the used instruments should be amagnetically.

References

- [1] Hashizume, M. & Tsugawa, K. Robotic Surgery and Cancer: the Present State, Problems and Future Vision Japanese Journal of Clinical Oncology, 2004, 34, 227-237
- [2] Omote, K.; Feussner, H.; Ungeheuer, A.; Arbter, K.; Wei, G.; Siewert, J. & Hirzinger, G. Self-guided robotic camera control for laparoscopic surgery compared with human camera control. Am J Surg, 1999, 177, 321-4
- [3] Zhang, X. & Payandeh, S. Application of visual tracking for robot-assisted laparoscopic surgery Journal of Robotic Systems, 2002, 19, 315-328

- [4] Krupa, A.; Gangloff, J.; Doignon, C.; de Mathelin, M.; Morel, G.; Leroy, J.; Soler, L. & Marescaux, J. Autonomous 3-D positioning of surgical instruments in robotized laparoscopic surgery using visual servoing *Robotics and Automation, IEEE Transactions on*, 2003, 19, 842-853
- [5] Uecker, D.; Lee, C.; Wang, Y. & Wang, Y. Automated instrument tracking in robotically assisted laparoscopic surgery *Journal of Image Guided Surgery*, 1995, 1, 308-325

Corpora aliena: Can radio- frequency- identification (RFID) solve the problem?

M. Kranzfelder^{1,2}, A. Schneider², H. Friess¹, H. Feussner^{1,2}

¹ *Klinikum rechts der Isar, Technische Universität München, Department of Surgery, e-mail: kranzfelder@chir.med.tu-muenchen.de*

² *Technische Universität München, Researchgroup MITI*

Abstract: The incidence of retained objects (corpora aliena) is still a relevant problem for all operative disciplines. Routinely used control systems (manual counting, x- ray) are very time consuming and often not reliable. We set up an experimental pilot study using RFID technology for monitoring all textile objects used during an operation. For continuous object detection three RFID antennas (OBID i-scan, Feig Electronic GmbH, Weilburg-Waldhausen, Germany; frequency 500 msec.) were positioned strategically (instrument table, phantom- model, dust bin), 20 sponges were equipped with passive RFID transponder chips (MOBY-D, Siemens, München, Germany) and open splenectomy (n = 5) with at least 30 object changes was performed. At the end of the operation, no sponge, one sponge and two sponges were retained in the abdominal cavity by purpose. The actual textile position was automatically registrated throughout the operation. The total amount of objects (n = 20) as well as their position after each object change (n = 30) was correctly registrated by the system throughout the operation (detection rate 100%). Retained objects were detected in all cases. By using the RFID system, a continuous registration of all a during an operation deployed sponges was possible (detection rate 100 %) and retained objects were detected correctly in all cases.

Introduction: The incidence of retained objects (corpora aliena) is still a relevant problem for all operative disciplines. Although the incidence has not yet been determined precisely, estimates suggest that such errors occur in 1 of every 1000 to 1500 intraabdominal operations [1,2]. In Germany, approximately 1000 cases are estimated each year. Routinely used control systems (manual counting, x- ray) are very time consuming and often not reliable [3].

Aim: A promising approach for the prevention of retained objects during an operation is the continuous registration of all deployed textiles and sponges by radio frequency identification (RFID) systems [4]. As the technology is suitable for a simultaneously tracking of different objects in real- time, we set up a pilot study for analysis and evaluation of radio-frequency identification devices monitoring all textile objects used during an surgical procedure.

Methods: The study was set up under experimental conditions using a phantom- model representing the abdominal cavity (ELITE, CLA, Coburg, Germany). For a continuous object detection, three RFID antennas (OBID i-scan, Feig Electronic GmbH, Weilburg- Waldhausen, Germany) were positioned strategically on the instrument table, under the phantom- model (both 37 x 23 cm flat antenna, ID ISC.ANT340/240) and in the dust bin (37 x 32 cm ring antenna, ISC ANT300/300-A) and connected via standard reader (ID ISC.MR200) with a laptop (Fujitsu Siemens, Germany) The scanning frequency was set to 500 msec., the antenna range averaged 30 - 40 cm. The registration was carried out with a specially developed RFID software (ID ISOStart V7.02) displaying the actual location of the textiles on a wall mounted monitor numerically and graphically (Fig. 1). 20 sponges were equipped with passive RFID transponder chips (MOBY-D, Siemens, München, Germany) and open splenectomy with installation of artificial blood into the surgical site (“bleeding”) was performed (n = 5). At the beginning of the operation, 15 sponges were placed onto the instrument table and registrated automatically by the RFID system. 5 sponges were added later on during the operation and registrated in the same way. At least 30 object changes were simulated, the sponges were therefore repeatedly placed into the abdominal situs, handed back to the instrument table and discarded into the dust bin. The distance between the antenna and transponder was less than 30 cm. At the end of the operation, no sponge, one sponge and two sponges were retained in the abdominal cavity by purpose. The actual textile

position (instrument table, abdominal situs, dust bin) was automatically registered throughout the operation and displayed on the wall mounted monitor. During the simulated procedure, a surrounding motion activity similar to a real operation was maintained.

In a second trial, the RFID system was tested with an antenna – transponder distance of more than 30 cm (Fig. 3) with a 5 cm gradation (30-35 cm, 35-40 cm, > 40 cm). In addition, the RFID systems was evaluated in an animal experiment (n = 2 pigs) to analyze the effect of high frequency cutting and coagulation current.

Results: In all 5 simulations, the amount and position of textiles was properly registered at the beginning (n = 15) and the end of the procedure (n = 20). All later on additionally added sponges (n = 5) were detected correctly. The total amount of sponges (n = 20) as well as their position after each object change (n ≥ 30) was correctly registered by the system throughout the simulated operation (detection rate 100%). Objects, which had been left within the abdominal cavity by purpose (no sponge, one sponge, two sponges) were detected reliably in all cases at the end of the operation (detection rate 100%, Fig. 2).

However, temporary registration inaccuracy of the total amount of sponges in each position occurred during fast performed object changes or increased motion activity of the operating team (e.g. side changing).

Whereas the moistening of the sponges showed no negative effect on the registration (detection rate 100%), the appliance of HF coagulation current led to a reduced detection rate of $95 \pm 5\%$.

Due to the limited range of the deployed antennas, the registration accuracy declined with an increased distance to the transponder (Fig. 3). The detection rate for sponges, positioned on the ventral abdominal wall of the phantom with an antenna – transponder range of 30 – 35 cm, was approximately 90%. A distance between antenna and transponder of more than 35 cm led to a rapid decline of the detection rate (35-40 cm: 5%, > 40 cm: no registration).

Conclusion: By using the RFID system, a continuous registration of all deployed sponges was possible within an antenna – transponder range of less than 30 cm (detection rate 100 %). Retained objects in the abdominal situs were detected correctly in all cases. Due to the high frequency transponder sampling rate, the actual amount of textiles in each localization could be

monitored in real time; therefore temporary inaccuracy of the textile quantity on the three detection spots are of subordinate importance.

The surrounding motion activity plays a decisive role for the correct detection of the RFID transponder chips, as well as the exact positioning of the antennas. Particularly on the instrument table with numerous metallic instruments disrupting the RF- field, a properly adjusted antenna position is indispensable for a reliable registration. A distance between antenna and transponder of more than 35 cm led to a rapid decline of the detection rate (35-40 cm: 5%, > 40 cm: no registration).

Beyond of an exact positioning of the antennas, an adequate shielding against the metallic surrounding (e.g. polystyrene panel on the instrument table) is essential for a reliable registration. The metallic instruments deployed during the operation in the abdominal situs are no source of interference.

With the introduced RFID system, the problem of a corpora aliena could, in principal, be eliminated effectively. However, the basic conditions have to be set up correctly. Besides the prevention of retained objects, the automatic textile documentation could reduce the strain of the operation team and enhance quality and safety [5].

References

1. Bani-Hani KE, Gharaibeh KA, Yaghan RJ (2005) Retained surgical sponges (gossypiboma); Asian J Surg 28(2):109-115
2. Yildirim S, Tarim A, Nursal TZ, Yildirim T, Caliskan K, Torer N, Karagulle E, Noyan T, Moray G, Haberal M (2005) Retained surgical sponge (gossypiboma) after intraabdominal or retroperitoneal surgery: 14 cases treated at a single center; Langenbecks Arch Surg. 2006 Aug;391(4):390-5. Epub 2005 Sep 17.
3. Gawande AA, Studdert DM, Orav EJ, Brennan TA, Zinner MJ (2003) Risk factors for retained instruments and sponges after surgery; N Engl J Med 348(3):229-235.

4. Macario A, Morris D, Morris S. Initial Clinical Evaluation of a Handheld Device for Detecting Retained Surgical Gauze Sponges Using Radiofrequency Identification Technology; Arch Surg. 2006;141:659-662.
5. Rogers A, Jones E, Oleynikov D. Radio frequency identification (RFID) applied to surgical sponges. Surg Endosc (2007) 21: 1235–1237.

Figures and legends



Figure 1. Screenshot of the wall mounted monitor. Amount and localization of the intraoperatively deployed textile objects. “Gesamt” = total amount, “es fehlen” = missing, “Anrichte” = instrument table, “Tisch” = phantom model, “Müll” = dust bin.

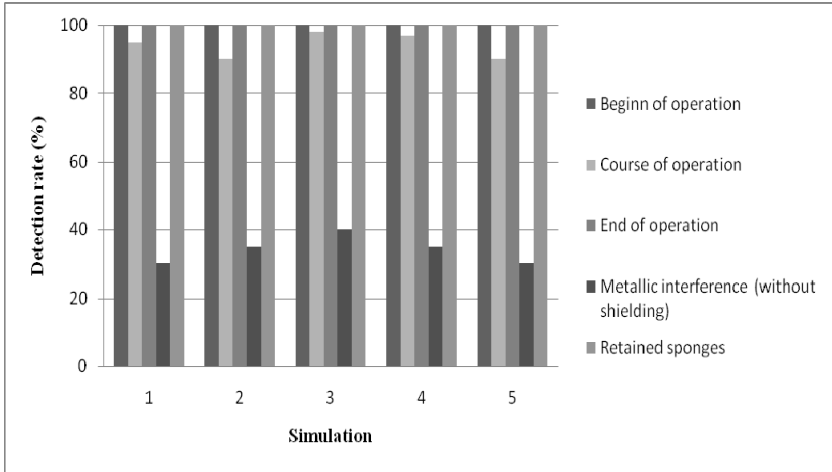


Figure 2. Detection rate (%) of the RFID System depending on the operation status, metallic interference as well as for retained objects at the end of the operation.

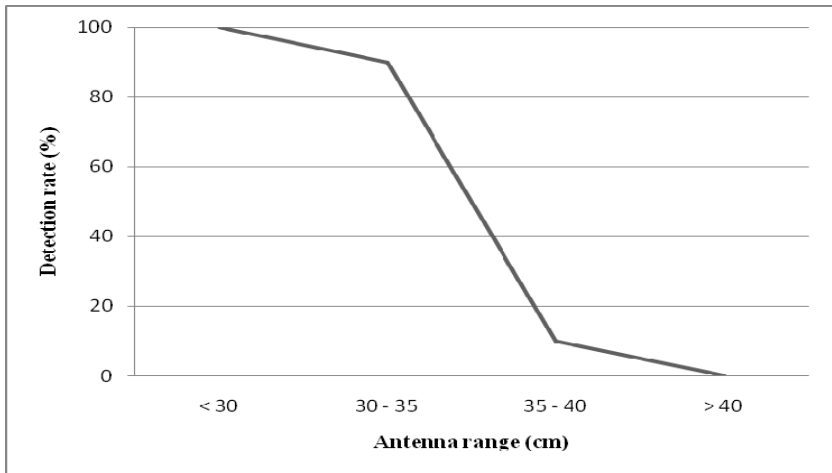


Figure 3. Detection rate (%) of the RFID System (passive transponder chip, MOBY-D, Siemens, München) subject to the antenna range (OBID i-scan, Feig Electronic GmbH, Weilburg- Waldhausen).

Patient Positioning using 3D Surface Registration

André Adelt¹, Christian Schaller¹, Jochen Penne¹, Florian Höpfl², Peter Nix²
and Joachim Hornegger¹

¹ Chair of Pattern Recognition, University of Erlangen-Nuremberg, e-mail:
Christian.Schaller@informatik.uni-erlangen.de
² softgate GmbH, Nögelsbachstr. 26, 91052 Erlangen

Patient positioning is a crucial issue in the field of radiotherapy. In a common workflow, a planning CT scan of the patient is acquired in order to plan the treatment process. The planning CT is usually acquired a few days or weeks prior to the treatment. Right before the treatment session starts, the patient has to be positioned accurately to ensure the treatment plan can be applied correctly. Recently, a new emerging imaging technology called Time-of-Flight (ToF) is available. This new technology uses a single sensor which is feasible to acquire 3D data in real-time. We present a method to correct the position of a patient by acquiring body surfaces using a ToF sensor. The ToF sensor illuminates the patient's body with an optical reference signal and provides a 3D point set of the observed scene. Given two 3D point sets of the patient's body, one acquired during the planning CT scan and a second acquired right before or even repeatedly during the treatment session, the patient's misalignment can be identified and corrected. The surface matching process is divided into a segmentation and registration process. Before the two point sets are registered the patient's body has to be separated from the background. After this preprocessing step an Iterative Closest Point (ICP) algorithm is applied to the datasets in order to determine translation and rotation parameters to correct the position of the patient. Current results show that for rigid phantoms it is possible to obtain a registration error of 2.88 mm and 0.28° respectively. Tests with real persons validate the robustness, stability and correctness of our algorithm. Here we obtained a mean registration error of 5.80 mm.

1 Introduction and Background

The number of annually new diagnosed cancer incidents has been continuously growing since the beginning of registering cancer cases [1]. Having more patients to be treated of course requires faster and more accurate treatment methods. Besides surgery, chemotherapy and medicinal treatment, radiotherapy is

one of the most commonly used therapy options. In a common workflow, the basis for all further treatment steps is a planning CT scan in order to elaborate the treatment plan. The planning CT is usually acquired a few days or even weeks prior to the treatment. Therefore, right before the actual treatment session starts, the patient has to be positioned accurately to ensure the treatment plan can be applied correctly. The positioning thereby has to ensure that the tumor is damaged, while healthy tissue is spared. Patient positioning is even more crucial as the dose is not applied in one single session but it is divided into multiple fractions. This is done due to the fact that tumor cells need more time to recover than healthy cells [2].

Nowadays there are various positioning methods and systems available being more or less accurate providing more or less convenient repositioning procedures. The easiest alternative is to paint markers onto the patient's body and adjust the table position manually. The most accurate systems use X-ray imaging devices to verify correct alignment [3]. While those conventional methods are either inaccurate or require additional exposure to the patient, latest developments are based on optical measurements providing really promising results [4].

We present a method to determine patient translation and rotation in 3D by the acquisition of the patient's body surface during the planning CT and again right before or during each treatment session with the help of a Time-of-Flight (ToF) camera. The comparison of each daily acquired surface with the initially acquired reference surface leads to the desired pose parameters.

2 Surface Based Positioning

The method is divided into three major steps: (1) calibration of the treatment couch, (2) segmentation of the patient and finally (3) the registration of the remaining body surface with a previously acquired reference surface.

Initially, a table plane has to be identified to enable patient body segmentation. Therefore, the empty patient couch is observed and a best fitting plane in the least-square-sense is fitted through all 3D points belonging to the table plane. The identification of a 3D point as a point of the patient couch is done via analysis of a three-dimensional histogram, whose axes are spanned by two normal angles between x- and z-axis and y- and z-axis and the z-coordinates of the 3D points.

In the second step, we use this best fitting plane to segment the patient from the background to eliminate potentially disturbing parts of the scene. Each

point's distance to the plane is calculated by inserting its coordinates in the plane equation. Points with a distance larger than a certain non-negative threshold are removed, hence only the patient's body remains in the scene. At this point the current data set may be saved as reference surface for later positioning.

The final step is to register a previously recorded reference surface with a currently acquired one to determine the patient's misalignment. Before we actually register both surfaces, we decrease the number of points for registration to reduce the computation time from the range of some minutes to some seconds. Only the border areas around the segmented body are utilized. The registration procedure itself uses an ITK¹ implementation of an Iterative Closest Point (ICP) variant [5], namely a three-dimensional rigid point set to point set registration, to identify translational and rotational pose correction parameters.

3 Experimental Results

First we attached a body phantom to a computer controlled robot arm. A reference surface was recorded and then the phantom was shifted arbitrarily into all three room dimensions. The euclidean distance between desired shift and the shift obtained by the registration process was used to measure the accuracy of our method. To judge rotation, the mean absolute rotational error of all rotations around the axes was computed. The mean registration error was 2.88 mm for translations and 0.28° for rotations.

We also tested the algorithm with six male candidates. To judge the registration error, we computed the minimum euclidean distance of all reference surface points to the transformed currently acquired surface points. The transform is defined by rotation and translation parameters, which were computed during the registration process. In order not to get additional disturbances caused by crinkling clothes, all measurement were done with naked upper part of the body. Four markers were fixed on the skin that were used as reference points for distance measurement. The persons laid on the table such that the upper part of the body and the markers were visible. To acquire images at the same point in the respiration cycle, the persons were told to breathe in and out again. Measurements were then generally performed in the point of maximum expiration. As usual, the first step was to acquire the reference surface. Then, the persons were told to move slightly and the registration process was started. After the registration finished, the registration errors at the markers were evaluated. Figure

¹Insight Segmentation and Registration Toolkit, <http://www.itk.org>

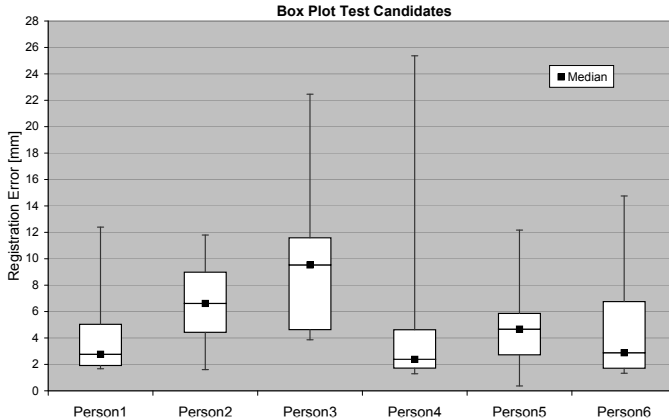


Figure 1: Box plot of the examined test candidates. Achievable registration accuracy is heavily dependent on the person.

1 shows the box plot of registration errors for each person. The overall mean registration error was 5.80 mm. Using only a fixed border area of the body surface, the time for registration was about 30-60 s, dependent on the person's body shape.

4 Summary and Conclusion

We proposed a surface based positioning method based on ToF acquisition of three-dimensional data. The procedure uses a three-dimensional histogram to select the treatment couch points out of the total scene. Using only the points assigned to the maximum histogram bin, the best fitting plane that coincides with the couch surface is calculated and is afterwards used to segment the patient's body from the background. The registration of this segmented body surface with a previously recorded one provides us with the necessary translation and rotation parameters to correct the position of the patient. The method was tested with a body phantom and persons and showed a mean registration error of 2.88 mm and 0.28° for the body phantom and 5.80 mm for real persons.

References

- [1] Batzler, W. U., Giersiepen, K., Hentschel, S., Husmann, G., Kaatsch, P., Katalinic, A., Kieschke, J., Kraywinkel, K., Meyer, M., Stabenow, R., Stegmaier, C., Bertz, J., Haberland, J., Wolf, U., Krebs in Deutschland 2003-2004. Häufigkeiten und Trends, 6. Ausgabe, Robert Koch-Institut und Gesellschaft der epidemiologischen Krebsregister in Deutschland e. V., Berlin, 2008
- [2] Kauffmann, G., Moser, E., Sauer, R., Schneider, B., Wunsch, C., Radiologie: Grundlagen der Radiodiagnostik, Radiotherapie und Nuklearmedizin, Urban & Schwarzenberg, München, Wien, Baltimore, 1996
- [3] Teh, B. S., Bloch, C., Galli-Guevara, M., Doh, L., Richardson, S., Chiang, S., Yeh, P., Gonzalez, M., Lunn, W., Marco, R., Jac, J., Paulino, A. C., Lu, H. H., Butler, E. B., Amato, R. J., The treatment of primary and metastatic renal cell carcinoma (RCC) with image-guided stereotactic body radiation therapy (SBRT), Biomedical Imaging and Intervention Journal 3, January-March, 2007
- [4] Schöffel, P. J., Harms, W., Sroka-Perez, G., Schlegel, W., Karger, C. P., Accuracy of a commercial optical 3D surface imaging system for realignment of patients for radiotherapy of the thorax, Physics in Medicine and Biology 52, 2007, pp 3949-3963
- [5] Besl, P. J., McKay, N. D., A Method for Registration of 3-D Shapes, IEEE Transactions on Pattern Analysis and Machine Intelligence 14(2), February, 1992, pp. 239-256

Rivet application for wound closure with flexible endoscopy in endoluminal endosurgery

Sonja Gillen^{1,2}, Adam Fiolka², Salman Can² Armin Schneider², Helmut Friess¹, Hubertus Feussner^{1,2}.

Technische Universität München, Klinikum Rechts der Isar, München, Germany, Department of Surgery¹ and Minimally Invasive Therapy and Intervention Research Group².

Email: Gillen@chir.med.tu-muenchen.de

Abstract:

Endoluminal endoscopy could be significantly enhanced by adequate approaches to wound closure. A new approach to sewing in flexible endoscopy is achieved with an endoluminal rivet system that allows wound closure without a limit to the dimension of the defect, because the tissue lips are sequentially fixed and adapted. Furthermore, the surgeon can adjust the pressure between the joint tissues.

Besides placing multiple sutures without withdrawing the device, system allows the application of several ligatures without reloading. Several rivets can be placed sequentially into the intestinal wall; the sharp magnesium tip is degraded in the stomach within the first few hours because of rapid corrosion to avoid damage to surrounding tissues. The rest of the rivet remains in the tissue until the healing process is completed. The first functional models were tested in a postmortem pig stomach. The endoscope was inserted through the esophagus, and the rivets were applied in the gastric mucosa. The elapsed time for 1 application was between 1 and 5 minutes. Comparing the rivets firmness with other wound closure methods, first results showed that the rivet seems to be nearly as reliable as a common open surgical suture. The development of the rivet application is still at a very early stage. Further clinical tests have to be performed.

Introduction:

Endoluminal endoscopy could be significantly enhanced by adequate solutions for wound closure. Current solutions are basically confined to clip applications.

Several attempts were made with wound closure techniques for interventional endoscopy. Because of the strict constraints of the endoscope's geometry,

hardly any practical solutions were found. There is, however, a high medical demand for wound treatment with flexible endoscopy.

A new approach to sewing in flexible endoscopy is achieved with an endoluminal rivet system. This system allows the application of several ligatures without withdrawing the rivet application device to reload. Furthermore, the rivet device inserted through a standard endoscope will successfully align and compress edges of transmural lesions of the intestinal tract. This new technique will allow the endoscopic treatment of lesions larger than 1 cm and the endoscopic construction of circular anastomoses. The first in vitro experiences are presented.

Material and methods:

A new attempt with the flexible endoscope was attained by a threadless sewing technique. This led to a rivet device that is operated in the trocar. The device can be inserted through a standard endoscope, using an accessory channel of 1.8 mm diameter. The manipulation of the rivets is completely carried out in the field of vision of the endoscope. For easy handling, the device has a pistol-like handle with 1 lever.

The rivet is applied by perforating first the edge of the lesion which is closed to the tip of the endoscope. In the next step, the edge of the lesion distant from the endoscope is perforated. As soon as the tip of the rivet has passed through the tissue the elastic wings are released and serve as an abutment. Gentle compression is exerted onto the rear part of the rivet, leading to the unfolding of the posterior wings. Thus, an adequate compression of both lips of the lesion is achieved. Finally the rivet is disconnected and the next one is ready without withdrawing the whole device.

First prototypes of the rivet have been tested in vitro closing a defined gastrotomy of a pig stomach. Viscerosynthesis was performed with prototypes of the rivet placed every 3-5 mm versus manual application of endoscopic clips every 3-5 mm, versus a closure with a stapler and the interrupted full thickness hand-sewn suture by a senior surgeon every 3-5 mm as a gold standard. The gastric specimens were filled with methylene blue colored normal saline solution and leaking pressure of the stomach was measured.

Results:

Several rivets (up to five 5 ones) can be placed sequentially into the gastric or intestinal wall. The rivet's diameter is 0.9 mm (20 gauge), and its length is 16 mm (Fig.1). After the insertion (Fig. 2), the magnesium tip is degraded

rapidly (Fig. 3) within the first few hours because of rapid corrosion and so damage to surrounding tissues and organs can be avoided. The rest of the rivet remains in the tissue until the healing process is completed.

In vitro tests measuring the burst pressure of the 3 different viscerosynthesis methods in a pig stomach showed, as expected that the hand sewn suture by a senior endured the highest burst pressures. The specimen with the endoscopic applicated clips leaked at the lowest pressures already. The specimen closed with rivet endured nearly the same pressure the wound closure with the stapler, which was nearly as much as the viscerosynthesis with the hand sewn suture beared (Fig. 4).

Discussion:

The new approach to sewing in flexible endoscopy described above with an endoscopic applicable rivet system allows wound closure in the intestinal tract without a limit to the dimension of the defect. At the moment the first in vitro experiments were performed showing convincing data concerning tightness of the wound closure technique. One of the advantages seems to be that, similarly to ordinary sutures, the surgeon can adjust the pressure between the joint tissues.

The rapid degradation of the magnesium is suitable for all aqueous dilutions. The pH value thereby needs to be less than 12, as it is for every organ of the human body. As the sharp tip of the rivet, which could potentially lacerate healthy tissue after implantation, is degraded in the stomach within the first few hours because of rapid corrosion (Fig. 3), the rest of the rivet remains in the tissue until the healing process is completed.

When penetrating the tissue with the rivet's tip, the lips of the wound recede. Thus, the tip of the rivet must be as sharp as possible. We assume that by optimizing the geometry of the tip, the recession can still be reduced further. Additionally, the recession of the tissue can be completely avoided by using an endoscope with 2 working channels and by inserting an alligator forceps into one of them. The forceps can simply grab and withhold the tissue.

This wound closure technique has several advantages. Besides placing multiple sutures without withdrawing the device, there is no limit to the dimension of the defect, because the tissue lips are sequentially fixed and adapted.

Outlook:

This new technique will allow the endoscopic treatment of lesions larger than 1 cm and the endoscopic construction of circular anastomoses.

The development of the rivet application is still at a very early stage. Further clinical tests with functional samples have to be executed to gain more precise functional results.

Furthermore, the application of the magnesium tip needs to be further examined. For this purpose, in vitro studies in different environments are currently being conducted. Moreover, analyses have to be conducted in the gastric acid, as well as in the gastric mucosa, intestinal mucosa, muscle tissue, and blood. At least efforts are made to transfer the functional models into prototypes made of degradable polymers.

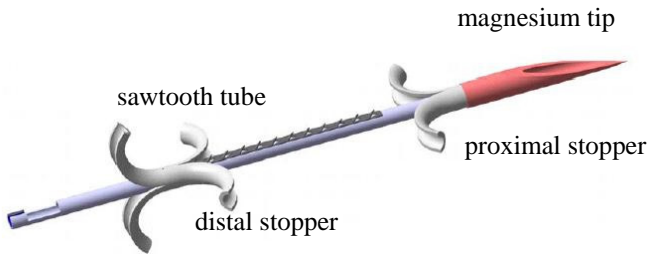


Figure 1. Rivet for endoluminal wound closure: The rivet's diameter is 0.9 mm (20 gauge), and its length is 16 mm.



Figure 2. **A**, The endoscopist focuses on the tissue perforation with the endoscope; then pushes the rivet device through the accessory channel and targets the wound. **B**, The lips of the wound are sequentially penetrated and fixed by an anchor. **C**, After applying the first rivet, the next one is ready, without withdrawing the whole device.

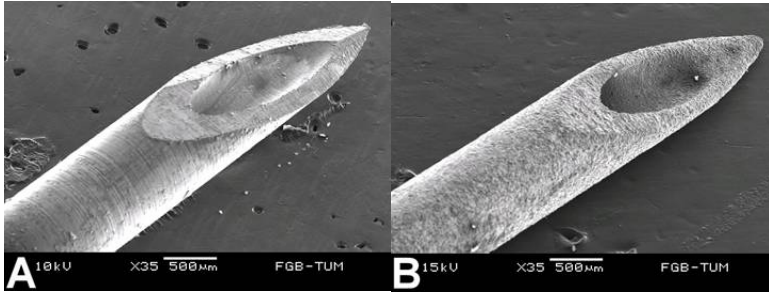


Figure 3. **A**, a 20-gauge cannula made of a magnesium-aluminium-zinc alloy. **B**, Degradation of the cannula after 12 minutes in 0.025 molar hydrochloric acid (pH 1.5; equivalent to gastric acid).

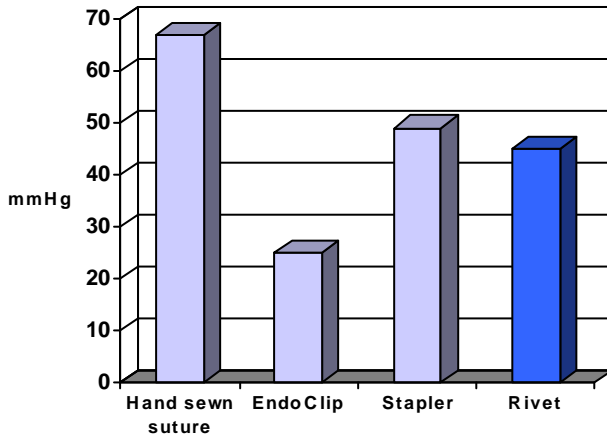


Figure 4. Four different kinds of viscosynthesis techniques are compared. After closure of a defined lesion in post-mortem pig stomach the burst pressures were measured.

Incidence, pathogenesis, and clinical diagnosis of implant associated nosocomial infections

Guggenbichler JP

Univ. Erlangen, Department of Pediatrics, Ped. Infectious Diseases and Preventive Medicine, Loschgestr. 15; D 91054 Erlangen, Germany

Abstract

An underrecognised cause of preventable mortality is healthcare-associated infection. Based on a conservative estimate of 10% of the European population that is hospitalised every year and considering that 5% of them suffer a nosocomial infection, this represents 1.75 million hospitalised patients with at least one episode of nosocomial infection. Assuming a conservative 10% attributable mortality rate, this equates to 175 000 deaths from these infections every year. These figures do not take into account the enormous cost of treating these infections and the disabilities that they cause, for which reliable estimates are lacking in Europe.

Introduction

Health care associated infections are the fourth leading cause of disease in industrialised countries and the most common complication affecting hospitalized patients. Based on a conservative estimate, 10% of the European population is hospitalised each year. Thereof, it is assumed that 5% (3.8 % on a general ward, 15.3 % in intensive care units) acquire at least one nosocomial infection. Based on these figures, it can be estimated that some 1.75 million hospitalised patients are affected annually by a nosocomial infection in Europe. Assuming a conservative 10% attributable mortality rate, this equals a minimum of 175,000 deaths every year. [1] The results of the Pan-European EPIC and of the German SepNet study suggest even higher numbers of affected patients [2, 3]. Reports from the US indicate that nosocomial infections account for 2 million infections and 90,000 preventable deaths per year. [4]

The most significant hospital-acquired infections, based on frequency and potential severity, are those related to the increasingly complex hospital environment, procedures e.g. surgical site infections and implantable medical devices, including urinary tract infection in catheterized patients, pneumonia in patients on a ventilator and bacteraemia related to intravascular devices. [5, 6, 7, 8, 9] Modern medical and surgical practices have increasingly utilized implantable medical devices of various kinds. Such

devices may be utilized as short-time or intermittently, for months, years or permanently. They improve the therapeutic outcome, save human lives and greatly enhance the quality of life of these patients. However, plastic devices are easily colonized with bacteria and fungi. Several multivariate analyses revealed that implantable medical devices as a major independent risk factor present on more than half of patients with positive blood cultures. [10, 11, 12, 13]

Microorganisms gain access to the body by multiple pathogenetic pathways. Despite the sometimes low virulence of invading microorganisms involved, the bodies own defence mechanisms are unable to eradicate the organisms effectively even when the host is fully immunocompetent. Underlying disorders like malignancies, diabetes and agents impairing host defence mechanisms e.g. administration of corticosteroids, antineoplastic agents and parenteral nutrition are well recognized additional risk factors. Risk for nosocomial infections is, among others, associated with duration of hospital stay, type of ward and intensity of care. [14, 15, 16]

Also an increasing number of highly vulnerable patients together with emerging of antibiotic-resistant microbes, especially *Staphylococcus aureus*, *Enterococcus species* and Gram-negative microorganisms producing extended spectrum beta-lactamases (ESBL) are encountered. [17, 18] The situation is aggravated by the fact that in the future there will be few new antibiotics under development to compensate for the increasing resistance. [19]

Multi-resistant nosocomial pathogens are the most common organisms difficult to eradicate because bacteria that cause these infections live in well-developed biofilms. [20] Biofilm is a microbial derived sessile community characterized by cells that are irreversibly attached to a substratum or interface to each other, embedded in a matrix of extracellular polymeric substances that they have produced.



Biofilm of *S. epidermidis*

on a polyurethane catheter.

Observations support the hypothesis that catheter encrustation in transurethral catheters is brought about by the activity of urease-producing biofilms and confirms that the main target in the control of catheter encrustation should be *P. mirabilis*. Urease catalyses the hydrolysis of urea to produce ammonia, with the result that the pH of the urine increases and the urinary electrolytes are precipitated in the biofilm.

An excess length of stay (mean, 10 d; median, 5 d; $p = 0.007$) and increased direct costs (mean difference, \$34,508; $p = 0.008$) have been described. In 2000, the US Centers for Disease Control and Prevention estimated the total costs of nosocomial infections to be in excess of 5 billion US \$. [4] In Germany, it is estimated that approximately 2.4 billion € are spent annually for treatment of these infections. [21] These figures don't include the disabilities caused by nosocomial infections, the decrease of healthy life expectancy, the impact on the loss of productivity due to early death or chronic illness. The demographic trend towards an ageing population enhances the risk of increasing infection as elderly people are prone to invasive medical procedures and are, in general, more susceptible to infectious diseases. [1]

While in developed countries the number of patients treated in hospitals and average lengths of stay decreased during recent decades, hospital acquired infections have increased.

Clinical assessment of implant associated infections

Clinical assessment prior to the explantation of a medical device is frequently difficult in patients with multiple pathology. The majority of clinical symptoms of infection can be due to a variety of factors including implant

related sepsis. Certain clinical, epidemiologic and microbiologic features however point toward an e.g. intravascular device as the source of fever and circulatory impairment:

- An intravascular device, especially a central venous catheter, in place at the outset of sepsis
- A patient who is an unlikely candidate for sepsis without underlying disease
- No obvious local infection to account for the picture of sepsis
- Local inflammation or purulent discharge at the insertion site. However inflammation at the insertion site is not a reliable predictor of a catheter related bloodstream infection with short term, non cuffed central venous catheters.
- Abrupt onset associated with fulminant shock suggestive of massive invasion of the bloodstream from an outside source.
- Sepsis refractive of antimicrobial therapy or dramatic improvement with removal of the infected device or discontinuation of the contaminated infusion
- Isolation of grampositive organisms especially coagulase negative staphylococci, enterococci or candida albicans from the bloodstream.

For evaluation of the clinical efficacy of an antimicrobial polymer in a clinical study a more precise diagnostic tool was established. On the basis of the CDC/HICPAC criteria and in accordance with the NIDEP study for nosocomial infections a scoring system was established which included the following criteria: [22]

High and rate of rise in body temperature,
attendant shivering,
identification of pathogens in blood and catheter tip cultures,
careful clinical observation regarding the improvement of the clinical course after catheter removal,
signs of catheter exit site inflammation and
extensive diagnostic tests for other possible sources of infection.

These criteria were graded using points on the basis of defined conditions (e.g. concomitant antibiotic therapy) in well defined time relations.

A definite diagnosis however can be made only after explantation of the catheter and microbiologic investigation.

Summary of various implant associated infections

- Peripheral venous catheters 0.2/1000
- CV catheters 1.5 – 12/1000 catheter days. av. 6.7/1000
- Sheldon catheters 35 %
- Hickman Catheter 0.7- 1.2/1000 Lit. KISS 1.97/1000
- PORT - catheter: 8 - 12 % infection, preliminary explantation 25 %
- Tenckhoff catheters 2 - 15 %
- Transurethral catheters: a cumulative rate of urinary tract infections of 5 – 8 % / day has been documented in several clinical studies
- External ventricular drainage systems: rate of ventriculitis 12. % meta analysis of 7 studies
- Thoracic drainage systems 25 %.
- Ventilator associated pneumonia, (endotracheal tube related infection 25 %) with a mortality between 25 and 80 %
- Joint implants primary infection 0.2 – 2.5 %. Recurrent infections after treatment of an infected joint implant 10 %

References

1. Report of the European Science Foundation: WWW:ESCMID.com; September 1, 2005
2. Vincent JL, Bihari D, Suter PM. The prevalence of nosocomial infection in intensive care units in Europe: the result of the EPIC study. JAMA 274: 639 – 644, 1995
3. Brunckhorst FM, Reinhardt K, Bone HG. Epidemiology of severe sepsis and septic shock in Germany results from the German prevalence study. Crit Care 2005, 9 (Suppl) 83 – 89
4. National Nosocomial Infections Surveillance (NNIS) Report, data summary from January 1992 to June 2000. Am. J. Infect Contr. 30. 458 – 475, 2002
5. Ecker DJ, Carroll KC: Investments in high payoff technologies could reduce toll of infections. ASM News: 71 (12) 576 - 581 2005
6. Smith RL., Meixner SM.-, Simberkoff MS., Excess mortality in critically ill patients with nosocomial bloodstream infections. Chest 100 (1991) 164 – 167.
7. Locci R, Peters G, Pulverer G.: Microbial colonization of prosthetic devices. Scanning electron microscopy of intravenous catheters

invaded by yeasts. *Zentralbl. Bakt Mikrobiol, Hygiene (B)* 107, 419 – 424, 1986

8. Odetola FO, Moler FW, Dechert RE, VanDerElzen K, Chenoweth C Nosocomial catheter-related bloodstream infections in a pediatric intensive care unit: risk and rates associated with various intravascular technologies. *Pediatr Crit Care Med.* 2003 Oct;4(4):432-6
9. Chu VH, Crosslin DR, Friedman JY, Reed SD, Cabell CH, Griffiths RI, Masselink LE, Kaye KS, Corey GR, Reller LB, Stryjewski ME, Schulman KA, Fowler VG Jr. Staphylococcus aureus bacteremias in patients with prosthetic devices: costs and outcomes. *Am J Med.* 118(12):1416 2005
10. Vincent JL: Nosocomial infections in adult intensive care units. *Lancet* 361. 2068 – 2077, 2003
11. Safdar N, Crnich CJ, Maki DG Nosocomial Infections in the Intensive Care Unit Associated with Invasive Medical Devices. *Curr Infect Dis Rep.* 2001 Dec;3(6):487-495
12. Lorente L, Henry C, Martin MM, Jimenez A, Mora ML Central venous catheter-related infection in a prospective and observational study of 2,595 catheters. *Crit Care.J* 9 (6):R631-635. 2005
13. Yoshida T, Tsushima K, Tsuchiya A, Nishikawa N, Shirahata K, Kaneko K, Ito K, Kawakami H, Nakagawa S, Suzuki T, Kubo K, Ikeda S. Risk factors for hospital-acquired bacteremias. *Intern Med.* 44 (11):1157-62. 2005
14. Richards MJ, Edwards JP, Culver DH, Gaynes RP. Nosocomial infections in medical intensive care units in the Unites States. National nosocomial infection surveillance system. *Crit Care Med.* 27: 887 – 892, 1999
15. Beghetto MG, Victorino J, Teixeira L, de Azevedo MJ Parenteral nutrition as a risk factor for central venous catheter-related infection. *JPEN J. Parenter Enteral Nutr.* 29(5):367-373 2005
16. Raymond J, Aujard J, The European Study Group: Nosocomial infections in pediatric patients: a European, multicenter prospective study. *European Study Group. Infect Control Hosp Epidemiol.* 21(4): 260

17. Paterson DL. Resistance in gram-negative bacteria: enterobacteriaceae. *Am J Med.* 2006 Jun;119(6 Suppl 1):S20-8;
18. Paterson DL. Serious Infections in the Intensive Care Unit: *Pseudomonas aeruginosa* and *Acinetobacter baumannii*. *Clin Infect Dis.* 2006 Sep 1;43 Suppl 2:S41-S42
19. Norrby SR, Nord CE, Finch R; European Society of Clinical Microbiology and Infectious Diseases: Lack of development of new antimicrobial drugs: a potential serious threat to public health. *Lancet Infect Dis.* 5 (2):115-9. 2005
20. Chambliss JD, Hunt SM, Stewart PS. A three-dimensional computer model of four hypothetical mechanisms protecting biofilms from antimicrobials. *Appl. Environ Microbiol.* 2006 Mar;72(3):2005-13
21. Frank U, Chojnacki T, Dettenkofer M, Daschner F. Cost-effectiveness of an antiseptic-impregnated central venous catheter in the ICU. Correspondence: *Int. Care Med.* 2002
22. Lugauer S, Regenfus A, Böswald M, Martus P, Gais C, Bechert T, Greil J, Guggenbichler JP: A new scoring system for the clinical diagnosis of catheter related infections. *Infection* 27, Suppl 1, (1999) 49 – 53

Prevention of implant associated nosocomial infections

Guggenbichler JP

Univ. Erlangen, Department of Pediatrics, Ped. Infectious Diseases and Preventive Medicine, Loschgestr. 15; D 91054 Erlangen, Germany

Abstract

Impregnation or coating of biomedical devices with antibiotics and disinfectants has been investigated but the results are less than satisfactory. Material modification i.e. impregnation of the entire matrix of implantable biomaterials with activated nanoparticles of silver provides an effective, non-toxic technology to endow catheters with excellent and long lasting antimicrobial activity on the surface and the lumen. The impregnation of catheter surfaces with anorganic acids also provides long lasting antimicrobial activity without adverse events. This has been documented in clinical studies with several hundred patients. The catheters are CE certified and on the market. The technologies, testing procedures, and results of clinical studies are presented.

Introduction

Strategies to minimise the risk of infection associated with implantable device related infections assume highest priority. It has to be emphasised that for maximum benefit an integral approach is necessary: Strict adherence to hygienic rules, vigorous barrier precautions during insertion or implantation of the device as well a continuing care are aspects of particular importance and require the need for the consistent application of guidelines. [1] Handwashing, ideally with an antiseptic containing preparation is “the single most important intervention in infection control” Included are also sterile gloves, a sterile long sleeved surgical gown, mask, cap and a large sterile drape including aseptic care and appropriate supportive measures. The implementation of an infection control program utilizing education of personnel skilled in the placement of intravascular devices, process control, and performance feedback has been shown to be associated with significant reductions in rates of IVD-associated bloodstream infections (BSI) and mortality. [2, 3, 4]

Material modifications:

The development of new materials which could withstand microbial adherence and colonization has become a major topic in recent years.

Impregnation with hydrogel, heparin and heparin like agents, antibiotics and disinfectants has been investigated with no or less than satisfactory results.

[5, 6]

Antibiotics and disinfectants show a

- Limited spectrum of activity,
- increasing resistance and emergence of *Candida albicans*
- Sessile organisms require 100 – 250 fold higher concentrations for eradication than MIC
- Rapid elution of antimicrobial activity
- Induction of resistance by subinhibitory concentrations, „small colony variants“
- No antibiotics for prophylaxis, which are used therapeutically!
- Expensive

Clinical experiments with impregnation of various implantable devices with various antibiotics in several thousands of patients showed no statistically significant prevention of device related infections.

Silver and other metals and metal salts

The antimicrobial activity of silver as well as copper and other metal ions, has been well known for centuries as oligodynamic activity. Silver is the element with the highest antimicrobial activity against the vast majority of pathogens and the lowest toxicity for animal cells. [7]

- Silver ions form insoluble compounds in the cell wall of bacteria and fungi with sulfhydryl groups which are essential components of enzymes responsible for the transmembranous energy metabolism, electrolyte transport and preservation of osmotic homeostasis. The result is either with hypertonic solutions a loss of fluid and electrolytes from the microorganisms, which dry out and shrink or a hyperinflation and blow up with hypotonic solutions.
- Silver ions block the respiratory chain of bacteria in the cytochrome oxidase and NADH-succinate-dehydrogenase region
- Silver ions enter the cell and bind to bacterial DNA. Intercalation of silver leads to an increased stability of the double helix and prevention

of splicing. Therefore no further proliferation occurs. This also explains the prevention of proliferation of adherent bacteria and the prevention of biofilm formation. Silver ions use calcium channels for penetration into the bacterial cell.

It must be emphasised that only free silver ions exhibit antimicrobial activity. This means, that sufficient concentrations of free silver ions can only originate from a large surface of silver⁰.

Technology Silver

A technology developed in our institution used a vast increase of the surface of silver⁰ in polyurethane which resulted in an increased release of free silver ions over a period of several months. It was technically feasible to fill the spaces between the thermoplastic polyurethane elastomers with billions of Nanoparticles of metallic silver (3 – 5 nm in diameter) evenly distributed throughout the polymer matrix providing a surface of > 2500 cm² of silver per g polyurethane. Silver nanoparticles are incorporated into the polyurethane matrix fixed on a carrier e.g. barium sulphate or titanium oxide. [8, 9]

Fig 1 a

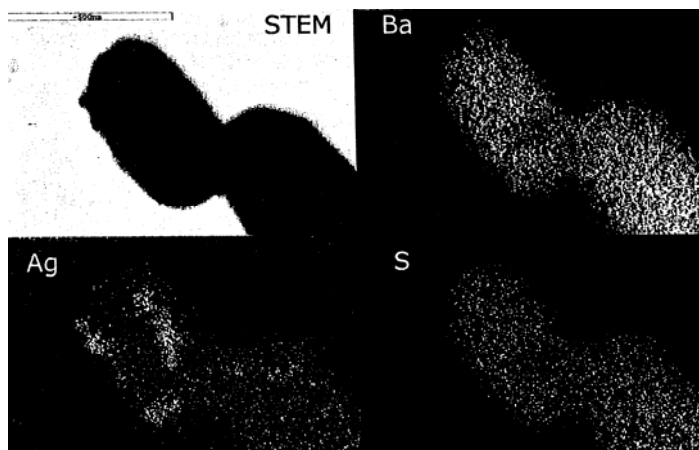


Fig 1 a: Demonstration of silver nanoparticles on a Barium sulfate carrier with STEM and element mapping.

For activation of the silver nanoparticles a few molecules of a largely water insoluble silver salt e.g. silver sulphate or silver orthophosphate are on top of each silver Nanoparticles.

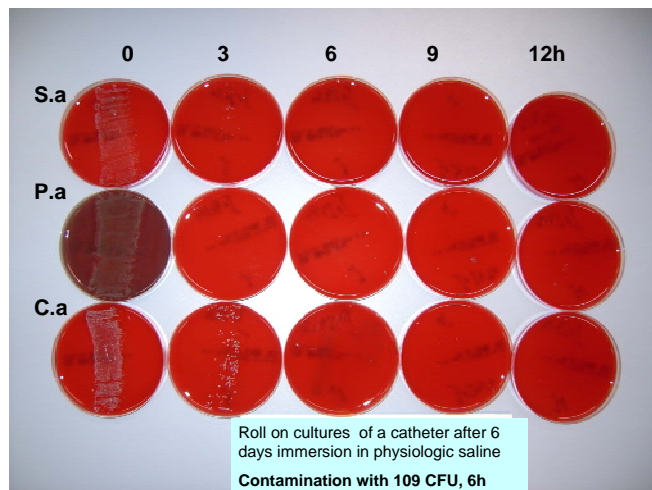


Fig 1 b: Results of roll on cultures after inoculation of a catheter with 10^9 CFU/ml over 6 hours. The catheter is rolled every 3 hours over the agar plate

Polyurethane and silicone catheters endowed with activated silver nanoparticles according to this technology show an excellent antimicrobial activity for months. The antimicrobial activity includes besides eradication of a bacterial inoculum on the surface also blockage of adherence, prevention of biofilm formation and proliferation.

Technology Metaloxide

A new technology where catheters are impregnated with metal oxides e.g. Molybdenum trioxide or Tungsten trioxide result in an acidic surface (pH 4.0) without elution of the acidity to the surface. The results of investigation of antimicrobial activity with roll on cultures shows eradication of the inoculum of 10^9 CFU/ml from a surface within 6 hours. [10] The materials are non-toxic and show an excellent biocompatibility. This material is ideal

for the use in urologic catheters as an acidic surface prevents incrustation and formation of struvites



Fig 2: Results of roll on cultures of a Molybdenum Trioxide impregnated silicon catheter after inoculation with 10^9 CFU/ml for 6 hours.

Clinical investigations

Materials with the silver Nano- technology have been used in central venous catheters (1 – 4 lumen catheters), catheters for neonates and premature infants, Hickman catheters, PORT catheters, external and internal ventricular drainage systems and transurethral catheters. Experimental investigations demonstrate lack of short term and long term cytotoxicity and thrombogenicity as well as excellent biocompatibility. The physical properties (kinking, elasticity) are unaltered compared to regular catheters. There is an excellent cost efficiency.

GMP conform (randomised, prospective, blinded) clinical investigations in 695 patients demonstrate a 70 % reduction of catheter related infections. [11] A case report study with 204 patients with central venous catheters in place for more than 10 days showed only one catheter related infection of the silver containing catheter with an expected infection rate of 12 – 15 cases with regular catheters. [12]

A study with long term implanted Hickman catheters demonstrated no infection in 5900 catheters days with the nanosilver impregnated catheters versus 3 patients with a catheter related infections in 5070 catheter days with a regular catheter. Mean duration of catheter placement was 8.5 months. [13] All catheters are CE marked and available in Europe. The catheters are marketed by Smiths Medical, Deutschland

A prospective randomised study in 120 patients with an external ventricular drainage showed a statistically significant reduction of ventriculitis of 85 %. Ventricular drainage systems are marketed by Spiegelberg KG, Hamburg. Transurethral catheters are intended to be in place for >8 weeks. Intensive investigations with antimicrobial urologic catheters are performed by UROmed, Hamburg .

The technology can also be used for Sheldon catheters, PORT catheters, endotracheal tubes, and tracheotomy tubes. This technology can also be used for antimicrobial endowment of plastic dental devices, toothbrushes and toothpastes with excellent protective activity against periodontitis. [14] In essence every implantable medical device can be endowed with antimicrobial activity with either one of these technologies; excellent clinical results can be expected.

References

- 1) Kluger DM, Maki DG: A metaanalysis of the risk of intravascular device related bloodstream infections Based on 223 publications. ICAAC, 1999 Nosocomial infections Abstract number 1913, 647
- 2) Sawyer RG Health-care-associated infections and prevention. Surg Clin North Am. 85(6):1137-1152 2005
- 3) Mermel LA, Farr BM, Sherertz RJ, Raad II, O'Grady N, Harris JS, Craven DE. Guidelines for mthe management of intravascular catheter-related infections. Clin Infect Dis. 32: 1249 – 1272, 2001
- 4) Orr Parras F: Impact of an educational program for the prevention of colonization of intravascular catheters. Infect. Control Hosp. Epidemiol. 15, (1994) 239 – 242
- 5) Bylock A Surface morphology of unused and used Hydromer coated intravenous catheters. Scan Electr Micr. (1986) 157 – 164
- 6) Pemberton LB, Ross V, Cuddy P, Kremer H, Fessler T, McGurk E. No difference in catheter sepsis between standard and antiseptic central venous catheters. A

prospective randomized trial. Arch Surg. 1996 Sep;131(9):986-9

- 7) Thurman RB, Gerba CHP: The molecular mechanisms of copper and silver ion disinfection of bacteria and viruses Crit. Rev. Environmental Control 18 (1989) 295 –315
- 8) Guggenbichler JP, Hirsch A, Patentschrift 1999
- 9) Bechert Th, Steinrücke P, Guggenbichler JP: A new method for screening anti-infective biomaterials: Nature medicine, volumen 6, number 8 (2000) 1053 – 1056
- 10) Guggenbichler JP, Wildner, Eberhardt, Martinz. Patentschrift 2007
- 11) Guggenbichler JP, Beer A, Böswald M, Braun GG, Burgmann H, Lugauer S. Regefus A, Baratto F, Carlon R, Meggiolaro M, Stoiser B, Frass M, Giron GP: Reduced rates of catheter related bloodstream infections by use of a silver impregnated central venous catheter: results of an European multicenter study..ECCMID Stockholm, 2000
- 12) Guggenbichler JP, Juhl G, et al. Clinical investigation with a new nanosilver impregnated catheter. Hyg Med. 28, 223 – 238 2003
- 13) Guggenbichler JP, Carbon R, Lugauer S., Geitner U, Regefus A, Böswald M, Greil J, Bechert Th, Hümmer P. Reduced incidence of catheter related infections in long term i.v. catheters in children by use of a silver impregnated catheter. ECCMID Stockholm 2000
- 14) W. Wanninger, Dissertation. Prevention of periodontitis with a silver impregnated toothpaste, 2007

Robust Speech Recognition for Human-Robot Interaction in Minimal Invasive Surgery

*Björn Schuller¹, Christoph Scheuermann¹, Salman Can²,
Hubertus Feussner^{2,3}, Gerhard Rigoll¹*

*¹Institute for Human-Machine Communication,
Technische Universität München (TUM), Germany
schuller@tum.de*

²Workgroup MITI, TUM, Germany

³Department of Surgery, Klinikum rechts der Isar, TUM, Germany

1 Introduction

Laparoscopic surgery as opposed to open surgery offers distinct benefits as reduced pain, shorter hospitality, and quicker convalescence to the patients. During laparoscopic interventions, a camera assistant usually holds the laparoscope for the surgeon and positions the scope according to the surgeon's instructions. The camera view may be suboptimal and unstable, because the telescope is sometimes aimed incorrectly and vibrates due to the assistant's hand trembling. The introduction of a telemanipulator system for guiding the telescope, in aim to replace the human assistant, is a significant step toward the solution of this problem. Most laparoscope positioning systems proposed so far use input devices such as joysticks, foot pedals, and similar human-robot interfaces. However, this type of interfaces poses additional burden on surgeons. Implementation of a voice control interface is an effective approach to overcome these drawbacks since the verbal instructions are natural for a human, and the use of neither hands nor feet is required in controlling the laparoscope. Voice control was introduced for several laparoscope positioning systems (c.f. e.g. [4]). However, due to long reaction time, limited reliability, and a user dependent interface these systems could not achieve the required acceptance. To improve this fact we introduced integration of social competence by acoustic emotion recognition in [1]. Although robustness could thereby be improved, appearing background noises in the operation room environment still result in insufficient reliability.

Therefore a novel speech control interface providing improved noise robustness in medical room environments achieved by using a Switching Linear Dynamic Model for the newly designed and produced laparoscope positioning system SoloAssist™ (AktorMed, Barbing, Germany) was developed. This paper emphasises on benefits obtained with model and feature enhancement to overcome unwanted movements of the tele-manipulator.

2 Laparoscope Positioning System

The laparoscope positioning system SoloAssist™ is the first mechatronic device with a fluid actuation system allowing enhanced power transmission and positioning compared to other technologies. Integrated pressure sensors for each actuation permit pushing the system manually at any time out of the operating field, which is a significant feature for patient safety. It resembles a human arm with an extended working range of 360° radius in both directions of movement, an inclination of up to 80° and penetration depth of maximal 250 mm depending on the current telescope length. Hereby the direction terms correspond to the speech interface commands for controlling the tele-manipulator by speech. A joystick integrated on a laparoscopic handhold with exchangeable instruments, a small hand panel, and a foot pedal are used input devices so far.

3 Automatic Speech Recognition

First, the *Speech In Minimal Invasive Surgery* (SIMIS) database including background noises and often being very emotional within the real life situation was recorded as introduced in detail in [1]. SIMIS covers 20 live surgeries with both headset and room microphone, both active condenser, in an operation room of the university hospital *rechts der Isar* with normally one main surgeon and 6 to 10 surgical assistants in 16 bit, 16 kHz of different minimal invasive surgeries as stomach and gall operations. These were automatically segmented into speech turns. Each surgery took 36-80 min; speech time from 5-17 min. The number of segments reached from 159 to 523.

Additionally, the system controlling commands were recorded of 5 male speakers saying each of 15 keywords 9 times resulting in 675 clean turns. These were artificially one-to-one interfered with 5 types of noisy non-speech SIMIS

recordings from the same headset providing highly similar conditions. Thus, 3375 noisy turns are available for testing and training. As a result of the superposition 21% of the noisy test utterances have an SNR below 10 dB, 12% are between 10-35 dB and the rest is beyond 35 dB.

The tele-manipulator possesses two moving modes: a short precise, and a long distance move. This fact leads to a highly limited vocabulary of 15 keywords, where the directions with a prepended move command represent the long distance move: *left*, *right*, *up*, *down*, *forward*, *backward*, *moveleft*, *moveright*, *moveup*, *movedown*, *moveforward*, *movebackward*, *stop*, *quit*. For every keyword a Hidden Markov Model (HMM) consisting of 8 states and 3 mixtures per state was chosen or the prepended *move* - command was treated as an extra model (see section 4) to reduce substitution errors, since, e.g. the commands *left* and *moveleft*, are subject to confusion. Furthermore, a word-based garbage model consisting of 10 states and 16 mixtures per state to exclude extraneous speech was trained on the SIMIS-recordings. Additionally the silence and the short pause model which is operating as a tee-state model sharing the middle state of the silence model, was trained on non-speech-recordings of minimal-invasive operations. The grammar is chosen as context free word-loop solution. MFCC 0-12 plus δ and $\delta\delta$ serve as features.

The model used in this work to improve robustness is based on modeling speech and noise as applied in [2]. Together with a model of how speech and noise produce the noisy observations, these models are intended to enhance the noisy speech features. In [3] a Switching Linear Dynamic Model (SLDM) is used to capture the dynamics of clean speech. Similar to HMM based approaches to model clean speech, the SLDM assumes that the signal passes through various states. Conditioned on the state sequence the SLDM furthermore enforces a continuous state transition in the feature space.

The modeling of noise is realised by using a simple Linear Dynamic Model (LDM) obeying the following system equation:

$$x_t = Ax_{t-1} + b + v_t \quad (1)$$

This LDM can be seen as simple multivariate Gaussian and corresponds to exclusively the lower line in Figure 1.

The modeling of speech is realised by a more complex dynamic model which also includes a hidden state variable s_t at each time t . Now A and b

depend on the state variable s_t :

$$x_t = A(s_t)x_{t-1} + b(s_t) + v_t \quad (2)$$

As can be seen in Figure 1, every possible state sequence describes an LDM which is non-stationary due to A and b changing over time. Time-varying systems like the evolution of speech features over time can be described adequately by such models. Hereby it is assumed that there are time dependencies among the continuous variables x_t , but not among the discrete state variables s_t .

Conventional EM techniques are used for training throughout.

A relationship of how speech and noise produce the noisy observations is obtained by a zero observation model with SNR interference which assumes that speech and noise mix linearly in the time domain corresponding to a non-linear mixing in the cepstral domain [3].

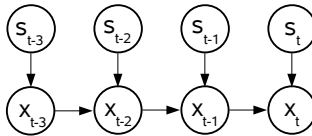


Figure 1: Switching Linear Dynamic Model for speech

4 Experiments and Discussion

To obtain performance on noisy speech we use the 15 keywords described in section 3. The evaluation strategy chosen is a 70/30 - training/test split. Table 1 shows word accuracies for two different model topologies. These are represented by identical models for each keyword and an extra model for the word *move* that can be prepended to each moving direction. For feature enhancement, a global speech SLDM of 32 hidden states was trained whilst the LDM modeling stationary noise was trained for each noisy test sequence using the first and last 10 frames of the utterance. As can be seen in table 1, SLDM slightly outperformed the best performance when using clean training with noisy test utterances. Matched conditions have to be interpreted as upper bench-mark, as they make use of full knowledge about the noise, which cannot easily be provided in a real use-case.

<i>Topology</i>	<i>clean/clean</i>	<i>noisy/noisy</i>	<i>clean/noisy</i>	<i>clean/noisy(SLDM)</i>
constant	89.63%	83.83%	77.08%	78.51%
sep. move	94.89%	94.02%	90.62%	90.80%

Table 1: Accuracies for permutations train/test clean or noisy: constant model parameters (upper row); separated model for the keyword *move* (lower row)

The presented results distinctively show that the use of SLDM increases recognition performance, but has its limits, since in a real life operation room one has to deal with non-stationary noise. Also, comparably lower overall SNR levels lead to lower benefit as e.g. in car noise environment (c.f. [2]).

Future work will investigate the benefit of the working prototype in a long term usability study in the operation room. Furthermore, the ASR shall be augmented by further noise reduction methods and an improved garbage model to reject extraneous speech shall be introduced.

References

- [1] Schuller, B., Rigoll, G., Can, S., Feussner, H.: Emotion Sensitive Speech Control for Human-Robot Interaction in Minimal Invasive Surgery, Proc. 2008 IEEE RO-MAN 2008, Munich, Germany, 2008.
- [2] Schuller, B., Wöllmer, M., Moosmayr, T., Ruske, G., Rigoll, G.: Switching Linear Dynamic Models for Noise Robust In-Car Speech Recognition, Proc. DAGM 2008, DAGM, Springer LNCS, Munich, Germany, 2008.
- [3] Droppo, J., Acero, A.: Noise robust speech recognition with a switching linear dynamic model. Proc. ICASSP 2004, Montreal, Canada, 2004.
- [4] Munoz, V.F., Vara-Thorbeck, C., DeGabriel, J.G., Lozano, J.F., Sanchez-Badajoz, E., Garcia-Cerezo, A., Toscano, R., Jimenez-Garrido, A.: A Medical Robotic Assistant for Minimally Invasive Surgery. Proc. 2000 IEEE Int. Conf. Robotic Automat., San Francisco, CA, pp. 2901-2906, Apr 2000.

Time-of-Flight Based Endoscopy for NOTES Interventions: Challenges and Limitations

Jochen Penne¹

Michael Stürmer¹

Dirk Wilhelm²

Hubertus Feußner²

June 1, 2008

Abstract

The emerging Time-of-Flight (ToF) technology is looking for its way to minimally invasive surgery. Detailed analysis of the clinical workflow and surgical challenges during **Natural Orifice Translumenal Endoscopic Surgery (NOTES)** interventions explicitly pointed out that finding the optimal access point to the peritoneal cavity as well as intraoperative collision control and navigation support are of utmost importance for the success of NOTES and have to be solved by methods of information science. ToF based endoscopy has the potential to address these issues successfully by **measuring the time of flight of an actively emitted modulated reference signal in each pixel and thus providing distance information for each pixel**. Various options for optimizing the overall signal **transmission of the modulated reference signal** and consequently the measuring uncertainty have been determined and are subject to current research. We furthermore describe how to correctly model the signal **transmission properties** of a ToF based endoscope and are thus able to draw valid conclusions on **an achievable measurement uncertainty less than 2mm**.

1 Introduction

The field of NOTES interventions [1] has again brought an issue into the focus of interest, which has already been investigated in the context of minimally invasive surgery for **a long time**: The acquisition of real-time three-dimensional information of the operation area via an endoscope optic which is an integral part of the operation room of the future [2]. Recent approaches mainly focused

¹Chair of Pattern Recognition, University Erlangen-Nuremberg, {penne,stuerm} @informatik.uni-erlangen.de

²MITI Research Group, Klinikum rechts der Isar, Munich, {dirk.wilhelm,hubertus.feussner} @mitigroup.de

on the extraction of three-dimensional information from a calibrated endoscope optic and a sequence of acquired images from a rigid operation area [4, 5]. Inherently, these approaches are not real-time capable. Other approaches projected patterns or structured light into the operation area [6]. Although, real-time constraints could be met by these techniques, the utilized modifications of the endoscope optic were too costly to make the approaches usable. The major contribution of our novel approach is utilization of a real-time capable sensor system with the ability to derive three-dimensional information of the operation area at constant lateral resolution. The utilized ToF sensor [3] computes the distance of the observed scene in every pixel by measuring the flight time of an actively emitted modulated optical light signal via the phase shift of the emitted and reflected signal. Such ToF sensors are also available as integrated parts of camera systems. Additionally, ToF sensors do not only provide distance information for every pixel, but also intensity information: As the intensity relates to the amplitude of the reflected modulated signal these intensity values are referred to as amplitude values.

By mounting a ToF sensor at the end of the endoscope optic and transmitting the oblique modulated optical light signal via the available optical fibers, the ToF measurement principle can be realized via an endoscope optic. The available data is the same as is available for ToF camera systems: Distance information, from which 3D coordinates can be easily computed, and amplitude values for every pixel.

Nevertheless, the two-dimensional color information provided by standard endoscope systems is of utmost importance for NOTES interventions and also for minimally invasive interventions in general. Thus, the proposed approach of only attaching a ToF sensor to the endoscope optic will hardly be accepted for use during NOTES interventions. This problem can be solved by additionally attaching an optical beam-divider, which projects the incoming optical signal onto a standard CCD sensor, which provides the color information, and onto a ToF sensor, which provides the 3D information. Having such a camera system calibrated using standard approaches [7] the 3D points can be virtually re-projected onto CCD sensor and a colored overlay of the 3D points can be provided. A scheme of this enhanced endoscope optic is given in Figure 1.

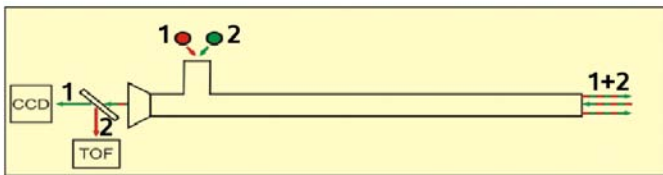


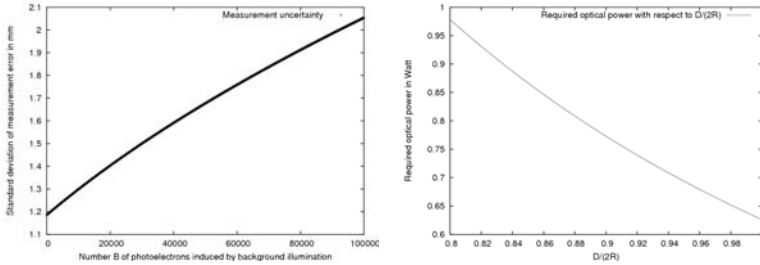
Figure 1: Scheme of the ToF based endoscope: Modulated light (1) and standard illumination (2) are simultaneously transferred in to the operation area (1+2). After being reflected the standard illumination light is projected onto a CCD sensor; the modulated light is projected onto a ToF sensor.

2 Modeling an appropriate ToF based endoscope

The measurement uncertainty of a ToF sensor can be modeled by [3]

$$\sigma = \frac{c}{2\sqrt{8}f} \cdot \frac{1}{M} \cdot \sqrt{B + \frac{M}{2}}, \quad (1)$$

where σ is the standard deviation of the range error, f is the modulation frequency, c is the speed of light, M is the number of photoelectrons generated by the modulated light signal and B is the number of photoelectrons generated by background light. Using $f = 100 \text{ MHz}$ and $M = 100000$ the achievable measurement uncertainty σ was computed for varying values of B . Figure 2(a) shows the results. It can be observed that a measurement uncertainty of 2 mm



(a) Measuring uncertainty σ in mm with respect to background illumination B . (b) Required optical power of illumination source with respect to $\frac{D}{2R}$ in the range of 0.8...1.0.

Figure 2: Measuring uncertainty and required optical illumination power.

can well be achieved even in the presence of as much background photoelectrons $B = 100000$ as signal photoelectrons $M = 100000$. This leads to two conclusions:

1. The light source used for the ToF endoscope has to be modulated with 100 MHz.
2. The generated light signal must generate approximately 100000 photoelectrons on the ToF sensor

In the following we want to discuss the second question in detail.

3 Conclusions for the hardware setup and achievable measurement uncertainty

The modulated light signal is emitted with an optical power P . During its way towards the object and back to the ToF sensor it is attenuated like every electromagnetic wave with respect to the traveled distance, which we call R (the distance of the observed object). Some amount of the light is absorbed by the object: This effect is modeled by the remission $\phi \in [0..1]$ of the object. The signal receiving unit (lens and ToF sensor) is modeled by the aperture D of the lens, the area A_S of the ToF sensor, the area A_P of one pixel on the ToF sensor, and the quantum efficiency $q(\lambda)$, which again relies on the utilized base wavelength λ . Finally, the factor $k \in [0..1]$ models attenuation effects introduced by utilized lenses and the parameter T models the integration time during which the measurement is accomplished. Briefly, this models how much of the incoming optical power is projected onto each pixel and how many photoelectrons N_e are generated in each pixel.

As $N_e = 100000$ have to be generated, conservative values are chosen for the other parameters of the model:

- $\phi = 0.8$, i.e. the observed object is not too absorbing; due to the fact that tissue in the operation area is relatively glossy, this assumption can be considered valid.
- $k = 0.3$, i.e. the utilized lenses attenuate the incoming signal strongly; this is valid as the optical lens system of an endoscope optic consists of many lenses and not only one single lens.
- $\lambda = 850nm$, i.e. the near infrared range is used; this is a valid choice for the wavelength as higher wavelengths are more likely to induce heat damages.
- $q(\lambda) = 0.9$, i.e. only a fraction of the incoming photons generate an electron.
- $T = 10ms$, i.e. the integration time is chosen small enough to enable real-time usage and take into account some time necessary for post-processing of the acquired data.
- The ratio $\frac{D}{2R}$ describes the ratio of lense aperture and object distance. This term is considered as a degree of freedom in the following discussion.

For the chosen parameter values, the necessary optical power P was computed with respect to the ratio $\frac{D}{2R}$, i.e. lense size vs. object distance. Thus, a value of $\frac{D}{2R} = 0.5$ means that the object is as far away as the size of the lens is. But this is only valid under the assumption that the object is a Lambert reflector and was practically validated with ToF cameras only for observable distances

in the range of several meters. Both assumptions are likely to be not fulfilled for endoscopic ToF data acquisition. Thus, we concentrate on the range of [0.8..1.0] for the ratio $\frac{D}{2R}$. The formula used for the computation of the necessary optical power is [3]:

$$P = \frac{N_e \cdot \frac{A_s}{A_p} \cdot h \cdot c}{\phi \cdot \left(\frac{D}{2R}\right)^2 \cdot k \cdot q(\lambda) \cdot \lambda \cdot T}. \quad (2)$$

The results are shown in Figure 2(b). It can be observed that a measurement uncertainty of 2mm can be reached under valid assumptions with an optical illumination power of approx. 1W, which is modulated with 100MHz.

4 Conclusion and future research

The previous discussion has determined the physical requirements for achieving a measuring uncertainty which initially makes the ToF based endoscope feasible for NOTES interventions and minimally invasive procedures. Future research will have to focus in the appropriate design and implementation of the illumination unit and once this is successfully accomplished on appropriate processing routines to provide threedimensional intraoperative navigation assistance and collision control.

References

- [1] D. Rattner and A. Kalloo and the SAGES/ASGE Working Group on NOTES. ASGE/SAGES Working Group on Natural Orifice Transluminal Endoscopic Surgery. *Surgical Endoscopy*, 20(2):329–333, February 2006.
- [2] H. Feußner. The operating room of the future – A view from Europe. *Seminars in Laparoscopic surgery*, 10:3:149–156, 2003.
- [3] R. Lange and P. Seitz. Solid-state time-of-flight range camera. *Quantum Electronics, IEEE Journal of*, 37(3):390–397, March 2001.
- [4] T. Thormählen, H. Broszio, and P. N. Meier. Automatische 3D-Rekonstruktion aus endoskopischen Bildfolgen. In *Bildverarbeitung für die Medizin*, pages 207–210, March 2002.
- [5] F. Vogt, S. Krüger, M. Winter, H. Niemann, W. Hohenberger, G. Greiner, and C. Schick. Erweiterte Realität und 3-D Visualisierung für minimal-invasive Operationen durch Einsatz eines optischen Trackingsystems. In H. Meinzer, H. Handels, A. Horsch, and T. Tolxdorff, editors, *Proceedings Bildverarbeitung für die Medizin*, pages 217–221, Berlin, March 2005. Springer.
- [6] D. Yelin, W. M. White, J. T. Motz, S. H. Yun, B. E. Bouma, and G. J. Tearney. Spectral-domain spectrally-encoded endoscopy. *Optics Express*, 15:2432–2444, March 2007.
- [7] Z. Zhang. Flexible Camera Calibration by Viewing a Plane from Unknown Orientations. In *Proceedings of the International Conference on Computer Vision*, pages 666 – 673, September 1999. Corfu, Greece.

**Aortic Aneurysm Therapy: EndoVascular Aortic Repair (EVAR)
What do we know and what should we know?**

R.Ghotbi, A. Sotiriou

Klinikum Munich-Pasing, e-mail: reza.ghotbi@gefaesschirurgie-pasing.de

Abdominal Aortic Aneurysm has been described as the "silent killer". 8-10% of the over 60 year old population has an AAA, more than 10000 Operations on the Abdominal Aorta are performed in Germany per year. 40% of which are emergency-cases with a high mortality rate.

Aneurysms develop in the degenerated aorta. Atherosclerosis is the most common cause for degeneration of the wall. Genetic components have been identified with a clear familiar occurrence with a risk of about 25% for first-degree relatives.

The aneurismal pathology is characterized by a chronic inflammation with destruction of the extracellular matrix, remodelling of the wall and reduction of smooth muscle cells. That led to changes in the tension of the aortic wall as well as reduced tensile strength, and finally the rupture of the aortic wall.

The standard therapy for years has been the open surgical repair with resection the AAA and interposition of a tube graft. It is a durable procedure, with high morbidity.

For the surgery, patients should have adequate cardiac and pulmonary condition. The Operation time is long and an extended hospital stay and a long period of recovery is needed.

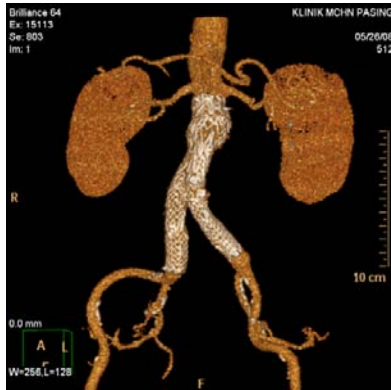
In the last decade the minimally invasive Stent Graft Implantation has revolutionized the treatment of AAA. EVAR has been greatly successful for certain patients with certain anatomy; it is the most important endovascular advance, safe and effective but far from perfect.

The diagnostics, operative planning and the performance of the surgery are more a matter of the quality of the available imaging than the surgical skills in a classic sense. Often combination of ultrasound, CTA, MRA and intraoperative fluoroscopy is indispensable. Since each of these imaging tools only provide partial information. Possible complications might result in malposition, endoleak, migration and enlargement of the aneurysm sac. Depending on the result of the surgery the same imaging techniques are necessary for the follow up.

The complications can occur because of unpredictable circumstances such as retrograde perfusion above lumbalarteries, mesenteric inferior artery or sever oxidative activity in the aortic wall.

The difference in the vessel-geometry still demands the use of various stent devices of different material and structure. The choice of a certain sort of device is based on the individual assessment of the surgeon.

The essential tasks for the future are to simplify the planning, improve the devices as well as minimizing unpredictable issues.



Current status of lymph node mapping in GI-cancer patients and future perspectives: towards application of a miniaturized beta-probe?

M. Burian¹, M.E. Martignoni¹, D. Wilhelm¹, H. Feussner¹, H. Friess

¹Technische Universität München, Chirurgische Klinik und Poliklinik, Klinikum rechts der Isar, Munich, Germany

The goal of oncologic surgery is to resect as much Tissue as is needed to remove the complete tumor, but to leave as much tissue possible in its origin place. The frequent occurrence of lymph node metastasis in GI-Tumors makes this effort quite difficult and therefore new and improved techniques are required to improve the detection and visualization of lymph metastasis to a surgeon during the operation. One solution to this problem may be the sentinel lymph-node visualization by submucosal technetium injection during resection for gastric cancer. Nevertheless, the limitations of this technique are the endoscopist and varying detection of the gamma-probe with orientation. Therefore, we develop a beta-probe that may only detect lymph nodes with high metabolism and could be given intravenously.

1. Introduction

Cancer surgery for GI malignancies normally requires resection of the primary tumor site with free resection margins, including an appropriate lymph node dissection, to remove potential lymph node metastasis. However, there is an ongoing discussion whether to perform an extended lymph node dissection or to adjust the extend of lymph node dissection to the tumor stage. Though extended dissection offers potential benefits concerning tumor free survival, it is combined with a higher postoperative morbidity and even after several RCTs it is not clear if this survival benefit justifies the higher morbidity.

If an adjusted lymph node dissection would be performed, one has to guarantee, that the lymphatic drainage of the tumor site is respected and removed. Therefore, the sentinel lymph node principle was introduced, which detects the area of lymphatic drainage. With this technique a surgical over treatment can be avoided and the risk of violation of oncologic principles is lowered.

2. Conclusion

Though most articles in this field of investigation describe sentinel lymph node mapping as highly reliable and sensitive, the technique still has its limitations. Due to the need of submucosal injection of the radioactive pharmaceutical technetium, which is highly depending on the experience of the applying endoscopist. Furthermore the intense of detection of the radioactive agent varies with the orientation of the detecting gamma-probe, its distance to the tissue and the accurateness of the surgeon.

Therefore, a marker which can be applied peripherally via a venous catheter, which accumulates at the tumour site and its area of lymphatic drainage would be of highest interest. FDG, radioactively marked glucose is a well known pharmaceutical which almost perfectly would fit for these needs and which is mainly metabolized in tissue of high cell activity, such as GI-tumours. Therefore, the drug is gaining increasing importance in tumour staging procedures and medical imaging. Actually it is typically detected by computertomograph-like devices with a gantry, but there is also a new developed miniaturized hand-held probe available, to detect the released beta radiation. With this probe an intraoperative mapping of the primary tumour site and its potential metastasis is getting possible.

Again the guidance of the probe itself represents an origin of inaccuracy. Using current optical or electromagnetic navigation devices and/or specific robotic arms, we intend to compensate the disadvantages of the beta probe. The direct detection of radiation also reduces the typical background noise, which normally decreases the resolution of positron emission tomography resulting in a next generation biologic imaging technique. Additionally, FDG guided surgery may omit frozen sections, as it only accumulates in lymph nodes with increased metabolism like lymph node metastasis.

Design and development of axial blood pump for implantable assist circulation system

D.V. Vashurkin, G.I. Itkin, E.V. Konisheva, O.V. Romanov

*Research Institute of Transplantology and Artificial Organs
e-mail: georgeitkin@mail.ru*

Mortality of patients from cardiovascular diseases is foremost at present in all developed countries. Only in Russia and the USA, about 2 500 000 persons die annually due to cardiac diseases.

Heart transplantation is the most effective method of treatment for patients in the terminal cardiac failure. About 2 000 heart transplant operations are performed in the USA per year, whereas the demand makes approximately 20 000. In Russia the transplantation requirement makes nearby 10 000 - 12 000 a year. With such number of patients, methods of mechanical cardiac performance support with application of assist circulation systems (ACS) are the only alternative to transplantation.

The real breakthrough in the field of mechanical systems for cardiac function support has been made in the world practice for the last few years. There were a considerable number of ACS, both extracorporeal and implantable using various types of blood pumps: pulsating and continuous flow. Clinical introduction of implantable systems thanks to which patients can get back to active life outside a hospital is being dynamically developing. Among these systems, considerable proportion has fallen on implantable rotary blood pumps over the last years that are owing to a number of their advantages towards pulsating systems (reduction of the mass/size characteristics and power consumption).

However, in spite of the fact that developments have been conducted almost in all developed countries and appreciable financial resources have invested in these works, for today neither of the systems meets the requirements to safe and reliable long-term operation to the full extent.

Research works in the field of development and making implantable assist circulation systems have been performed in the Research Institute of Transplantology and Artificial Organs in the last 3 years.

The performed analysis of developments available in the world made possible to define the basic trends and directions in development of implantable assist circulation systems. Existing own experience in development and making extracorporeal and implantable centrifugal blood pumps enabled to choose objectively the optimum direction for the

researches based on designing of implantable axial pump system with built-in motor (Fig. 1).

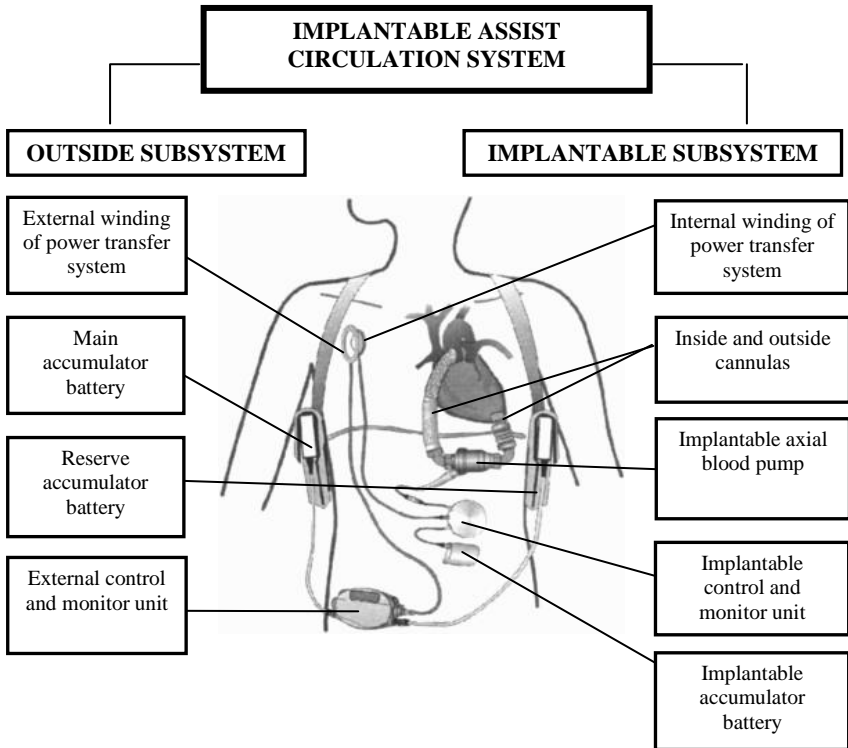


Fig. 1. Assist circulation system.

The basic problems of designing such system are minimization of blood trauma caused by the pump and thrombosis probability. After carrying out of the analysis of the principal causes leading to blood trauma, three basic groups were distinguished: mechanical, biological and hydrodynamic. These groups define set of the criteria to determine characteristics of pumping part of the system being designed. Difficulty in criteria definition is that frequently it is impossible to estimate unequivocally impact of various designs.

Therefore, to search for optimal solutions, system analysis was performed for all working elements of axial blood pumps construction designs existing for today on the basis of the distinguished quality criteria. Since full and trustworthy information is not available for many parameters of the chosen construction designs, the performed analysis is based on expert comparative estimations.

As a result of the research has been carried out, best working elements of the selected construction designs were chosen and structure of axial blood pump design was generated.

On the basis of the classical calculating theory of pump units, geometrical parameters of impeller were obtained. It has been proven, that classical calculating methods are impossible to be used for parameterization of small-type low-flow as these methods do not allow to evaluate many important parameters of the pump, such as flow pattern in blade channels, presence or absence of stagnation zones and considerable shear stresses which are to be the key ones for a blood pump. Besides, classical calculating methods do not consider parietal adhesion conditions, blood viscosity value, conditions of turbulence and other parameters.

To study blood flow pattern in blade channels of the blood pump as well as to estimate and generate optimum geometry for impeller blades, carrying out of integrated mathematical simulation of flow processes inside the working elements of an axial pump being designed is required. It can be implemented only using up-to-date computer methods of computational fluid dynamics, so-called, CFD-methods which general algorithm is shown in Fig.2.

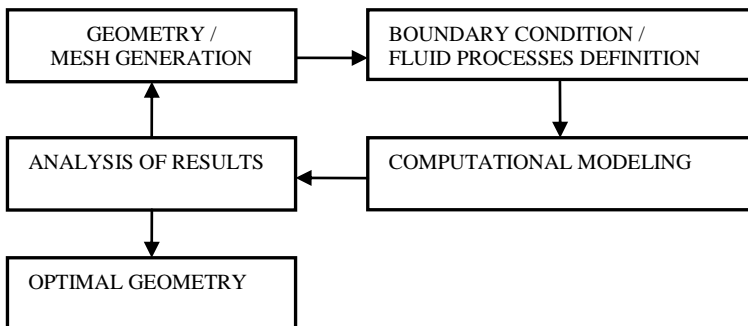


Fig. 2. Computational fluid dynamic algorithm.

Optimum geometry of the impeller bush was defined through simulation by least pressure losses criterion. Losses were estimated by the difference of average integrated values of full pressure to have been defined in the planes located before and after the entrance bush of the impeller.

Three-dimensional solid-state model of the impeller was designed in computer engineering software systems. The constructed impeller model underlay the blood flow model in blade channels. Integrated simulation of blood flow physical processes was performed on the basis of the built model resulting in the best geometrical parameters for working elements of axial pump construction design.

As a result of all implemented studies, model prototypes and designs of pre-production models of axial blood pump for hydrodynamic tests to be carried out were made. One of pre-production models is shown in Fig. 3.

The flow-head characteristics which were taken out at specially developed hydrodynamic stand proved full conformity to medical-technical requirements. In particular, the control working point corresponding to the flow of 5 l/min at the counterpressure of 100 mm hg was obtained at the rotor speed of 7500 rpm.



Fig. 3. Axial blood pump prototype.

For today, the pre-production model design which characteristics are approached to final appearance of the product as much as possible has been developed and built. Possibility of full or partial disassembling of the pump for control of internal surfaces after durability tests was provided. Versions of the most critical parts of the pump – sleeve bearings were computed and developed. DC non-contact motor with rotor built in impeller of the pump

was developed. In the near future after manufacturing of the pre-production model from biocompatible materials, the basic bench tests for hemolysis and thrombosis will be performed.

Obtained results of the performed work for making ACS hold out a hope of that the resulted construction design will not only meet all the medical-technical requirements but be also the initial step on the way to making the first domestic implantable assist circulation system of non pulsating type which could be recommended for clinical application in the coming years after bench and experimental studies.

Mathematical model of human cardiovascular system for implantable rotor blood pump research

K. Dozorov¹, G. Itkin², D. Surkov³

¹ *Moscow aviation institute, e-mail: kndozorov@mail.ru*

² *Research Institute of Transplantology and Artificial Organs*

³ *Moscow aviation institute, e-mail: ddd125@mail.ru*

Many people all over the world suffer of heart diseases. Some of them need heart transplant, but heart donors are rear and can cover less than 10% of suffers. One of the possible ways to help them is to use artificial organs, ventricular assistive devices. To develop and test them without risk for living beings, especially at first implementation stages, is preferable to use mathematical or physical models of device and its environment. In this paper we introduce mathematical model of human cardiovascular system. Presented model is used to research control algorithms for left ventricular assist device based on rotary pump.

Modeling

The model of cardiovascular system has following assumptions [1, 2]:

- Most physical parameters of the model are linear and lumped;
- Blood is Newtonian fluid;
- All blood vessels combined into general reservoirs (arterial, venous and capillary);
- The heart valves open and close instantaneously, and hence there is no backflow.

The proposed mathematical model consists of 6 main interconnected blocks: 1-chamber heart (as left ventricle), general arterial reservoir, general capillary reservoir, general venous reservoir, oxygen metabolism and neural control [3]. There is also human individual parameters block and rotor blood pump block.

The common model structure is shown on Fig. 1.

Each block of the model may be subdivided into control, resistive and non-resistive. Control blocks are human individual parameters block, oxygen metabolism and neural control. They are used to change parameters of all other blocks and they do not describe heart or vessels themselves. Resistive blocks are heart and capillary reservoir, and non-resistive blocks are arterial and venous reservoirs.

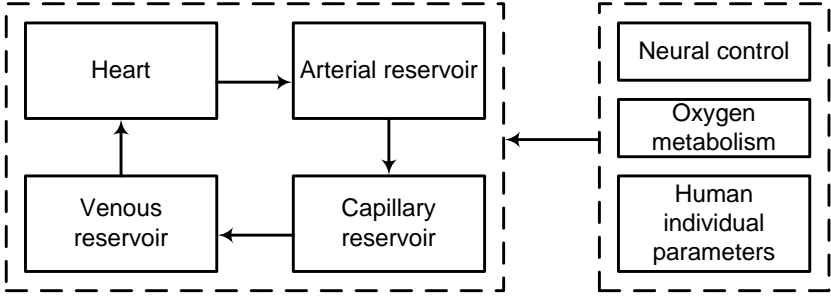


Figure 1. Structure of cardiovascular model

Resistive blocks are characterized by inlet and outlet resistance, stiffness, initial volume and tensionless volume. Non-resistive blocks are characterized by stiffness, initial volume and tensionless volume.

Non-resistive blocks have input parameters as flows (into and out of the block) and output parameters as pressure in the block. The general equations for non-resistive blocks are the following:

$$\dot{V}_i = F_{i_IN} - F_{i_OUT} \qquad P_i = (V_i - V_{i_tl})G_i$$

Resistive blocks have input parameters as pressures (at the ends of the corresponding vessel) and output parameters as flows. The general equations for resistive blocks are the following:

$$F_{i_IN} = \frac{P_{i-1} - P_i}{R_{i_IN}} \qquad F_{i_OUT} = \frac{P_i - P_{i+1}}{R_{i_OUT}}$$

$$\dot{V}_i = F_{i_IN} - F_{i_OUT} \qquad P_i = (V_i - V_{i_tl})G_i$$

Where F_{i_IN} – blood flow into the i-th block,

F_{i_OUT} – blood flow out of the i-th block,

V_i – volume of the i-th block;

V_{i_tl} – tensionless volume of the i-th block;

P_i – pressure in the i-th block;

G_i – stiffness of the i-th block;

R_{i_IN} – inlet resistance of the i-th block;

R_{i_OUT} – outlet resistance of the i-th block.

Human individual parameters include weight [kg], height [cm], sex [M or F] and relative blood volume [ml/kg], which allow computing Body Surface Area, Total Blood Volume and Oxygen Consumption.

Oxygen metabolism block has inputs as relative oxygen consumption (according to physical activity) and volumetric blood flow, and output as oxygen debt.

Neural control regulates heart activity (heart rate and stroke volume) and vascular tone (peripheral resistance, vessels stiffness). Output of the neural control block is neuro-humoral factor (γ). Heart rate depends on neuro-humoral factor:

$$HR = 60\gamma$$

Stiffness of arterial, venous and capillary blocks are linear to neuro-humoral factor:

$$G_i = A_i + K_i\gamma$$

Where G_i – stiffness; A_i , K_i – constants; γ - neuro-humoral factor.

Peripheral conductance (reciprocal value of resistance) depends on neuro-humoral factor and oxygen debt:

$$Y_i = Y_{i0} + K_{iDO2}DO2 - K_{i\gamma}\gamma$$

Where Y_i - peripheral conductance;

Y_{i0} , K_{iDO2} , $K_{i\gamma}$ – constants; $DO2$ – oxygen debt; γ - neuro-humoral factor.

Heart stiffness is non-linear and described by “double Hill” function [4]:

$$G_{LV}(t) = G_n(t_n)(G_{\max} - G_{\min}) + G_{\min}$$

Where G_{\max} , G_{\min} – constants, related to end-systolic and end-diastolic stiffness;

t_n – time within heart beat period:

$$t_n = \frac{t}{K_{HR}T_{HR}}$$

K_{HR} – constant;

$G_n(t_n)$ is normalized “double Hill” function:

$$G_n(t_n) = 1.55 \left[\frac{\left(\frac{t_n}{0.7}\right)^{1.9}}{1 + \left(\frac{t_n}{0.7}\right)^{1.9}} \right] \left[\frac{1}{1 + \left(\frac{t_n}{1.17}\right)^{21.9}} \right]$$

Model of rotor blood pump has two input parameters: differential pressure between aorta and heart, and rotor speed of brushless DC motor that drives the pump. Output parameter of blood pump model is flow rate.

$$F_{PUMP} = K_{\omega 1} \omega + \sqrt{K_{\omega 2} \omega^2 + K_p \Delta P}$$

Where $K_{\omega 1}$, $K_{\omega 2}$, K_p – experimental constants; ω - velocity of pump impeller; ΔP - differential pressure.

Modeling results

Normal heart

Four conditions were simulated: rest, light exercise, medium exercise and heavy exercise. Those conditions were simulated by changing oxygen consumption (see Table 1). Simulation results are shown on Fig. 2-5.

Table 1. Simulated conditions

Condition	Oxygen consumption, mlO ₂ /min/m ²
Rest	140
Light exercise	400
Medium exercise	1200
Heavy exercise	2000

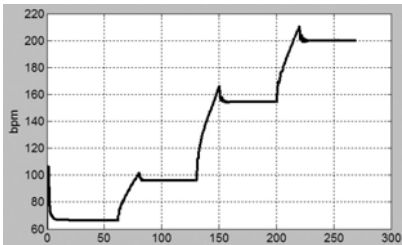


Figure 2. Heart rate

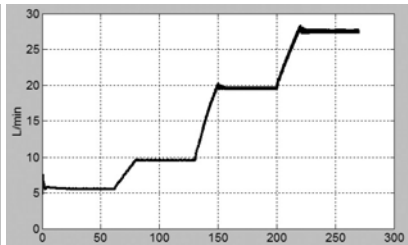


Figure 3. Blood flow

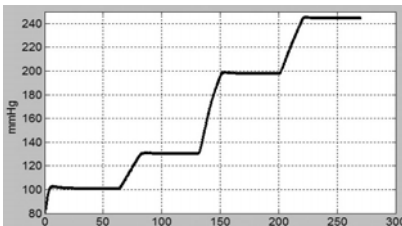


Figure 4. Mean aortic pressure

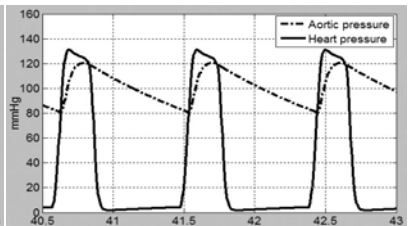


Figure 5. Aortic and heart pressure

Failed heart

Simulation with failed heart were conducted at state of rest (oxygen consumption = 140 mlO₂/min/m²) by limitation of heart wall stiffness. Maximum value of stiffness $G_{max} = 1$ mmHg/ml, minimum value $G_{min} = 0.07$ mmHg/ml. Results are shown on Fig. 6.

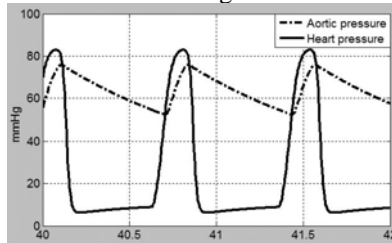


Figure 6. Aortic and heart pressure

Conclusions

Proposed mathematical model of cardiovascular system gives possibility to conduct more accurate calculations of desired processes and states. Researcher can tune this model so its processes get close enough to ones of human (in according to entered values of weight, height, mass and sex). Model includes neural control and oxygen metabolism blocks which provide to vary some parameters (heart rate, stiffness, resistance).

References

1. G.A. Giridharan, M. Skliar, D.B. Olsen, and G.M. Pantalos. Modeling and Control of a Brushless DC Axial Flow Ventricular Assist Device. // *Asaio J*, vol. 48, (3): 272-89, 2002;
2. J. McLeod. PHYSBE – a physiological simulation benchmark experiment. // *Simulation*, 1966;
3. D.A. Surkov. Research and develop of models, algorithms and hardware-and-software for measure-control solution of biotech system (by example of left ventricular assist devices). Ph.D. thesis. 2006;
4. N. Stergiopoulos et al. Determinants of stroke volume and systolic and diastolic aortic pressure. // *Am. J. Physiol. Heart Circ. Physiol.* 270, p. H2050.

Hemodialysis with using biological regeneration of dialysis fluid

N.A. Bazaev, V.M. Grinvald, V.L. Eventov^{*}, S.V. Selishchev

*Moscow State Institute of Electronic Technology (Technical University),
e-mail: sersel@miee.ru*

^{}Russian Scientific Surgical Center, Moscow*

Biodialysis (hemodialysis) was developed as a method for life support in patients waiting for liver transplantation. Chronic hemodialysis is also used in patients with terminal uremia waiting for kidney transplantation. The many attempts to develop artificial liver have not been so far successful. Methods based on blood pertusion through containers filled with liver tissue pieces or liver cells, as well as the use of special absorbents and anion exchangers, also proved ineffective. The properties of artificial liver were nearly implemented in the Mars system. In this system the patient's blood is brought in contact with recirculating albumin solution through a special mass exchanger. This provides diffusion of protein-bound water-soluble substances from the blood to the solution. In the recirculation contour, albumin is regenerated in an artificial kidney hemodialysis system and two columns filled with charcoal and anion exchanger. The high cost of disposable units (\$3000) and insufficient efficiency of elimination of protein-bound toxins are the main disadvantages of this system.

The principle of the biodialysis (BD) system considered in this work is that a healthy subject through a system of mass-exchangers exerts a healing effect on the patient. Blood of the healthy subject and patient is perfused through individual mass exchangers (dialyzers, hemodiafilters, hemofilters, etc.) connected hydraulically with recirculation fluid (0.9% sodium chloride, blood substitutes, ultrafiltrate, albumins, etc.). Metabolites accumulated in the patient's blood diffuse along the concentration gradient to the transport medium and then to the blood of the healthy subject, where they are metabolized. Similarly, metabolites synthesized in healthy subject diffuse along their concentration gradients to the transport medium and then to the blood of the patient.

The BD method and design of the corresponding system are protected by a Russian Federation patent.

Our survey of biodialysis efficacy revealed that hemodialysis provided necessary life support in patients with hepatic insufficiency waiting for liver

transplantation, patients with transplant failure, and in small children intolerant to conventional hemodialysis.

This work was performed in two stages.

At stage I we studied model systems of double mass transport *in vitro*. At stage II we studied the efficacy of the BD method in treatment of experimental animals with hepatic or renal insufficiency.

Transport of urea and potassium ions between two model organisms was studied in the first series of model experiments *in vitro*. One organ was simulated by 10 liters of 0.9% sodium chloride solution containing 32 mM urea; the other organ, by 10 liters of 0.9% sodium chloride solution containing 17 mM potassium. The transport medium contained 300 ml of 0.9% sodium chloride solution. The flow rate of model solutions and transport medium was 250 and 500 ml/min, respectively. An IDEMSA 25 H dialyzer was used.

Concentrations of potassium and urea in the model organs were equalized within 1 h 15 min and 2 h, respectively. Thus, the model experiments demonstrated that this system mediated transfer of substances from one model organ to another.

Recirculation of 3 liters of plasma was studied in the second series of model experiments *in vitro*. The plasma was obtained by plasmapheresis in a patient with mechanical hepatitis. It contained 420 μM total bilirubin and 106 μM direct bilirubin. The healthy organism was simulated using 3 liters of healthy human plasma containing 15 μM total bilirubin and 2.1 μM direct bilirubin. Three hundred milliliters of healthy human plasma containing 11 μM total bilirubin and 1.9 μM direct bilirubin was used as recirculating transport medium. The model solution flow rate was 250 ml/min; transport medium recirculation rate, 500 ml/min. Fresenius F-80 hemodiafilters were used in the experiment.

Within 2 h of experiment concentration of total and direct bilirubin in the "ill" organism declined to 186 μM (by 56%) and 82 μM (by 23%), respectively. Within the same period the concentration of total and direct bilirubin in the "healthy" organism increased to 180 μM (12-fold) and 56 μM (26-fold), respectively. Within 2 h of experiment the concentration of total and direct bilirubin in the transport medium increased to 132 μM (12-fold) and 68 μM (36-fold), respectively.

Thus, it was demonstrated that clinically significant amounts of water-soluble protein-bound substances were transported through two membranes of the mass exchanger and transport medium. This provided a methodological basis for further tests in experimental animals *in vivo*.

Experiments were performed in pigs because blood perfusion in this case did not cause erythrocyte degradation.

Two pigs of the *large white* breed (40.5 and 68 kg) were used. The two pigs were catheterized in the jugular vein. The "ill" animal was subjected to bilateral nephrectomy (a model of renal insufficiency). The first 8-h BD session was performed 29 h after nephrectomy using a Frezenius F-5 dialyzer. The blood flow rates in the healthy and ill animal were 120-140 and 130-140 ml/min, respectively. The flow rate of recirculation fluid (0.9% sodium chloride solution) was 230-250 ml/min. The second 11-h BD session was performed 51 h after nephrectomy. The blood flow rates in the healthy and ill animal were 150-175 and 180-200 ml/min, respectively. The flow rate of recirculation solution was 230-250 ml/min. The third 6-h BD session was performed 77 h after nephrectomy. The blood flow rates in healthy and ill animal were 220-240 and 230-250 ml/min, respectively. The flow rate of recirculation fluid during this session was increased from 250 to 600 ml/min. The fourth 10-h BD session was performed 100 h after nephrectomy. The blood flow rates in healthy and ill animal were 240-260 and 250-270 ml/min, respectively. The flow rate of recirculation fluid was 600 ml/min. From results of experiments follows, that in the ill pig the concentrations of urea, creatinine, and potassium decreased during BD and increased during the interval between dialysis sessions. In contrast to that, in the healthy pig the concentrations of urea, creatinine, and potassium were increased during BD and brought to a normal level during the interval between dialysis sessions. The two animals easily tolerated the BD sessions.

We calculated the percentage of clearance of ill animal blood from urea, creatinine, and potassium during BD sessions by the following formula:

$$\text{Percentage of clearance} = 100\% \cdot (C_1 - C_2) / C_1,$$

where C_1 and C_2 are the concentrations of the parameter of interest in animal blood before and after BD session, respectively. The results of calculation are given in Table 1.

TABLE 1. Percentage of Clearance of Ill Animal Blood from Urea, Creatinine. and Potassium during BD Sessions

BD session	Urea	Creatinine	Potassium
1st	50.0	43.9	27.6
2nd	40.2	40.0	24.1
3rd	41.9	41.1	18.2

Calculations showed that BD could be used in clinical practice to purify blood from uremic metabolites, though with lower efficacy than conventional hemodialysis. The weight of the experimental animals was changed during the BD sessions by regulating blood pressure in the extracorporeal contour of the dialyzer.

To study the transport BD function from healthy to ill animal, 20% glucose solution was infused to the healthy pig up to concentration 17.1 mM, and glucose concentration in blood of ill pig was followed. Glucose concentrations in the blood of the healthy and ill pigs were brought to an equilibrium level (11.4 mM) within 16 min.

Two pigs of the *large white* breed (60 kg, healthy; and 35 kg, ill) were used in the second series of experiments. The two pigs were catheterized in the jugular vein. The ill animal was subjected to bile duct ligation (model of mechanical hepatitis). The first BD session was performed 3 h after imposition of the ligation using AN 69 ST hemodiafilters. The blood flow rates in the healthy and ill animal were 150 and 130 ml/min, respectively. The flow rate of recirculation transport medium (16% albumin solution) was 500 ml/min.

Two BD sessions were carried out (16 and 14 h with 20-h interval between them). The percentage of total and direct bilirubin elimination from the ill pig blood during session 1 was 12 and 10, respectively; during session 2, 10 and 8, respectively. The concentration of total bilirubin in the transport medium increased from 0 to 68 μM .

In contrast to the Mars system, BD efficacy does not decline with time, and a BD procedure can be continued until the required effect is obtained.

In the next series of experiments we studied between-species BD compatibility. In these tests various mammal species can be used as the healthy organism. In the first experiments hemofiltrate of human blood of patients with chronic renal insufficiency was injected to the peritoneal cavity of rats and blood of rabbits.

Sexually mature rats (weight, 140-160 g) for 24 days were subjected to daily intraperitoneal injections of 4 ml of hemofiltrate of human blood of patients with chronic uremia. Control animals received saline. General view, state of fur cover, and behavioral reactions of experimental rats were indistinguishable from control. The weight of the rats did not change as a result of intraperitoneal injection of hemofiltrate.

The state of the central nervous system of rats was assessed by motor activity using an Ugo Basile cage (Italy). Each rat was tested for 3 min. The results of the tests showed that motor activity and behavioral reactions of

experimental rats did not change as a result of intraperitoneal injection of hemo-filtrate. Parameters of peripheral blood count in experimental rats were indistinguishable from those in the control group.

After tests experimental and control rats were sacrificed and the weights of internal organs were measured and these organs and tissues were examined for pathological changes. Morphometric analysis revealed no pathological changes in heart, liver, spleen, and pancreas. It also showed that weight coefficient of these organs and tissues did not change after 24 days of intraperitoneal injection of hemofiltrate. Therefore, *post mortem* examination of rats receiving intraperitoneal injection of hemofiltrate revealed no difference from control animals.

Rabbits (weight, 2.9-3.4 kg) for 28 days were subjected to daily intravenous infusion of 29-34 ml of hemofiltrate of human blood of patients with chronic uremia. Control animals received a similar amount of 0.9% sodium chloride solution. Blood parameters, body weight, and body temperature were monitored. There was no significant difference between these values in control and experimental animals.

Thus, injection of foreign hemofiltrate obtained from patients with chronic renal insufficiency to rats and rabbits had no effect on the state of health of the experimental animals. This provides a basis for interspecies BD, which is planned to be performed between pig and sheep.

BD safety for patients is based on two membranes of mass exchangers separating blood from transport medium and on bacterial safety of transport medium, which was tested in special tests.

The results of our experiments were reported at the Committee for Ethics, Russian Scientific Surgical Center, Russian Academy of Medical Sciences, Moscow, headed by Academician B. V. Petrovsky (03.06.03). The Committee adopted clinical use of the BD method in certain classes of patients: first, for reperfusion of albumin dialyzate without regeneration and second, in the ill child–mother system.

Thus, in our opinion, the BD method suggested in this work can be used in clinics for normalization of certain parameters in patients with hepatic and renal insufficiency. Remarkably, BD can also mediate transport of certain substances from the healthy to ill organism (potassium, sodium, calcium, ammonium, vitamins, microelements, carbonate, amino acids, glucose, catecholamines, histamine), providing thereby a promising opportunity for treating a number of diseases. The XX1st century will be an epoch of biotechnology, and BD is expected to play a significant role in modern medicine.

New approaches to development of means for respiration by multicomponent gas mixtures

Sudarev A.M., Isaev I.A.***, Kantor P.S.,
Korotich E.V.***, Dvornikov M.V.***, Buhtiyarov I.V.****

**Institute of a radio engineering and electronics of RAS, ** CONSTEL ltd.,
*** State Institute of military medicine MD RF
e-mail: sudarev@constel.ru*

In modern medicine the methods using artificial respiratory gas mixtures play the appreciable role. These mixtures are formed for creation hypoxia, hyperoxia, hypercapnia conditions etc.

The interval hypoxia training method for correction of a functional condition, increasing of physiological reserves and stress-stability to extreme influences is most often used in a clinical practice. It is used also as non-medication mean at treatment of a bronchial asthma, chronic obstructive diseases of lungs, a coronary disease of heart, an arterial hypertension, a neuro-circulatory asthenia, a neurodermite, a psoriasis, to allergic diseases, etc.

The methods using respiration by artificial gas mixtures, are applied to a preparation for surgery and to a narcosis, for a postoperative aftertreatment, an aftertreatment after cardiovascular diseases, a syndrome of chronic weariness, for rising working capacity, to preparation for long flights, change of time zones, to rise in mountains and diving, for rising efficiency by other kinds of sports.

Existing techniques of carrying out interval hypoxia therapy are based on inflexibly programmed pulse changes of oxygen concentration in inspired mixture. The monitoring of physiological parameters of the patient is carried out, basically, under indications of a pulse oximeter. In these techniques a specific features of the patient are not considered and besides manual management of oxygen concentration in a respiratory mixture leads to increase of a subjectivity during decision-making at the choice of this or that parameter of a course of hypoxia therapy.

Besides to us devices which can create artificial respiratory mixtures which structure is capable to vary on the certain algorithm depending on the meanings of physiological parameters of the person measured in real time (bioadaptive control) are unknown.

In this connection development of methods and tools with bioadaptive control for respiration by multicomponent gas mixtures is perspective. For

this purpose CONSTEL Ltd. in cooperation with Institute of a radioengineering and electronics of RAS and State Institute of military medicine MD RF have been designed a hardware-software tool with much wide functionalities than existing hypoxia control tools. The machine consists of following units:

1. The device of artificial gas mixtures formation (BARS-GD);
2. Sources of the compressed gases;
3. The medical monitoring system;
4. The desktop computer with the specialized software.

Structure of the BARS-GD includes:

- Regulators of gases streams;
- The mixer of the specified gases;
- The unit producing an overpressure in respiratory mask;

As sources of the compressed gases cylinders with the compressed gases (oxygen, nitrogen, a carbon dioxide, etc.) and the medical air compressor can be used. The BARS-GD provides following operating modes:

- Submission of a respiratory gas mixture in a CMV/Assist mode with (without) creation of an overpressure in respiratory mask;
- Continuous flux of a respiratory mixture with (without) creation of an overpressure in respiratory mask;
- A HFJV and other patterns of respiration used in a practice of artificial ventilation.

In all these operation modes the device can generate a respiratory mixture from the specified gases of any accessible partial combination.

The BARS-GD measures and transfers instant meanings of volumetric rate of an inhaled admixture (an inspiratory curve) that allows to determine duration of inspiratory phases and an exhalation and frequency of respiration in the personal computer.

The medical monitoring system is a set of the physiological measuring equipment connected to a personal computer and allowing to carry out the dynamic control of a current condition of the patient over carrying out of examination (training). It consists of a computer electrocardiograph (ECG), a pulse oximeter (SaO_2) with the channel of a photoplethysmogram (PPG), a arterial blood pressure meter (BP) by a tachooscillometric method. In addition the complex includes the analyzer of the contents of oxygen in a inspiratory mixture.

The specialized software carries out following functions:

- Registration and the analysis of the data received from physiological monitoring devices in real time;

- Displaying the signals and measured physiological parameters (ECG, PPG, BP, frequencies of respiration and pulse).
- Control of BARS-GD, the partial pressure of oxygen, overpressure etc.;
- Database management of the physiological signals and parameters, and also information of patients and tests.

The given complex is intended for performance of following kinds of treatment and inspections (trainings):

- Definition individual hypoxia fastness;
- Carrying out normobaric interval hypoxia trainings for therapy of the broad variety of diseases and increase the functional reserves of an organism;
- An opportunity of carrying out the functional loading with gas mixtures.

Creation of a apparatus allows to realize system for a dynamic interval hypoxia with a bioadaptive principle of control. Thus dynamic management of patterns of respiration and partial gas mixture structure for achievement of the maximal physiological efficiency will be carried out by controlling computer on the basis of monitoring a current individual condition of the person, in particular, dynamics of the parameters reflecting a functional condition cardiac and respiratory systems.

Besides using and other gases, such, for example, as nitrous oxide, 100 % oxygen, a carbon dioxide, a xenon, etc., it is possible to form multicomponent gas mixtures for expansion of a spectrum of physiological influences.

The conclusion

As a result of the tests of the designed equipment lead on volunteers, it has been shown, that it surpasses existing similar devices on the functionalities.

Characteristic responses cardiac and respiratory systems on various dynamic influences by variable gas mixtures are received. It allows to estimate type of individual reactions to influence and to model algorithms of bioadaptive management.

Besides the equipment realizes series of essentially new functions, allowing to use it for carrying out of perspective methods of treatment and trainings in which varies not only the partial pressure of oxygen, but also other gases.

Work is supported by RFBR grant 08-07-00436.

An automated complex for respiratory apparatus training

N.V.Ivakhno

Tula State University
e-mail: ivakhno@rambler.ru

One of the main problems of public health services now is effective preventive maintenance and treatment of chronic nonspecific diseases of lungs. The big attention is given rehabilitation of this group of patients and restoration of their working capacity. Besides general improving health therapy the actions directed on improvement of other systems of an organism, in respiratory rehabilitation improvement of mechanical properties of lungs, drainage respiratory ways, increase in force and endurance of respiratory muscles always is required, and also normalization of the central regulation of breath is required.

One of methods of not medicamentous treatment of patients with bronchopulmonary and other diseases is training of respiratory muscles for which realization respiratory simulators are used. They are intended for biological imitation of respiratory loadings by similarly what arise during performance of improving physical exercises.

Direction of development of modern respiratory simulators is creation of the automated complex, described reliability, standardized characteristics, an opportunity of exact regulation and individual selection of size of artificial resistance in the respiratory contour, possessing convenience, simplicity of use and providing the control of correctness of performance of elements of respiratory exercises.

The developed training complex is presented by hardware and program parts. Resistance to a breath is created by an adjustable throttle. Change of the area of an aperture of a throttle is carried out by the stepping motor with a reducer. The stepping motor copes the microcontroller. The difference of pressure is perceived by the sensor of pressure. The signal of the sensor is passed through the filter of low frequencies and will be transformed to the digital form by means of the analog-digital converter of the microcontroller. Further the information on pressure is transferred through the consecutive transceiver in a computer where there is a display and preservation of received data. The program, or the operator sets reciprocal commands of management which are transferred the microcontroller and are fulfilled by a throttle by means of a mechanical drive. Thus, the developed training

complex measures difference of barometric pressure at various sizes and kinds (constant, variable) resistance of an air stream.

The design of a throttle is resulted in figure 1.

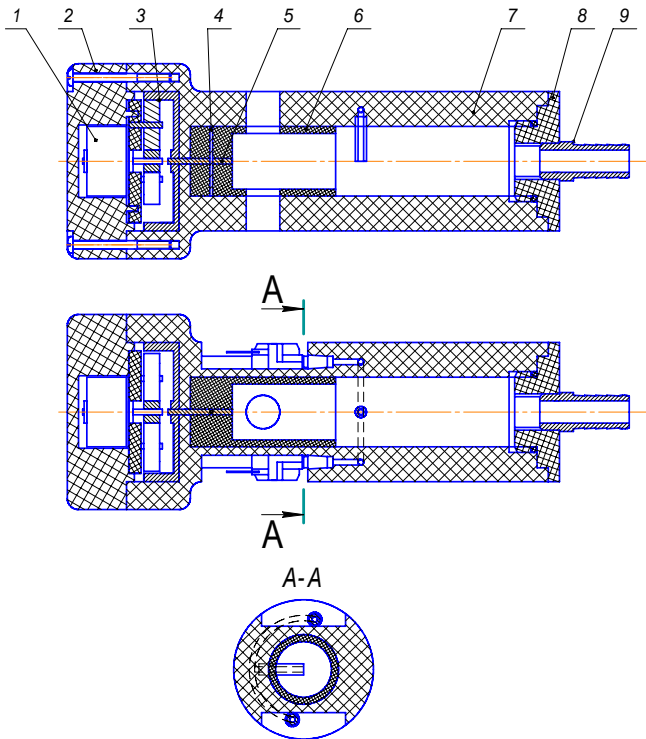


Fig. 1 - Design of an adjustable simulator.

The case of a simulator consists of three parts: the basis 7, a cover 8 with the entrance union 9, a back cover 2 which fastens to the basis two screws 3x35. Resistance to an air stream is regulated by overlapping of apertures of a tube 6 and the bases 7. Change of the area of blocking of apertures is made by rotation of the tube rigidly fixed on a target shaft of 5 reducers 3 pin 4. The entrance shaft of a reducer is resulted in rotation by the stepping motor 1 placed in a back cover. The union 9 incorporated with connector. The arrangement of sensors is resulted on section A-A, sensors are

informed by the channel in the basis of the case of a simulator. Tightness of the case of a simulator is provided with rubber sealants.

For program management of a simulator dependence of the area of carrying apertures on quantity of steps of the engine is received:

$$S(n) = \frac{\pi R^2}{45} \arccos\left(\frac{\pi r n}{240R}\right) - \frac{\pi r n}{60} \sqrt{R^2 - \frac{(\pi r n)^2}{57600}}$$

where the S-area of an aperture; n - quantity steps of the motor; R, r - radius of an external and internal tube of a throttle (fig.2).

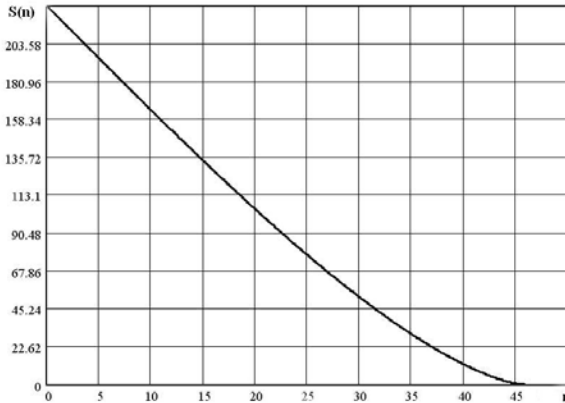


Fig. 2 - Schedule of function S (n).

The program part of a training complex is intended for installation by the operator of the area of an aperture of a simulator, display and preservation of size and speed of change of pressure, the organization of data exchange with the microcontroller through a serial port of a computer.

On the basis of the developed design, the electric basic scheme and the software the operating breadboard model of a respiratory simulator is collected, schedules of change of pressure in a respiratory contour are experimentally received at the various areas of a carrying aperture of a simulator (fig.3,4).

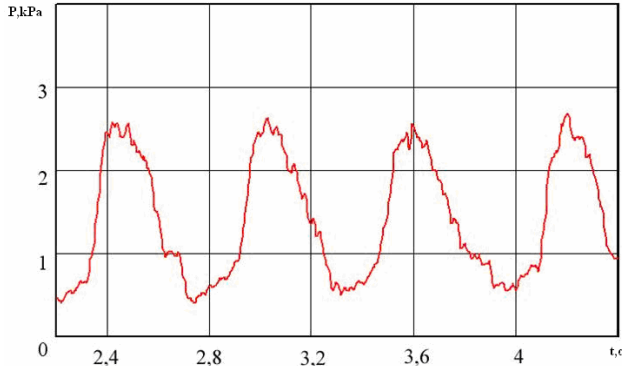


Fig.3 - Schedule of pressure in phases of an exhalation at the installed area of an aperture.

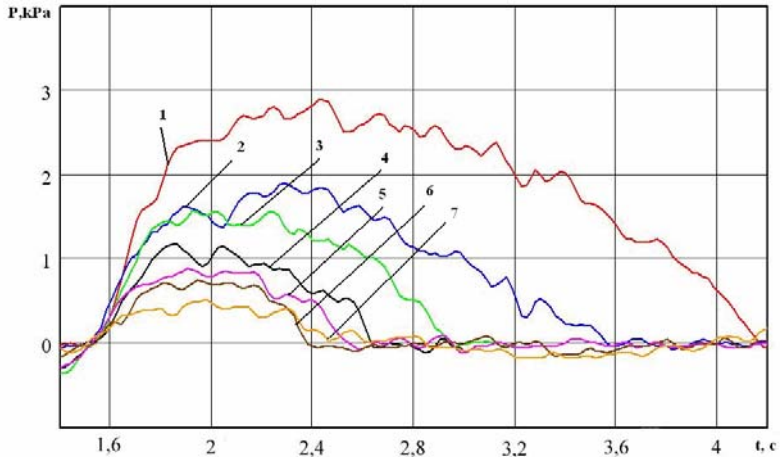


Fig.4 - Dependence of pressure at an exhalation from the area of an aperture of a simulator (1 – $S = 23\text{mm}^2$, 2 – $S = 45\text{mm}^2$, 3 – $S = 68\text{mm}^2$, 4 – $S = 90\text{mm}^2$, 5 – $S = 113\text{mm}^2$, 6 – $S = 136\text{mm}^2$, 7 – $S = 158\text{mm}^2$).

The developed automated complex provides exact adjustment of a kind of training influence for bodies of breath with simultaneous registration of quantity indicators of a functional condition of pulmonary system.

Technical realization of the external counterpulsation equipment

Sudarev A.M., Isaev I.A., Kantor P.S., Korotich E.V.

*Institute of a radio engineering and electronics of the Russian Academy
of Science, CONSTEL ltd.,
e-mail: sudarev@constel.ru*

Modern cardiology, surgery and reanimation deal more widely with means replacing pump function of the diseased heart, partially or completely, temporary or constantly.

Methods of the temporal help to heart and replacements of its pumping ability with mechanical devices, are integrated into the concept “assist circulation”. The methods of an intraaortal balloon counterpulsation (IABP) and an external (non-invasive) counterpulsation (ECP) have a wide distribution.

The external counterpulsation – clinically proved effective method. It is widely used currently in our country and abroad. ECP is the alternative of an intraaortal counterpulsation and can be considered as a noninvasive and non-traumatic method.

During ECP procedure the cuffs are put on legs clasping accordingly calfs, lower and upper parts of thighs with capture of buttocks of the patient. This cuffs are pumped with air (up to 300 mm Hg) consequently from calfs to buttocks. The moments of the compression beginning are tuned so that the pressure wave of a blood superseded from the bottom extremities by arteries in a retrograde direction reaches an aorta during a diastole. The blowoff occurs before the beginning of a systole.

The method has received the greatest propagation after introduction in a clinical practice of such updating a method, as the enhanced external counterpulsation (EECP). It differs from ECP as so-called diastolic augmentation during procedure is achieved. After carrying out in the USA the successful large research at University Stony Brook, NY, and also multicenter clinical research (MUST-EECP) in the middle of 1990th years the method has spread widely in the USA and China.

The equipment for an external counterpulsation is not made in Russia, and currently any domestic researches and development in this area completed with the experimental sample are not known to authors. In this case, we have designed the equipment set of an external counterpulsation during 2004-2006. The machine is named «CARDIOPULSARtm» and now its

medical certification comes to finish. Also preparations for serial producing were made.

All currently known foreign devices use a source of compressed air, inflatable cuffs and pneumatic actuator devices for creation of a compression of the bottom extremities as a rule. The hydraulic drive is not applied now.

Our machine uses a electrocardiogram signal (ECG) for synchronization of a compression with cardiac cycle and a photoplethysmography (PPG) for observation over hemodynamic effects in the same manner as foreign ECP analogues.

Monitoring of the most important physiological parameters (an ECG, heart rate, SpO₂, the NIBP) for an objective estimation of a current patient condition, synchronization with cardiac cycle and parameters of influence control in real time are carried out by means of the specially developed software. Synchronization includes a problem of the ECG outline analysis in "real" time and definition of a QRS-complex with no more than tens milliseconds delay. The actuator part of machine constitutes the electropneumatical device with microcontroller connected to a personal computer. Influence is synchronized with phases of a cardiac cycle by means of the control commands sent from the personal computer to the microcontroller.

Essential difference from foreign analogues consists in the block diagram of pneumatic elements for creation of pressure pulses in compression cuffs. So we use immediate control of pressure in cuffs without preliminary setting desired pressure in intermediate receivers.

The high pressure of a compressed air source on an input of actuator elements allows us to use the valve with relatively small orifice. It allows us to use the standard industrial pneumatic valves in the scheme of the device. However, such decision demands the reliable scheme of protection.

In particular, we apply the scheme in which the compression channel is normally closed but the blowoff channel is normally opened. Such pneumatic scheme is most safe and dumps pressure in cuffs in supernumerary situations. We applied the scheme of protection against cuffs pressure excess above the safe level including the gauge of pressure, an electronic protection circuit and the valves with electric and electropneumatical control. Such decision is well-taken because the reliability, resource and speed of operation of modern valves of such type are not below than at mechanical passive elements. Besides such decision allows us to carry out monitoring of a situation on the personal computer that enables to provide a technical diagnostics.

The technical decision of the influencing unit is patented.

The equipment most important specifications:

1. Synchronization of pressure pulses with an cardiac cycle is carried by ECG. A choice of ECG leads used for synchronization is automatic.

2. A range of pressure in cuffs – $0 \div 360$ mm Hg

3. Rise/fall time of pressure pulses – no more than 150 msec.

4. Arbitrary (within the limits defined by cardiac cycle duration) setting of the compression pulse duration, and also of a delay between calfs, lower and upper parts of thighs compression pulses allows to arrange parameters of the time chart of influence for achievement of the maximal haemodynamic efficiency.

5. Some modes of exposure can be used: a continuous regimen (on every cardiac cycle), with the miss of one cycle of influence on 1, 2 or 3 cardiac cycle.

6. The software allows to visualize in real time all measured physiological signals and parameters, and also pressure in cuffs that allows the operator to adjust modes of exposure and change them in real time by means of visual "control panel".

7. The set of cuffs of the different sizes, considering anthropometric features of the overwhelming majority of patients is designed.

8. The design of functional bed is developed providing convenience to patients of different body height and weight for long (1-2 hours) procedures.

Thus, the domestic equipment is developed for an assist circulation by a method of an external counterpulsation with functional, technical and ergonomic characteristics not worth than those of foreign analogues. It is confirmed by technical and medical tests for enough plenty of patients.

Work is supported by the grant of the Russian Federal Property Fund 06-07-89321a.

Near real-time stereo depth estimation on GPU

I.I.Leonochev, G.M.Shestopalov

*Department of Biomedical Systems, Moscow State Institute of
Electronics Technology(Technical University)
e-mail: gkgk1@yandex.ru*

Introduction

Stereovision is the ability to perceive objects by two eyes which provides additional information like their surface or positioning in space.

In order for autonomous robots to effectively process, segment, analyze and navigate in real-life environment it is a prerequisite that such system obtains data about surrounding world in a format that can be easily used to reconstruct that environment. Amongst different vision systems this could be the one capable of 3 dimensional representation of the real world. For humans such reconstruction task is achieved quite naturally since early age and soon it becomes our second nature to accurately judge distances, perspective and space. However, when human vision system is analyzed it becomes apparent that the brain uses a multitude of techniques to give us a sense of the three dimensional world in which we live.

Three dimensional scene data can be obtained from various sources including motion parallax data, structured light or laser range finders. But perhaps the most obvious technique is stereo vision. Similarly to a pair of human eyes, the output of two cameras observing the same scene can be analyzed and the differences between the two images can be used to compute object depths and hence the overall scene model can be built.

1. Stereo reconstruction

In order to calculate the scene point depths we have to find points in both the left and right camera images which represent the same real world coordinate. Perhaps the most important contributing factor in terms of the accuracy of the final reconstruction is a system's ability to find a comprehensive solution for this problem.

All stereo vision algorithms can be described by four steps:

1. matching cost computation;
2. cost (support) aggregation;
3. disparity computation / optimization;
4. disparity refinement.

Two groups of methods are proposed for third step: *global* and *local*.

Global methods use a prior world model. The proper selection of that model determines the robustness of final solution, and it becomes a crucial problem for these methods. The solution is found by minimizing a global function, usually comprising in two terms: one represents the world model with all its assumptions, while the other measures the consistency with input images.

Local methods come out from the assumption that global optimization is not needed. On the contrary, the local image information is sufficient for correct formulation of the matching task.

In the local methods, the matching is performed based on selecting the most similar matching elements. Each matching element has assigned a signature, which describes its characteristics. Over the signatures a statistics, evaluating their similarity, is defined, which allows matching pairs selection. The cost of the signature depends only on the local image properties (in predefined neighborhood/window) of the matching element. Therefore, the core of local methods lies in the definition and selection of the appropriate windows-representing signatures, and the statistics computed over these signatures.

The typical statistics defined for computing matching costs are sum-of-squared differences, sum-of-absolute differences, normalized cross-correlation, etc. Based on these statistics, the correspondences are selected. Matching principle selection has primarily importance, because it straightforwardly influences the results quality.

2. Graphics hardware stereo implementation

While many stereo algorithms obtain high-quality results by performing optimizations, today only correlation-based stereo algorithms are able to provide a dense (per pixel) depth map in real time on standard computer hardware.

Just a few years ago even correlation-based stereo algorithms exceeded the performance of standard computers so a special hardware was necessary to achieve real-time performance.

In the meantime, with the tremendous advances in computer hardware, software-only real-time systems begin to merge. All these systems used a number of techniques to accelerate the calculation, most importantly, assembly level instruction optimization using Intel's MMX extension. While this provides sufficient performance to obtain dense-correspondences in real-time, there are few CPU cycles left to perform other tasks including high-

level interpretation of the stereo results. Furthermore, the most approaches use an equal-weight box-shaped filter to aggregate the correlation scores, so the result from the previous pixel location can be used in the current one. While this simplifies the implementation and greatly reduces computational cost, the aggregation window size has a significant impact on the resulting depth map.

All these algorithms can be adopted for implementation on graphical processor unit (GPU). In following sections describe three major steps for near real-time stereo vision: cost computation, cost aggregation and disparity selection.

2.1. Matching cost computation

A widely used algorithm for matching cost is the absolute difference between the left and right pixel intensities. We use the separate program module to compute the per-pixel absolute difference, which is written to the framebuffer object. To search over N disparity hypothesis, N rendering passes are needed.

2.2. Cost aggregation

While it is possible to assign disparity values directly based on the per-pixel difference values from multiple images, it is necessary to use larger support region in the stereo case with only two input images.

Stereo algorithms typically sum the matching cost over a small window to increase the robustness to noise and texture variation. However, choosing the aggregation window size is a difficult problem. The probability of a mismatch goes down as the size of the window increases. However, using larger windows leads to a loss of accuracy and to the possibility of missing some important image features. This is especially true when large windows are placed over occluded boundaries. We deal with this problem by using multi-resolutional approach, which suits well for GPU-based implementation.

2.2.1. Multi-resolution approach

By observing correlation curves for a variety of images, one can observe that for large windows the curves mostly have a single strong minimum located in the neighborhood of the true depth, while for small windows they often exhibit multiple equivalent minima. However, for small windows the minima are typically well localized. Therefore, one would like to combine the global characteristics of the large windows with the well-localized minima of the small windows. The simplest way to achieve this in hardware consists of adding up these different curves.

Summing two difference images obtained for windows differing by only a factor of two (one mipmap-level) can be easily and efficiently implemented by using the mipmap functionality available in contemporary GPUs. This approach is more general and quite efficient for certain types of convolutions.

Modern GPUs have built-in box-filters to efficiently generate all the mipmap levels needed for texturing. Starting from a base image the following filter is recursively applied.

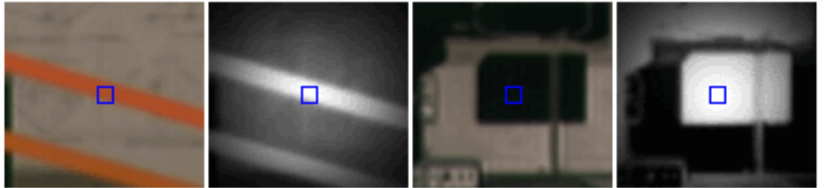
Additional difference images can be easily summed using multiple texturing units that refer to the same texture data, but have different mipmap level biases.

2.2.2. Adaptive Weight

We have used Adaptive weight algorithm described by Kuk-Jin Yoon and In So Kweon. In that algorithm the weight value of each pixel is described by the sum of color weights together with distance similar pixels (see formula 1).

$$w(p, q) = \exp\left(-\left(\frac{\Delta c_{pq}}{\gamma_c} + \frac{\Delta g_{pq}}{\gamma_p}\right)\right) \quad (1)$$

Images below (pic.1 b,d) show how pixels with identical color strengthen the importance of area concluded in a blue rectangular. By grey gradation the contribution of the neighbor points is shown, the brighter pixel the more significant contribution it has. On the image it is visible as spherical diffusion from the central point.



a) ref. window	b)weight of (a)	c) target win.	d) weight of (c)
----------------	-----------------	----------------	------------------

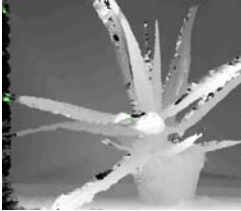
2.3. Disparity selection

Typical in real-time stereo algorithms, we use a “winner-take-all” strategy that assigns each pixel to the disparity value with the minimum cost. This step in fact can be combined with the previous aggregation step. Once a pixel’s matching cost at a certain disparity is computed, it is sent to the framebuffer as a depth value while the disparity value is encoded as the color.

3. Results

In our work we had implemented several algorithms on GPU. Results with corresponding calculation speed are presented in tables below for 3 different graphic cards.

Picture Aloe. Resolution 424x370, disparity 64

Video Card \ Algorithm	MipMap (4 level) fps	Adaptive Weight (win. 17x17) fps
GF 8500 GT	10,75	5,88
GF 8600 GTS	11,76	16,6
GF 8800 GT	16,5	27,4
Error %	12,69	14,6
Left Image	Depth Map	Depth Map
		

Picture Moebus. Resolution 464x370, disparity 72

Video Card \ Algorithm	MipMap (4 level) fps	Adaptive Weight (win. 17x17) fps
GF 8500 GT	10	5,26
GF 8600 GTS	9,61	13,83
GF 8800 GT	14,3	25,5
Error %	21,72	26,5
Left Image	Depth Map	Depth Map
		

Real-time Control of the Defibrillation Waveform with Digital Signal Processor

A. M. Antropov, V.A. Bespalov, B. B. Gorbunov, A. N. Gusev,
K. A. Mamekin, I. V. Nesterenko and S. V. Selishchev*

*Moscow Institute of Electronic Technology (Technical University),
* Zelenograd Innovation-Technological Center, JSC
e-mail: alex@bmslab.miet.ru*

Department of Biomedical Systems of Moscow Institute of Electronic Technology works with real-time shaping technology of defibrillation waveforms since 1995. Our technology allows producing defibrillation pulse with fixed duration and energy, regardless of patient impedance, with sufficient defibrillation current even for high impedance patients. “Ural Optical & Mechanical Plant” company has released first defibrillator with our technology, named DFR-2, to production in 2003. Feedback loop has been done with analog components. Main limitations of the technology were limited accuracy and speed, complexity of the analog control loop.

With the current state of digital signal processing it looks possible to increase precision and speed of the control loop, along with significant simplification of analog part. Extensive PSpice simulations have been by authors to prove such possibility.

General view of defibrillation pulse-shaping unit with real-time control is presented on Fig. 1.

The unit contains several independently controlled power cells with reversible polarity, stacked in series to provide maximum voltage on the output up to 3600V, voltage and current sensors to measure patient voltage and current, smoothing inductor to prevent rapid current changes during regulation and digital signal processor (DSP) based control unit to control the power cells. Unlike the preceding technology, all feedback control actions can be calculated in digital domain.

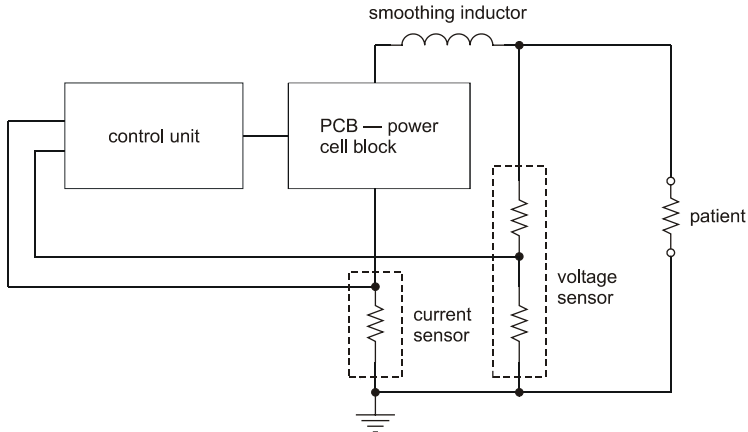


Fig. 1. Defibrillation pulse-shaping unit.

During the delivery of pulse control unit continuously samples the signals from current and voltage sensors and makes analog-to-digital conversion. Based on sampled values DSP calculates difference between the actual and reference waveforms and takes required control action to the power cells, by switching power cells on and off. Several control strategies can be implemented, including delivery of fixed energy and fixed current pulses. Shape of the waveform can be made insensitive to impedance changes during delivery of the pulse. Implementation of the control loop with DSP provides the increased noise immunity and decreased quantity of analog components.

Algorithms of defibrillation pulse-shaping control by means of DSP have been simulated on P-Spice-model. The sampling period of analog signals has been chosen equal $5\mu\text{s}$, and time for analog signal conversion and data processing is set equal $2\mu\text{s}$.

Results of simulation are shown on Fig. 2, 3 and on Fig. 4, 5 for for Gurvich-Venin defibrillation pulse and biphasic truncated exponential defibrillation pulse respectively, for patient impedances of 50Ω and 100Ω . Control strategy with predefined current shape has been used.

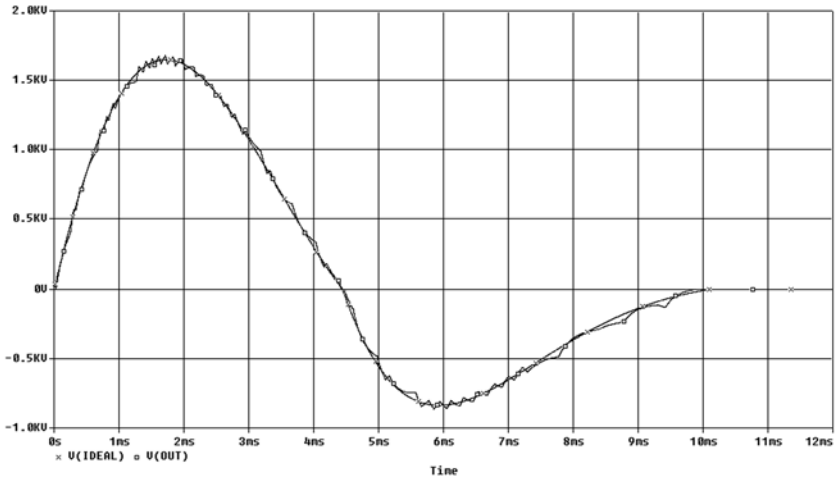


Fig. 2. Result of modeling for Gurvich-Venin pulse on 50Ω load (the amplitude of current of first phase is 33A).

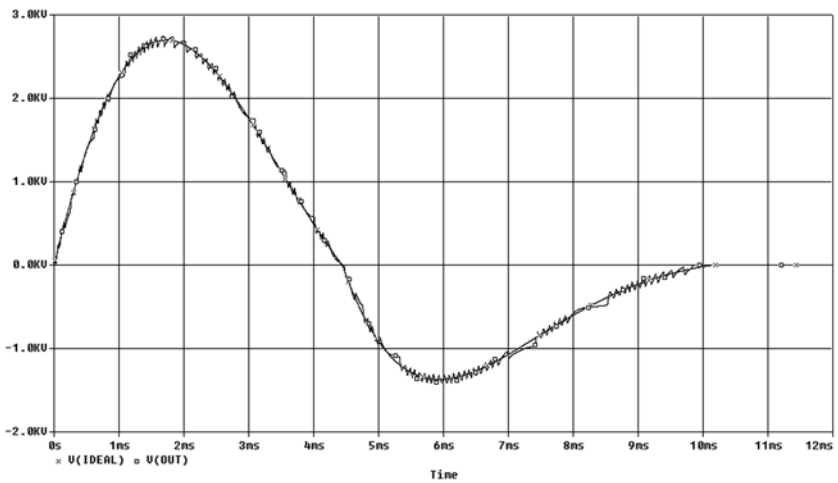


Fig. 3. Result of modeling for Gurvich-Venin pulse on 100Ω load (the amplitude of current of first phase is 27A).

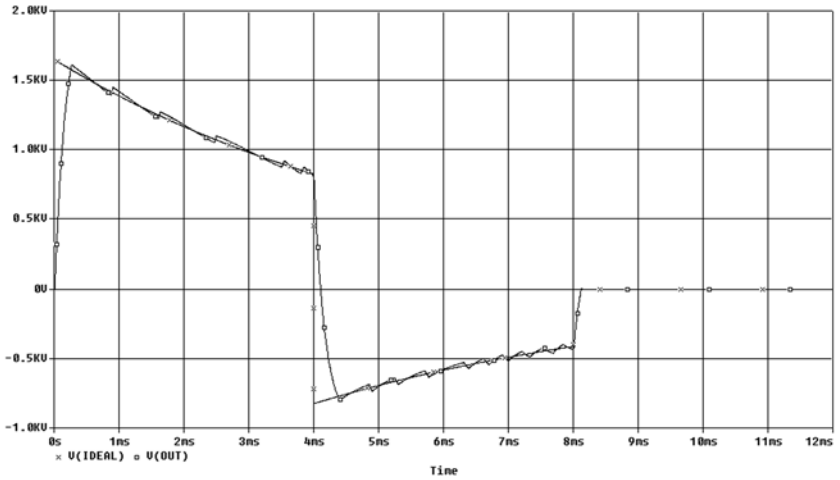


Fig. 4. Result of modeling for biphasic truncated exponential pulse on 50Ω load (the amplitude of current of first phase is 33A).

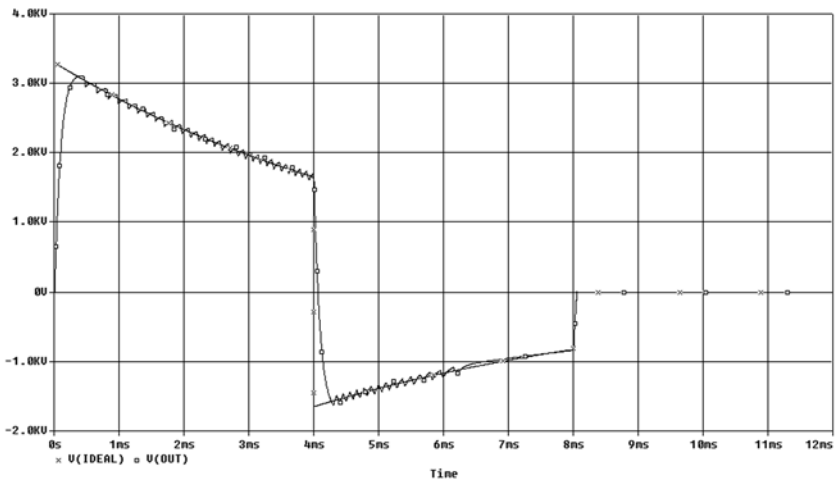


Fig. 5. Result of modeling for biphasic truncated exponential pulse on 100Ω load (the amplitude of current of first phase is 33A).

Based on the results of simulation we can conclude that implementation of defibrillation pulse-shaping unit with DSP feedback unit can be implemented.

The given work is executed at partial financial support of the Russian Fund of Basic Researches, project N 05-08-50300.

Section 3

Therapeutic and diagnostic systems

(Bio) sensors based on nano-scale arrays and films of novel electrocatalysts

A.A. Karyakin

*Chemistry faculty of M.V. Lomonosov Moscow State University, 119991,
Moscow*

e-mail: aak@analyt.chem.msu.ru

According to their definition, biosensors are based on the transducer, typically electrocatalyst for reduction-oxidation of coupled reaction products, and of immobilized enzyme.

Prussian Blue – advanced electrocatalyst for hydrogen peroxide reduction

Hydrogen peroxide (H_2O_2) sensors are important not only for clinical diagnostics and environmental control, but also for elaboration of biosensors based on enzymes oxidases. The latter are terminal ones for more, than 90% of enzyme based analytical devices.

We first proposed to use Prussian Blue as electrocatalyst for H_2O_2 reduction to elaborate biosensors [2]. H_2O_2 registration by its electro-reduction allows to decrease working potential and achieve maximum sensor selectivity. Due to thorough optimization of Prussian Blue synthesis we succeeded to elaborate the electrocatalyst, which is *three orders of magnitude* more active and selective compared to the commonly used platinum (table 1). The cost of electrocatalyst, which contains only inorganic ferric salts is also three orders of magnitude lower. Considering both catalytic activity and selectivity of Prussian Blue, it was denoted as “artificial enzyme peroxidase” [3]. Optimal electrocatalytic activity of Prussian Blue is observed at its thickness 50 – 100 nm [1].

Prussian Blue based nano-electrode arrays

Miniaturization of electrodes leads to improvement of signal-to-noise ratio and to decrease the sensor detection limit. To avoid the necessity to register ultra-low currents the micro-electrode arrays are elaborated by means of photo- and electronic lithography.

We proposed electrochemical synthesis of nano-electrode arrays [4] by nano-structuring of Prussian Blue onto inert electrode support. Indeed since activity of the support (gold, carbon) in H_2O_2 reduction is negligibly low compared to the electrocatalyst, the diffusion of hydrogen peroxide should be directed exclusively to nano-structures of Prussian Blue, where it is consumed (reduced to water). For optimal nano-electrode array the diameter of individual nano-structures should be equal to their separation distance [1].

Developing the approaches for nano-structuring (deposition through templates, deposition at nucleation stage) we succeeded to synthesize Prussian Blue nano-structures close to the required geometry. Thus elaborated hydrogen peroxide sensor displayed high sensitivity, low detection limit (1 *nanomol* L^{-1} , or 0.03 ppb) and linear range prolonged over 7 orders of magnitude of H_2O_2 concentrations. The achieved analytical performance characteristics are *record* ones among known electrochemical sensors [1].

Table 1. Electrocatalysts for H_2O_2 reduction

Transducer	Selectivity $j_{H_2O_2}/j_{O_2}$	Electrochemical constant, cm/s
Pt	0.1	$4 \cdot 10^{-6}$
peroxidase electrode	30-40	$1 \cdot 10^{-3}$
Prussian Blue	400-600	$1 \cdot 10^{-2}$

Novel protocol for enzyme immobilization

Maximum reproducibility can be achieved by forming enzyme containing films on the basis of already prepared polymer. The latter obviously water insoluble is able to form uniform and stable membranes only from its real solutions. This causes the requirement to expose the enzymes to organic solvents [5].

After exposing to water-organic mixtures with the high (80-95%) content of organic solvent the enzymes are able to remain up to 100% of their initial activity and to be even activated in certain cases [5]. The immobilization protocol is thus simplified to suspending of the enzyme in

concentrated organic solvents with stabilization by the membrane-forming polyelectrolyte, dipping the suspension to the target surface and drying.

The advantages of the novel approaches in biosensor science are usually demonstrated elaborating the corresponding glucose biosensor. Combination of the advanced electrocatalyst (Prussian Blue) with the novel protocol for enzyme immobilization has lead to elaboration of glucose biosensor with the best analytical performance characteristics (fig. 1) [6].

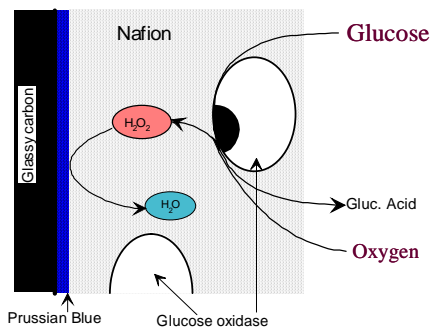


Fig. 1. Scheme of glucose biosensor

Planar and micro-(bio)sensors, analytical systems

Innovative potential of the fundamental results obtained is realized in chemical and biological sensors and analytical systems. Planar (bio)sensors on the basis of three-electrode strips made by screen printing technology as well as micro-sensors are elaborated (fig. 2). To involve (bio)sensors in analytical systems the novel flow-through wall jet cell was constructed.

Novel (bio)sensors are applied in different areas from clinical diagnostics to food quality control. Hydrogen peroxide sensor is used in development of new express, simple and valuable approach for evaluation of total antioxidant activity. Besides that, detecting various compounds it's possible to differentiate natural and non-natural food products. For instance, technology for manufacturing of dry grape wines excludes addition of sugar. The latter is added by certain companies to compensate low quality of raw materials. However, grape does not contain sucrose, and due to the presence of the latter it's possible to differentiate natural wines from surrogate. Similarly, due to the presence of lactate it's possible to discover natural kvass, due to lactose – qualitative dairy products etc.

Correct diagnostics is highly important for curing strategy. In collaboration with Institutes of Pulmonology and Tuberculosis the elaboration of novel methods for diagnostics of pulmonary deceases on the basis of (bio)sensors is carried out. It was shown, that in cases of inflammatory deceases hydrogen peroxide concentration in the non-invasively collected condensate of exhaled breath (EBC) is sharply increased. Hence, with such non-traumatic method just analyzing EBC it's possible to discover the correct therapy.

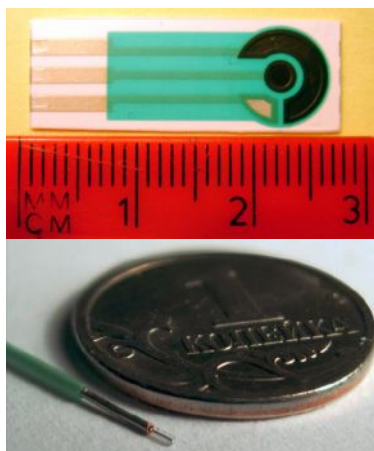


Fig. 2. Planar (top) and micro-sensor

1. A.A. Karyakin, E.A. Puganova, I.A. Bolshakov, E.E. Karyakina. *Angewandte Chemie Int. Edition* 46 (2007) 7678-80.
2. A.A. Karyakin, O.V. Gitelmacher, E.E. Karyakina. *Analytical Chemistry* 67 (1995) 2419-23.
3. A.A. Karyakin, E.E. Karyakina, L. Gorton. *Analytical Chemistry* 72 (2000) 1720-3.
4. A.A. Karyakin, E.A. Puganova, et al. *Analytical Chemistry* 76 (2004) 474-8.
5. A.A. Karyakin, E.E. Karyakina, L. Gorton, O.A. Bobrova, L.V. Lukachova, A.K. Gladilin, A.V. Levashov. *Analytical Chemistry* 68 (1996) 4335-41.
6. A.A. Karyakin, E.A. Kotel'nikova, L.V. Lukachova, E.E. Karyakina, J. Wang. *Analytical Chemistry* 74 (2002) 1597-603.

Apparatus-program system for diagnostics and correction of autonomous nervous system dysfunctions

**V.S. Kublanov^{1,2}, V.A. Shmykalov⁴, V.B. Kostousov³, Y.E. Kazakov¹,
Kh.Z. Brainina¹**

¹Institute of Medical Cell Technology, 620095, Russia, Ekaterinburg, 25, Sobolev St.

²Ecological and medical equipment (science researches and industrial designs), 623400, Russia, Kamensk-Uralsky, 29, Tchaikovsky St.

³Institute of mathematics and mechanics Ural branch of the Russian Academy of Sciences, 620219, Russia, Ekaterinburg, 16, S. Kovalevsky St.

⁴ FSUE «Production association «October», 623400, Russia, Kamensk-Uralsky, 8, Rjabov St.

Corresponding author: V. Kublanov, [mailto: kublanov@usp.ru](mailto:kublanov@usp.ru)

The development of diagnostic methods of an autonomous nervous system state (ANS) and corrections of its disturbances is an actual problem of *public health services* at definition of organism reserve under its adaptation to environment.

Transition from health to illness is not sudden: between these two states some prenosological states exists formed at consecutive transition of organism through different degrees of adaptation to various loads: adaptation process can be urgent when there is a fast adaptation of organism to his work, and long-term at which the structural rearrangement occurred by reason of effects accumulation in organism due to many time repeated urgent adaptation are observed [1].

The adequate level of organism functioning and its adaptive response is defined by system of the functional reserves. Their most informative indicators are blood circulation characteristics. The important role in the arrangement of human adaptive activity belongs to autonomous nervous system (ANS). Since functional reserves of organism are defined by interaction of cardio-vascular system and ANS it is possible to use their dynamic characteristics in determination of adaptive human abilities.

For the diagnostics of autonomous dysfunctions the apparatus-program complex apply the function $F(t)$ which is defined by the relation of wavelet-transformations spectral characteristics intensity of slow waves of first order $LF(t)$ and respiratory waves $HF(t)$, variability of heart rate. For the improvement of spectral time-frequency irregularities identification in

sequence $R-R$ the wavelet-transformation is carried out by means of modified analyzing basic *Morlet* wavelet $\psi_{mod}(x)$ which represents the sum complex *Morlet* wavelet $\psi_{mod}(x)$ and additional function $\xi(x)$ [2]:

$$\psi_{mod}(x) = \psi(x) + \xi(x), \quad (1)$$

$$\xi(x) = C \cdot \theta^q(x), \quad (2)$$

$$\theta = \begin{cases} 0, & \text{if } \cos(mx)F(x, \mu, \sigma) < 0 \\ \cos(mx)F(x, \mu, \sigma), & \text{if } \cos(mx)F(x, \mu, \sigma) \geq 0 \end{cases}$$

$$C = \frac{-\int \psi(x)dx}{\int \theta^q(x)dx}, \quad (3)$$

where

$\psi_{mod}(x)$ - analyzing standard complex *Morlet* wavelet,

$$\psi(x) = \left[\exp\left(i\omega_0 x - \frac{x^2}{2} \right) \right],$$

$\xi(x)$ - additional function, continuous but not differentiated, and the its integral is equal with a minus sign to integral from complex *Morlet* wavelet $\psi(x)$, $F(t, \mu, \sigma)$ - function of density of the normal Gauss distribution, defined by expectation value μ and meansquare deviation σ ; $m, q > 0$.

In the equations (2) and (3) parametres m, μ, σ and q define the level of lateral petals of modified *Morlet* wavelet.

In fig. 1a and 1b give the curve of functional $F(t)$, healthy patient S., age 23, and patient B., age 81, suffering from arterial hypertension (stage II) with high risk of cardiovascular complications, for states of functional rest (FR) and as a functional loads, are used passive orthostatic (O) and clinostatic (C) assays.

Apparently from the curve of functional $F(t)$ change, it is not smooth function, and the parameters of its "anticipatory ringing", or local dysfunctions, change at functional loads, and these changes depend on the clinical status of the patient.

The decision making rule is applied to definition of functional $F(t)$ local dysfunctions A_F

$$F(t) \geq \Delta, \quad (4)$$

where Δ - a decision-making threshold of practically healthy patients.

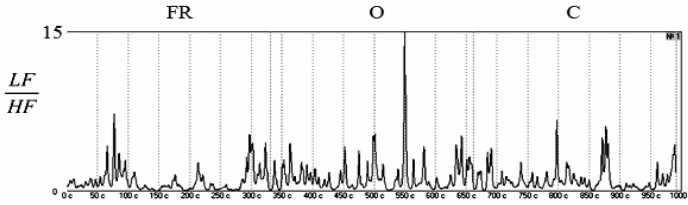


Fig. 1a. Patient S, age 23, practically healthy

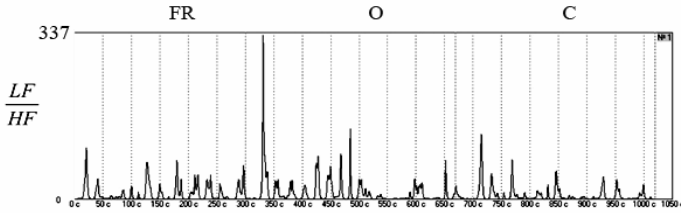


Fig. 1b. Patient B, age 81, arterial hypertension

As parameters of local dysfunctions A_F the quantity of dysfunctions N , maximum value A_{max} of dysfunctions amplitude A_i and their intensity $\tilde{A} = \sum_{i=1}^N A_i^2$ on an interval of observation are used [2].

In table 1 quantitative estimations of parameters of functional $F(t)$ local dysfunctions A_F , presented in fig. 1a (here and then for *tilt test* assays $\Delta = 10$) are resulted.

Table 1

Patient S.	Research mode								
	FR			O			C		
	N	A_{max}	\tilde{A}	N	A_{max}	\tilde{A}	N	A_{max}	\tilde{A}
	0	7	0	1	15	15	0	6	0

In table 1 showed that at all functional conditions at patient S. the quantity of local dysfunctions A_F and their parameters N , A_{max} and \tilde{A} considerable exceed similar characteristics of patient B. in table 2.

For correction of ANS functional disturbances we offer a way of dynamic correction of activity of sympathetic nervous system (DCASNS) which allows to activate the certain regulation mechanisms participating in the arrangement of organs and tissues blood supply. By DCASNS algorithm

design the property of biological systems to keep a steady non-equilibrium thermodynamic state is used at changes of external and internal perturbations. The system of a cerebral blood circulation is also arranged in a similar way that important physiological parameters are supported without disturbances of a cardio-hemodynamic homeostasis due to interaction of humoral, metabolic, myogenic and neurogenic mechanisms. DCASNS corrects autonomous dysfunctions by the control of neurogenic mechanism, whose functions are carried out by sympathetic ganglion of ANS. The influence target is the stellate ganglion or most close located to it the cervical ganglions of sympathetic nervous system [3].

The procedure DCASNS is carried out by means of «SYMPATHOCOR-01» device which generates the spatially-distributed rotating field of electric current impulses for transcutaneous influences on sympathetic ganglions. «SYMPATHOCOR-01» is developed by design office «Ecological and medical equipment (scientific researches and industrial design)», is authorized to manufacture, sale and application in Russia and serially produced by «Production association «October».

"SYMPATHOCOR-01" is applied more than in 200 clinics in Russia in treatment of patients with migraine and cephalgias, consequences of brain trauma, alcoholic and narcotic abstinence, arterial hypertension, neuropathic pain, neurosensory deafness, optic nerve atrophy, hyperhidrosis, syndrome of orthostatic hypotension, vestibulopathy, pharmaco-resistant epilepsy, in rehabilitation after stroke. As a rule, the period of remission is not less than 6 months, after a repeated course remission is enlarged. Adverse effects during and after carrying out procedures were not noted.

The approaches examined above are realized as a part of the apparatus-program complex we use for diagnostics and correction of vegetative dysfunctions in Sverdlovsk regional clinical psychoneurological hospital for war veterans since 2005.

As an example, the results of aforesaid patient B. treatment by technique DCASNS are mentioned lower, and in table 2 - estimations of changes of its *adaptive abilities* (local dysfunctions A_F).

Before treatment: complaints of frequent headaches, periodic risings of arterial pressure up to (160-180)/(95-110) the expressed prevalence of parasympathetic VNS and the expressed strain regulatory systems with active mobilisation of protective mechanisms.

After treatment: positive dynamics of indicators autonomous, immune and the endocrine systems *defining adaptive abilities of organism*; reduction

of intensity and frequency of the headaches; stabilized arterial pressure at level of 132/82.

Table 2

Patient B.	Research mode								
	FR			O			C		
	N	A_{max}	\tilde{A}	N	A_{max}	\tilde{A}	N	A_{max}	\tilde{A}
Before	20	104	202	27	337	443	17	132	192
After	1	10	10	10	183	213	4	38	47

The apparatus program complex for diagnostics and correction of vegetative dysfunctions is a perspective at human recovering of functional reserves lowered as a result of adverse influence of medium factors or as a result of illness.

References:

1. Baevsky R.M, Berseneva A.P. «The estimation of adaptive ability of an organism and risk of development of diseases»//M: Medicine, 1997, 236 p.
2. Kublanov V.S, Kostousov V.B., Popov A.A., Kazakov Y.E. «Heart rate variability analysis by modified wavelet in the task of human adaptive parameters estimation problem of an estimation », Biomedical radioelectronics, №1-2, 2008, p. 13-25
3. Kublanov V.S. «About some possibilities of an electrophysical method of correction of activity of sympathetic nervous system», Physiatrist, № 8, 2007, p. 39-43

Mobile radio-physical system for the functional researches of brain

V.S. Kublanov^{1,2}, V.A. Dorofeev², V.B. Kostousov³, A.V. Glazkov¹

¹Institute of Medical Cell Technologies, 620095, Russia, Ekaterinburg, 25, Sobolev St.

²Ecological and medical equipment (science researches and industrial designes), 623400, Russia, Kamensk-Uralsky, 29, Tchaikovsky St.

³Institute of mathematics and mechanics Ural Branch of the Russian Academy of Sciences, 620219, Russia, Ekaterinburg, 16, S. Kovalevsky St.

Corresponding author: V. Kublanov, <mailto:kublanov@usp.ru>

It is known, that in the construction of brain activity the complex interrelated biophysical systems are involved: neural networks, neuroglia, pachymeninx, liquor and blood circulation system. Changes in control of this system can lead to various kinds of functional disturbances. Most important of them are the intersystem changes defined by interaction of central and autonomous nervous systems, humoral, metabolic, myogenic and neurogenic mechanisms in cerebral blood circulation system.

The modern methods of functional diagnostics do not allow to identify the role of each system in pathophysiological arrangement changes in real time, especially in prenosological organism status.

The one of the perspective line of investigation at the decision of similar problems is registration of dynamic processes reflecting the physiological changes in organs and systems of organism using the multi-channel biotechnical system (BTS) in the realtime scale. It is necessary for such BTS, that one of its measuring channels (target channel) can be reflect the information changes directly in the object of research, and other (additional) channels - changes in other mechanisms providing the functioning of this object.

One of the possible approaches to similar BTS concept, designed for research of functional brain disturbances is discussed below.

It is known, that during human vital functions physical parameters of its organs and tissues changes: permittivity, impedance, magnetic susceptibility, temperature, voltages and currents potentials, tissue density, volume viscosity, shear viscosity, etc. The consequence of this is changing of own human physical fields: electromagnetic, acoustic, electric and magnetic [1]. The multi-channel microwave radiothermograph is chosen as the target

channel in discussed system, which provides the registration of brain own electromagnetic radiation defined by *metabolic activity* in local areas of brain tissue and the status of neurons, glia, local blood flow, etc.

Fluctuations of radiation $\delta U(t)$ depend on permittivity fluctuations $\delta\epsilon(t)$

$$\delta U(t) = \frac{k}{2\pi\lambda^2} \frac{\delta\epsilon(t)}{\bar{\chi}} T(t) ,$$

where $\bar{\chi}$ - average absorption factor, $T(t)$ – absolute thermodynamical temperature, κ – Boltshman constant, λ - wavelength of radiation.

The fluctuations of radiation $\delta U(t)$, as shown in [2, 3], are defined by blood and liquor dynamic changes, intercellular liquid transport in deep brain structures, and also functional changes of autonomous nervous system, neurohumoral processes of cardiovascular system, etc. Therefore as additional measuring channels of this system it is reasonable to apply the passive measuring devices, using for neurophysiologic researches, such as electrocardiograph and electroencephalograph.

The fig. 1 gives the general view of mobile radio-physical complex MRTRS which realizes the strategy of multi-channel BTS exposed above for research of functional brain disturbances.

The fig. 1 gives the block diagram of mobile radio-physical complex MRTRS in which the strategy of multi-channel approach of BTS exposed above is realized.

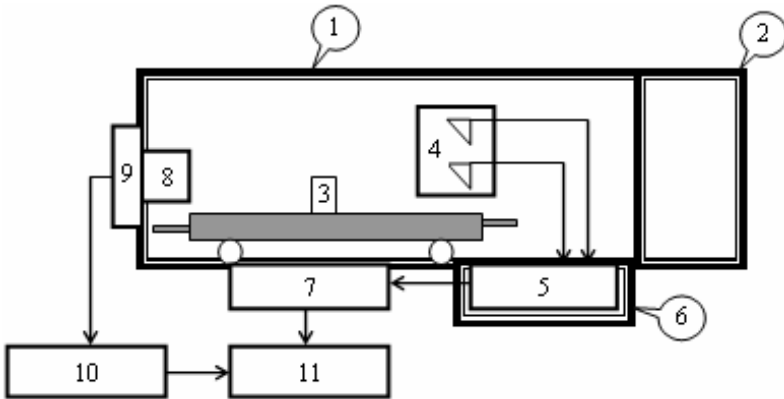


Fig. 1. Block diagram of mobile radio-physical complex MRTRS.

The complex MRTRS structure consists of: shielded chamber (1), shielded chamber entrance sluice (2), mobile stretcher (3), antenna assembly (4), medical multi-channel microwave radiothermograph MRT-40 (target channel), consisting of the thermo-balance block (5) and processor (7), shielded compartment for the thermo-balance block (6), gauges of additional measuring channels (8), block of VHF in-line filters (9), amplifier-converter devices of additional measuring channels (10), computer (11). The radiotopographer antenna-applicators (4) and the additional channels sensors (8) are located inside the shielded chamber (1). The communication of sensors (8) with the amplifier-converter devices (10) is carried out through the block of VHF in-line filters (9).

Fig. 2 presents the general view of complex MRTRS.



Fig. 2. General view of complex MRTRS.

In choosing of frequency range of brain own electromagnetic radiation, we followed from the necessity of monitoring the processes located in brain tissues on depth up to 4-5 cm. The optimum frequency range of the radiothermograph reception circuits is the frequency band from 650 to 850 MHz: technology in this case allow to receive in a radiometer receiver a

percentage bandwidth (20-30) % from average frequency f_0 and fluctuation sensitivity not less than $0,05 K/\sqrt{Hz}$.

Original structural concepts of entrance cascades of radiometric receiver microwave radiotopograph MRT-40 [5] allow to carry out of brain functional researches during 30-60 minutes.

Due to the high level of man-made statics in the chosen frequency range, the measuring of brain electromagnetic radiation is probable only at electromagnetic shielding of patient. Necessary electro-tightness in this case is defined by a concrete electromagnetic situation: as has shown operating experience of microwave radiothermographs in clinical conditions level of decoupling 50-60 dB is sufficient.

In clinical conditions, especially in acute periods of disease, it is not always possible to realize the researches of brain functional changes in condition of shielded room because of complexity of patients transportation and the management of the research (the influence of operator on registered process must be excluded). The more preferable is a mobile variant when shielded chamber carried out in the form of a capsule placed on the mobile carrier (bogie landing gear) that allows to approach the researches to the patient and to realize them without any limitations.

The choice of additional measuring channels of complex MRTRS is defined by research purposes and problems. Now we use more often the cardiointervalographer which allows to estimate in current time the autonomous nervous regulation of heart and changes in neurohumoral regulation of cardiovascular system.

The software computer provides patient data registration and storage, control of investigation process, registration in a common time scale of measuring channels output signals, to make their post-processing and the analysis and visualization of registered signals with application of correlation methods, time-and-frequency methods based on modified basic *Morlet* wavelet and methods of nonlinear dynamics [4].

The mobile radio-physical complex MRTRS is developed for brain functional researches by design office «Ecological and medical equipment (science researches and industrial designes)» and now realizes clinical tests in Republican clinical hospital of wars veterans of Republic Mary El (Ioshkar Ola) and in Institute of Medical Cell Technologies.

Creation of similar diagnostic systems answers the development concept of modern public health services in which priority is reserved to the prevention: main problem is diagnostics *of human functional reserves*

lowered as a result of adverse influence of environment in prenosologic status and in clinical practice at late stages of these disturbances development.

References:

1. Guljaev J.V., Godik E.E. «Physical fields of biological objects»//Bulletin AS the USSR. A series physical, 1983, №8, with. 118-125
2. Kublanov V.S., Dovgopol S.P., Azin A.L. «Research of a functional condition of a brain by methods of a multi-channel microwave radiothermography»//Biomedical radio electronics, №3, 1998, with. 42-49
3. Azin A.L., Gruzdev D.V., Kublanov,V.S. «Dynamics of intercellular transport in a brain tissue (the radio physical approach to research)»//the Bulletin of new medical technologies, 2002, т. IX, № 4, s.74-79
4. Kublanov V.S., Kostousov V.B, Popov A.A., Azin A.L. «Application of methodology of the wavelet-analysis at research of a functional condition of a brain». Works of the Russian scientific and technical A.S.Popov society of a radio engineering, electronics and communication. A series: Digital processing of signals and its application ». Issue VII//M: 2005, p. 489-494
5. Kublanov V.S., Dorofeyev V.A., al et «The zero radiometer», RU patent № 2091805, filing date 01.09.1992

Polygraphic DC amplifier for biomedical application.

Dmitriy Prilutskiy

Medical Computer Systems Ltd.

e-mail: pdima@mks.ru

A modern requirements of biomedical data acquisition hardware was based on long history of physiological researches. The physical type, input impedance, dynamic range, frequency band are defined for more width type of physiological values as electrocardiogram (ECG), electroencephalogram (EEG), electromyogram (EMG), impedancogram (IMG), respiration, seismic cardiogram (SCG), galvanic to skin reaction (GSR), photo plethysmogram etc. [1]. Of course, the list of channels and a necessity interchannel synchronization depend from current investigation. For example, some methods need synchronic acquisition for measure of jitter between ECG, ICG, SCG and photoplethysmogram and to calculate functional reserve of human cardiopulmonary system [2].

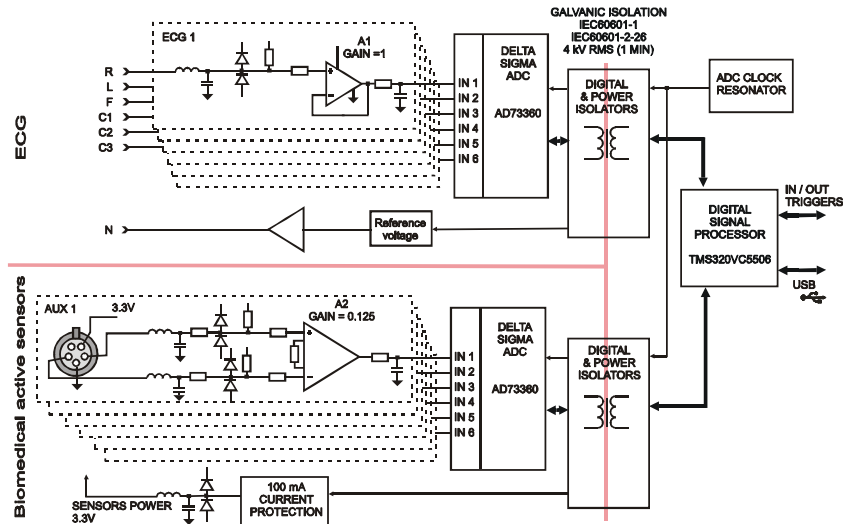
Typically the research acquisition hardware consist of a personal computer connected to lot of specialize amplifiers by universal analogy to digital board. Bioelectrical signals can be input to amplifier directly by electrodes. Non-electric signals as pressure, force, impedance etc transform to voltage output by sensors and signal conditioners. This is special electronic, electro-mechanic or electrochemistry devices. Common problems for researcher is cables between boxes, strong channels synchronization and common price of the system.

Was developed polygraphyc direct current (DC) amplifier KARDi2-NP for synchronous acquisition up to 6 ECG channels and up to 6 multi purpose differential channels of the auxiliari sensors. This is portable (155x140x40 mm), lightweight (300gram) computer device with USB interfaces without additional power supply.

Six monopolar ECG channels can used for calculation of standard lead (I-aVF, V1, V2) or Nebh lead [3] by software. A dynamic range of ECG channels is software-selectable from set $\pm 820, 410, 200, 100, 80, 40, 20, 10$ mV. ECG channels noise level less 15uV peak-peak (3 uV RMS) for 0.5-75 Hz pass band.

Six auxiliary sensors can connect to full differential channels with dynamic range ± 2.9 , 1.5 or 0.75 V. The voltage 3.3 V from filtered analog power used for sensor powering. A current of 15 mA limited for each active sensor.

Two a input digital TTL triggers built for synchronies detection of external events. Two a similar output triggers used for control of external devices.



KARDi2NP consist of ECG and auxiliary patient parts and computer part. The synchronies delta-sigma technology [4] was used for analog to digital converting (ADC) by front-end chip AD73306 [5]. The chip contain: 6 programmable gain arrays (PGA), 6 delta-sigma 2 MHz modulators, and 6 digital filters. Before ADCs was placed: input RF and EMC protection nets, preliminary DC amplifiers, a simple RC anti-aliasing filters. The instrumentation amplifiers were used for auxiliary channels. Common clock resonator for ADCs guaranteed synchronic acquisition for all channels. A 16 bit, 32 kHz ADCs data stream convert to 250, 500, 1000, 2000, 4000 Hz output sampling rate by digital signal processor (DSP) TMS320VC5506 [6]. DSP produce multi stage digital filtration, decimation [7] and transferring data via USB port. For example, a pass band 0 - 150 Hz (-3dB) correspond to 500 Hz sampling rate.

The device has strong galvanic isolations between computer and ECG parts, computer and auxiliary parts and ECG and auxiliary parts. All isolation barriers is reinforced according to IEC60601-1 standard for 4000V AC RMS 1 minute test voltage. Therefore using ECG and other sensors possible at same time without interferences and electrical risks.

Blue light around auxiliary connectors indicate a acquisition mode of device.



Was developed lot of NeoSENS™ auxiliary sensors for KARDi2-NP :

- respiration sensor belt (thorax / abdomen),
- galvanic skin response sensor,
- air-flow respiration sensor (nose flow),
- acceleration sensor,
- photo plethysmography finger sensor,
- complex impedance sensor (rheography),
- tremor sensor.

The Windows XP / Vista driver, application dynamic link library (DLL) and software demo samples created for designers of biomedical systems . The universal Windows program designed for researchers. The program functions is: channel definition, data acquisition, filtering and popular EDF+ format [8] storing.

So, the KARDi2-NP device is modern multi task biomedical amplifiers for next application:

- biomedical research,
- clinical polygraphy & somnography,
- clinical cardiology,
- screening,

- polygraphy as a part of the "lie detector".

References

1. Rangaraj M. Rangayyan. Biomedical Signal Analysis: A Case-Study Approach // Wiley-IEEE Press Series on Biomedical Engineering, 2002, p.552, ISBN: 978-0-471-20811-2
2. Baevskiy R.M., Baranov V.M. Bersenev E.U., Funtova I.I., Semenov U.N., Grigoriev A.P., Prilutskiy D.A. Method of estimation functional reserve of human cardio respiration system./ Russia Federation Patent №2240035 –2004
3. Malmivuo J., Plonsey R.: Bioelectromagnetism - Principles and Applications of Bioelectric and Biomagnetic Fields // Oxford University Press, New York, 1995
4. Kurikov S.F., Prilutskiy D.A., Selishchev S.V. Sigma-Delta analogue-to-digital converters in multichannel ECG and EEG acquisition systems // Medical & Biological Engineering & Computing, vol. 37,sup.1,1999, pp.286-287.
5. AD73360 datasheet. Six-input channel analog front-end. // Analog Device, 2000, www.analog.com
6. TMS320VC5506 data manual. Fixed-point, digital signal processor. – SPRS375A// Texas Instruments, 2007, www.ti.com
7. Fliege N. J. Multirate Digital Signal Processing: Multirate Systems - Filter Banks – Wavelets // Wiley, 1999, p. 352, ISBN: 978-0-471-49204-7
8. Kemp B., Olivan J. European data format 'plus' (EDF+), an EDF alike standard format for the exchange of physiological data. // Clinical Neurophysiology, 114 (2003): pp.1755-1761

Low power wireless ECG sensor

I. Chepiga, D. Prilutskiy, A.Ustinov

*Medical computer systems, Moscow institute of electronic engineering
e-mail: chivan@mks.ru, pdima@mks.ru, uartyom@mks.ru*

Current systems of electrocardiograph (ECG) analysis successfully solve problems of clinical diagnosing [1]. ECG is an electrophysiology signal registered from surface electrodes. Base ECG frequency range is 0,5–60 Hz, peak value 3–4 mV. Continue ECG monitoring practiced only for critical patients. It concerned with technical, economical and exploitation limitations. Cheap and ergonomically wireless ECG sensors may monitor essentially more patients and achieve early cardiological help.

Was developed 4-channels wireless ECG sensor. It's portable device with battery powering, his operating range is about 30 meters in housing. Sensor was integrated in a chest belt with electrodes, like Polar WearLink transmitter. For transmitting used wireless IEEE 802.15.4 standard [2] and originally high-level protocol, which allows operate together more then ten devices. Low power consumption of the sensor allows work up to 24 hours without charging.

Selection of wireless technology

Technical and exploitation characteristics of personal ECG sensor mostly depend from wireless protocol. Its type defines:

- safety of patient and operator;
- speed and quality of data transeiving;
- noise level of ECG sygnal;
- opportunity to simultaneous combined work with several sensors;
- length of data transeiving;
- electro-magnetic compatibleness with other medical devices;
- need to license or registrate channel;
- power consumption and endurance of autonomous work;
- dimensions of sensor;
- ergonomical characterictics.

For wireless transeiving on the distanse about dozen metres usually use radio or optical (infrared) channel. Infrared channel has some limitations, like high power consumption, low data speed and need to direct optical connection between receiver-transceiver. But in advantage for this protocol is

a missing of any law limitations. Radio-frequency transceiving is more attractive for sensor. It doesn't demand direct positioning of receiver-transceiver, has big operating distances and provide high speed data transferring.

Frequency range 2400-2500 MHz hasn't any law limitations and dedicated to free using. Ranges with cental frequencies 433 and 915 MHz have larger operating equipment. Negative factor of using 2,4 GHz range is it's popularity. Probability of interference with other devices is very high, it will be showed in degradation of data speed. For decreasing this effect used some various coding algorithmes. Some 2,4 GHz wireless solutions are presented in the list:

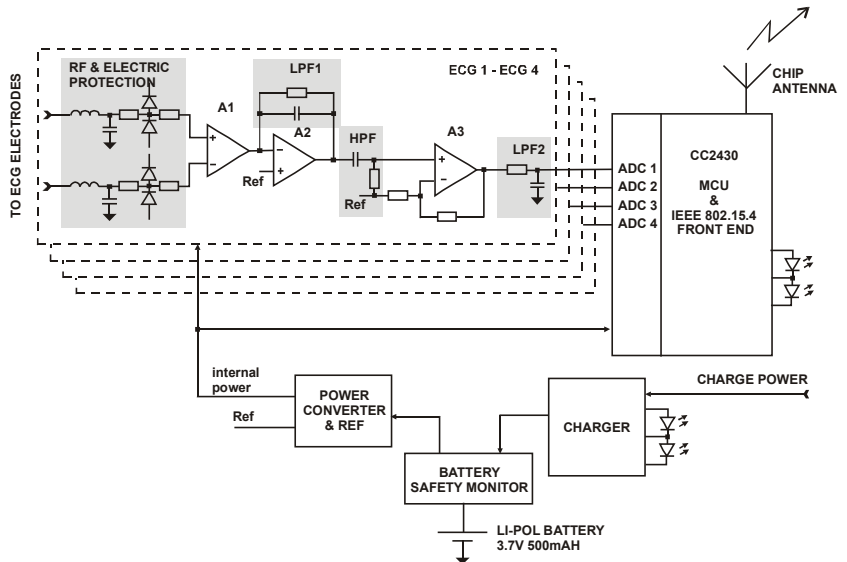
- IEEE 802.15.11 / WiFi;
- IEEE 802.15.1 / Bluetooth;
- IEEE 802.15.4 / ZigBee;
- nRF24AP1 Nordic technology;
- IEEE 802.15.4a / Nanotron Chirp Spread Spectrum technology.

IEEE 802.15.4 / ZigBee is verified and commercial accessible solution, allowing to develop low power devices and nets. There are a lot of manufacturers, supporting this technology. Protocol has great data transfer rate and allows using up to 16 data channels.

There are various medical ECG sensors, used IEEE 802.15.4 / ZigBee protocol, like wireless ECG system LifeSync [3] or NetGuard [4]. But these devices have some disadvantages, like big dimensions (LifeSync) or small number of channels (NetGuard).

Portative sensor with ZigBee radio channel

Pic. 1 illustrated scheme of ECG sensor. Circuit of this sensor builds on microprocessor CC2430 [5]. Built-in analog-to-digital converter processes data from 4 differential channels ECG and transmits them through 2,4 GHz 50 Ohm chip-antenna, manufactured by Antenna Factor. Each channel consists of differential amplifier A1 and operating amplifiers A2, A3, which provide signal gain and stabilization. To the input of A1 amplifier attached noise-protection diodes. LPF1 and HPF filters provide 0,15 – 100 Hz filter window. LPF2 is anti-aliasing filter.

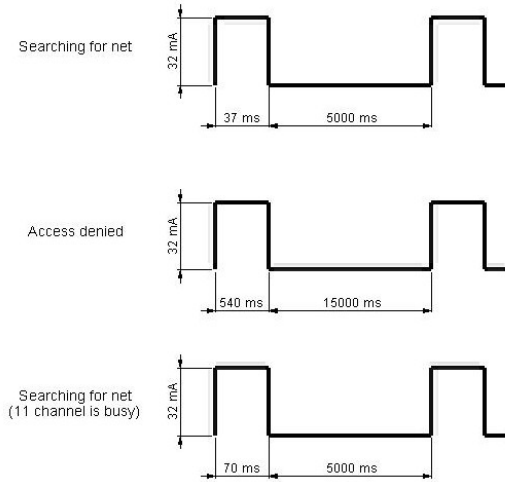


Pic.1. Wireless ECG sensor diagram

Chip-antenna is optimal for sensor, because has small dimensions and delivered in compact SMD package. Previous version of ECG sensor used a PCB-antenna, but it was very large (5x47 mm instead of 5x15 mm for chip-antenna). Sensor's output is 12 pin crimping connector. Device uses a 500 mAh Li-Pol rechargeable battery, charging made by miniature power supply connector. For indication of charge level and operating mode used two light emission diodes.

Personal telemetric sensor can operate in one of modes (with various current consumptions):

- sleep-mode (max 1 mA)
- searching for net (max 32 mA, see pic.2)
- transferring data (max 38 mA)



Pic. 2. Sensor's current consumption

For connection with personal computer used USB dongle, manufactured by Integration Associates, also may be used any other USB dongle.

For development software used official Texas Instrument manual and some software libraries, delivered with USB dongle, also made application for testing ECG sensor.

Conclusion

Usage of serial integral microprocessor with IEEE 802.15.4 radiochannel allow to developed cheap portative 4-channel ECG sensor. This sensor allows to processing and transceiving physiological signals within appartment up to 200 m². Device can perform long-term autonomous ECG monitoring of one patient or group of patients by creating wireless net. This net may combine ECG sensor with other types of devices working on IEEE 802.15.4 / ZigBee. Foreseen opportunity to connect special transceiver to improve working distances of sensor.

Apparently that these sensors may be used not only in clinical medicine and research centers, but in some industries, where important to control human operators, like atomic power stations or transporting systems. Sport or home ambulant patient's monitoring is another important areas for wireless ECG sensors.

References:

1. Davey P. The ECG in Clinical Decision Making. RSM Press, 2004
2. IEEE Standard 802.15.4. Wireless Medium Access Control and Physical Layer Specifications for Low-Rate Wireless Personal Area Networks. 2003
3. The LifeSync Wireless ECG system // LifeSync Corp, www.lifesynccorp.com
4. Steward S. Wireless ECG Enables Economic Patient Monitoring // MPMN journal, May 2008
5. CC2430 datasheet. A True System-on-Chip solution for 2.4 GHz IEEE 802.15.4 / ZigBee® – SWRS036F // Texas Instruments, 2007, www.ti.com

Electrodes' Requirements for Precardiac Measurements

A.V.Kobelev, S.I.Schookin

Department of Biomedical Techniques, Bauman Moscow State Technical
University, Moscow, Russia
ak_2@mail.ru

Introduction

Bioimpedance measurements provides useful information about living tissues, a human body and organs structures, physiological state and functions. Nowadays rheocardiomonitoning systems are widely used in reanimation and intensive care units. [1]

Heart movements give the main contribution in the pre-RCG signals. So they provide a way to determine and monitor parameters of the heart pump-function, for instance stroke volume.

Usually symmetric tetrapolar electrode assembling is used for the precardiac measurements [5] as well as in other bioimpedance measurements [3,4]. The present paper examines electrodes' requirements, including interelectrode spacing and electrodes' diameters which let you solve inverse problem [6] for horizontally layered model of precardiac tissues.

Results

Heart occupies a small region between the third and sixth ribs in the central portion of the thoracic cavity of the body. It consists of 4 chambers: 2 atriums and corresponding ventricles.

Because of the anatomic proximity of the heart to the lungs, the right ventricle does not have to work very hard to drive blood through the pulmonary circulation, so it functions as a low-pressure (40 mmHg gauge) pump compared with the left side of the heart, which does most of its work at a high pressure (up to 140 mmHg gauge) to drive blood through the entire systemic circulation to the furthest extremes of the organism. Therefore, right ventricle has wall thickness on the order of one-third that of the left ventricle, up to about 4 mm. Also right ventricle is placed very close to the chest. [2]

So it is possible to represent the pre-cardiac right ventricle area as a horizontal two-layer structure (Fig. 1) with the following parameters: the 1-st layer (upper-soft tissues) has height if about 20 mm and specific resistance of

about 8 Ohm-m; blood in right ventricle (the 2-nd layer) has specific resistance of about 1,35 Ohm-m.

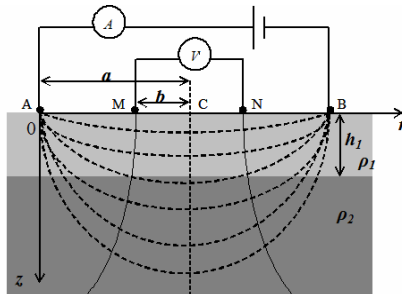


Fig. 1 A horizontal multi-layer model the precardiac area and a scheme of a symmetric tetrapolar electrode assembling

To avoid interference from other tissues, interelectrode spacing between current electrodes (Fig. 1, distance $2a$) should be equal or less than the length of the right ventricle, which is about of 60 mm.

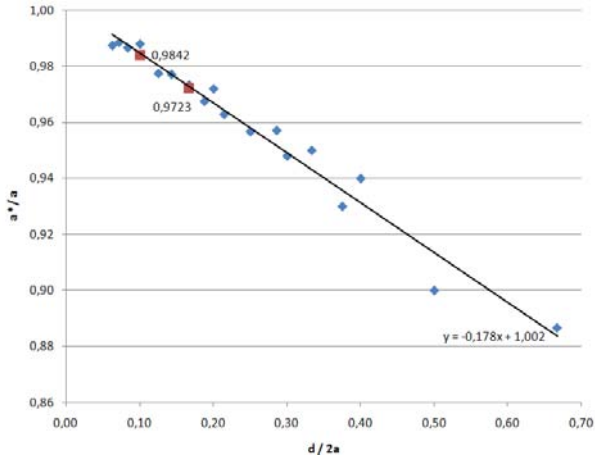


Fig. 2 Effective interelectrode distance depends on current electrode's diameter

The diameter of current electrode affects on “effective” interelectrode distance (Fig. 1, distance $2a$), that is introduces systematic error into inverse

problem solution [6]. We have estimated dependency (Fig. 2) between ratio of “effective” a^* to “real” a distance and current electrode’s diameter d using finite element analysis [7]. In particular, for 10-mm electrodes you should keep in mind real a distance is equal to $0,9723a$. Note that this result does not depend on layers’ conductivity.

On the other hand, diameter of measurement electrodes affects on inverse problem solution as well (Fig. 3). Unlike current electrode’s diameter, measurement electrode’s diameter d does not affect on “effective” b^* distance in case 10-mm electrodes we have used.

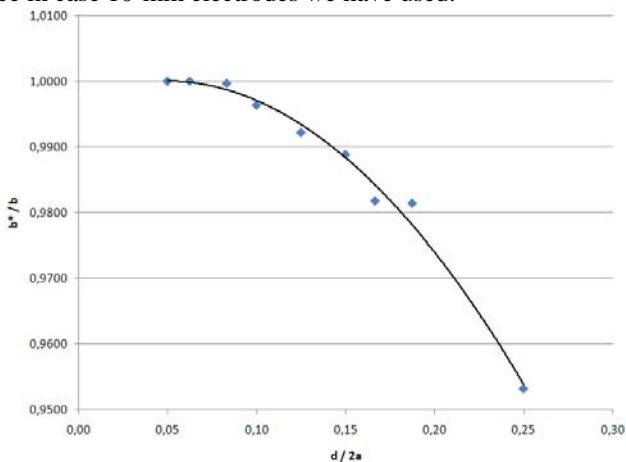


Fig. 3 Effective interelectrode distance depends on measurement electrode’s diameter

Conclusion

Requirements for electrode assembling let us solve inverse problem of precardiac tissues with smaller errors which improves determination and monitoring parameters of the heart pump-function.

Acknowledgment

This work was supported by Grant #07-02-01453 of the Russian Foundation for Basic Research.

References

1. S.I. Schookin, L.P. Safonova, I.K. Sergeev, O.S. Medvedev (2007) **Mapping and Monitoring of Cardioactivity: Multi-Channel Impedance Technology and System.** IFMBE Proceedings Vol. 17
2. Ed. Joseph D. Bronzino (2000) **The Biomedical Engineering Handbook, Second Edition.** CRC Press LLC
3. R.P. Patterson, and F. Yang (2007) **Modelling the measurement of thoracic tissue impedance layers with local electrode arrays.** IFMBE Proceedings Vol. 17
4. J. Väisänen, V-P. Seppä, P. Kauppinen, J. Malmivuo, J. Hyttinen (2007) **Sensitivity of the Tetrapolar Lead Configurations on the Impedance Changes of the Lungs.** IFMBE Proceedings Vol. 17
5. L.P. Safonova, S.I. Schookin (2005) **Impedance precordial mapping of cardioactivity: information capacity study.** Biomedical technologies and radioelectronics 9:4-11 (In Russian)
6. Tarantola, Albert. **Inverse problem theory and methods for model parameter estimation.** QA371.T357 2005 515.357—dc22
7. **Release 10.0 Documentation for ANSYS.** Operations Guide.

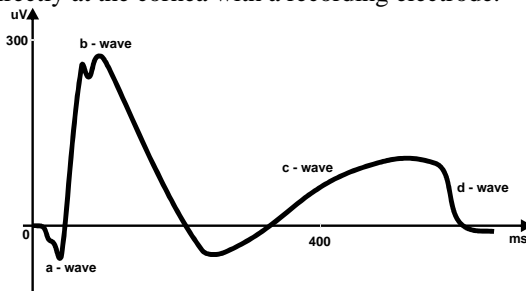
Hardware and software system for single-flash electroretinogram

*Sergey V. Rezvykh, Igor N. Spiridonov,
Marina V. Zueva, Irina V. Tsapenko*

*Bauman Moscow State Technical University
Moscow Helmholtz Research Institute of Eye Diseases
lkjfly@mail.ru, inspiridonov@yandex.ru,
zueva_mv@mtu-net.ru, sunvision@mail.ru*

The full-field electroretinogram measures the overall rod- and cone-generated retinal responses and is the only electrophysiologic test that assesses rod-generated activity. The full-field electroretinogram (ERG) is essential in the diagnosis of numerous disorders including cone dystrophy, retinoschisis, congenital stationary night blindness and others. The ERG should be used in the conjunction with a thorough ocular examination and when necessary other tests such as visual field and fluorescent angiography.

The ERG waveform (picture 1) represents a summation of the electrical activities of all cells of the retina. The physiologic origin of an ERG response is dependent on the adaptive state of the retina, stimulus intensity and duration, stimulus type, and stimulus color. So, the ERG response is produced by light-induced movements of ions in the retina. This activity is measured indirectly at the cornea with a recording electrode.

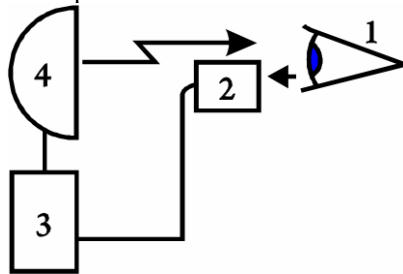


Picture 1

The essential shortage of modern system for ERG examination is the subjectivity of ERG parameters estimation. So, our aim is the automation of ERG examinations which will decrease the subjective factors of ERG interpretation and increase the precision of ERG parameters evaluation. But correct automation is impossible without elaboration of requirements to the diagnostic parameters and hardware system.

Requirements to the ERG responses are matched to the standards of International Society for Clinical Electrophysiology of Vision. One of the longstanding ISCEV goals is to establish worldwide standard clinical protocols for electrophysiological examinations. Based on input from many members, ISCEV has published the compilations of protocols. We used these compilations, carried on an investigation and formulated the requirements.

Simplified scheme of ERG examination consists on 4 elements (picture 2). The electrode (2), which is made from methylmethacrylate, is placed on the cornea (1). The pupils should be fully dilated with pharmacologic eye drops, because small pupils reduce retinal illuminance and ERG responses. The flash ERG stimulus is delivered in a white full-field dome (4). After electrode placement, impedance and baseline signals are evaluated to assess electrical noise interference and artifacts from eye movement and blink. The ERG signal is small compared to the electrical noise from power current and from heart, muscles, and brain. Differential amplifiers (3) amplify the difference in input between the recording and reference electrodes and reject signals common to both inputs.



Picture 2

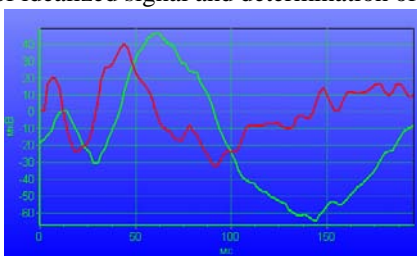
For diagnosis of eye diseases we need the knowledge of cellular contribution in ERG responses. This contribution will be analyzed by components researching of ERG. Knowledge of the physiologic origin of ERG components is derived primarily from animal studies by intraretinal microelectrode recordings and ERG changes in response to chemicals with known retinal cellular effects.

Granit and Riddell demonstrated that the ERG waveform is a summation of three processes or potentials called PI, PII and PIII. PI is a slow positive potential from the retinal pigment epithelium that contributes primarily to the c-wave. PII is a positive inner retinal potential related mostly to bipolar cell activity and makes a major contribution to the ERG b-wave. PIII is related to Muller cell and photoreceptor activity.

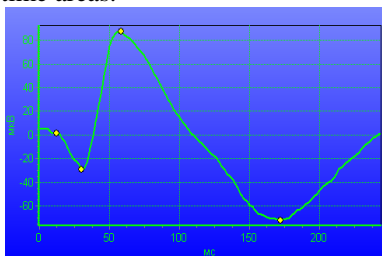
We analyzed the latest works of head researchers and carried out our investigations. We suggested advanced model of component PII. Experiments on the rabbits confirmed our model.

Determination of parameters of single-flash ERG in global maximum and minimum of ERG response is the main instrument of quantitative description in clinical practice. However the amplitude and peak latency of a- and b-waves don't provide us the accurate quantitative information about distribution of alteration in retina. In this case the complex of methods (standard and original) is used for determination of character of pathology. Combined parameters allow us to estimate the topography of alterations.

Contour analysis (picture 3) of single-flash ERG in conjunction with correlation analysis allows us to detect and identify essential points (picture 4). This method realizes the convolution of ERG and the component sample of idealized signal and determination of time areas.



Picture 3



Picture 4

The software for ERG processing has been created. Now it is used in Moscow Helmholtz Research Institute of Eye Diseases. This software allows us to convert different formats of ERG, evaluate ERG parameters, simulate single-flash retinal signal and permit to plot the distribution of derivative to view the development of this parameter in time.

Research of Fingerprints Minutiae Position Stability

E.V. Sologub, I.N. Spiridonov, A.A. Khrulev

*Bauman Moscow State Technical University (BMSTU),
s-katherina@yandex.ru, inspiridonov@yandex.ru,
andrey.khrulev@gmail.com*

Biometrics belongs to those areas of modern technologies which rate of development steadily grows during last ten years. It is promoted by development of computer technologies, expansion of automation spheres and growth of information value. It is possible to allocate among the areas using identification or verification of the person: access control systems, information, time control system and registration of visitors, carrying out of electronic payments, verification on Web-resources, biometric passport and visa documents, biometric identification cards.

Last years fingerprint verification and identification of the person is most widely used. Advantages of fingerprint access are simplicity of use, convenience and reliability. A local level fingerprint systems of person identification divides into systems of identification on local or global irregularity finger pattern. And in turn systems of identification on local irregularity finger pattern divide into types minutiae and pores. Systems based on minutiae are widely used.

In this connection, there is a question: what quantity of minutiae it is possible to consider sufficient for identification or verification. Is worthy the quantitative criterion offered in the beginning of 20 centuries by French criminalist Baltazar. The results received by it testify that concurrence of 17 attributes can meet only in 17 billion 179 million 869 thousand 184 fingerprints, i.e. the found out concurrences of 17 details probably at research 1,7 billion person. As then the population of globe did not exceed 1,6 billion person this quantitative attribute has been assumed as a basis. In some countries in view of a population the quantity of conterminous attributes has been reduced up to 12. Long time the quantitative criterion equal 12 operated in practice of judicial bodies and expert establishments of the country. In some countries it is used at present. The mathematical basis of calculation is correct and there was no such case, when at concurrence of 12-17 minutiae (at absence of distinctions certainly) would be drawn an erroneous conclusion. On the contrary, this criterion is obviously overestimated also its use in practice is artificial limited opportunities of examination. Thus, if to

consider the qualitative party of attributes for identification the smaller quantity of attributes is required. So it is important to determine minutiae in the central or peripheral areas of fingerprint.

During this research it was considered and analyzed minutiae fingerprints position stability at removal from the center of a fingerprint. 350 fingerprints (35 finger patterns with 10 realizations each) have been processed. Minutiae were fixed by special software for visualization of allocation of local features (MinutMeasure).

Displacement feature Sm_j^i (where i - number of minutia, j - number of realization) is calculated under the formula (1):

$$Sm_j^i = \sqrt{(X_{dm} - X_{dt})^2 + (Y_{dm} - Y_{dt})^2}, \quad (1)$$

where (X_{dm}, Y_{dm}) – the displaced coordinates of a minutia,
 (X_{dt}, Y_{dt}) – the displaced coordinates of fingerprint center.

Radiuses of minutiae R^i (where i - number of a minutia) is calculated under the formula (2):

$$R^i = \sqrt{(X_{im} - X_t)^2 + (Y_{im} - Y_t)^2}, \quad (2).$$

where (X_{im}, Y_{im}) – the coordinates of a i -th minutia,
 (X_t, Y_t) – the coordinates of fingerprint center.

Linear correlation analysis of the radius and displacement of minutiae dependence in considered fingerprints showed the presence of statistically significant correlation ($\alpha=5\%$), with the value of correlation coefficient $r = 0,921 \div 0,945$.

On the basis of the lead researches of minutiae stability depending on distance from fingerprint center, it was drawn a conclusion on linear reduction of minutiae position stability from the center to peripheral parts of a fingerprint. Thus during identification process it is expedient to set different thresholds for comparison of the central and peripheral fingerprint areas, with more confidence degree for minutiae located in the central part of fingerprint.

Voice-based biometric identification

O.V. Vasilevskaya, A.A. Khrulev, J.G. Gorshkov, I.N. Spiridonov

*Bauman Moscow State Technical University (BMSTU)
VasilevskayaOlga@bk.ru*

Biometrics refers to the automatic identification of a person based on his/her physiological or behavioral characteristics. This method of identification is preferred over traditional ones including passwords methods.

Various types of biometric systems are used for real-time identification, the most popular ones are based on face recognition and fingerprint matching. Other biometric systems use iris and retinal scan, speech, facial thermograms and hand geometry.

Depending on the context, a biometric system can be either a verification (authentication) system or an identification system. In the identification task the goal is to recognize the unknown speaker from a set of N known speakers. In verification, an identity claim (e.g., a username) is given to the recognizer and the goal is to accept or reject the given identity claim.

This paper is focused on the biometric identification by speech.

There are many different algorithms of speaker identification. We collected a speaker database of 167 speakers and evaluated the performance of 2 different algorithms of speaker identification based on the pitch and the formants extraction. The results are given in Table 1.

Table 1. Identification rates of different speaker identification algorithms.

Algorithm	Signal length, sec	Identification rate, %
Based on the pitch	> 30	32.0
	16 – 96	60.5
Based on the formants	> 96	61.1

So we received unacceptable results. After that we analyzed different identification algorithms and focused on one of the best. This algorithm is based on the vector quantization (VQ) [1-3]. The structure of VQ-based speaker identification system is illustrated in Figure 1. There are two phases in the speaker identification: training and recognition. In the training phase we construct for each speaker a mathematical model from his/her reference speech signals, using feature extraction and vector quantization. The models

are stored in the database. After that a recognition phase begins. We take a speech signal of an unknown speaker and extract features by the way mentioned above, measure the distance between the extracted features of an unknown speaker and stored speaker models of reference speakers. At the end of the process we make an identification decision by the smallest distance between vectors.

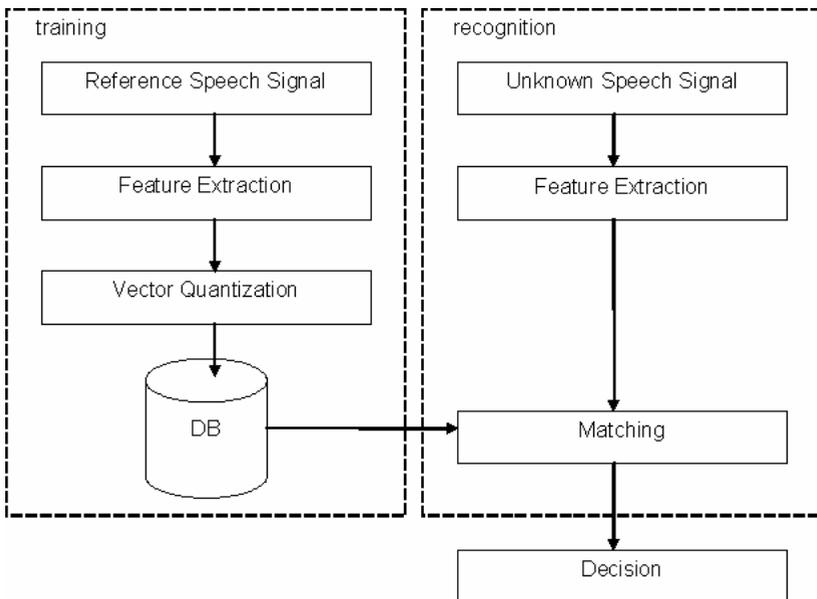


Figure 1. VQ-based speaker identification system

Feature extraction begins with the short-term spectral analysis. This means that the signal is first divided into fixed-length short frames, e.g. 30 milliseconds. The neighboring frames usually overlap, e.g. by 10 milliseconds. After framing, these short-length “subsignals” are considered as independent signals. For each frame, a fixed-length feature vector is computed, which describes the acoustic behavior of that particular frame.

Before frequency analysis, we apply a window function to the frames. The most simple windowing function is the rectangular window, i.e. “no window at all”. However, usually smoother functions are used, and the most

common in speech processing is the Hamming window. Smoother functions are better than rectangular window because the latter has abrupt discontinuities in its endpoints, which is undesirable for the frequency analysis.

After receiving a set of frames we apply cepstral function to each frame (see Formula). The output is a vector with the desired number of cepstral coefficients, for example 12. Cepstral coefficients are the features of our signal.

$$f_{s_k^q}(n) = \text{Re} \left[\frac{1}{N_t^{win}} \sum_{l=1}^{N_t^{win}} e^{i \frac{2\pi(l-1)(n-1)}{N_t^{win}}} \ln \left\{ \sum_{\tau=1}^{N_t^{win}} s(\tau) e^{-i \frac{2\pi(l-1)(\tau-1)}{N_t^{win}}} \right\} \right], n = 0, N_t^{win} - 1 \quad (1)$$

where N_t^{win} – length of frame;

$s(\tau)$ – speech signal;

To reduce the amount of data after feature extraction procedure and therefore to remove the difficulties of time and memory requirements we apply VQ. The main idea of VQ is to divide a set of points into parts (clusters) and to determine the centre of each cluster (cluster centroid). In this way for each speaker we create the so-called codebook – vector of clusters centroids. The codebook represents the speaker model which is stored in the database. In our algorithm we used k-means clustering.

So we began to implement this algorithm in order to receive the results that will allow us to incorporate this method in the general identification system.

Bibliography:

1. Kinnunen T., Kilpelainen T., Franti P. Comparison of clustering algorithms in speaker identification., IASTED Int. Conf. on Signal Processing and Communications (SPC'00), Marbella, Spain, 222-227, 2000.
2. T. S. Chang, S.D. Van Hooser. Two new methods for speaker recognition using cepstral analysis., CNS-Spring, 1996.
3. Kinnunen T., Franti P. Is speech data clustered? – statistical analysis of cepstral features., European Conf. on Speech Communication and Technology, (EUROSPEECH'2001), Aalborg, Denmark, Vol. 4, pp. 2627-2630, September, 2001.

A multiscale algorithm for P-wave parameters estimation

Shchepetov D.S.

*Moscow Engineering Physics Institute
(State University),
email : dshchepetov@mail.ru*

Estimation of main parameters of P-wave, like a P position, width and amplitude is a quite complicated task for automatic analysis of ECG. However the results obtained from such analysis (given these parameters are estimated accurately) could be essential to determine patient health status[1,2].

To simplify this problem almost all of current P-wave detection algorithms are working under assumption that all R-waves of QRS complexes are known. However, even in this case there are many problems encountered by analysis algorithm developer. The main problems are:

1) Amplitudes and durations of basic ECG structural elements of are listed in the table 1. As follows from this table there are many parasite signals (noise, previous QRS complex T-wave) having amplitude greater than P-wave one.

Табл. 1. ECG structural elements.

Elements name	Amplitude, mV	Duration, sec.
Motion artefacts	> 1.0	>0.3
QRS Complex	1.0	0.04-0.10
T-wave	0.25	0.1-0.25
P-wave	0.06	0.1(in a normal state)
Noise	0.05-0.07	<0.02

2) In addition to correct P-wave detection and estimation the algorithm have to handle following situations correctly: no P-wave presented(e.g. ciliary arrhythmia), too many P-waves presented (atrial flutter).

3) P-wave duration, polarity, and form could change during the ECG investigation.

4) Previous complex T-wave, current QRS could collide P-wave. In this case many modern algorithms (i.e.[4]) are ineffective.

We propose a new approach, which could be able to detect P under almost any conditions.

Let us describe assumptions, under which we will detect P-wave. ECG in the concerned section is of the form:

$$\text{ecg}(t) = P(t) + \text{move}(t) + \text{noise}(t) + \text{prevT}(t), \quad (1)$$

where $P(t)$ – a P-wave, $\text{move}(t)$ – motion artifacts, $\text{noise}(t)$ – high-frequency noise, $\text{prevT}(t)$ – a T-wave of a previous QRS. Let us discuss characteristics of signals concerned. Consider that $\text{move}(t)$ in the concerned section that has duration of 0.25-0.5 secs. could be approximated (quite accurately) by second order curve

$$\text{move}(t) = a + b \cdot t + c \cdot t^2, \quad (2)$$

This estimation is based on the model described in [3].

Then, we consider the high-frequency noise to be a random process with known density and zero correlation.

P-waves and T-waves belong to a small number of known families parametrized by amplitude, width and position. For example, we could use the family of following form:

$$f_{a,p,v} = a \cdot \frac{1}{\cosh^2\left(\frac{x-p}{v}\right)}, \quad (3)$$

This model was introduced in [2]. In this case width, amplitude and position are denoted v, a, p respectively. As shown in table 1 P-wave have a set of parameters $\{v, a, p\}$ different from it for QRS and T-wave.

Finding of P-waves consists in estimating all high-amplitude waves' parameters and throwing out waveforms which parameters are lies beyond the range of interest.

For this purpose consider the following one-parametric family of filters

$$f_w(t) = \sum_{i=0}^{i=9} (f_d(i) + (f_d(i+1) - f_d(i)) \cdot \frac{x - i \cdot w}{w}) \cdot \delta_{i,w}(x),$$

$$\delta_{i,w}(x) = \begin{cases} 1, & x \in [i \cdot w, (i+1) \cdot w] \\ 0, & \text{otherwise} \end{cases}, \quad (4)$$

A representative of this family is shown on the fig.1.

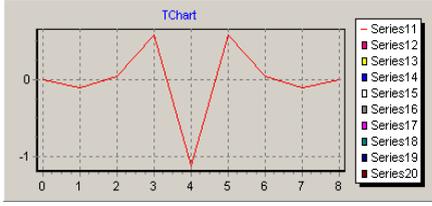


Fig.1 Filter representative

For filtered signals $move(t)$ and $noise(t)$ we have

$$F_w[ecg(t)] = \int_0^{9w} ecg(t+x) \cdot f_w(x) dx$$

$$F_w[move(t)] \equiv 0 \quad , \quad (5)$$

$$F_w[noise(t)] = \varepsilon(t) : \frac{1}{N} \int_0^N \varepsilon^2(t) dt \approx \left(\frac{1}{N} \int_0^N noise^2(t) dt \right) \cdot \frac{0.84}{w}$$

Thereby, these signals are suppressed by this filter with increasing w . The filter gain is the greater the closer filter middle is to the P-wave position.

Filter gain also depends of w . If this dependence is monotone one might deduce a width parameter (v) of P-wave from filter parameter w^* , that satisfy the following condition $|F_{w^*}[P(t)]| = \max_w |F_w[P(t)]|$.

The search and the analysis of waves performs as follows: an ECG section having duration of 64-128 points(0.25-0.5 sec. with sampling rate of 250 Hz) is filtered in 6 scale ranges with $w = \{1,2,4,8,16,32,64\}$. Scale range with $w = 0$ is used to estimate noise standard deviation(SD). Significant extremes (filtered signal extremes having a filtered signal value less than a user-defined thresh within their neighborhood)) are selected from ranges with $w = \{4,8,16\}$ and w^* is calculated for these extremes. For the purpose of optimization w^* is defined using the following procedure:

$$\begin{aligned} w_i^* &= \text{estim}(w_{i-1}^*, w_{i-1}^l, w_{i-1}^h) \\ w_i^l &= w_i^* > w_{i-1}^* ? w_{i-1}^l : w_{i-1}^* \\ w_i^h &= w_i^* < w_{i-1}^* ? w_{i-1}^h : w_{i-1}^* \end{aligned} \quad (6)$$

where $\text{estim}(\dots)$ is a three-point parabolic estimation of extremum position. The waves having parameters lying beyond the range appropriate for P-wave parameters are rejected. Depending of waves accepted the following

decisions could be made: no P-wave presented (if there is no accepted waves), atrial flutter (if the number of waves accepted is greater than 3), P-wave (in this case we mark the wave having the set of parameters that most resembles the previously marked P-wave ones as P-wave)

This algorithm was tested on three groups of artificial signals containing 100000 samples and having different noise SD(0,50%,100%), on the AHA DB and MIT databases, and on 30 manually marked holter ECG records. The results are listed in the table 2.

Табл. 2. P-wave estimation quality.

	Percent of correctly marked P	Percent of errors due to estimation or underestimation of accepted waves	Percent of inexact P-wave parameters estimation (relative error greater than 20%)
An artificial signal, noise SD 0%	100	0%	0%
An artificial signal, noise SD 50%	98%	0%	2%
An artificial signal, noise SD 100%	96%	1%	3%
AHA	97%	1%	2%
MIT	96%	1%	3%
30 holter records	98%	1%	1%

Examples of quite noisy ecg, when P is marked stable is listed on the fig.2



Fig.2 P-wave detection examples

References

1. Hatziyianni I. et al. «P-wave dispersion evaluated on ecg or 24h-ECG is a predictor of paroxysmal atrial fibrillation in essential hypertension», American Journal of Hypertension, 2004,17, 149A–150A
2. Nakamura A. et al. «clinical significance of prolonged P wave width after right atrial appendage pacing in sick sinus syndrome», Circulation, 2003 Jun, 67(6), 485-489
3. Huflejt M., «Modelling and simulation of skin-stretch-caused motion artefacts in single-channel ECG signal. 41», Jahrestagung der DGBMT - Deutschen Gesellschaft für Biomedizinische Technik im VDE, Aachen, September 2007
4. M. Sabry-Rizk et al. «Novel decision strategy for P-wave detection utilising nonlinearly synthesised ECG components and their enhanced pseudospectral resonances», IEE Proceedings - Science, Measurement and Technology, 2000, 147(6), 389-396
5. McFalan H.W. et al. Comprehensive Electrocardiology:Theory And Pratices, NY Press, 1978

Design and Application of the Method for Biolocation Data Processing

L. N. Anischenko, V. B. Parashin.

*Bauman Moscow State Technical University, E-mail:
Anishchenkol@inbox.ru*

The method for people location and diagnostics is based on the reflected signal modulation in time with move of the body surface and internals especially while breathing, heart beating and articulation. This method could be named as biolocation. The main advantages of biolocation are possibility of a remote detection and contactless receiving of information about functional state of a human and a human presence behind the optically opaque obstacle[1-3].

Another no less important field of application of biolocation is medicine. There are such possible fields of application for biolocation as somnology, cardio reanimation, functional diagnostics, breath and pulse monitoring(e.g. in burn centers when it is difficult to use the contact sensors), contactless estimation of the examinee psycho-emotional state(e.g. for operators of a compound machine complex).

There are experimental gears of prototypes in some of listed fields of application especially for detection people behind building structures. However medical applications are not adequately explored and well-grounded in many respects. It presents absence or imperfection of methods for a biolocation aperture use.

While rejection the transmitter penetrating signals and the signals reflected from top beacons (TB) it is possible to achieve high sensitivity for detection of the objects surface of which is subjected to mechanical fluctuations. Radio frequency signal sensitivity for Giga HertZ range waves potentially achieves 10^9 m.

In practice observation of alive objects using biolocator is carried out against a background of signal reflections from TB. Usually the energy reflected from TB outbalances the energy reflected from the examinee and parts of his body. At the same time reflected from a human signals are characterized by modulation in time with breathing and heart beating. Signals reflected from TB have not such a modulation or they have another time and frequency content. It is the base of the methods for detection and registration of signals reflected from alive objects against a background of TB.

Final result of the signal processing in a biolocator with the range gating is getting “range-frequency” matrix with following selection of the breathing and heart beating signals in the target range cell. This matrix contains all possible signal reflection from the TB located in different range cells, all of them have zero or approach zero features. The suppression signals from TB is carried on by rejection of the matrix components for the approach zero frequencies.

It is possible to separate breathing and heart beating signals much as the suppression signals from TB namely using rejection frequency components corresponding to breathing from the “range-frequency” matrix. In the simplest case cells of the “range-frequency” matrix are set to zero.

Example of the signal reflected from an examinee for one of probing frequencies is shown in Fig.1. The examinee seated at the 1.5 m distance from the locator antennas. At a quiet state heart beating frequency for the examinee was approximately 75 beat per minute, breathing frequency was 18 breath per minute. Since the fluctuation amplitude and lungs volume significantly greater than similar heart parameters then cardiac muscle contractions are observed as the high-frequency modulation against a background of thorax contractions. It can be seen in Fig.1.

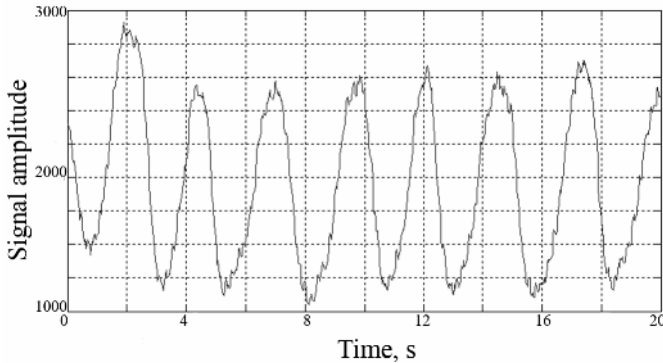


Fig.1. Radar signal reflected from the quiet breathing examinee seated at the 1.5 m range.

The “range-frequency” matrix for the same experiment before and after breathing harmonics rejection is given in Fig.2.

Reconstruction of breathing and heart beating signals is carried out using Fourier inversion the matrix row corresponding to the distance to the examinee. Phases of Fourier inversion corresponding to “range-frequency” matrixes from Fig.2 are shown in Fig.3.

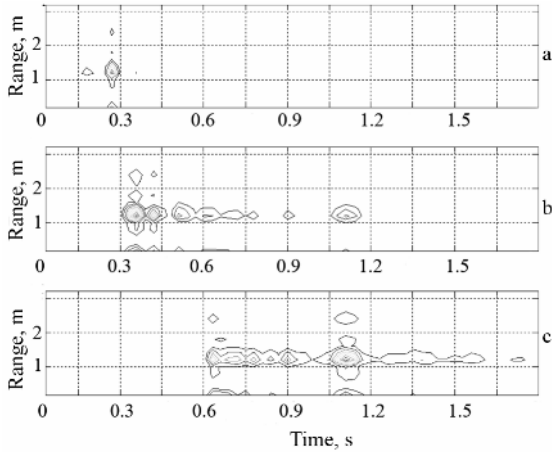


Fig.2. The “range-frequency” matrix for the examinee at 1.5 m range:
 a - before breathing harmonics rejection, b – after breathing harmonics rejection, c - after rejection of the second breathing harmonic.

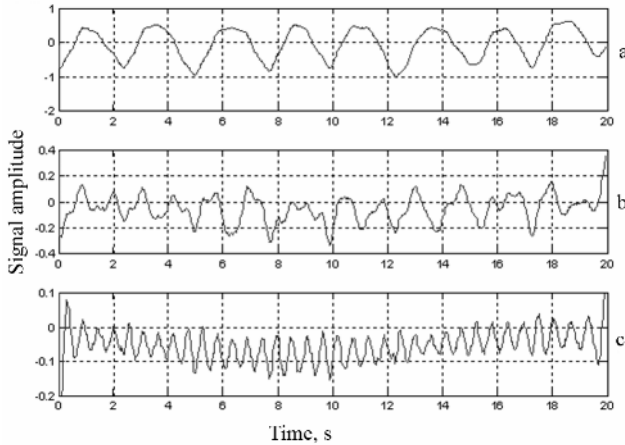


Fig.3. Reconstructed breathing and heart beating signals of the examinee corresponding to “range-frequency” matrixes from Fig.2.

Results of experimental data processing show that the method of the breathing harmonics rejection allows to part breathing and heart beating signals.

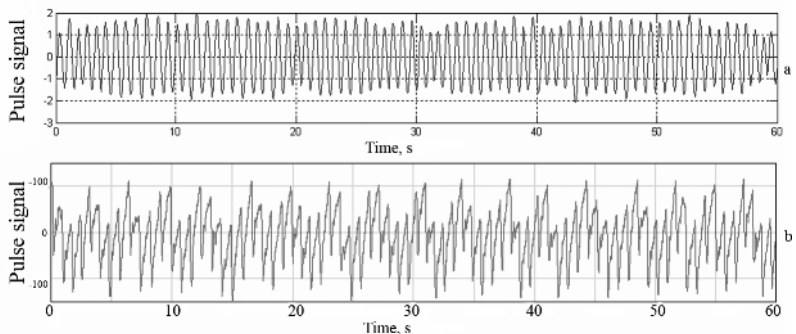


Fig. 4. Heart beating signal obtained using biolocator(a) and “RheoCardioMonitor”(b).

“RheoCardioMonitor” developed at BMSTU was used for the heart beating signal verification. Pulse signals obtained using biolocator and “RheoCardioMonitor” are given in Fig.4a, b. Histograms for the pulse intervals determined according to these signals are shown in Fig.5a, b.

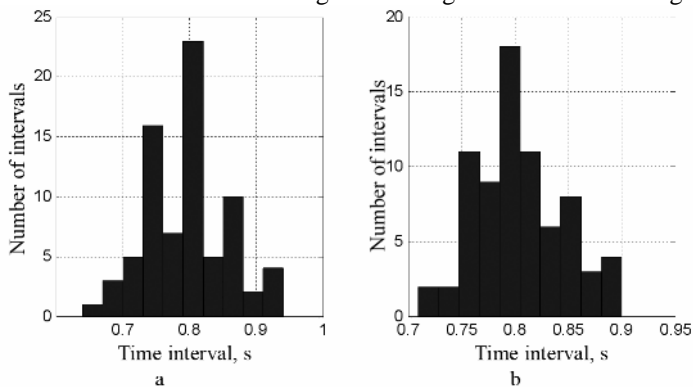


Fig. 5. Histograms for the pulse intervals for signal obtained using biolocator(a) and “RheoCardioMonitor”(b).

A test bench for remote measuring breathing and heart breathing parameters was created within the bounds of national project “Education”. At present the test bench is part of Laboratory of noninvasive biomedical technologies attached to Bio-Medical Engineering faculty of BMSTU.

References

[1] Bugaev A.S., Chapursky V.V., Ivashov S.I. Mathematical Simulation of Remote detection of Human Breathing and Heartbeat by

Multifrequency Radar on the Background of Local Objects Reflections. 2005 IEEE International Radar Conference Record, Arlington, Virginia, USA, May 9-12, 2005.

[2] Detection of Human Breathing and Heartbeat by Remote Radar. S.I. Ivashov, V.V. Razevig, A.P. Sheyko, I.A. Vasilyev. Progress in Electromagnetics Research Symposium (PIERS 2004), March 28 -31, 2004, Pisa, Italy, pp. 663-666.

[3] A.S. Bugaev, V.V. Chapursky, S.I. Ivashov, V.V. Razevig, A.P. Sheyko, I.A. Vasilyev, Through Wall Sensing of Human Breathing and Heart Beating by Monochromatic Radar. Proceedings of the Tenth International Conference on Ground Penetrating Radar, GPR'2004, June 21 -24, 2004, Delft, The Netherlands, Vol. 1, pp. 291 -294.

Electrochemical instruments and sensors based on nanocrystalline materials for Bio- , chemical analysis and medical diagnostics

Kh.Brainina^{1,2}, A.Kositzina^{1,2}, V.Kublanov¹, Ya.Kazakov¹, M.Khodos².

¹Institute of Medical Cell Technology, 620095, Russia, Ekaterinburg, 25 Sobolev St.

²IVA Ltd, 620219, Ekaterinburg, 8 Marta St, 62, <http://iva.usue.ru>

Corresponding author: Kh.Brainina, mailto: baz@usue.ru

Abstract

Electrochemical screen-printed sensors, based on carbon (metal) nanoparticles containing transducer and organic/inorganic receptor, immobilized on/in transducer material are proposed for environmental, clinical and food analysis.

Three aspects of the topic are considered:

- application of nanomaterials in transducers for biosensors, immunosensors and chemical sensors construction;
- application of nanomaterials as labels for immunosensors.
- application of nanoparticles in immunoanalysis with magnetic separation.

A method based on mediator system and potential measurement as source of information on antioxidant/oxidant activity of the analyzed media is presented. Multifunctional potentiometric analyzer MPA-1 (IVA, Russia) and sensor containing metal nanoparticles are used. New information on antioxidant state of living organism in normal and stress situations is available. A chain, including diet, therapy, oxidative stress, can be traced, that will create a basis for choosing the most effective strategy of treatment.

The proposed potentiometric method of measuring AOA presents a good and prospective alternative to the existing methods, which is confirmed by close correlation between the data obtained with the use of potentiometric and traditional methods. The advantages of the proposed method are its simplicity, cost effectiveness, possibility to be used for on-site and on-line analysis. The method is one of the useful tools for linking basic science to clinical practice. Fields of application: environmental monitoring (toxic metals and oxidants); food, nutrients and drugs quality monitoring (toxic metals and antioxidant activity); medical diagnostic

Key words: Sensors, Nanostructured materials, Immunoanalysis, Oxidative stress, Antioxidant activity.

The environmental pollution, which is due in particular to industrial wastes, changes the human habitat and entails serious problems with the health of the current generation of people and on the genetic level. In addition appearance of new fast by passing dangerous infection diseases, reality of bioterrorism make the problem of environmental monitoring and infection diseases express diagnostics one of the health protection priorities.

The majority of biochemical reactions, which ensure life of cells, organs and the whole body, run with formation and in presence of free radicals. Negative impact of excessive insolation, ionizing radiation, and invading xeno-biotics can lead to excessive formation of free radicals and result in oxidative stress. Relations between antioxidant activity, various pathologies (cardiovascular, nervous, lungs, eyes, and blood) and age-related changes have been extensively reviewed [1].

A rapid development and wide application of Electrochemical analysis and research methods that have taken place in recent decades are explained by a low detection limit, high sensitivity, selectivity and speed of the methods, low cost of equipment. Electrochemical analytical methods, particularly stripping voltammetry, are being revived, which is caused by the demand in trace analysis for environmental monitoring and medical diagnostics, development of new technique of preliminary electrochemical concentration of the determined substance on the electrode surface, the use of screen printed technologies, which resulted in creation of new electrodes so cheap that they can be easily disposed and there is no need in regeneration the solid electrode surface, application of nanostructured materials as transducers and labels. Possibilities to manipulate molecular matrix of the electrode or its surface combined with large-scale electrochemical research methods led to the “explosion” in development and application of biosensors and chemically modified sensors. Bio-chemically and chemically modified sensors possess high selectivity and sensitivity. Biosensors include electrodes modified with bio-stuff: enzymes, DNA, antibodies, vegetable tissue, microorganisms.

Immobilization of bioactive material on/in the electrode allows combining bio-reaction selectivity with sensitivity of electrochemical detection. Wide application of potentiometric methods, including ion-selective electrodes use for mineral components determination and pH measurement, is observed in clinical laboratories.

A new approach in potentiometry based on mediator system and potential measurement as source of information on antioxidant/oxidant activity of the analyzed media is proposed [2, 3].

Data available prove the need for complex environmental and health monitoring. Some attempts to contribute into solving these very complicated problems are given below.

Electrochemical screen-printed sensors, based on carbon (metal) containing transducer and organic/inorganic receptor, immobilized on/in transducer material are used (Fig.1) for blood, water and food analysis. Metal ions (Cu, Pb, Cd, Zn, Hg, Ni, Cr, Sn, As in waters; Cu, Pb, Cd, Zn in food and blood) are recognized with the use of Stripping Voltammetry (Fig.2). Graphite containing screen printed sensor, modified with mercury insoluble compound is used for evaluation of Thiol-Disulphide ratio in biological fluids.

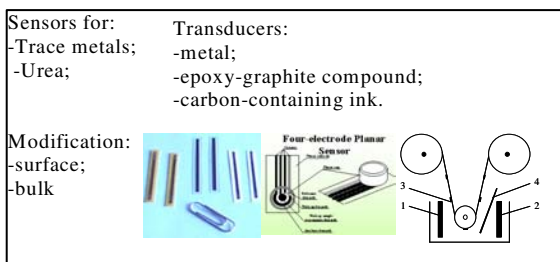


Fig.1. Sensors and transducers.

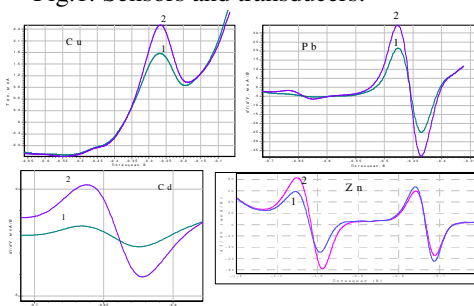


Fig. 2. Stripping voltammograms of metals in the whole blood:
1-blood; 2-spiked blood

Magnetic nanoparticles Fe_3O_4 (30 nM) synthesized in inverse micelles is used in hybrid immunoanalysis including magnetic separation and detection of inactivated *Salmonella typhimurium* concentration. Antibodies were immobilized on screen-printed thick film graphite containing transducer surface. Signal proportional to pathogen concentration was measured as iron ions concentration after nanoparticles dissolution with the use of Stripping voltammetry method (Fig.3).

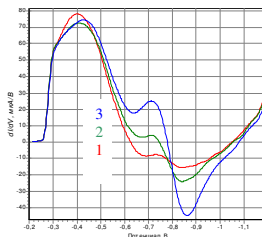


Fig. 3. Cathodic voltamperogram of adsorbed of pyrocatechol with Fe^{3+} complex. Background electrolyte - 1; sample – 2; spike - 3.

The antioxidant activity of food (juices, tea, bear) and real biological fluids, has been evaluated.

Table. Antioxidant activity of blood fractions and Dialysis liquid

Sample	Erythrocyte mass		Plasma		Dialysis liquid	
	$X \pm \Delta X$	Sr	$X \pm \Delta X$	Sr	$X \pm \Delta X$	Sr
1	$18,6 \pm 0,3$	0,05	$1,0 \pm 0,04$	0,03	$0,40 \pm 0,01$	0,03
2	$19,5 \pm 0,4$	0,03	$1,1 \pm 0,07$	0,03	$0,15 \pm 0,04$	0,01
3	$25,5 \pm 0,6$	0,07	$1,59 \pm 0,02$	0,05	$0,09 \pm 0,01$	0,04
4	$18,5 \pm 0,6$	0,03	$0,99 \pm 0,06$	0,03	$0,1 \pm 0,01$	0,06
5	$16,9 \pm 0,5$	0,04	$0,96 \pm 0,03$	0,03	$0,25 \pm 0,01$	0,02
6	$22,8 \pm 0,6$	0,04	$1,20 \pm 0,08$	0,02	$0,20 \pm 0,01$	0,02
7	$22,2 \pm 0,8$	0,04	$1,06 \pm 0,04$	0,02	$0,14 \pm 0,01$	0,03
8	$18,8 \pm 0,4$	0,03	$1,09 \pm 0,05$	0,03	$0,11 \pm 0,01$	0,04

Results of plasma AOA were compared with independent spectrophotometric method results. Stable radical biphenylpicrylhydrosil served as model one. Correlation coefficient for 8 samples was equal to 94%. We think, that the cumulative AOA of the sample as the integrated parameter, rather than a simple sum of individual antioxidants should be taken into consideration. Thus, performance of known and unknown antioxidants and their synergistic interaction be assessed.

Combination of achievements in screen-printing and nanotechnologies, bio- and electroanalytical chemistry served as a base for development of new sensors, software and hardware for environmental and health monitoring.

1. Chemically modified sensors, based on nanocarbon containing transducer for trace metal ions in environment (Cu, Pb, Cd, Zn, Hg, Se, As) and blood (Cu, Pb, Cd, Zn) are proposed.
2. Metal nanoparticles (Au, Ag, Fe₃O₄) conjugated with biomolecules and pathogen cells are used in immunoanalysis (with magnetic separation including) as information generating substance (label) in enzyme free electrochemical immunosensors.
3. A method based on mediator system and potential measurement as source of information on antioxidant/oxidant activity of the analyzed media is presented. Sensor containing metal nanoparticles is used. Express method for estimation of antioxidant activity of foodstuff, nutrients and biological fluids is proposed.

New information on antioxidant state of living organism in normal and stress situations is available. A chain, including diet, therapy, oxidative stress, can be traced, that will create a basis for choosing the most effective strategy of treatment. Novelty of the approaches that are described in this paper concludes in hybridization of electrochemical, immune, biochemical analysis methods, nano and screen-printing technologies, that opens up new possibilities in health monitoring.

Multifunctional potentiometric analyzers MPA-1 and Voltamperometric analyzer IVA based on sensors containing metal or carbon nanoparticles are developed and manufactured by IVA Ltd (IVA Ltd, Russia [4]).

The methods are one of the useful tools for linking basic science to clinical practice.

The authors would like to thank ISTC (Project 2132), Russian Federal Fundamental Investigation Fund (Project 07-03-96071-r_ural_a,) for financial support.

References:

1. Beljakova, N.A., Semesko, S.G., Antioxidant activity of human biological fluids: methodology and clinical value. *Efferent therapy*, 11:5-21; 2005.
2. Brainina, Kh.Z., Ivanova, A.V., Sharafutdinova, E.N., Lozovskaya, E.L., Shkarina, E. Potentiometry as a method of antioxidant activity investigation. *Talanta*. 71:13-18; 2007.
3. Brainina, Kh.Z., Kositzina, A.N., Ivanova, A.V. Screen-printed enzyme-free electrochemical sensors for clinical and food analysis. *Electrochemical sensor analysis*. 49:643-666; 2007.
4. <http://iva.usue.ru/>;
http://www.usue.ru/files/video_for_downloads/video_iva_eng.avi

New biofeedback technology for electromagnetic therapy of vascular diseases

L.A. Shamkina, P.V.Luzhnov, S.I.Schookin

*Bauman Moscow State Technical University,
e-mail: peterl@hotmail.ru*

Abstract: In the given work the bioadequate electromagnetic therapy synchronized by a signal of respiration is proved. The synchronization by pulse bloodfilling and phases of respiration simultaneously method is determined. The algorithm of alternating reographic cycles on inspiration and an expiration phases model is developed. Models of respiration for several group of patients are investigated. Using of algorithm with application of breathing model and extrapolation for on-line synchronization is proved.

Now one of the most widespread diseases are inferior extremities blood vessels diseases. Among them it is possible to refer to the chronic venous insufficiency (CVI), obliterating atherosclerosis of inferior extremities arteries (OAOEA), diabetic microangiopathy (DMA). The cause of these diseases usually are hormonal diseases, diabetes, smoking, improper feeding, hypodynamia.

In Schookin S.I., Semikin G.I., Morozov A.A., Kastrov A.J., Luzhnov P.V. researches [1,2,4,6] it was shown, that bioadequate electromagnetic therapy (BEMT) is effective for inferior extremities blood vessels treatment. Asynchronized stimulation and stimulation synchronized by pulsewave have been developed. The mode, intensifying arterial blood inflow, and the mode, increasing venous blood outflow are determined. It was proved, that therapy efficiency depend on breathing phases [5,7]. At present the most relevant question is synchronization of BEMT by pulse bloodfilling and breathing phases simultaneously.

The bloodfilling of bloodstream region consist of two components: arterial inflow and venous outflow. In conditions of a natural blood circulation the part of blood is pumped over from venous department to arterial at every heartbeat. Thus pressure in vessels varieties in depends on their capacity and expansibility. Arterial pressure and arterial inflow is caused by blood stroke volume pulsation during systole. Systemic venous pressure (SVP) is equal to pressure in right auricle (2-4 millimeter of mercury). Normally SVP is variety in rather wide diapason synchronously by

a respiratory and heart rhythm. The muscular pump, pumping heart function, change of venous capacity, the respiratory (breathing) pump are factors influencing on fluctuations of venous return.

In Belayev K.R, Kuz'minich N.J researches [3] the opportunity of breathing signal extraction from reocardiogram base impedance signal has been shown. In Luzhnov P.V. researches [5,7] the opportunity of breathing signal extraction from reovasogram pulsewave signal has been shown. For this purpose 2-nd order Chebyshev filter with 1.2 Hz frequency cut-off has been developed. The delay of this filter is more than 0.5 seconds (127 point at 200 Hz sampling rate). Thus it is possible to determine a phase of breathing with delay time more than half duration of the current reographic cycle. It makes unsuitable such filtration for a problem of synchronization therapy stimulation by breathing phases, because BEMT impulse shape should be known at the moment of the reographic cycle start.

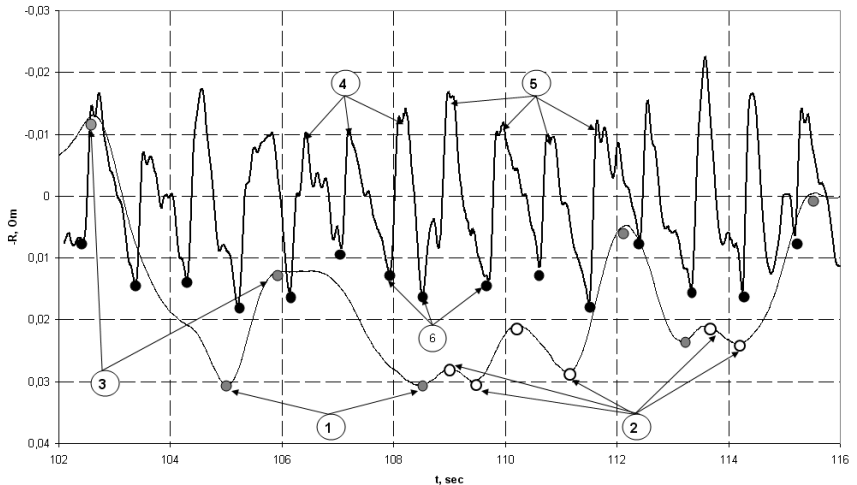


Figure 1 – Example of breathing signal filtering from reographic signal and division reocycles (pulse waves) into breathing phases (1-start of inspiration, 2- start of expiration, 3- start of imperfect inspiration or expiration, 4-reocycles during expiration, 5-reocycles during inspiration, 6- start of reocycle)

In the given work algorithm of treatment synchronization by breathing with algorithm extrapolation by models using has been suggested. Researches

breathing types and models using reogram signal have been carried out (see fig.1).

According to the developed algorithm on the base of received gradation the map of breathing reocycles situated on an inspiration phase is indexed by “0”, on an expiration phase is indexed by “1”. Then a function change of such type reographic cycles during time is formed (fig.2).

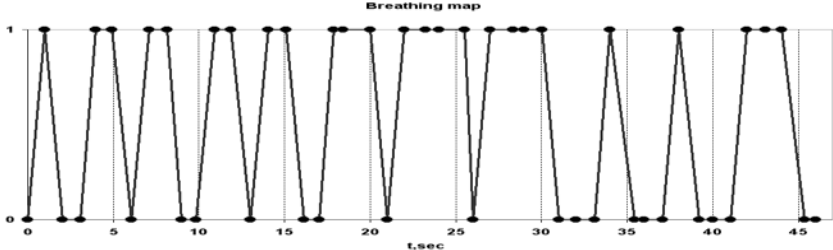


Figure 2 – Example of breathing map – type of reocycle (0 – reocycle during inspiration, 1 – reocycle during expiration) in the moment of its start

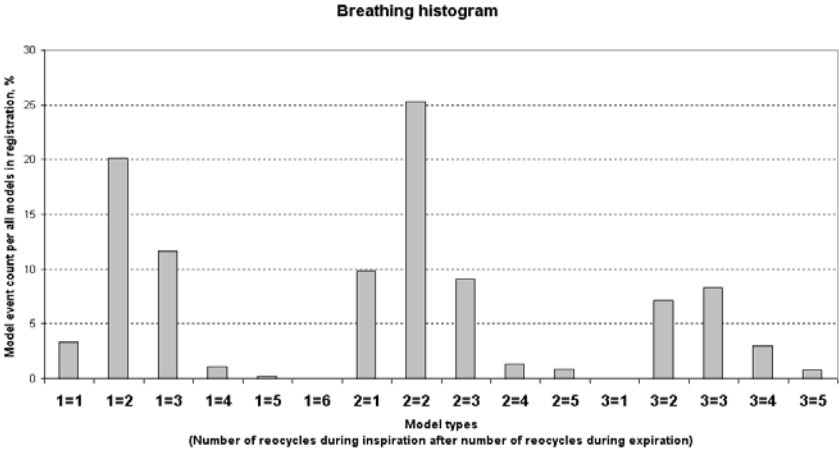


Figure 3 – Example of breathing histogram (Model event count per all models in reografic registration, where model is number of reocycles during inspiration after number of reocycles during expiration)

By the developed breathing map with using special software, which has been developed, breathing histogram is formed. And the most frequently occurring model of inspirations and expirations alternating is extracted (fig. 3).

In this work breathing rhythms are researched and breathing model for three experimental group is constructed. The reovasographic signal registration from inferior extremities was carried out in a quiet, laying state. On the base of experimental data the most widespread breathing model was marked out (see table 1).

Table 1 – Typical breathing map for three experimental group

Modes	Model types (Number of reocycles during inspiration after number of reocycles during expiration)						
	2=3	2=2	2=1	1=3	1=1	3=2	1=2
1-st group	0,49	0,15	0,17	0,1	0,06	-	0,03
2-nd group	0,13	0,12	-	-	-	0,1	0,65
3-rd group	-	0,54	0,18	0,08	-	-	0,2

If the typical for current patient breathing model is marked out, it is possible to use models as show on table for synchronization by breathing phases in on-line active therapy.

References

1. Schookin S.I. Apparatus and systems for bioadequate electromagnetic treatment and active diagnostics //Biomedical radio electronics. – 1999. - №3. – P.6-16. (in Russian).
2. Elektenrically mediated growth mechanisms in living systems //Ann.N.Y.Acad.of sci.. 1974. V. P.238-593.
3. K.Beliaev, N.Kuzminyh. Breath waves filtration in bioimpedance cardiography. The 15th international EURASIP conference EuroConference BIOSIGNAL 2000.- Brno, Czech Republic, p.133-5
4. Luzhnov P.V., Morozov A.A., Schookin S.I. The elements of software of system for biosynchronized electromagnetic treatment //Biomedical technologies and radio electronics. – 2002. - №9. – P.42-48. (in Russian).
5. Luzhnov P.V., Morozov A.A. Elaboration of hardware and software of system for bioadequate electromagnetic treatment //Biomedical radio electronics. – 2000. - №9. – P.33-38. (in Russian).

6. Schookin S.I., Semikin G.I., Luzhnov P.V., Kastrov A.Yu., Rodionov R.V. Basic types of peripheral rheogramm variations induced by electromagnetic fields //Life systems' technologies. – 2005. – T2. - №6. – P.16-24. (in Russian).

7. Luzhnov P.V., Schookin S.I., Ermakov P.A. Investigation of rheoencefalogramm signal's variability by biosynchronize electromagnetic influence //Biomedical technologies and radio electronics. – 2005. - №9. – P.12-17. (in Russian).

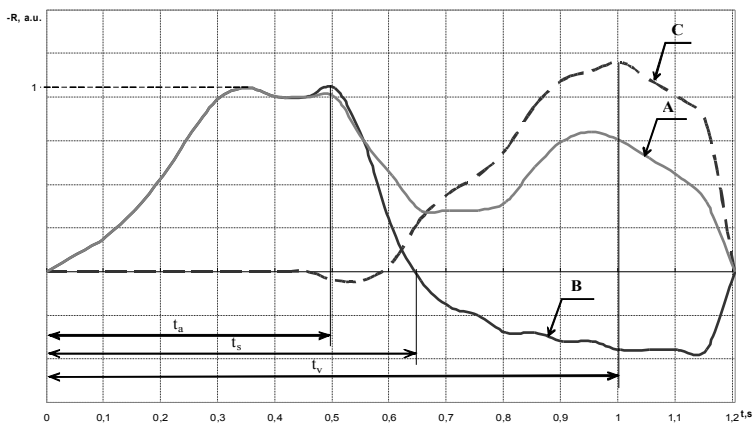
Features of joint brain electric activity and hemodynamics research

E.M.Astapenko, P.V.Luzhnov

*Bauman Moscow State Technical University,
e-mail: peterl@hotmail.ru*

Today the special attention is given to noninvasive diagnostic methods of cardiovascular system (CVS). It is associated with growth of number of cardiovascular system diseases including cerebral vessels. Therefore the purpose of our work is formation of a diagnostic parameters complex of rheoencephalographic (REG) signal which gives opportunity of REG analysis both for case of obvious abnormality of blood circulation and for low-grade pathologies.

In a basis of mechanism of blood pulse wave formation the formation of arterial and venous waves and transformation of pulse wave on a site of peripheral vascular resistance (PVR) are lied. According to heart work two phases of cardiac cycle for extraction arterial and venous component from rheogram are considered: systole and diastole [2].



A – rheocycle, B – arterial component, C – venous component

Fig. 1 – Rheogram and its component decomposition

According to figure 1 the arterial component consists of positive and negative half-waves. The positive half-wave corresponds to systolic phase of cardiocycle and negative – to diastolic phase. There is a blood inflow in arterial bed owing to blood expulsion from ventricles on a site from the rheocycle beginning to the maximum amplitude of arterial component. Then the negative phase comes (t_a-t_v). It reflects ejection of an arterial bed in connection with blood moving in a venous bed through PVR vessels. The last site of the arterial component up to the end of rheocycle is characterized by dominance of blood inflow in an arterial bed from aorta and main arteries, i.e. from area with higher pressure.

The venous rheogram pulsation is formed by one positive half-wave which beginning is late in relation to the beginning of an arterial pulsation. There are two sites for the venous component description. The first is a positive phase (t_s-t_v), i.e. the dominance of blood inflow in the venous bed from high pressure area (through PVR) and the second is a negative phase which terminates by the end of rheocycle and in which duration there is blood return of the venous bed to the initial value at the expense of blood outflow in the heart.

Subsequently the decomposition of rheographic curve on the arterial and venous components will allow defining volumetric venous blood flow. Time and amplitude rheocycles parameters obtained from their division into arterial and venous components allow receiving the additional information about microcirculation in the vascular bed. Besides, they contain the auxiliary information for rheocycles division on the arterial and venous types.

Now following parameters are widely used for the rheographic analysis: amplitude, dicrotic index (DCI) and diastolic index (DSI) [1]. DSI – the relation of dicrotic amplitude to the systolic amplitude, which reflects veins tone level and the venous blood outflow and is determined by peripheral vascular resistance:

DCI – the relation of incisura to the systolic amplitude, which gives the information about a tone of average and fine arteries:

where A_s – a systolic amplitude;

$$DSI = \frac{A_d}{A_s} \cdot 100\% \quad (1)$$

A_d – a diastolic amplitude;

A_i – an incisura.

$$DCI = \frac{A_i}{A_s} \cdot 100\% \quad (2)$$

We have introduced following parameters for the estimation of microcirculation and venous outflow changes: S_1 , S_2 , $|S_1|$ and A_{neg} (fig. 2):

S_1 – the area between a straight line connecting amplitudes of a systolic wave and an incisure and rheogram (fig. 2A, B);

$|S_1|$ – the module of S_1 (fig. 2A, B);

S_2 – the area between a straight line connecting amplitude of incisure and the end of rheocycle and rheogram (fig. 2A, B);

A_{neg} – negative wave amplitude of rheogram (at presence) (fig. 2B).

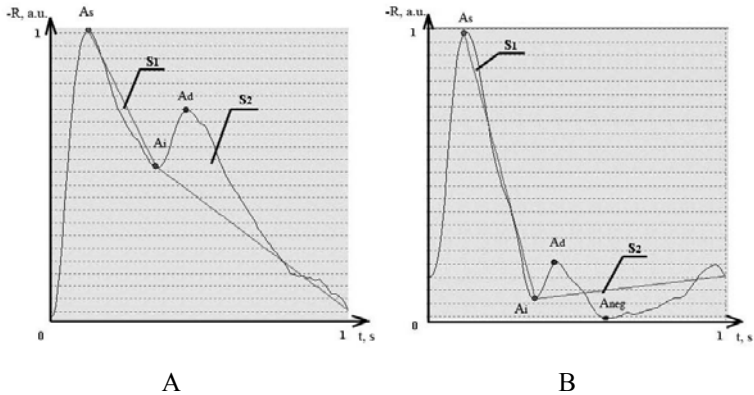


Fig. 2 – REG-parameters definition

We carried out REG-signal registration in the lying position in three leads (F-M, O-M and T-T1) by tetrapolar rheographic method. REG-signals has been registered by means of two-channel rheograph with the sampling frequency of 200 Hz. Results of REG-analysis depending on a breath phase are presented in table 1.

Table 1 – Results of REG-analysis depending on a breath phase

Lead Parameter/ Breath phase	F-M		T-T1		O-M	
	Inspiration	Expiration	Inspiration	Expiration	Inspiration	Expiration
A, Ohm	0,105	0,098	0,074	0,053	0,034	0,028
DCI, %	7,07	42,6	59,26	52,44	11,36	-39,29
DSI, %	34,41	35,02	73,37	79,17	25,45	10,07
$ S_1 $, a.u.·10 ⁻⁴	19	21	5	4	4	6
S_1 , a.u.·10 ⁻⁴	-16	-10	1	0,5	-3	-4
S_2 , a.u.·10 ⁻⁴	74	55	48	25	34	27

As follows from table 1, parameters DCI in F-M and O-M leads, DSI in O-M lead and S_2 in all leads considerably change. Meanwhile parameter S_1 varied insignificantly. Examples of REG-parameters calculation for each of three leads are presented in fig. 3-5.

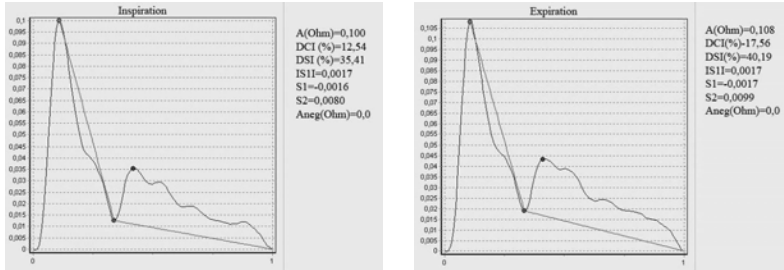


Fig. 3 – REG-signal. F-M lead

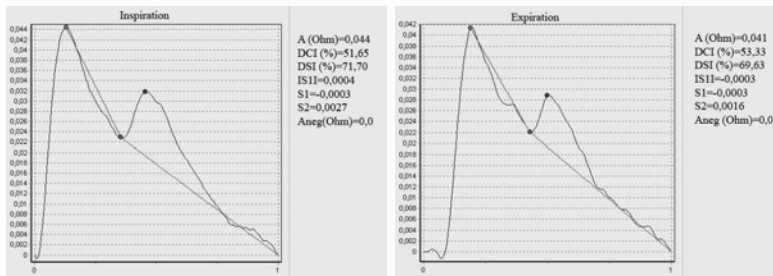


Fig. 4 – REG-signal. T-T1 lead

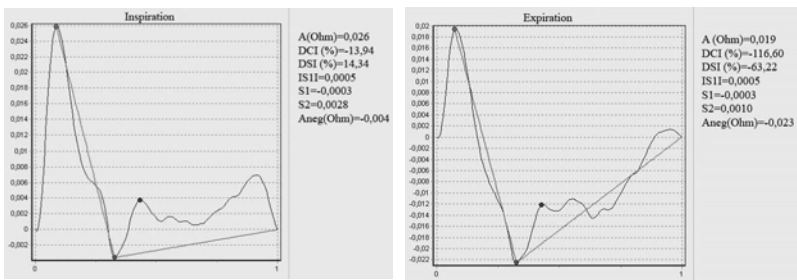


Fig. 5 – REG-signal. O-M lead

On the basis of the above-stated it is offered to use the following parameters complex for REG-analysis:

- 1) DCI, DSI;
- 2) Amplitudes of arterial and venous components, time parameters t_v - t_a , t_s - t_a ;
- 3) Parameters S_1 , S_2 , $|S_1|$ and A_{neg} depending on parameters DCI, DSI and investigated lead.

It is possible carrying out of REG-rheocycles classification on arterial and venous types by means of offered complex. Also with use of indicators of the offered complex there is possible a carrying out of differential diagnostics, namely, microcirculation changes estimation via parameters S_1 , $|S_1|$ and changes in venous bed via parameters S_2 and A_{neg} . The given parameters complex gives the opportunity to carry out qualitative diagnostics both for signals with the expressed structural elements and for more difficult cases in the analysis.

References

1. Иванов Л. Б., Макаров В. А. Лекции по клинической реографии: – М.: АОЗТ "Антидор", 2000.
2. Яруллин Х. Х. Клиническая реоэнцефалография. Л.: Медицина, 1967.

Algorithm of automatic fibrillation detection

N.A. Bazaev, A.N. Gusev, A.V. Mikitas*

*Moscow Institute of Electronic Technology (Technical University),
e-mail: simple210@yandex.ru*

**Zelenogradskii Innovative Technological Centre*

Every year more than 300 thousand people die from sudden heart arrest in Russia. One can restore the proper work of heart via injection of adrenaline, heart massage or via transmitting a short electrical impulse of current of high power through heart (procedure of defibrillation). The efficiency of such procedure rapidly falls with time and the faster defibrillation is accomplished the more chances the patient has to survive. In case of providing the procedure of defibrillation in time, many people who became victim of sudden heart arrest, could be saved. That is why development of devices for automatic analyzing of ECG and making decision of necessity of shock therapy is a very actual task.

The algorithm that had been used in the first domestic defibrillator possesses high characteristics of sensitivity and specificity (99 % and 100 % corresponsive), however its actuation time is relatively high - till 15 seconds. Later a solution for decreasing of the action time was found: the intra threshold time-frequency algorithm was developed which auction time equaled to 4.1 seconds. However, its sensitivity and specificity turned out to be not so good (71.0 % and 93.3 % corresponsive). The aim of this work was to increase parameters of the intra threshold time-frequency algorithm.

The chances of developing an algorithm based on one critical parameter that possess high sensitivity and specificity are not high. That is why the result algorithm should be a combination of several critical parameters. During the work some known critical parameters were analyzed and also some new were suggested. Only four of them were used in the final algorithm.

1. Relative number of samples that are outside the informative interval.

This critical parameter was used in the method of Intra Threshold Time-Frequency Analyze. The informative interval is $(-0.2 \cdot \text{MaxAmplitude}; 0.2 \cdot \text{MaxAmplitude})$. In this method the number of samples that are outside the informative interval is counted and this number is divided to the number of all samples in the analyzed window. In this way we get the relative frequency. That method gave possibility to define different type of signals.

It's linear and that means it is easy programmable and works fast. It's very important to define no shock rhythms as fast as possible because these are most of situations.

$$Wd = \frac{N_1}{N_1 + N_2},$$

where N_1 is the number of samples that are outside the informative interval and N_2 is the number of samples that are inside it. It was decided that in case Wd is less than 0.47 the episode is classified as no shock rhythm. Otherwise fibrillation is detected. It was found out that the best window length is 4 seconds. Selectivity and specificity of this critical parameter are 79.9 % and 83.9 % corresponsive.

2. VF-Filtering method

It is said that in case of fibrillation the spectral power is mostly between 1 and 9 Hz. And otherwise the spectral power is distributed between 1 and 30 Hz. That is why one can filter the initial signal, in other words to cut 0-9 constituents from it and compare the power of initial ECG-signal with the power of filtered ECG-signal. The critical parameter is counted due to the following equation:

$$P_w = 255 \cdot \frac{\sum_i FilteredECG_i}{\sum_i InitialECG_i}.$$

If P_w is less than 75 then the episode is decided to be no shock. If P_w is larger than 110 then the episode is decided to be shock. Otherwise we need an additional parameter to make a decision.

3. Method of subtracting a combined signal.

The idea of this method is to get the residual of the absolute initial signal and the combined signal that is unique for every window. At first, one need to find picks that cross the threshold of $0.9 \cdot MaxAmplitude$. Then the combined signal is formed. The combined signal is equal to the initial signal from the beginning of the window and to the first pick and from the last pick to the end of the window. Between two picks that go one after another the combined signal is counted due to formula:

$$R = \frac{1}{2} \cdot MaxVal \cdot \left(\sin\left(\frac{\pi}{2} + \frac{2 \cdot \pi \cdot t}{T}\right) + 1 \right),$$

where T is the time interval between two picks, $MaxVal$ is the maximum value in the taken window. The critical parameter is calculated in the following way:

$$S = \left| \sum_i ECG(i) \right| - \left| \sum_i R(i) \right|.$$

If S is lower than 600 the rhythm is considered to be shock. It is very critical to use prefiltration before using this parameter, because signals may contain drift of isoline. The necessary correction can be made with help of Kaiser Filter. The window length is taken 4 seconds and is considered to be optimal. The selectivity and specificity of this critical parameter are 77.0 % and 93.1 % corresponsive.

4. Number of picks that cross threshold of $0.3 \cdot MaxVal$

As it was found out, there is correlation between the number of picks that cross the mentioned threshold and fibrillation. In case of fibrillation the number of picks was more than 25. The length of the window was also taken equal to 4 seconds because it was supposed to be used in combination with the previous critical parameter. It was analyzed how the threshold influence the quality of separating fibrillation from other rhythms. It was found out that one can choose any threshold from the interval: $(0.2-0.5) \cdot MaxVal$. Separation of fibrillation from other rhythms will be of the same quality. But one has to take into consideration that the critical number of picks should be recalculated for a certain threshold. Selectivity and specificity of the critical parameter are 78.7 % and 95.1 % corresponsive.

Algorithm of automatic fibrillation detection

As the first link it is suggested to use the relative number of samples outside the informative interval because it is the fastest algorithm and it can detect sinus rhythms very well. Its specificity on signals that contain sinus rhythms is more than 99 %. In order to raise the quality of detection ranges of values of three critical parameters were divided into 3 areas: one responsible for no shock rhythms, one responsible for shock rhythms and one responsible for undefined rhythm. And the range of values of one critical parameter (number of picks that cross the threshold) is divided into 2 areas that are responsible for shock and no shock rhythms. This critical parameter is used as the last (the third one) link of the algorithm in order to make final decision. The second link is used to separate shock and no shock rhythm using two

other critical parameters. The block-scheme of the algorithm is given in the figure 1.

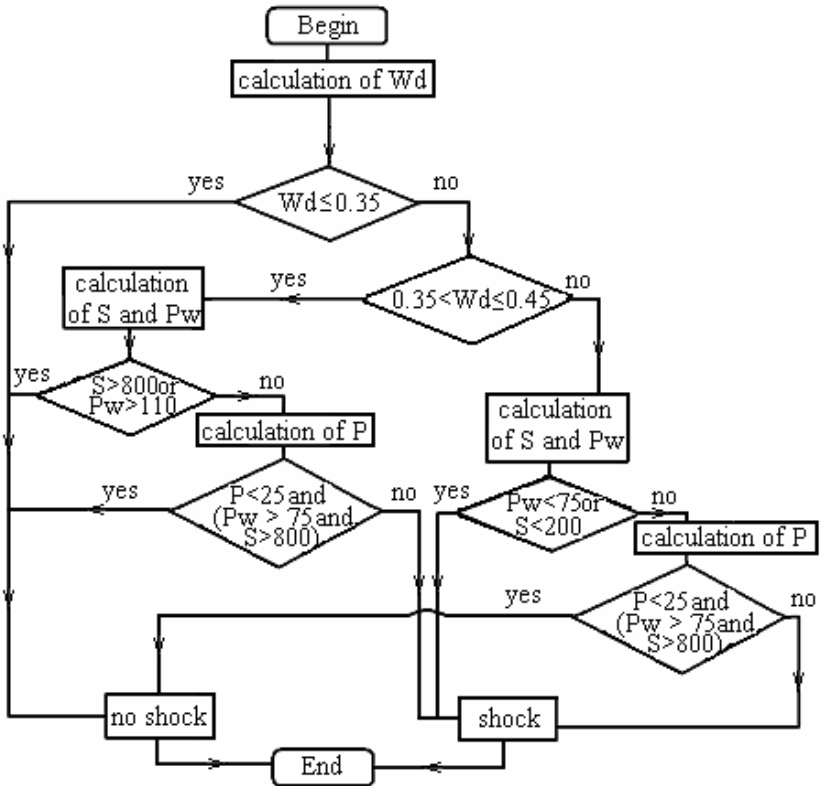


Figure 1. Block-scheme of the algorithm.

Sensitivity and specificity of the algorithm are 94.3 % and 98.4 % corresponsive. The prefiltration included the use of Butterwort filters and Kaiser Filter. The mentioned results were received with the order of filters 4 and 16 corresponsive. As a result we have the algorithm which action time is 4.1 seconds, but with sensitivity of only 94.3 %. That is not enough, so the future work will be devoted to how to raise it. And of course of it will be possible to raise specificity to at least 99 %.

The given work is executed at partial financial support of the Russian Fund of Basic Researches, project N 05-08-50300.

EEG segmentation based on Higuchi fractal dimension in automatic sleep stage classification.

Gendel I., Doroshenkov L.

*Department of Biomedical Systems, Moscow State Institute of
Electronics Technology (Technical University)
e-mail: leonid216@mail.ru*

80 years ago Austrian psychiatrist Hanz Berger had introduced a technology for recording human brain's electric potentials. It is called electroencephalography (EEG) and it is now one of the main methods for brain activity research and analysis. Human's state during sleep can be divided into several stages, corresponding to different EEG rhythms and their characteristics. Usually 6 stages are differentiated. These are wake, 4 slow sleep stages 1-4 and fast sleep stage REM, which stands for rapid eye movement. Sequence of sleep stages corresponding to an EEG record is called a hypnogram.

Power spectrum analysis was widely used for sleep research, but it appears to be inappropriate method because it is supposed to be used only with stationary processes and EEG is an extremely nonstationary process. Its' probability – statistical characteristics (as mean value, variance) change with time. For example the variability of power even for short segments ranged up to 50-100% percent. On the picture below there is an example of the Fast Fourier Transform of a 4 minute EEG record made at 100 Hz. It is obvious that this result can not give us any valuable information.

Two types of EEG nonstationarity are being distinguished. First group is transient events, such as sharp waves (which last about 200-400ms), sleep spindles and spikes (which last about 50 ms and usually happen with brain disordered patients, e.g. epilepsy). As we can see on Fig. 2 all of them have specific patterns and they are easy to identify. Second type is alternation of relatively homogeneous segments. Identification of these segments require certain theoretical basis and that's why we need some boundaries detection techniques.

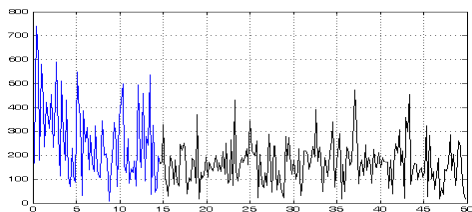


Fig. 1. FFT of a nonstationary segment

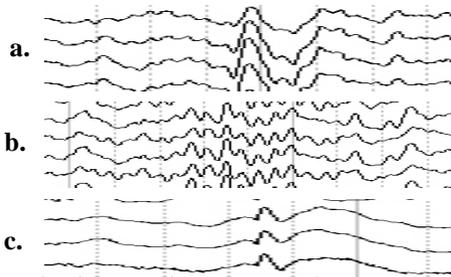


Fig. 2. Transient events. a). sharp waves, b). sleep spindles, c). spikes

Higuchi fractal dimension was introduced in late 80's as an index for describing irregular time series. The advantage of that technique is that it's calculated directly from a time series without embedding the data in phase space. One of the main ideas that it uses the property of a fractal curve: each part of the curve can be considered as a reduced scale

image of the whole. As we consider our time series as a curve, Higuchi fractal dimension is always between 1 and 2. 1 is a dimension of a straight line and 2 is a dimension of a plane. So, the higher signal's complexity (that is the more it fills the plane) makes the bigger fractal dimension.

Let's consider a time series. Observations are taken at a regular interval.

$$X(1), X(2), X(3), \dots, X(N). \quad (1)$$

Then we construct k subset series using the formula.

$$X(m), X(m+k), X(m+2k), \dots, X\left(m + \left[\frac{N-m}{k}\right] \cdot k\right) \quad (m = 1, 2, \dots, k) \quad (2)$$

Where $\left[\right]$ - denotes the integer part of a fraction, m - the initial time and k - the time interval. In case $k = 3$, $N = 100$ we will generate 3 new subset series:

$$\begin{aligned} X_3^1 &: X(1), X(4), X(7), \dots, X(97), X(100) \\ X_3^2 &: X(2), X(5), X(8), \dots, X(98) \\ X_3^3 &: X(3), X(6), X(9), \dots, X(99) \end{aligned} \quad (3)$$

Then we need to calculate the lengths of each subset series.

$$L_m(k) = \left\{ \left(\sum_{i=1}^{\left[\frac{N-m}{k}\right]} |X(m+ik) - X(m+(i-1)k)| \right) \frac{N-1}{\left[\frac{N-m}{k}\right] \cdot k} \right\} / k \quad (4)$$

Where $\frac{N-1}{\left[\frac{N-m}{k} \right] \cdot k}$ - denotes the normalization factor.

So we receive k lengths. To obtain the length of the curve corresponding to k time interval we're taking the average.

$$L(k) = \frac{\sum_{m=1}^k L_m(k)}{k} \quad (5)$$

This way we can calculate a set of lengths corresponding to a set of time intervals k. If the following law is being obeyed we can say that the curve is fractal with the dimension -D.

$$L(k) \sim k^{-D} \quad (6)$$

To find this coefficient we plot set of lengths against set of time intervals on a doubly logarithmic scale. The data should fall on a straight line. And the slope could be found using the least-squares procedure.

$$D = \frac{n \sum (x_k y_k) - \sum x_k \sum y_k}{n \sum (x_k^2) - (\sum x_k)^2} \quad (7)$$

Where $y_k = \ln L(k)$, $x_k = \ln \left(\frac{1}{k} \right)$, $k = k_{\min}, \dots, k_{\max}$, n - number of different values of k for which L was calculated.

Several clinical hypnograms were analyzed and mean values of fractal dimension were found corresponding to the classical sleep stages.

<i>Wake</i>	1.6	$\leq D$	
<i>St. 1</i>	1.525	$\leq D <$	1.6
<i>REM</i>	1.475	$\leq D <$	1.525
<i>St. 1</i>	1.385	$\leq D <$	1.475
<i>St. 1</i>	1.305	$\leq D <$	1.385
<i>St. 1</i>		$D <$	1.305

The segmentation technique based on Higuchi's fractal dimension could be formulated as follows: we split an EEG record in regular segments, then find the dimension for all of them and combine neighbor segments with dimensions belonging to the same mean interval.

To analyze the segmentation results we will construct a hypnogram - for each segment we assign stage 1 through 4 sequentially - this way we can

see the borders of the segments. Then we compare them with the stage borders set by human expert (Fig. 3).

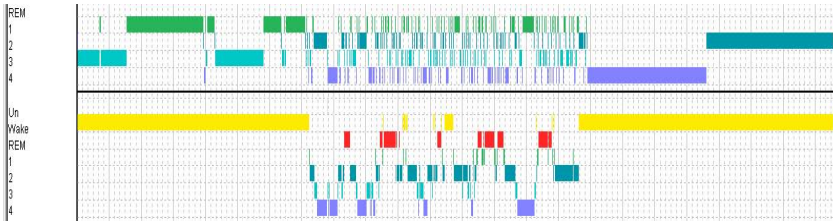


Fig. 3. Upper picture shows the segmentation results.

As we can see there is a good correspondence between large segments and wake stage, 4th stage segments were identified well too.

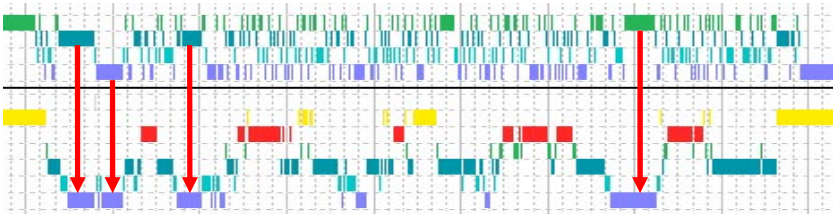


Fig. 4. Upper picture is a piece of segmentation without wake segments. Lower – a piece of the expert's hypnogram

If we calculate FFT for the segments corresponding to wake stage and 4th stage we will see the dominant frequencies typical for these stages.

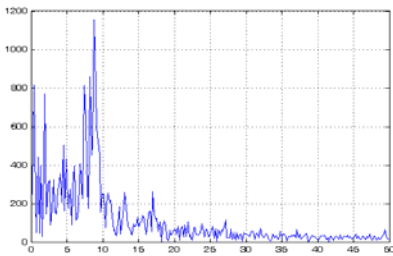


Fig. 5. FFT for 4th stage segment. Delta waves (0,5 – 5 Hz) are identified

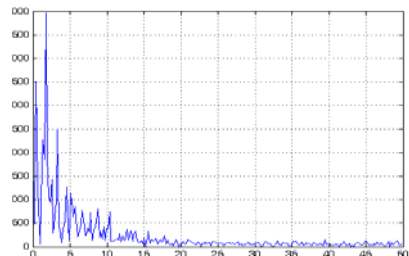


Fig. 6. FFT for wake segment. Alpha waves (8 – 13 Hz) are identified

Higuchi's fractal dimension could be used not only for EEG segmentation, but also for sleep stage classification. We can define for each segment a sleep stage it corresponds to according to its fractal dimension. The obtained hypnogram will be compared with the expert's hypnogram.

Example. Accuracy between expert hypnogram and hypnogram which obtained using fractal dimension is about 83%.

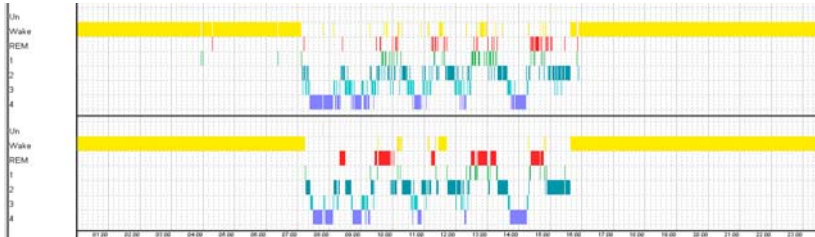


Fig. 7. Upper hypnogram is obtained using fractal dimension mean values. Lower hypnogram is done by an expert

Higuchi's fractal dimension can be used for EEG segmentation into stationary pieces. It also can be used for sleep stage classification instead of neural network classifier, like HMM. Higuchi's fractal dimension gives relatively high accuracy and requires much less time for calculation than a neural network.

References

1. Rechtschaffen A., Kales A.A. A Manual of Standardized Terminology, Techniques and Scoring System for Sleep Stages of Human Subjects. Washington DC: U.S. Government Print. Office, Nat. Inst. Health Publ., 1968
2. Higuchi T. Relationship between the fractal dimension and the power law index for a time series: a numerical investigation. *Physica D* 46. 1990.
3. Higuchi T. Approach to an irregular time series on the basis of a fractal theory. *Physica D* 31. 1988.
4. Flexer, A., Gruber, G., and Dorffner, G., "Improvements on Continuous Unsupervised Sleep Staging", *Neural Networks for Signal Processing XII, Proceedings of NNSP 2002*, Institute of Electrical and Electronics Engineers, Inc., New York, NY, pp. 687-695, 2002.
5. Malinowska U., Durka P.J., Blinowska K.J., Szelenger W., Wakarow A., "Micro- and Macrostructure of Sleep EEG", *IEEE Eng. Med. Biol. Mag.*, Vol 25, no. 4, pp. 26-31, 2006.

Comparison characteristics of magnetometers based on ceramic superconductors in biomedical applications

L.P. Ichkitidze¹, M.V. Belodedov²

¹*Moscow State Institute of Electronic Technology (Technical
University),*

e-mail: leo852@inbox.ru

²*Moscow State University of Printing Arts,*

e-mail: m.belodedov@mail.ru

Magnetic field of the biological objects contemporary investigation successes, therefore are closely related to the progress of ultrasensitive low magnetic field sensors creation as well as the measuring systems based on their designing. Liver, pulmones and other organs diagnostics using the noninvasive magnetic control which are one of the fundamental medical tasks too, also rely on the progress in that area. By force of magnetic susceptibility or magnetization measuring in magnetic field about $\sim 10^5$ nT, pathology degree (for example, of human liver [1,2]) can be determined. Diagnosis accuracy in this procedure directly depends on the measurement accuracy of the patient organ or tissue magnetic susceptibility or magnetization.

Various magnetometers are well known for low magnetic fields ($\mu_0 H_0 \leq 1$ nT) measuring in biomagnetic applications at present: SQUIDs (Superconductor Quantum Interference Devices), optical and NMR magnetometers and others. The most sensitive of them are the SQUIDs, however magnetic field absolutely value can not be measured by them, its increment only. Magnetic field absolutely value can be measured by a flux-gate meter [3] and by numerous magnetometers based on it. Their measurement errors increase in low field area $\mu_0 H \leq 1$ nT while they have moderate pass band (≤ 5 kHz) and measurement dynamic range ($D \leq 75$ dB). Better magnetic field resolution was obtained of flux-gate meter using permalloy core with single-domain magnetic structure in comparison with that with multi-domain magnetic structure [4]. Data signal was read in both cases on quadratic component and magnetic sensitivity for permalloy flux-gate meter with single-domain magnetic structure $S = dU/d(\mu_0 H_0)$ was mounted to 6 kV/T with magnetic field resolution $\delta(\mu_0 H_0) \geq 0.1$ nT. However flux-gate sensor possesses bulky gabarit and mass and non-fair accuracy for

magnetic flux measurements $\delta\Phi \geq 100 \Phi_0$, where $\Phi_0 = 2.07 \times 10^{-7}$ Wb – magnetic flux quantum.

Any other material with sufficiently nonlinear magnetic characteristics may be used in the flux-gate magnetometers instead of the ferromagnetic material. Ceramic high-temperature superconductive (HTSC) materials, being the multiple Josephson medium, hold distinct non-linear magnetic characteristics (nonlinear magnetization, susceptibility, voltage-current characteristic in low fields < 1 mT), therefore just after HTSC discovery the attempts to apply them in analogous to flux-gate magnetometers were realized. Indeed, flux-gate magnetometers with ceramic HTSC core having formulation Y-Ba-Cu-O (Y-123) were established just in the first efforts [5] to possess fair magnetosensitivity characteristics. Thus, magnetic field resolution of a magnetometer described comes to about 1 nT, whereas after improvements of ceramic Y-123 technology and of sensor design and optimal magnetometer operating mode selections, $\delta(\mu_0 H_0)$ value was decreased to 100–50 pT [6]. Magnetometers with ceramic HTSC core having formulation (Bi,Pb)-Sr-Ca-Cu-O (Bi-2223) were obtained $\delta(\mu_0 H_0) \sim 100$ pT, wide magnetic field measurement range $\sim (-1 \div +1)$ mT and actually neglect Earth magnetic field influence on the S and $\delta(\mu_0 H_0)$ values [7,8].

Thus, magnetometers with HTSC core have the magnet field resolution $\delta(\mu_0 H_0) \sim 100\text{--}50$ pT, and wide range for dynamic measurements $D \geq 110$ dB. These characteristics exceed much more analogous characteristics of HTSC SQUIDS ($\delta(\mu_0 H_0) \sim 1$ pT, $D \geq 110$ dB), working at liquid nitrogen temperature ~ 77 K [9,10] and being in use at present time in biomagnetic measurements.

Known low magnetic field magnetometers with ceramic HTSC core have been analyzed and the paths to improve their magnetosensitivity characteristics have been indicated in present article.

Ceramic high-temperature superconductors are granular materials with Josephson junctions on boundaries between granules. Such a “Josephson medium” has strong magnetization and magnetic susceptibility nonlinearity in a moderate external magnetic field ≤ 1 mT, that underlies the low magnetic field sensor design. The active induction sensors (also called magnetomodulation sensors) are produced on basis of the ceramic HTSP material. Principle of their operation is analogous to that of well known flux-gate sensors and lies the following. Core out of material with nonlinear curve $B(H)$ is placed into a coil creating an alternating external magnetic field:

$$H(t) = H_0 + H_1 \cos(\omega t), \quad (1)$$

where B – magnetic induction in core, H_1 and ω – alternating magnetic field amplitude and frequency respectively. According to the Faraday law, the voltage is inspired in sensor secondary winding wound on the same core, that is proportional to magnetic flux through the sample modification rate and, owing to the core B-H curve nonlinearity, contains not only probe signal main frequency ω but their multiple harmonics 2ω , 3ω and so on. In the absence of the probe signal direct component H_0 secondary winding signal contains only the odd harmonics (3ω , $5\omega, \dots$). Thus by measuring the quadratic (or any other even) response harmonic amplitude with vanishing them probe signal direct component may be gained to be equal to measured magnetic induction. Direct component H_0 is produced in flux-gate magnetometers by the subsidiary winding, magnetic field of which is proportional to the current running in it. Such magnetic field measuring device belongs to the magnetomodulation magnetometers (MMM).

The first MMM with ceramic HTSC core having formulation Y-Ba-Cu-O have possessed threshold sensitivity about their internal noise $N_B \sim 0,4 \text{ nT}/(\text{Hz})^{1/2}$ in frequency band 1 Hz at low frequencies close to 10 Hz [5]. Further sensor construction improvement has permitted to reduce threshold sensitivity up to $0,02 \text{ nT}/(\text{Hz})^{1/2}$ [6]. The best noise indices are obtained by present time of the magnetic field sensor based on HTSC ceramic Y-Ba-Cu-O, operating on binary excitation principle [11]. Sensor threshold sensitivity was obtained about noise level $5 \text{ pT}/(\text{Hz})^{1/2}$ with the absolute HTSC core noise absence. Paper [11] authors believe the ceramic superconductive core to possess its internal noise level $N_B \sim 1 \text{ pT}/(\text{Hz})^{1/2}$ and approach to a DC SQUID with the same operating frequency running at $\sim 77 \text{ K}$.

In numerous magnetic field sensors operating at $T \sim 77 \text{ K}$, it has been using as the core ceramic HTSC samples having formulation Y-123 with $T_c \sim 90 \text{ K}$ [5,6,11,12]. Such a choice is due to circumstances that their operating $T \sim 77 \text{ K}$ and critical $T_c \sim 90 \text{ K}$ temperatures are closed to each other, and in that case Josephson junction nonlinearity is more sharply expressed as at temperatures $T \ll T_c$. Hence the helpful signal as well as magnetosensitivity are great enough. Indeed the evaluation expression [6,13] may be added for the characteristic $S = dU/d(\mu_0 H_0)$, where U is the quadratic component:

$$S \sim \mu_0 \omega N A (H_1 / H^*)^2, \quad (2)$$

where N is the number of coils on the core, A – core profile square, $H^* \sim 1.5 H_{\max}$ – static magnetic field optimal value by which the maximum on $U(\mu_0 H_0)$ curve takes place [13], $H_{\max} \sim J_{cj}$, J_{cj} – Josephson junction critical current density. While fulfilling the S values comparison estimation of ceramic HTSC materials Y-123 and Bi-2223 it is necessary to take into

account that their T_c values are equal to 90 K and 108 K respectively. The T_c value of cylindrical bar with radius r according to Ambegaokar-Baratoff expression is assessed as:

$$J_{cj} = (\Delta(T)/4e\rho_n r) \text{th}[\Delta(T)/2kT], \quad (3)$$

$$\Delta(T) = 1.76kT_c(1-T/T_c)^{1/2}, \quad (4)$$

where Δ is energy gap width, e – electron charge, ρ_n – Josephson junction in normal state specific resistance, k – Boltzmann constant. Numerical evaluations show, that at the same values of ω , N , A , H_1 , ρ_n , r parameters (by different T_c) at operation temperature $T \sim 77$ K the value S of yttrium ceramic (Y-123) is approximately 7 times more than it of bismuth ceramic (Bi-2223). At the same time Y-123 sensor must have low dynamic measurement diapason since its value is determined by field H_{\max} , which is 2.7 times lower than it in Bi-2223 sensor due to (3) and (4). This conclusion is confirmed by experiments. H_{\max} value of HTSC bar of Bi-2223 ceramic is shown in paper [7] to be equal $H_{\max} \sim 0,8$ mT that is much greater than $H_{\max} \leq 0,3$ mT of HTSC bar of Y-123 ceramic being in use as low magnetic field sensor [5,6,11,12]. Hence the measurement diapason is equal to $\pm 0,8$ mT in the first case, and to $\pm 0,3$ mT in the second.

Ceramic HTSC material of Bi-2223 composition in low magnetic field magnetomodulation sensor using instead the ceramic HTSC material of Y-123 composition not only expands measurement diapason but also raises its resolution. If the ceramic Bi-2223 is used as the core for low magnetic field sensor [7,8], the difference between the operation temperature $T \sim 77$ K and $T_c \sim 108$ K is much greater than that for Y-123 ceramic – $T \sim 77$ K and $T_c \sim 90$ K [5,6,11,12]. Hence always at the same conditions in Y-123 ceramic summary noise of different reasons must be greater than in Bi-2223 ceramic.

The MMM described in [7], has the ceramic Bi-2223 core and possesses $S \sim 400$ V/T and equivalent resistance ~ 50 Ohm. These values involve threshold sensitivity estimation at Nyquist thermal noise level being equal to $N_B \leq 1$ pT/Hz^{1/2}. At the same time internal noise of a quill cylinder made of ceramic HTSC material Bi-Sr-Ca-Cu-O measured by HTSC SQUID device destined for biomagnetic metrology [14], marks lesser magnitude. Thus, if it is possible to discern the internal noise of ceramic HTSC material Bi-Sr-Ca-Cu-O then its magnitude ought to be equal $\leq 0,1$ pT/Hz^{1/2}. This conclusion allows to formulate that the internal noise of a sensor with core of ceramic HTSC material of Bi-Sr-Ca-Cu-O composition will not exceed the magnitude $\sim 0,1$ pT/Hz^{1/2}. Therefore the sensor would be designed and built up in such a way that the noises of other nature: of preamplifier, construction,

external interference, magnetic hygiene non-observance and other were minimal –would not surpass the core internal noise.

At the same time it is necessary in most cases to measure biomedical objects magnetic fields of about (0,5÷10) pT (humans heart and other organs magnetic fields [15]) and higher or to measure with high precision those susceptibility in external magnetic field ~ 0,1 mT (liver and lungs diagnostics [1,2]). It would be suitable for achieving those aims to use the MMM based on ceramic HTSC material of Bi-2223 composition prototype of which is in [7,8] considered. Apparently such a magnetometer has all the affirmative properties, inherent to the flux-gate converters: the capability of magnetic field absolute component measuring, high magnetosensitivity, simple construction, manufacturing simplicity, non-intricate electronic system and other. This magnetometer also possesses affirmative properties inherent to HTSC SQUID devices. Such magnetometer should have the following characteristics: high magnetosensitivity, high magnetic field resolution $\delta(\mu_0 H_0) \leq 1$ pT high magnetic flux resolution $\delta\phi_0 \leq 0,01\phi_0$, high spatial resolution, low threshold sensitivity live $1 \text{ pT/Hz}^{1/2}$, the wide measurement diapason ($10^{-3}\div 10^{-12}$) T, that correspond to $D \geq 120$ dB. At the same time the magnetometers proposed exceed SQUID devices on following parameters: construction simplicity, degradation stability, their prime cost would be at 100÷1000 times less then that of HTSC SQUID devises.

Authors are expressing the appreciation to professor S.V.Selischev for supporting this research.

REFERENCES

1. Fischer R., and et al. 13 th Int. Conf. Biomagn. August 10-14, Jena, Germany. BIOMAG2002. abs. 231. P1.
2. Zheng Y., and et al. 14 th Int. Conf. Biomagn. August 8-12, Boston, Massachusetts, USA. BIOMAG2004. P1-5. P. 267.
3. Afanas'ev Yu.V. Flux-gate devices.: Energoatomizdat, 1986. - 188 P.
4. Deak J., and et al. Appl. Phys. Lett., 1996, V. 69, № 8. P. 1157.
5. Gallop J.C., and et al . IEEE Trans.Magn., 1989. V. 25, № 3. P. 896.
6. Belodedov M.V., Chernykh S.V. Inst.Exper.Tech. 2001. № 4. P. 157.
7. Grigorashvili Y.E., Ichkitidze L.P., and et al. Phys. C., 2006.V. 435. P.140.
8. Ichkitidze L.P. 2nd Int. Conf. FPS. 2006. Moscow, 2006. P. 249.
9. Dilorio M.S., and et al. Appl. Phys. Lett., 1995. V. 67(13). P. 1926.
10. David B., et al. Supercond. Sci. Technol., 1996. V. 9. P. A96.
11. Ignat'ev V.K., Yakimec A.L. Measur. Tech., 2000. №10. P. 49-52.
12. Golovashkin A.I., and et al.. Tech. Phys., 2006. V. 76, №.3. P. 81.

13. Kuzmichev N.D. JETP Letters, 2001. V. 74, № 5. P. 291.
14. Kirscher I., et al. Sensors and Actuators A, 1994. V. 41-42. P. 58.
15. Kneppo P., Titomir L.I. Biomagnetic measurements. Energoatomizdat, 1989. – 288 P.

Mathematical model of apnea diagnostics data-measuring system

O. Merkulova, N. Ivakhno

*Tula State University,
e-mail: merkulovaolga@list.ru,*

According to medical statistics apnea is one of the most widespread and serious disorder directly connected with the sleep. The heavy forms of this disease can lead to the man's death.

The central sleepy apnea (CSA) is characterized by the respiratory movements cessation of a diaphragm and absence of the respiratory stream. In this article CSA diagnostics method is offered.

The offered method is noncontact and based on the ultrasonic sensor application. The ultrasonic sensor radiates impulses with the defined frequency in the patient's thorax direction. According to Doppler effect the signal is reflected from the thorax in the modified form. It is registered, filtered, amplifies and goes to the computer where is exposed to mathematical treatment.

According to offered method the apnea diagnostics data-measuring system (ADDMS) has been developed.

The simulation of signals which appear in the ADDMS during its functioning has been executed by means of MathCAD 2001.

If the thorax movement rate can be described by the harmonious law then it changes according to following expression:

$$V(t) = V_0 \sin(2\pi f_{thorax}t), \quad (1)$$

where V_0 is an amplitude of the thorax movement rate,
 f_{thorax} is the oscillation frequency of the thorax.

At the normal functioning of the respiratory system during man's sleep the variables in expression (1) have following meanings: $V_0 = 5$ mm/sec and $f_{thorax} = 14$ breath/min. Then the thorax movement rate changes as in figure 1.

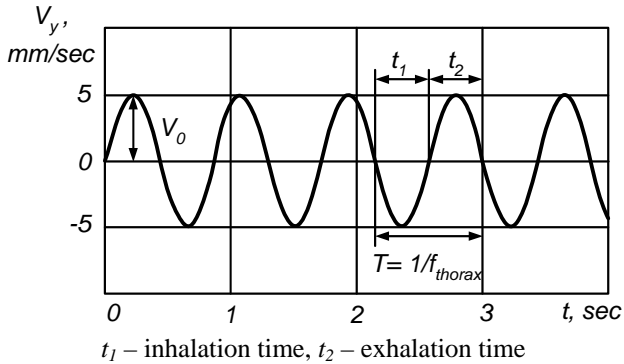


Figure 1 – Rate projection of the thorax movement on the direction of the ultrasonic wave radiation at $V_0 = 5$ mm/sec and $f_{thorax} = 14$ breath/min

To describe sleep's respiratory disorder, the value table of rate amplitude and oscillation frequency of the man's thorax (table 1) has been made.

Table 1
Values of rate amplitude and oscillation frequency of the man's thorax for several time intervals

N_0	Time interval t , sec	Oscillation frequency f_{thorax} , breath/min	Rate amplitude V_0 , mm/sec
I	0 ... 22	12	9
II	22 ... 55	14	9.5
III	55 ... 85	10	8
IV	85 ... 112	6	6
V	112 ... 135	2	2
VI	135 ... 143	0	0
VII	143 ... 200	4	5

So according to expression (1) the thorax movement rate of the patient with CSA during sleep has been found for different values of frequency and rate amplitude. Figure 2 shows the results of calculation.

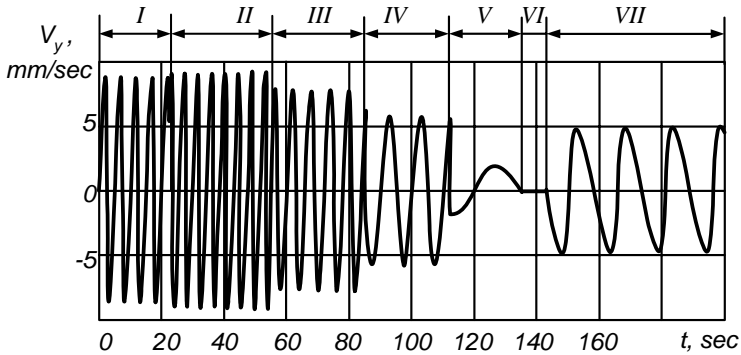
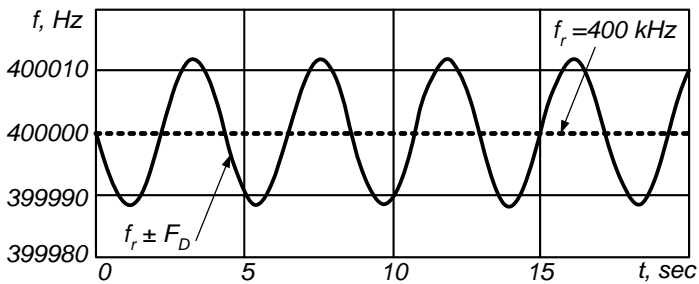


Figure 2 – Rate projection of the thorax movement on the direction of the ultrasonic wave radiation at the rate with variable amplitude and frequency

At the next simulation stage the frequency curves of the echo signal from the man's thorax have been received for the normal functioning of the respiratory system during sleep (figure 3) and for the breathing of the patient with CSA pathology (figure 4).



$f_r = 400 \text{ kHz}$ – radiator frequency,
 $f_r \pm F_D$ – echo signal frequency,
 F_D – Doppler frequency

Figure 3 – Frequency curve of the echo signal at the normal functioning of the man's respiratory system during sleep

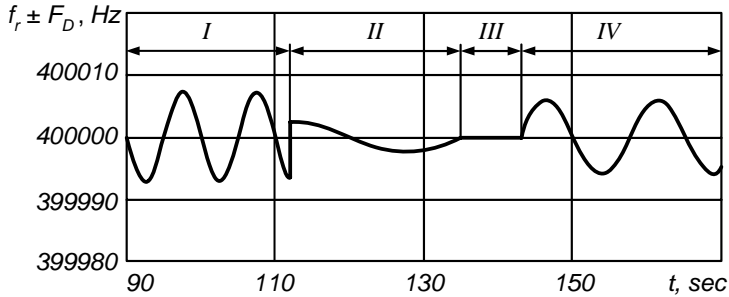


Figure 4 – Frequency curve of the echo signal from the thorax at the breathing of the patient with CSA pathology

Figures 5 and 6 present Doppler frequency curves which have been constructed according to expression (2):

$$F_D = \frac{2|V \cos \alpha| f_r}{c}, \quad (2)$$

where V – the thorax movement rate,

α – the corner between the direction of the ultrasound propagation and the man's thorax movement,

$c = 340 \text{ m/sec}$ – speed of sound,

f_r – radiator frequency.

Figures 5 and 6 shows the simulation results of the Doppler frequency which appears in the ADDMS at the normal functioning of the man's respiratory system during sleep and at the breathing of the patient with CSA pathology.

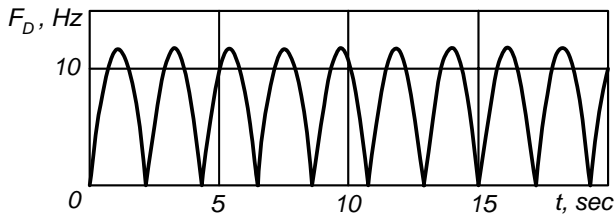


Figure 5 – Doppler frequency variation at the normal functioning of the man's respiratory system during sleep

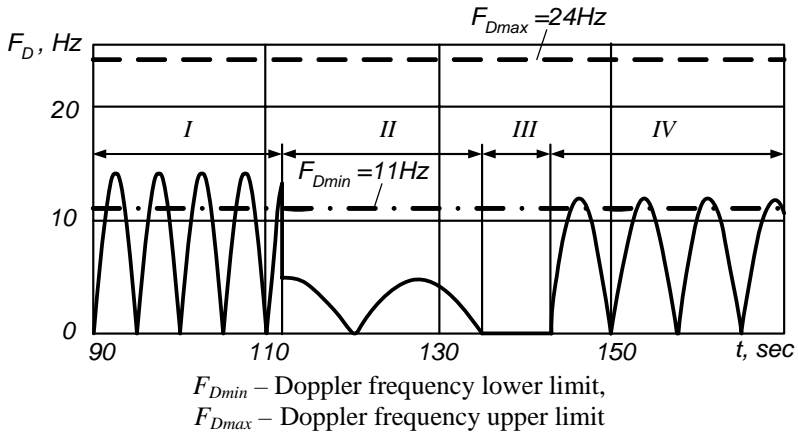


Figure 6 – Doppler frequency variation at the breathing of the patient with CSA pathology

Figure 5 presents Doppler frequency variation at the amplitude of the thorax movement rate $V_0 = 5$ mm/sec and the oscillation frequency of the man's thorax $f_{thorax} = 14$ breath/min.

Figures 4 and 6 shows graphs which have been constructed according to data presented in table 2.

Table 2

Results of calculation of Doppler frequency for several time intervals at the breathing of the patient with CSA pathology

№	Time interval t, sec	Parameters of the thorax oscillation		Maximum Doppler frequency F_D, Hz
		Rate amplitude $V_0, mm/sec$	Frequency $f_{thorax}, breath/min$	
I	90 ... 112	6	6	14.12
II	112 ... 135	2	2	4.71
III	135 ... 143	0	0	0
IV	143 ... 200	5	4	11.76

Thus, comparing measured Doppler frequency with its threshold values, it is possible to monitor man's breathing during sleep.

Mental states BCI

D.E. Romanov

*Department of Biomedical Systems, Moscow State Institute of
Electronics Technology(Technical University)
e-mail: demaroman@yandex.ru*

Introduction. Brain-Computer Interface (BCI) is a human-machine interface, which allows user to control external devices only by mind activity.

The first BCI concept was proposed at 1960. Today there are about one hundred groups all around the world, which are trying to create robust and universal BCI systems. Theoretically, BCI gives to user more facilities than any other interface. It is reasonable to expect the BCI usage in game industry in near future for faster interactions. Already today BCI has been successfully used to give locked-in patients the way to communicate with other people and devices.

Overview. Any BCI system consists of:

- EEG cap – set of electrodes preinstalled at specific head places, which register electrical fields from the skull surface.
- Amplifier – device to amplify weak EEG signals and convert data to digital format.
- PC to accept EEG data, show to user some stimuli and give him a bio-feedback after signal processing.
- Software – programs to process bio-potentials, recognize patterns and generate stimuli.

All these components are quite necessary to build BCI, but in this presentation we will focus only on software part, because exclusively here we can see all differences between BCI systems.

There are many approaches to built BCI. Most popular among them are:

- P300 – detection of P3 complex, which appears due to operator attention to some rare stimulus.
- μ -rhythm – energy level changes during user's imaginary left or right hand squeezing;
- Slow Cortical Potentials (SCP) – using the EEG shifting components related to imaginary emotional states;
- Steady-State Visual Event Potentials (SSVEP) – analysis of stable visual potentials.

- Mental states – recognition of mental tasks via analysis of bio-potentials distribution.

In current presentation only mental states BCI will be further described.

Mental states BCI uses analysis of bio-potential distribution, while person voluntarily performs some mental task at arbitrary moment. We have used four tasks:

- Imaginary left hand compression
- Imaginary right hand compression
- Imaginary cube rotation
- Mental subtraction

Such a set of mental tasks was chosen because the difference between brain areas involved in performing that imaginary activity. Left and right hand activates motor areas in reciprocal right and left hemispheres; cube rotation activates visual cortex; and mental subtracting conditions the activity of frontal cortex.

Regional separability of task-involved areas gives us the reasons to speculate that all these mental tasks can be divided one from another.

BCI users were learned by following scheme:

- 1) System asks user to perform one of mental tasks by showing picture on computer screen with desired task. That task was selected randomly with uniform distribution to generate representative learning samples.
- 2) After saving to database EEG data were feed to a classifier.
- 3) Classifier calculates its output and at the same time learns data in real time mode.
- 4) User observes the result of classification by the bio-feedback rectangle with variable height and color, both reflecting the classification success.

To form one learning session these steps were repeated for about 7 minutes. The duration of one task was approximately 20-30 seconds.

In that type of BCI system both classifier and user are mutually learning and accommodate to each other.

The aim of classifier training is to separate one mental task patterns from another in the best possible way. Of course, such complex process as thinking probably can not be described by a simple linear model, that's why the choice of proper classifier is crucial.

The aim of user training is to obtain the best separation. It is very important for user to gather skills of keeping his/her attention at required level and to switch fast between various mental tasks.

The hardest part of training is the user learning. Such training might take several weeks to get acceptable classification rates. On other hand, classifier learning time depends mainly on model complexity and varies from several minutes to few days.

Recognition of bio-potential patterns is done like that:

- 1) User performs some mental task at any time s(he) wants. System doesn't know which task is performed right now.
- 2) Classifier recognizes the mental task type by finding the task with maximum likelihood coefficient.
- 3) System sends control command based on index of winner task to device.

Such steps are repeatedly executed till user stops communicating with the system.

The practical realization of mental states BCI has next contents:

- 1) To parameterize EEG signal amplitude the Fourier spectrum was calculated in bands from 4 to 32 Hz with 1 Hz step. Overall bands number is 27 ($32 - 4 + 1$). Two last seconds of EEG data while performing task were used for calculations at learning phase.
- 2) EEG was recorded from 19 active channels relatively to referent channel on right earlobe.
- 3) The brain activity pattern consists of 19 vectors with dimension equals to number of bands (27) concatenated one after another. As a result, full feature vector has a dimension $19 \times 27 = 513$.
- 4) Pattern recognition was done every 0.5 s. Taking into account that data analysis window was 2 s, neighbor patterns might overlap 75% of their length.
- 5) Mental task set consists of four tasks: imaginary left/right hand squeezing; imaginary cube rotation; mental subtracting.

During classifier selection 15 different candidate models were considered, some of them were statistical classifiers, other were based on neural network.

Classifier should provide several features.

Necessary:

- Maximal learning accuracy.
- Possibility to real time classification.

Less necessary:

- Minimal learning time.
- Possibility of real time learning.

Only classifiers which satisfy such demands can be considered as classifier candidates for mental states BCI systems. All analyzed classifiers were compared by two parameters:

- Learning capacity: the percent of correctly recognized patterns in learning sample.
- Testing capacity: the percent of correct recognized patterns in testing sample.

Table 1 below summarizes the comparison results.

Table 1. Results of classifiers comparison

Classifier name	Learning accuracy, %	Test accuracy, %
Least square method	84	65
Parabolic classifier	89	63
Polynomial classifier	91	60
Linear classifier	82	68
Radial classifier	80	61
Two-layers perceptron (20 neurons)	88	61
Two-layers perceptron (100 neurons)	95	60

In fact testing accuracy has greater priority than learning accuracy. The best classifier is Linear classifier (one-layer perceptron in neural networks paradigm). Advantages of this classifier are high learning speed and realization simplicity.

The main problem of task classification is that the human mind can't focus on a single task. All the time a user performs one of the mental tasks there are a lot of background processes in his brain. Some of these background processes involve the same areas of brain as the target mental task that's why the background activity might affect classification.

As a result there are a lot of noised patterns in testing samples. It's easy to see from test accuracy values that error can amount up to 30-40 percents even in case of using the strongest classifiers. Filtration helps to overcome this problem. The idea of filtration is based on following:

- Some last results are summarized with descending coefficients.
- In case that sum exceeds some predefined threshold, then BCI sends command corresponding to found task index.

Advantages of the filtration:

- Smoothing effect removes the noise patterns.
- Error rate falls from 40% to 5%.

Disadvantages of the filtration:

- Delay of filter “acceleration” arises.
- Number of sent commands decrease.

The performance of that mental BCI was checked in experiments with three BCI users. Their learning results are represented in table 2.

Table 2. Results of interface learning

User ID	Number of learning days	Accuracy, %
1	4	45
2	6	55
3	14	95

It's easy to see that accuracy increase while training period becomes longer. The best user achieved 95% accuracy after 14 days of training (about 7 ours of pure training).

Conclusions:

- Very simple classifier models can be effective because of re-training possibility.
- Accuracy generally grows with user training progression.
- Filtration increases the accuracy, but makes the classification more inert.
- It's possible to reach 95% accuracy.
- 7 hours of training is enough for qualitative result.

Multifrequency electrical impedance diagnostics of biotissues in oncological surgery

D.V. Belik, K.D. Belik

*Novosibirsk State Technical University,
e-mail:beliki1@mail.ru*

At the present time used for diagnostics of space-occupying lesions of human's biological tissues hardware methods (rentgenoscopy, NMR, US and etc.), especially with minimum occurrence of disturbance of form-building processes and their functions give wrong results because of the presence of the various forms of malignant neoplasms, phlogotic processes in the tissues, artifacts and others that is difficult to classify without pathologic study. In this case clinician often deals with hard restricted diagnostic "instrumentality", oriented and permitting to get only integral information about state of functions or state of result of complex vital functions of dozens of cells, tissues, and sometimes of organs, without permitting to define the type of neoplasm in the whole dimension of its structure, particularly at low differentiated and first forms.

In cases when configuration of the tumour itself or internal phlogistic area has complicated picture, so as in the organ's surface and in its depth it is impossible to make a macroscopic assessment of the size and borders of the oncologic tumour that does not allow surgeon to be sure in its total surgical removal.

Exception to this rather common rule is cytological and histological methods of diagnostic, in which researcher is guided by morphological characteristics of cellular and tissue levels. But morphological analysis needs the impressments from the organism necessary substance, and this procedure may be successful only in case of aiming surgical intervention, so this method is not only invasive, but looking to cumulative action (search "center" of process, material sampling in conditions of through-tissue puncture or by biopsy of volume from 10000 to 100000 cells) is traumatic and far behind 100% reliability. Unfortunately, even cytological screening gives the mistake amount in diagnostically procedure about 30%.

Considering stated disadvantages no one aforesaid methods can not be used in electrosurgical system for diagnostics in vivo in time of surgical operation carrying out and provide controlled by system reliable ablation of neoplasm against the healthy biotissue.

In this situation actuality is the search of new highly sensitive and minimum invasive methods of tissue condition diagnostics, allowed not only to indentify early manifestations of pathological centre, but perhaps to forestall morphological analysis in the time of vital (life-time) diagnostics. The most perspective method in this regard is considered to be method with using radio-frequency current.

At the same time, impedance HF-diagnostics can be perspective diagnostic tool even in simplified version of registration and estimation of total values.

It is known that electric impedances of the different biotissues of one organ appreciably differ from each other.

Except of small number of cases, differences between electric impedances of the nearby biotissues inside one organ is so high and it is not collided neither individual features of patients nor temperature changing of impedance.

As well it was proved the opportunity of estimation of biotissue structure in the time of surgical operation, authors carried out measuring of the impedance of biotissues on the several frequencies, as well as correlations of theses impedances which are called polarization efficiency (E_p), and it gives the opportunity of estimation of biotissues electric characteristics which allowed to differentiate the healthy biotissue and neoplasm with high reliability.

The purpose of researching of pathological biotissues, as well as healthy is the characterization of the impedance and due to them it is possible to construct biophysical and mathematical models which determinant reliability of pathological biotissues ablation. Non-malignant growths and malignant neoplasms were referred to pathological biotissues by us, as well as nonneoplastic cytological neoplasm – dysplasia, metaplasia. Diagnostic reliability of estimation of biotissue electric characteristic is proved by histological study.

It is not always alterations Tarusov's E_p give high degree of self-descriptiveness difference between biotissues because the testing of biotissue is always carried out on two frequencies.

As a result of numerous experiments carried out in different conditions, it was discovered the disadvantages of this method, determined by high receptivity to electromagnetic interference, impossibility of differentiation of cell types which form growth, its age, homogeneity of neoplasm and presence rather small its cellular construction against the healthy biotissue. To increase self-descriptiveness of electro impedance diagnostics of cytological alteration of tissue and oncopathology in particular is allowed the transfer to multifrequency electroimpedancmetry and to estimation of integral characteristic of graphic charts of electroimpedance from frequency ($Z(f)$) for healthy and cytological altered biotissue. In view of it is possible the administration particular E_p , the number of which is determined by the number of quantity of value of significant frequency for electroimpedance characteristic.

Particular E_p on the frequencies 2 kHz and 5 kHz is defined by ratio:

$$K_{II f_{2,5}} = \frac{Z_{f_2}(\Delta Z_{f_2})}{Z_{f_5}(\Delta Z_{f_5})},$$

where Z_{f_2} , Z_{f_5} – absolute value of electroimpedances (for one biotissue), and ΔZ_{f_2} , ΔZ_{f_5} – tissue electroimpedance differences in normal and pathological condition on the frequencies 2 kHz and 5 kHz accordingly.

Thus, every curve $Z(f)$ can be defined not by one K_{II} , but their set, every of them characterizes to the utmost certain type of biotissue in certain physiological conditions. The certain definition of this dependence is possible in further, in time of enrollment statistically reliable quantity of values of particular K_{II} for certain types of biotissues as well as their physiological conditions.

Comparison of particular K_{II} for biotissues in normal and pathological conditions gives more roomy diagnostic result for electroimpedance value, defined in admissible conditions of estimation (interference and other), than value of K_{II} and ΔK_{II} , defined on the base of dual-frequency method.

In the most of practical cases of value, carried out in operating-room, reliability of values of impedance in certain point of curve $Z(f)$ can be

decreased as the result of external factor influence. Using the multifrequency signal of generator and following bandpass filtering on these frequencies helps to exclude the role of some of them in distortion of reliable value view, but can't influence to interference intervention on the frequencies near to generator frequencies. In the case of this, using the diagnostic of biotissue type (and some criteria of physiological condition) based on calculation of area under the curve $Z(f)$, helps excluding particular estimations to pass to integral characteristic of biotissue where particular doubtful values of electroimpedance on the certain frequencies will be graded in the certain degree.

Thus, integral characteristic can be defined as:

$$Z_s = \sum_{f=1}^n Z_f,$$

where n – quantity of reference frequencies,

$$\text{or as } Z_s = \int_{2(10)^{k/f_H}}^{500k/f_H} Z(f)df.$$

Table 1 – The value integral parameter for different types of healthy and pathological biotissues.

Type of biotissues	№ experiment	K_n (2,500kHz)	Specific integral parameter, Z_s/n
Serous tunic of large intestine, norm	1	1,05	326,08
	2	1,46	355,19
	3	1,27	301,11
	4	1,45	343,73
<i>Serous tunic of large intestine, pathological</i>		<i>1,1</i>	<i>145,22</i>
Serous tunic of small intestine, norm	1	1,1	257,01
	2	1,31	232,81
Liver tunic, norm	1	1,84	479,89
	2	1,83	471,52

Thus, integral characteristics Z_S allow to carry out accurate diagnostics of type and physiological conditions (norm, or oncologic growth) of biotissues (table 1) as well as expand their classification. Differential principle of particular E_p realizing on the base of multifrequency electroimpedancemetre (type of cells of its component, the age of neoplasm, homogeneity of structure and so on) and thus its using increases the exactness of diagnostics of these conditions.

As a result of using of aforesaid algorithms is inevitable the using of the evaluative method for definition of type and biotissue condition, which can be realized either by comparison received values of particular K_{Π} and Z_S (specific Z_S) with values from data base, or by means of comparison of estimated values of these parameters for researching (diagnosed) of biotissues in normal and pathological conditions and following definition of correlation score between these values which characterized the degree of cytological alterations passed in the biotissues in compared with surrounding its healthy biotissue.

These correlation parameters can be the ratios of particular K_{Π} for the same frequency areas of estimated values of electroimpedance and the ratio of squares under the curves $Z(f)$ for the healthy and pathological biotissues (as well as difference of these squares).

As experiments show, self-descriptiveness of biotissues differences both healthy in their types and healthy from pathological increases and gives the opportunity to differ cellular arrays cytological altered biotissue with square which is not less the square of measuring electrode, which used for carrying out the testing. Aforesaid increasing of descriptiveness of multifrequency electroimpedancemetre allows to create the systems of reliable ablation of pathological and conditionally pathological biotissues (oncologic and non-malignant growth, nonneoplastic cytological alteration of biotissues and vascular neoplasm).

As a result of using defined principles of biotissues diagnostic on the base of electrosurgical impedance system it is provided the opportunity of carrying out of marking on healthy biotissue the route of ablation, excluding histological expertise as cytologically altered as healthy biotissue as well as electrosurgical effect under the result of diagnostic and as a result it shorten the time of operating and decrease the possibility of further metastasis.

Corresponding parameters of bio-object response to phototherapy in the task of bio-dosimetry control system development

Zmievskey G.N., Karpukhin V.A., Kosorukov A.E., Galkin M.A., Kostyukov D.V.

Bauman Moscow State Technical University; Zmievskey@mail.ru

The modern medicine cannot be presented without wide application of laser technique, both in medical and in the diagnostic purposes. Today it is possible to establish a fact that in laser medicine the backgrounds of quantity into quality transition have ripened. Just, the problematic of health preservation carrying global character also is unprecedented become aggravated in Russia and CIS, not so much saturation of medical establishments by modern technique, how many development of modern medical-technical technologies giving the peak effect at the underlay expense of forces and resorts demands. It in full measure concerns both to medical and to diagnostic applications of lasers.

From the systemic point of view the medical action is either destructive one (surgical) or control response one (therapeutic). The diagnostic action can be viewed as informative one. All views of action are called in a result to recover a homeostatic state of living system; more close is possible to norm. In itself concept of norm is rather difficult as the living system exists in continuous interaction with a surrounding medium.

Let's define a dose as a generalized quantitative measure of action on bio-object producing the diversions from norm. Such definition of a dose which are taking into account basically any actions, requires a concrete definition that it could be viewed as working for a particular view of interactions.

Refer to laser medicine it is accepted to view a dose or as energy of electromagnetic radiation of an optical range incident on unit area of a bio-object surface (surface dose), or as energy cumulative in unity of volume of bio-object (volume dose). Already such a "discrepancy" sets a trap, as the quantitative measure of action, being key concept, should not have of several definitions.

Viewing bioobject as the black box, on which the exterior action is carried out, it's necessary to discharge the response of bio-object to this action. If there is no opportunity to trace and quantitatively to characterize the response, there is no opportunity and to predict the results of interaction, even if all parameters of laser radiation are known. But the concept of the

response demands special definition, taking into account complexity of object and constantly meaning the system character of interaction.

Let's perceive the response plurality of all the results that can to some extent be connected with the given action. A quantitative measure of the response is the population of assigned parameters, admitting measuring by accessible means. Measuring these *assigned parameters*, it's possible to predict the resulting biological effect, not knowing of all parameters of the bio-object.

Thus *basic problem of a dosimetry* can be formulated as follows: build-up of a functional connection between population of laser action parameters and assigned response parameters and use of this functional connection for guidance of action itself.

Note that the second part of the put problem can be solved only at an already known functional connection between action parameters and assigned response parameters. Usually this dependence in the literature is called "dose-effect", but if to view it in the simplified treatment which is not taking into account the parameters population completeness, both actions and response, the absurd deductions are inevitable, with which the literature on practical laser medicine dazzles. The exact forecast of the response can be made only in that case, when the build-up of function action-response (FAR) is carried out correctly. In concrete problems, where the action results are expressed major and a priori unknown parameters amount, the build-up FAR includes all plurality of heuristic devices of research character.

The low-intensity optical radiation (LIOR), first of all laser one, has found wide application in medicine.

There are many operations on study of mechanisms of LIOR action on biological objects for a different organization level - from molecular one up to whole organism one. In light of necessity of examination SBE without finding-out of these mechanisms there can not be a correct statement of the basic problem of a dosimetry. However till now there is no standard concept of the mechanism of activity LIOR on living organisms. There are some alternate points of view explaining the individual phenomena or experiments.

The use of the term LIOR, instead of LILR (low-intensity *laser* radiation) is caused by the fact that the basic performances of laser radiation, first of all, matter a wavelength and spectral density. A coherence and polarization of laser radiation influence medical effect to a lesser degree though to approve that they have not at all value; there are no sufficient foundations.

The problem of finding-out of mechanisms of LIOR action on bio-objects is central as for physicians and biologists, and developers of the equipment during here already more than 40 years of development of low-intensity laser therapy (LILT). While it is far from the resolution, though the fact of sharp pinch of interest to LILT in last 10 years speaks about improvements in its study.

In medium of physicians and biologists the representation about specificity and non-specificity of interaction LIOR with alive organisms was generated. Specific term interaction of light and bio-object bound with an intensive molecular light absorption, i.e. such, for which sets "specific" photo-acceptors exercising a primary light absorption and starting then a series of "specific" photochemical reactions. A typical example of such interaction is photosynthesis. Accordingly, it is considered to nonspecific interaction then, when the biological response is great, and light absorption so it is not enough that unequivocally to establish a primary acceptor it is not obviously possible. Just this aspect — the establishment of primary acceptors at absence of strong uptake — also produces the most fierce discussions, as the transmutation of nonspecific interaction in specific uncloses a trajectory to practical application LILT not on empirical, and on a strictly scientific basis, as allows to carry out advance in the solution of a problem of a dosimetry.

The spectral range, in which the laser therapeutic apparatus work, corresponds to "spectral window" of bio-tissues (600-1200 nm) and is far from reference strips of electronic uptake of all known chromophores of an organism (exception consists colorants of an eye). Hence, about any by considerable (in comparison with incident) the absorbed energy cannot be and speech.

Nevertheless, under activity LIOR a lot of clinical effects are observed which for a long time form the basis LILT. If to try to extend all these effects, it is possible to formulate nonspecific integrated activity on a cellular level: the laser radiation influences on cellular functional activity. Thus it does not change the function, but can enhance its intensity. Or else, under activity LIOR the velocity of cellular metabolism processes varies. In physical-chemical tongue it means, that the potential hills of key biological responses change its height and breadth. In particular, LIOR can strong affect membrane potential. With body height of a field gradient of a membrane the activation barriers of enzymatic reactions fastened on membranous transport, are reduced, providing thus exponential velocity height of enzymatic reactions.

Through the photo-excitation of the dissolved molecular oxygen accompanied with direct generation singlet oxygen, it is accepted to name activation of cells by light-oxygen effect. Oxygen is present at the nature everywhere — from the elementary organisms up to cells of a human body, therefore as a primary acceptor of photons it satisfies to an empirical condition of non-specificity.

Introduction in blood of an optimum singlet molecular oxygen doze generated due to resonant radiation absorption with certain length of a wave causes increase of erythrocytes activity up to a highest level. It causes restoration of oxygen supply of tissues, normalization of their power and gradual improvement of a condition of an organism as a whole, irrespective of the local diagnosis. So that fact can be explained, that laser and photo-therapy possess "wonderful" non-specific property, i.e. are «a medicine for all diseases».

The stimulation of the blood-circulation being most clearly expressed medical effect at low-intensity of photo-therapy, can be used as a measure of the response of an organism and accordingly for management of photo-influence in a mode of a biological feedback.

In our experiments bio-photometric sensors and skin-galvanic reactions sensors were applied to the control of intensity of a peripheral blood-groove (Fig. 1-3).

Two-channel photo-plethysmograph (Fig. 1) allows to investigate of a peripheral blood-circulation dynamics during photo-therapeutic influence with possible reactive hyperemia corresponding finiteness. Use of two-channel system allows to reveal two important diagnostic parameters at once: size of a gain of amplitude after occlusion and shift of phases between reference and occlusion channels. These parameters can serve as assigned response parameters at the set influence on an organism.



a)

b)

Fig.1 Two-channel photo-plethysmograph: a) external view; b) device with connected up sensors and computer cable

The express-spectrophotometer (Fig. 2) is intended for the control of dynamics of a peripheral blood-circulation intensity over a spectral range of 400-650 nanometers, meaning, that reflected by a surface of bio-object radiation contains the information not only on a blood-circulation, but also on the maintenance of other pigments (bilirubin, melanin) which influence on a signal of a feedback should be minimized. Investigating the data on spectral structure of radiation, it is possible to receive the information not only on amplification of a blood-circulation, but also on change of ratio between various derivatives of hemoglobin in blood.



Fig.2. Express-spectrophotometer: a) external view; b) measurement process

The express-analyzer electric-dermal activity (Fig. 3) measures an electric impedance of a skin and skin-galvanic reaction in researched points. On change of parameters of electric activity of a skin of the person, determined during physiotherapeutic influence, it is possible to judge intensity of processes, to him it caused, so and about efficiency of the influence. Moreover, if to influence are exposed receptor fields of a skin or biologically active points all complex of the listed nonspecific changes can lead to increase or downturn of excitability of the certain receptors (elements of nervous system) and by that to change character regulatory influences on the part of the central nervous, vegetative and hormonal systems on cardiovascular, immune and other functional systems of an organism.

These data supplement the information received by photometric devices and allow to add a set of assigned parameters for management of photo-action.



Fig.3. Electric-dermal activity express-analyzer (external view)

The Determination of Optical Characteristics for a High Scattering Medium on the Base of Enhanced Diffusion Model

A.A.Danilov

*Moscow Institute of Electronic Technology (Technical University)
e-mail: realswat@rambler.ru*

Now one of the basic directions of medical engineering is the creation of diagnostic and therapeutic devices and systems using laser radiation. In this connection the development of methods for the description of interaction between laser radiation and biological tissue is an urgent task.

Two kinds of radiation interaction with medium take place under the propagation of laser radiation through biological tissue. These kinds are the absorption and the scattering of radiation. Therewith the scattering is a more probable process than the absorption. Therefore, the use of approximation of pure absorbing medium, as it is in x-ray computed tomography, is impossible.

The basic method for the description of transmission of laser radiation through HSM is the radiation transport equation (RTI), representing equation of energy or particles balance in closed volume. RTI has not the analytical solution. Thus it is necessary to make the additional assumption, simplifying a RTI.

Today the classical diffusion model (CDM) is the most popular method for description the laser radiation transport in biological tissue. It is simple model allowing in some cases to receive exact results. However CDM has a number of drawbacks. In particular, in this model the source term is represented as a point isotropic source displaced deep into medium on a distance z_0 (free path of photons). This assumption reduces accuracy of CDM and area of its application. In particular, CDM poorly describes behavior of photons near to borders of medium, sources, and as is inapplicable for the description of passage of laser pulses through thin scattering layers, with thickness of the order z_0 .

As alternative for CDM is offered enhanced diffusion model (EDM). In this model the mono directivity of initial radiation is taken into account. It raises accuracy of model and, in particular, allows using it for the description of passage of laser radiation through thin scattering layers.

For an experimental research of laser radiation transport through biological HSM the system including the pulse semi-conductor laser with duration of a pulse 75 ps and the detection channel, working in a mode of the single photons counting was used. The time resolution of system was made 200 - 230 ps.

In a fig. 1 the results of measurement of absorption coefficient of model HSM with CDM and EDM are presents. The accuracy for both model has made $\pm 0,001 \text{ mm}^{-1}$ (in a figure is not shown because of smallness).

For small concentration of scatterer the absorption coefficient of model medium should remain constant. Meanwhile, at volume concentration of scatterer less than 0,01 in both models the abnormal picture is observed - absorption coefficient decreases in process of growth for concentration of scatterer. It is connected that in the given area the scattering properties of model medium are expressed poorly and both models appear are inapplicable. At meanings of concentration of scatterer more than 0,01 scattering properties of medium begin to prevail above absorbing. In this case in both models of meaning of absorption coefficient practically do not vary at increase of concentration of scatterer.

In a fig. 2 are given received in CDM and EDM of dependence of reduced scattering coefficient on concentration of scatterer. The accuracy for CDM has made $\pm 0,015 \text{ mm}^{-1}$. The accuracy for EDM has made $\pm 0,012 \text{ mm}^{-1}$.

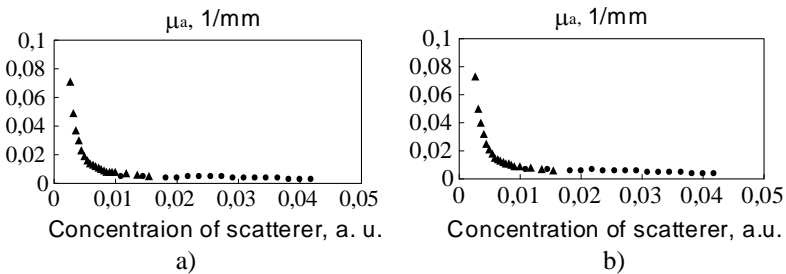


Fig. 1. Absorption coefficient of model medium vs concentration of scatterer received in CDM (a) and EDM (b). The thickness of the slab is 400 mm (▲) and 200 mm (●)

For meanings of concentration of scatterer less than 0,01 both models as give abnormal results, reduced scattering coefficient decreases in process of increase for concentration of scatterer. At concentration of scatterer more than 0,01 reduced scattering coefficient are increased linearly in process of

growth for concentration of scatterer. A approximating curve (the shaped curve in a fig. 2) passes near to a point (0,0). That corresponds to negligible scattering properties of pure water.

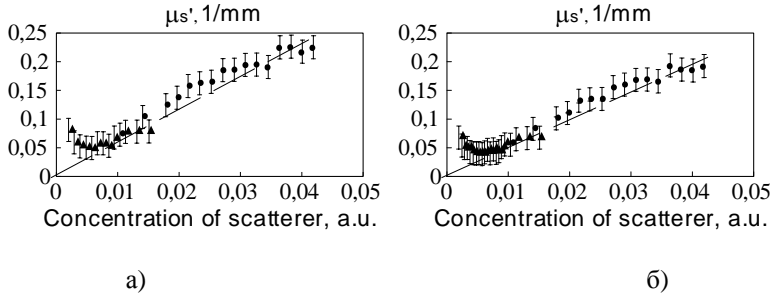


Fig. 2. Reduced scattering coefficient of model medium vs concentration of scatterer received in CDM (a) and EDM (b). The thickness of the slab is 400 mm (▲) and 200 mm (●)

As the absorption and scattering coefficients in different models have a different physical meanings, it is impossible to compare the obtained results directly. Therefore after definition of meanings for absorption and reduced scattering coefficients with CDM and EDM the curves of theoretical dependencies of full width at half maximum (FWHM) and displacement of a maximum for temporary distribution of a detected intensity on concentration of scatterer were constructed. The theoretical curves were combining with experimental (fig. 3, 4).

The results received with CDM and EDM, will be agree to experimental data. The dependence for FWHM of concentration of scatterer received with EDM has not a relative maximum, as a dependence, received with CDM. Thus, EDM correspond to experimental data better than CDM. Received with EDM dependence for displacement of a maximum for temporary distribution of a detected intensity on concentration of scatterer predicts earlier occurrence of temporary distributions with the displaced maximum. It again corresponds better to experimental data.

It is shown the existence of a range for concentration of scatterer, in which CDM and EDM can be applied for the description of passage for laser pulses through HSM. As is shown, that the results received with EDM, correspond better to experimental data.

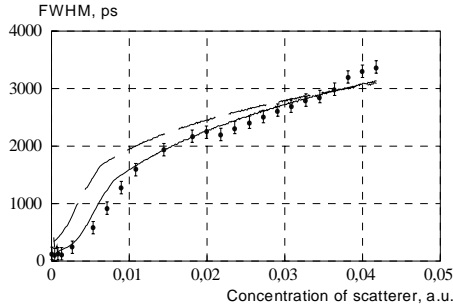


Fig. 3. The experimental (●) and theoretical (CDM – solid curve, EDM – shaped curve) dependencies of FWHM vs concentration of scatterer.

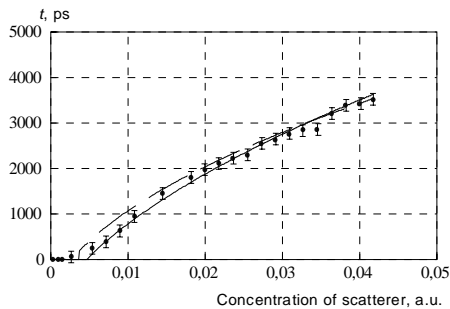


Fig. 4. The experimental (●) and theoretical (CDM – solid curve, EDM – shaped curve) dependencies for displacement of a maximum for temporal distribution of a detected intensity vs concentration of scatterer.

References

1. A. Ishimaru. Wave Propagation and Scattering in Random Media. – New-York, Academic Press, 1978. – 600 p.
2. Patterson M.S., Chance B., Wilson B. C. Time resolved reflectance and transmittance for the noninvasive measurement of tissue optical properties // Applied Optics, 1989. – Vol. 28, No. 12, P. 2331 – 2336.
3. Tereshchenko S. A., Danilov A. A., Podgaetsky V. M. A Refined Diffusion Model of the Interaction of Laser Radiation with Biological Tissue// Optics and Spectroscopy, 2007. – Vol.102, No.5, P.771-777.

Methods of processing, analysis and definition of QRS in ECG

A.N.Gusev, I.V.Nesterenko, D.B. Rygalin*, D.V. Telyshev

Moscow Institute of Electronic Technology (Technical University),

** Zelenograd Innovation-Technological Center*

e-mail: telyshev@bmslab.miet.ru

Cardiovascular diseases have the first place in the world by death-rate. Electrocardiogram is a most widespread method which diagnose of heart patient. The basic component of ECG signal is the QRS which is responsible for ventricular depolarization. The doctor diagnoses the patient using features of the given component. The important factor is the measurement of intervals time between R-peaks (variability of an intimate rhythm) QRS of ECG signal. All above described factors can be measured using an automatic mode that will allows to simplify doctor's job or it will allows to diagnose when the doctor is absent.

The important factor that influence on ECG detection are noises.

The noises, presented in ECG, we can divide into two basic categories:

- noises caused by external physical factors;
- tool noises caused by the ECG device.

The external factors are caused by physiological features of a person, and tool factors are caused by features of measuring engineering, used for registration of a signal.

The most important noises caused by external physical factors are:

- noises of power electrical lines;
- noises of contacting electrodes;
- electrical activity of muscles;
- jumps or displacement of isoline;
- drift isoline owing to respiratory activity;
- noise of the peripheral equipment.

It is possible to allocate some strips in a spectrum ECS, in which the major capacity of noise is usually concentrated, while the capacity of a useful signal in the data is minimal.

Such strips are:

- frequency less than 0.5 Hz – the basic capacity of drift isoline noise;
- 50/60 Hz - noises of electrical power lines;
- 35-40 Hz - noises of muscles electrical activity;
- more than 100 Hz- high-frequency noises of a different nature.

The basic capacity of QRS is concentrated in the field of frequencies 2-20 Hz with presence of a maximum on frequency about 15 Hz.

These above parameters should be used for ECG processing.

In a course of standard ECS representation is possible to determine, that the greatest amplitude meaning has R wave, of a QRS. Tracing intervals between waves R is possible to check meaning of the pulse in a real time, and trace that's changing. Threshold meaning, which can carry adaptive character or have the certain meanings, can be used for these purposes.

The detecting QRS by threshold meaning assumes for the following operations:

- choose the threshold meanings of a researched signal, supposed, that all R wave should be stacked in the given interval (for example, the interval from 0,75 mV up to 5 mV), and it is possible to use adaptive threshold meaning;

- makes the binary signal, all the meanings of the voltage which have got inside researched interval are equated to 1, all meanings outside researched interval are equated to 0.

First R wave settles down in the middle of the threshold and is calculated under the formula:

$$T_R = \frac{t_2 - t_1}{2}, \quad (1)$$

where t_1 - transition from 0 in 1, t_2 - transition from 1 in 0

The next method QRS detection is based on the assumption, that speed of QRS increasing is the greatest in comparison with other components.

The signal ECG is represented as array: $x(1), x(2), x(3), \dots, x(k)$, where k - amount of elements in array. The comparison of three following one after another report of a signal ECG is made:

$$x(n) - x(n-1) > 0,125 \text{ mV}$$

and

$$x(n+1) - x(n) > 0,125 \text{ mV}, \quad (2)$$

if the condition (2) is implement, the meaning of array is equated to 1, if no, to 0.

Two above described methods have formed the basis for development of QRS detecting algorithm in ECG.

The algorithm works with adaptive threshold meanings, amplitude of the filtered signal and first derivative. It combines an opportunity to investigate a signal on the maximal meaning both on increasing and decreasing speed of a signal front. The threshold meanings get out according to duration of a researched interval.

Initially signal is passed through 2 FIR Kaiser filters. The first filter is high-pass filter 26-th order with a passband equal to 8 Hz, second filter is low-pass filter 8 order with a passband equal to 24 Hz.

The detecting process assumes the following operations:

- filtered signal is represented as array $X(n)$, and first derivative is searched under the formula:

$$Y(n) = |X(n+1) - X(n-1)|; \quad (3)$$

- time interval choice, in which will be investigated arrays $X(n)$ and $Y(n)$, and allocation subarrays $x(n)$ and $y(n)$ on a researched interval;

- searching maximal meaning of array $x(n)$ and maximal meaning of array $y(n)$, and the threshold meanings are allocated according to the formula:

$$\begin{aligned} A &= 0,6 \max[x(n)], \\ B &= 0,6 \max[y(n)]; \end{aligned} \quad (4)$$

- allocating the meanings appropriate from array $x(n)$ according to the following criterion:

$$0,3 \text{ mV} < \max[x(n)] < 5 \text{ mV},$$

and

$$x(i) > A \text{ and } x(i) > 0,3 \text{ mV}, \text{ where } i = 0, 1, 2, \dots, n-1; \quad (5)$$

- allocating the meanings appropriate from array $y(n)$ according to the following criterion:

$$\max[x(y)] < 2 mV ,$$

and

$$y(i) > B, \text{ where } i = 0, 1, 2, \dots, n - 1 ; \quad (6)$$

- then these conditions are combined, and the new array consisting from zero and one is formed. As far as one of the above described conditions is done, enters one in array, otherwise zero. There is one more condition: as soon as first one is found out following one can be found out only through 150 ms. Thus, in a new array the ones will correspond to QRS detection of an initial ECG.

The given algorithm was analyzed by a MIT-BIH Arrhythmia database, which contains 48 records by duration 30 minutes everyone. Below in a table, are given data for algorithm working for time intervals: 1 s, 2 s, 4 s.

Table

Results data of detecting

Length of window (s)	Sensitivity (%) Se	Specificity (%) Sp
1	99,96	96,62
2	99,77	98,95
4	99,67	99,28

Parameters of sensitivity and specificity of the developed algorithm, using a window in 4 s, have made: 99,67% and 99,29%

These data are comparable with results of QRS detecting of the best algorithms.

The given work is executed at partial financial support of the Russian Fund of Basic Researches, project N 05-08-50300.

Tissue functional topography and inhomogeneity of metabolic processes observed by the spectrophotometric method

L.P. Safonova, V.P. Nevzorov

*Bauman Moscow State Technical University
e-mail: larisa.safonova@gmail.com*

INTRODUCTION

The viability of biological tissues is associated with the level of metabolic processes and the tissue respiration. The intensity of the last one is determined by the oxygen absorption velocity per a mass unit of a tissue. The adequacy of the tissue respiration is governed by the following factors: oxygen partial pressure in the atmosphere, oxygen transport to the blood by the breathing system, oxygen transport to tissues by the cardiovascular system with account of hemoglobin properties, and a ratio of aerobic and anaerobic processes.

The effectiveness of oxygen transport to tissues is estimated with the help of spectrophotometry – by the tissue oximetry method [1,2]. Multi-distance spectrophotometry of biological tissues reflects distributions of the main tissue chromophores, including oxy- and deoxyhemoglobin, inside the probed tissue volume.

TISSUE OXIMETRY PRINCIPLE

Quantitative biotissue parameters registered by the tissue oximetry method are the absorption coefficient μ_a (1/cm) and the reduced scattering coefficient (μ_s') with regard of the scattering anisotropy parameter (g); $\mu_s' = \mu_s(1-g)$, where μ_s denotes the scattering coefficient (1/cm).

Spectrophotometric estimation of these parameters with the high precision is possible with the aid of modulation regimes of tissue irradiation: by short laser pulses ($\sim 10^{-10}$ to 10^{-12} s), or by the modulated light usually in the frequency range 30 MHz to 1000 MHz. Used in these case red and near infra-red light (680 to 900 nm) penetrates in biotissues on several centimeters. By using the mentioned above irradiation regimes it is possible to separate absorption and scattering phenomena [2].

When N chromophores are present in a tissue, the absorption coefficient μ_a (1/cm) at wavelength λ_j is defined by an equation:

$$\mu_a(\lambda_j) = \sum_{i=1}^N \varepsilon_i(\lambda_j) C_i,$$

where ε_i and C_i correspond to the molar extinction coefficient ($\mu\text{M}^{-1}\text{cm}^{-1}$) and the molar concentration (μM , micromolar= 10^{-6} moles per liter) of the i th chromophore.

The regime of the modulated intensity is the more often used and is characterized by the high time resolution (10 mc) and the spatial resolution (1-5 mm) and by the relative simplicity of the technical realization. In this case quantitative values of the optical parameters are determined by changes of the light parameters (the intensity, the depth of modulation, and the phase shift) with multidistance testing. The light penetration depth depends on the optical probe configuration (source-detector distances) and the tissue optical properties (μ_a and μ_s'). The instrument calibration is necessary and performed on homogeneous silicone blocks with the added TiO_2 powder. The optical properties of the calibration block are known and similar to the tested tissue optical properties [2-5].

EXPERIMENTAL METHOD AND INSTRUMENTATION

In the experimental research the two-channel tissue oximeter "OxiplexTS" (ISS, Inc., USA) was used. This instrument has the following characteristics: the intensity modulation frequency is equal to 110 MHz; wavelengths of multiplexed light sources are equal to 690 nm and 830 nm; there are 8 sources (laser diodes) and one photodetector (a photomultiplier tube) per a measuring channel (four diodes of each wavelength); time multiplexing is up to 100 Hz. A flexible fiber-optic probe is designed with prisms and has four different source-detector distances that are from 2.0 to 3.5 cm; a diameter of each source fiber is equal to 400 micrometers; a diameter of a detector fiber is equal to 3 mm.

Twenty five volunteers of the age of 20 to 22 years were participated in two series of experimental measurements with different probe locations and measurement methods. At the first experimental part the optical probe was located above the quadriceps femoris muscle of the thigh during bicycle exercising of low and medium power. At the second experimental part the optical probe was located on the forehead during breathing tests (20-second end-tidal breath holdings, 40-second hyperventilation periods, and 40-60-second breath holdings after deep inhale) in the supine position.

RESEARCH RESULTS

The multidistance spectrophotometric method reflects the distributions of oxy- and deoxyhemoglobin concentrations and derivative parameters such as the total hemoglobin concentration and tissue oxygenation inside the tested tissue volume.

In Fig. 1 measurement results are presented for a physically well-trained volunteer (a,b) and for a physically weak volunteer (c,d). Values of the tissue oxygenation StO_2 (a,c) and the concentrations of the total hemoglobin THb (b,d), oxyhemoglobin O_2Hb , and deoxyhemoglobin HHb are various for different light penetration depth. Numbers “1” – “3” on the graphs correspond to the ordinal number of the tissue depth beginning with the superficial layers (skin and adipose tissue); number “4” corresponds to the tissue parameters calculated for the whole tested tissue volume, all penetration depths. The first vertical marker on the graphs indicates the start of the 15-minute bicycle exercising; the sixth marker corresponds to the end of the exercising and the beginning of one-, three-, five-, and eight-minute recovery periods indicated by the vertical markers at the end of each period.

The received results represent significant dissimilarities in StO_2 , THb, O_2Hb , and HHb for layers of different depths.

At the group of physically well-trained volunteers changes in the total hemoglobin concentration (proportionally to the tissue blood circulation volume changes) were up to two times larger than the same parameter changes at the group of physically weak volunteers. The well-trained volunteers demonstrated relative constancy of the tissue oxygenation during exercising. The physically weak volunteers demonstrated considerable lowering of the oxygenation level of the functionally active tissues during bicycle exercising.

The greatest differences in the parameters' values and changes for the various depths were observed for the thigh tissues in comparison with the forehead tissues because of the significant thickness of adipose tissue above the quadriceps femoris muscle of the thigh. Figure 2 illustrates the results of the measurement on the forehead during breathing exercises in the supine position. The black lines correspond to the upper layer signals (THb, O_2Hb , and HHb); the gray lines correspond to the deepest layer signals. Skin influence was minimal under the used optical probe configuration. Tissues with the higher metabolic rate were characterized by the higher values of the total hemoglobin and deoxyhemoglobin concentrations as that was also observed for the measurements on the thigh.

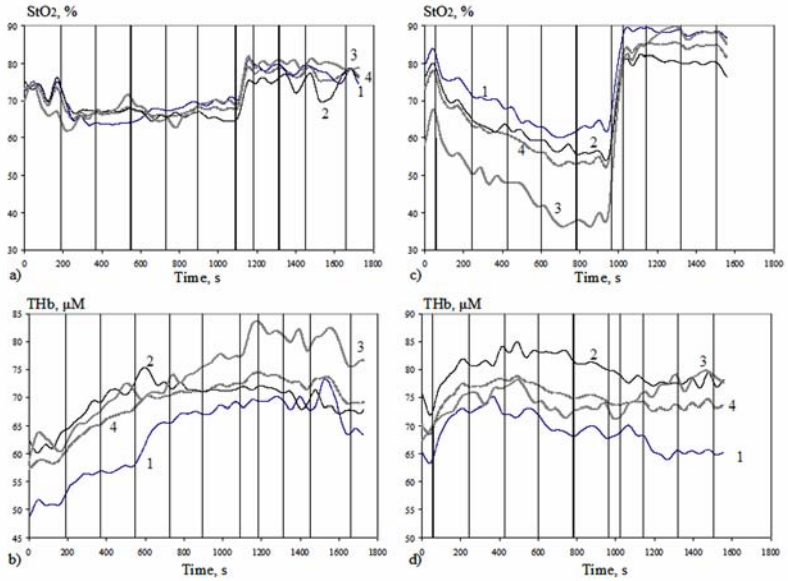


Fig. 1. Tissue oximetry above the quadriceps femoris muscle of the thigh during bicycle exercising

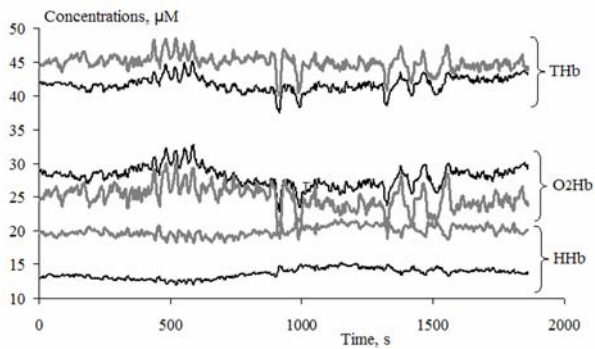


Fig. 2. Tissue oximetry with the forehead location of the optical probe during breathing exercises

CONCLUSION

The multidistance spectrophotometric method may be used to observe functional topography and inhomogeneity of metabolic processes of living tissues.

The configuration of the multidistance optical probe for muscle tissues and for intracranial tissues greatly depends on the thicknesses of skin and adipose tissue.

Possibilities of the spectrophotometric method examined in this research would be more completely pronounced with the help of the three-dimensional presentation of the measured data.

REFERENCES

1. Localized irregularities in hemoglobin flow and oxygenation in calf muscle in patients with peripheral vascular disease detected with near-infrared spectrophotometry / U. Wolf, M. Wolf, J.H. Choi, et.al. // *Journal of vascular surgery*. 2003. Vol. 37, № 5. P. 1017–1026.
2. Tuchin V. *Tissue optics. Light scattering methods and instruments for medical diagnosis*. SPIE PRESS, 2000. 353 p.
3. Semi-infinite geometry boundary problem for light migration in highly scattering media: a frequency-domain study in the diffusion approximation/ S.Fantini, M.A.Franceschini, E.Gratton// *Journal of the optical society of America*. 1994. Vol. 11, № 10. P. 2128–2138.
4. Quantitative determination of the absorption spectra of chromophores in strongly scattering media: light-emitting-diode-based technique / S. Fantini, M.A.Franceschini, E.Gratton// *Applied optics*. 1994. Vol. 33. P. 5204–5213.
5. Frequency-domain multichannel optical detector for noninvasive tissue spectroscopy and oximetry / S. Fantini, M.A. Franceschini, J.S. Maier, et.al. // *Optical engineering*. 1995. Vol. 34. P. 32–42.

Estimation of subject emotional state from speech parameters

Vinokurova M., Solovjeva E., Tarasov R.

*Department of Biomedical Systems, Moscow State Institute of
Electronics Technology (Technical University)
e-mail: roman@neurobotics.ru, solo_helena@mail.ru*

The provision of voice communication is an important part of Human-Computer interface. The reason of increased interest to emotion recognition from speech is related to the fact that large portion of information in speech is transferred in nonverbal way. That's why researches in this area are targeting both emotional speech synthesis and emotion speech recognition. The existing systems differ from each other by number of emotions being classified, database structure, acoustic parameters and classification algorithms. But still automatic recognition of speaker emotional state is the actual task of speech signal processing.

The purposes of current work are defining of the most informative speech features set, estimating the dependence between the basic speech features and basic emotional human states, and selecting the optimal set of classification features.

The emotional content of speech signal is expressed through the changes of it's linguistic parameters (emphasis, intonation, average sentence length, speech parts usage statistics). It's also expressed through paralinguistic parameters, such as pitch, tempo, loudness, pauses, nonlinear characteristics, etc. In spite of high information capacity, linguistic parameters are difficult to be expressed in numeric form, which makes research results based on them more prone to subjective judgment. In contrary, paralinguistic parameters more easy to extract and analyze by various statistical methods, which provides an opportunity to express the results in numeric form.

For our research we choose the next acoustic features: jitter, shimmer; maximum difference and standard deviation of fundamental frequency for all sentence, intra- and inter-segment maximum difference and standard deviation of fundamental frequency, the non-linear energy estimation in 3 lowest critical bands via Teager Energy Operator (TEO). As a basic set of emotions for our research we choose: neutral state, anger, fear, happiness and sadness. As experimental material we used a subset of EmoDB database, containing 187 records of 5 speakers.

We have employed objective and subjective research methods (perceptual test). During perceptual test we offered to 20 subjects to listen records from that database and to define the emotion type for every record. Every subject got the same records, but in random sequence. The results of perceptual test are presented in table 1.

Table 1. Perceptual test results (in %)

	neutral	anger	happiness	sadness	fear
neutral	84	1.57	0.26	14.2	0
anger	7.85	82.3	7.14	1.19	1.42
happiness	19.5	5.6	68	2.39	4.34
sadness	6.05	0.26	0	90.7	2.89
fear	11.7	3.8	3.4	3.46	77.5

In this table we can see how subjects have recognized different emotions from database. The sum of cells in every row is 100%. The crossings of columns and rows with identical names give us a percentage of correct recognitions. The names of rows are the names of emotions in records and the names of columns are the names of possible subject answers. As a result we can see that total percentage of correct recognitions is about 80%. For sadness state of correct recognitions were 90.7 %, for neutral state – 84 %, for anger – 82.3 %. We also found 4 records that were recognized incorrectly by all subjects.

As objective research methods we use single factor dispersion analysis, correlation analysis and multidimensional scaling. Single factor analysis had revealed the weight of each parameter in emotional state recognition. Weight definition at dispersion analysis is based on comparison of component conditioned by intergroup dispersion and component conditioned by dispersion inside group.

The result is assumed to be statistically correct if the error level is below 0.005. Thus, we found, that shimmer, minimum and maximum energy values do not depend on emotional state changes practically. Also we found that parameters related to fundamental frequency (maximum difference and standard deviation of fundamental frequency for overall sentence, as the ones for intra- and inter- speech segments) separates stenic and astenic emotions poorly (anger vs. happiness). Nonlinear features badly separates astenic emotions (neutral vs. fear, neutral vs. sadness), but they are good for classification different stenic emotions (anger vs. happiness). Jitter is good for separating stenic emotions.

Multidimensional scaling is a method for optimal object placing, which approximately keeps ranges between objects. Multidimensional scaling places objects in the space with given dimensionality and checks how precisely obtained configuration keeps ranges between objects. Figure 1 show the perceptual test results in 3-D space.

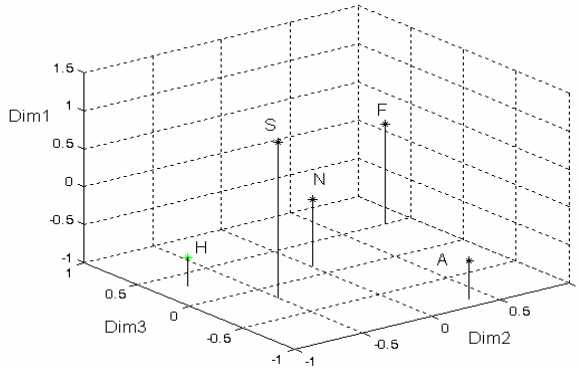


Figure 1. The results of perceptual test in 3-D space

Spearman test was performed to check the correlation between averaged speech features and emotion coordinates in 3-D space. We elaborated the next results. No significant correlation of Dim1 dimension and speech features was found. Dim2 correlates well with TEO at 250 Hz critical band and partially correlates with fundamental frequency. Dim3 has a correlation with TEO at 51 Hz critical band and standard deviation of signal energy. It means that Dim3 is conditioned by signal energy.

For emotional state classification we used MATLAB realization of multilayer perceptron (MLP). The classification results for training and testing set are presented in tables 2 and 3.

Table 2. MLP classification results (training set)

	neutral	anger	happiness	sadness	fear
neutral	75.7	6.06	9.09	0	6.06
anger	2	93.8	0	4.08	0
happiness	29.6	3.7	62.9	0	3.7
sadness	9.5	19.04	4.76	61.9	4.76

fear	18.1	0	4.54	4.54	72.7
------	------	---	------	------	-------------

Table 3. MLP classification results (testing set)

	neutral	anger	happiness	sadness	fear
neutral	83.3	0	0	0	16.6
anger	0	80	0	20	0
happiness	0	11.1	44.4	33.3	11.1
sadness	0	20	40	40	0
fear	33.3	0	0	0	66.6

After series of experiments we have chosen the following structure of MLP feature vector: standard deviation of fundamental frequency values, intra-segment standard deviation of fundamental frequency values, TEO, standard deviation of energy. The experiments have shown that the following MLP structure as optimal:

- number of neurons in second layer – 45
- number of training cycles – 1000
- activation coefficients for first and second layer – 0.1 and 0.1
- training speed for first and second layer – 0.1 and 0.1.

Thus, the percentage of correct recognitions of MLP classifier for neutral state, anger and happiness doesn't differ significantly from perceptual test results. The performance of classifier for sadness and fear state is slightly worse. It's connected partially with difficulty to divide some emotions even for human brain, for example to divide anger and happiness, or neutral state and sadness.

Summary. During current research the effective speech features set was selected from variety of speech characteristics. As revealed by statistical analysis the proposed feature set correlates well with basic emotional human states. For automatic estimation of emotional state the MLP classifier was introduced. Its classification results are compatible with subjective emotional state estimation by human listeners via perceptive test.

References

1. Burkhardt F., Paeschke A., Rofles M., Sendlmeier W., Weis B. A database of german emotional speech // Interspeech 2005;

2. Jovicic S., Rajkovic M., Dordevic M., Kasic Z. Perceptual and statistical analysis of emotional speech in man-computer communication // SPECOM'2006, Saint-Petersburg;
3. Schroder M. Speech and emotion research: An overview of research frameworks and a dimensional approach to emotional speech synthesis // PhD thesis;
4. Zwicker E., Fastl H. Psychoacoustics. Facts and Models // Springer Series in information sciences, v. 22, Berlin, 1999;
5. Rosenfield E., Massaro D., Bernstein J. Automatic Analysis of Vocal;
6. Manifestations of Apparent Mood or Affect // USA Department of Psychology, University of California at Santa Cruz, 2003;
7. Teager H., Teager S. Evidence for Nonlinear Production Mechanisms in Vocal Tract // Speech Production and Speech Modeling v.55, pp.241-261, 1990;
8. Zhou G., Hansen H., Kaiser J. Nonlinear Feature Based Classification of Speech under Stress // IEEE Transactions on Speech & Audio Processing, v. 9, № 2, pp. 201-216, 2001;
9. Kwang-Dong J., Oh-Wook K., Emotion recognition for affective human-robot interaction // SPECOM'2006, St.Petesburg, June, 2006;
10. Fernandez R. A computation model for the automatic recognition of affect in speech // Ph.D. Thesis, MIT Media Arts and Science, Massachusetts Institute of Technology, 2004.

Multifunctional laser noninvasive diagnostic system for medicine

Sidorov V.V.¹⁾, Rogatkin D.A.²⁾

¹⁾ SPE “LAZMA” Ltd., Moscow, lazma@plusnet.ru

²⁾ Moscow Regional Research and Clinical Institute “MONIKI” named after M.F.Vladimirsky, Moscow, laserrog@mtu-net.ru

In recent 10-15 years the general medical practice has been successfully enriched with different new methods of noninvasive optical diagnostics such as a Laser-Doppler Flowmetry (**LDF**), Laser Fluorescent Diagnostics (**LFD**), Optical Tissues Reflectance Oximetry (**TRO**), etc., which all in totality we now call a “Medical Noninvasive Spectrophotometry” (**MNS**). All these methods allow a doctor to evaluate “in vivo” and more exactly a clinical condition of soft tissues, especially to study the finenesses of respiratory processes and blood microcirculation processes in a skin and mucosa [1, 2]. This report describes a new multifunctional laser noninvasive diagnostic system (**MLNDS**) for medicine which combines LDF, LFD and TRO diagnostic technique in a single equipment, what makes it possible to use them together during one diagnostic procedure to collect all necessary “MNS” diagnostic data from the same anatomic “point” of the examined tissue. This way and some advantages of that in a modern medicine were recently predicted by one of the authors in [1]. Now a first compact pilot prototype of MLNDS (SPE “LAZMA” Ltd., RF) goes a clinical trial in “MONIKI”.

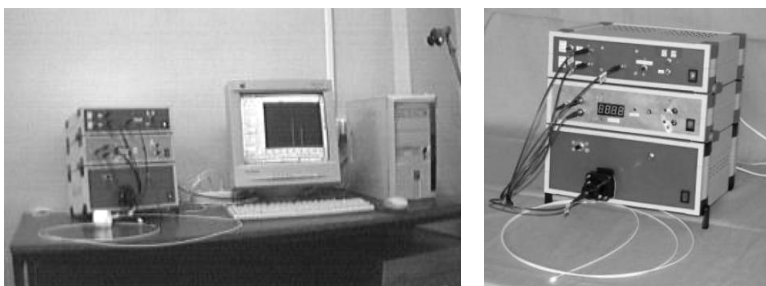


Fig.1. First compact pilot prototype of MLNDS.

The prototype of MLNDS (Fig.1) is a small opto-electronic and low-energy laser diagnostic system with a computer. It is a table-held diagnostic system with an optical cord in a capacity of diagnostic probe. So it is useful

for different external clinic examinations as well as for various inner endoscopic (gastroscopic, etc.) procedures. MLNDS consists of typical and some special lasers, optical and electronic units (lasers drivers, spectrometer, photodetectors, etc.) integrated in a complex diagnostic system (Fig.2). Used spectral band in it: 360-1000 nm.

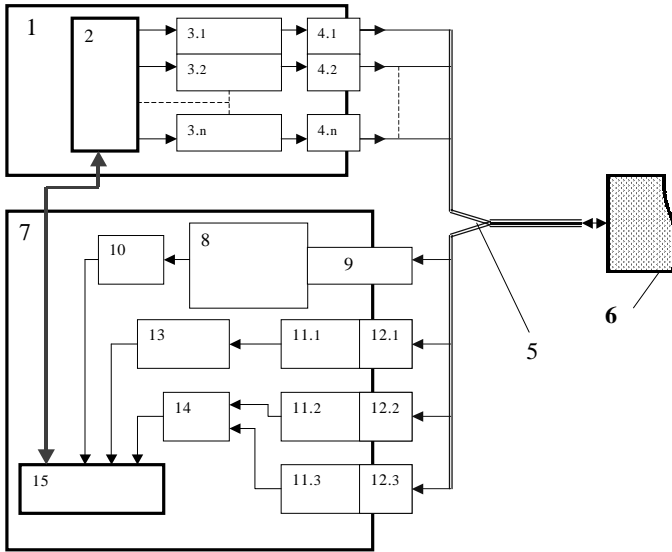


Fig.2. Schematic hardware setup of MLNDS.

In a source unit 1 of MLNDS under the control of laser drivers 2 laser modules 3.1...3.n produce necessary laser light energy, which flows through optical connectors 4.1...4.n into different optical fibers of optical cord 5 and then into a tested tissue 6. Induced by the laser illumination a backscattered, fluorescent, etc. radiation is collected from the tissue by the same optical probe 5 and transferred back to the analyzer unit 7. In the unit 7 a one part of it through an optical collimator 9 passes into spectrometer 8 to analyze a spectral composition of a fluorescent flux. Another part of that goes through optical connectors 12.1...12.3 and optical filters 11.1...11.3 into special units 13 and 14, in which a power of collected radiation for each used laser wavelength (unit 13) as well as a Doppler shift of initial frequency of laser radiation (unit 14) are analyzed. A computer 15 operates MLNDS in a total and all diagnostic data are collected and processed in it as well.

Special software allows a doctor to form a database of patients and to calculate all final medical diagnostic parameters. They are summarized both from particular diagnostic data of each diagnostic technique and from the complex united data on the base of additional calculations. Today the main final medical diagnostic parameters in MLNDS are:

- tissue's blood perfusion (**M**) as a function of time;
- functional transcutaneous saturation of oxy-hemoglobin fraction in a mixed peripheral blood (**S_tO₂**) as a function of time;
- relative volume of all fractions of hemoglobin into a tested tissue volume (**V_b**) as a function of time;
- an index of a perfusional saturation of the oxygen in a blood (**S_tO_{2m}**);
- parameter of a specific oxygen utilization (uptake) in a tissue (**U**);
- a number of coefficients of tissue's fluorescent contrast (**K_f**) which indicate (see below) an existed biochemical composition of tissues on a level of cells' respiratory enzymes: flavins (**FP**), **NADH**, lipopigments (**LP**), protoporphyrins (**PP**), etc.

A number of data processing algorithms have been included in the software to calculate existed biological rhythms of microhaemodynamics in the tested tissue's volume (miogenic rhythm, neurogenic one, etc.). So, we can say with a confidence, that in the up-to-date MNS the mentioned set of diagnostic parameters today is a unique set for a real medical practice.

It must be special noted, that parameter S_tO₂ is registered and calculated in MLNDS as an average value between venous (S_tO₂^v) and arterial (S_tO₂^a) saturation, close to venous saturation, so the evaluation of specific oxygen uptake U in a tissue become possible [3]:

$$U = (S_t O_2^a - S_t O_2) / V_b . \quad (1)$$

Moreover, all parameters with the use of MLNDS can be measured during different conventional functional tests - tests with functional loads on the system of microcirculation. For example: test with occlusion, test with a heating (cooling), medicinal test, etc. So, our MNLDS allows a doctor to produce a multi-parametrical diagnostics examination of patient's tissues on the microcirculatory and biochemical levels "in vivo". It is very effective in different branches of medicine: in oncology [4], gastroenterology [5], angiology [2], occupational diseases therapy [6], etc.

An example of recorded LDF and TRO diagrams (base parameters M, S_tO₂ and V_b versus time) in a case of arterial occlusion test is shown in the Fig.3. All presented data was collected from a 3-distal finger bulb skin. An arterial occlusion was applied to a middle of the finger during 6 min.

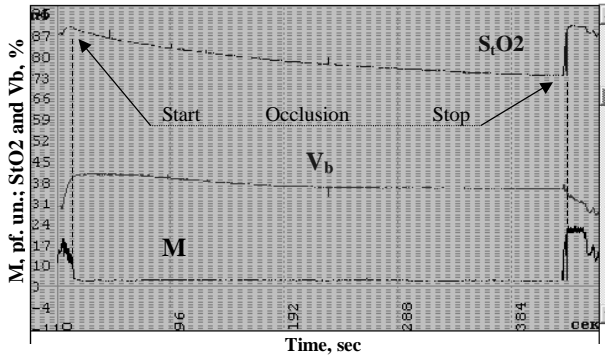


Fig. 3. An example of combined LDF and TRO diagnostic data versus time in the case of a functional test with arterial occlusion. Time of occlusion was 6 min.

A complex index of a perfusional saturation of the oxygen in a blood can be calculated at any time and versus time as follows [3]:

$$S_tO2m = S_tO2 / M . \quad (2)$$

A typical autofluorescent spectrum of oral mucosa in a case of 532 nm excitation wavelength is presented in Fig.4.

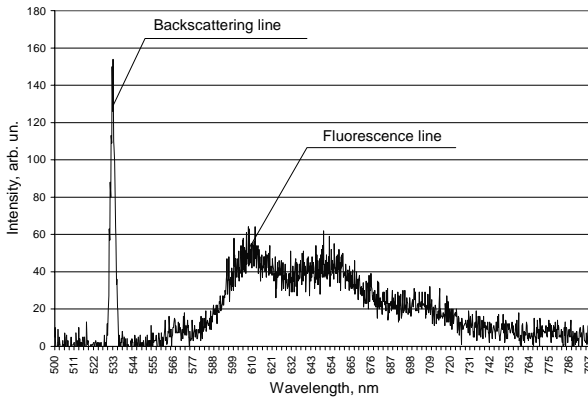


Fig. 4. An autofluorescent spectrum of oral mucosa (excitation line 532 nm).

In this case in the capacity of a diagnostic criterion we have used our standard methodology of the fluorescence contrast coefficient K_f [4-6], when the K_f in different waveband is determined as follows:

$$K_f = 1 + (I_f \cdot \beta - I_{bs}) / (I_f \cdot \beta + I_{bs}), \quad (3)$$

where: K_f is the fluorescence contrast coefficient ($0 < K_f < 2$); I_f – registered light flux intensity in the maximum of a fluorescence spectrum line; I_{bs} – intensity of the registered backscattered laser radiation in the excitation line; β – device’s reduction coefficient ($\beta \approx 1000$ for 532 nm excitation line).

For different waveband and different excitation wavelength K_f characterize in a tissue a presence or absence of different cells’ respiratory enzymes: FP, NADH, LP, PP, etc. And, as it is known, relative concentrations of them in a tissue are a quite good indicator of various metabolic processes in tissues and organs. So, the integration of three kindred optical diagnostic methods in single diagnostic equipment allows a doctor to have a complex diagnostic conception about tested tissues in terms of blood microcirculation and oxygen utilization in tissues. It allows a doctor, in instance, to estimate a chronic hypoxia area in tissues, what is very important, for example, in the up-to-date radiology. It is well known in oncology that different processes of blood microcirculation and tissues oxygenation in malignant tumors have a strong influence on a radiotherapy efficacy. But there are in the modern radiology only few methods to prognosticate a positive radiotherapy outcome. So, for this purpose the united possibilities of LDF, LFD and TRO technique with the use of our MLNDS can be applied as well [4].

In conclusion we can say that a total ideology of MLNDS are protected now by both a Russian patent (positive decision on the patent application form No. 2007117381/14, priority since 11.05.2007) and a “PCT” patent application form. MLNDS is not very expensive equipment, so it is really ready for international transfer, next manufacturing, state certification, clinical examination, etc. like an excellent innovation product.

References

1. D. Rogatkin and L.Lapaeva, *Biomed. Engineering*, 2003, **37**(4), 217-222.
2. *Laser Doppler flowmetry of blood microcirculation* / Ed. By A. I. Krupatkin and V.V. Sidorov, 2005, Moscow, Medicina (in Russian).
3. A. Krupatkin, D. Rogatkin and V. Sidorov, *Abstr. Book of the VI-th Int. Conf. “Haemorheology and microcirculation”*, RF, Yaroslavl, YGSU, 2007, p.106.
4. V. Tchernyi, D. Rogatkin et al., *Proc. SPIE*, 2005, **5693**, 336-343.
5. D. Rogatkin, S. Tereschenko, et al., *Proc. SPIE*, 2002, **4613**, 286-294.
6. V. Tchernyi, D. Rogatkin et al., *Proc. SPIE*, 2006, **6078**, 607828.

Opportunities of Method of Dynamic Filtration in Allocation of Significant Markers of EEG Activity

A.F. Indyukhin, M.Y. Khabarova

Tula state university, induke705@mail.ru

L.N. Tolstoi pedagogic state university, physiology@tspu.tula.ru

Having closed a task of diagnostics of a rough pathology, electroencephalography in the increasing measure addresses to the analysis of a functional condition of a brain and diagnostics of neurologic infringements - sight, hearing and the minimal brain dysfunction. Electrophysiological markers we shall name such parameters EEG which authentically distinguish between nosological groups.

Bioelectric activity traditionally divides on caused and spontaneous. Revealing of the first one represents a separate task and mainly used method of synchronous accumulation does not leave alternative of definition of other parameters, except for peak and temporary. Attempts of application of frequency methods of allocation of the caused activity while had no great success. Over the analysis of spontaneous activity is predominated with a frequency method.

The method of dynamic filtration of EEG [4, 5] in our understanding is carried out as follows. The electric signal of brain activity is filtered by the band filter. The central frequency of the filtration band changes with the speed proportional to the size of time pieces between the moments of passage through zero, maximal and minimal values of signals of brain activity and a signal received as a result of a filtration in such a manner that at passage of zero, maximal and minimal values by a signal of electric activity of a brain before a signal received as a result of a filtration the central frequency of a band of a filtration decreases, and at passage of zero, maximal and minimal values by a signal of electric activity of a brain after the signal received as a result of a filtration the central frequency of a band of a filtration increases.

The program complex is constructed on the basis of mathematical model of the band filter with transfer function

$$W(p) = \frac{2\Delta\omega_{\Pi}p}{\omega_H^2(u) + 2\Delta\omega_{\Pi}p + p^2},$$

Where: ω_H - resonant frequency of the filter;
 $\Delta\omega_{\Pi}$ - half of passband;
 u - a control signal.

In our works we repeatedly addressed to finding of electrophysiological markers of a condition minimal brain dysfunctions [1 - 3]. The dynamic filtration was applied to achieve the following purposes:

1. Detection out of the signal of EEG activity of a dominating rhythm, definition of its amplitude, frequency and character of modulation.
2. Detection out of the signal of EEG activity of the response to individual external stimulus, definition of amplitude and latency peaks.
3. Definition of frequency of a maximum of synchronization of two EEG signals, the maximal and average factor of synchronization (alternative of a level and frequency of a maximum coherence).

In the first case two groups of children in the age of from 3 to 9 years, 14 normal children and 18 children with the minimal brain dysfunction have been examined.

For primary data of frequency, amplitude and lengths of "spindle" of a dominating rhythm following statistical characteristics were measured: the population mean and standard deviation, the maximum and minimum of the values, factors of linear regress, factor of correlation and the reliability of the factor of correlation with dependence on the examinees years.

At comparison of frequency of a dominating rhythm in control group despite of insignificant differences of average value (in assignment O_1 - 9,55 Hz; O_2 - 9,40), disorder of fluctuations considerably above in the right hemisphere. The return tendency is observed at amplitude of a rhythm, disorder of fluctuations above in the left hemisphere.

Average value of length of "spindle" above in the right hemisphere, and the size of disorder has made 21,33 %. Average duration of length of "spindle" at children in the age of from 7 till 10 years makes 5-8 seconds whereas for children of the Tula region this parameter is located in a range 1 - 3 seconds.

At examinees of group of the minimal brain dysfunction lower frequencies of a dominating rhythm in comparison with control group and average value of frequency is more in the right hemisphere.

The difference of average values of frequency of a dominating rhythm on hemispheres in group of the minimal brain dysfunction is less.

In group of the minimal brain dysfunction essential decrease in amplitude, in the left assignment of 17,85 %, and in right - 14,62 % was marked. Difference has increased in average values of amplitude between two assignments, value of amplitude is more in the right hemisphere.

For group of the minimal brain dysfunction average value of length of "spindle" is 11,02 % greater.

In group of the minimal brain dysfunction authentic factors of correlation of frequency and amplitude of a rhythm concerning age of examinees are received, in group of normal children the length of "spindle" of a rhythm with the years correlates.

In the second case EEG with frequency of 1 Hz was registered at group of examinees under rhythmic photo stimulation. Examinees mentally counted relevant flashes of light. The group included children and teenagers (N = 40 persons, 24 boys and 16 girls) in the age of from 9 to 17 years old with distinct domination in EEG an alpha rhythm. The Most part from them (28 person, the basic group) had functional and organic neurological infringements. Control group consisted of 12 person of healthy patients.

Latency of the response to the first stimulus in control group in both hemispheres is smaller than on the second stimulus. In the control group it is observed only in the left hemisphere. The minimum of the latency is achieved in the left hemisphere, in the basic group - on the first stimulus, in control - on the third. The disorder of values latency in control group is more, than in the control group. At presentation of the fifth stimulus of value of disorder are practically equal.

The amplitude of the response tends to decrease with repetition of stimulus. The tendency is broken only on the fourth stimulus, at which amplitude is higher in both groups, in the right and left hemispheres. At submission of the first stimulus the control group has a higher amplitude response. On the subsequent stimulus of distinct prevalence is not present. The disorder of amplitudes in control group up to the fifth stimulus is less, than in control.

The tendency of dependence latency on age is more characteristic for control group, however it is formed not simultaneously in the right and left hemispheres.

There are authentic ($p < 0,05$) correlations of amplitude of the answer with the years in a basic group and control groups.

Authentically parameters of the response to the fourth stimulus differ both basically, and in control groups. The first stimulus has the least probability that has found reflection in the maximal amplitude at rather small latency.

In the third case in group there were children in the age of from 6 to 9 years, 14 normal and 14 children with the minimal brain dysfunction. 63 electrophysiological markers have been detected by functions of coherence, 20 of them are average level coherences and 43 of them are average frequency ones. The average frequency of coherence function in the frequency range, signaling about the tendency to increasing or decreasing of the function and it also showed high sensitivity the analysis procedure of a functional condition of a cerebral cortex.

At mathematical modeling on the input of the band filter product of two channels EEG moved. The filter was automatically adjusted on the frequency equal to double frequency of the maximal synchronization of examined channels. The average and maximal factor of synchronization was simultaneously determined.

Comparison of results of calculations of functions coherence and mathematical modeling has shown concurrence from 75 up to 85 %. The dynamic filtration allows to find electrophysiological markers of neurological infringements in more simple way.

Thus, in all three examined cases the dynamic filtration of EEG activity has shown high efficiency in a finding of significant attributes of researched infringements of brain development.

References:

1. Андриевская И.А., Жеребцова В.А., Прудникова С.А., Хабарова М.Ю., Индюхин А.Ф. Визуализация типовых паттернов биопотенциалов детей в норме и при минимальной мозговой дисфункции // Системный анализ и управление в биомедицинских системах, 2003. - Т. II. - № 3. – С. 233 – 235.
2. Жеребцова В.А., Индюхин А.Ф. Математическое моделирование типовых процессов ЭЭГ у детей в норме и при неврологической патологии // Валеология, 2003. - № 3. – С. 18 – 27.
3. Zherebtsova V.A., Indyukhin A.A., Indyukhin A.F., Khabarova M.Y. Method and software of the dynamic processing EEG recorded from normal children and children with neurological violations // Abstracts of the international conference «The contemporary aspects of maternal and child care». Актуальные проблемы охраны материнства и детства: Сборник материалов Международной российско-американской научно-практической конференции. Тула, 2004. – С. 62 – 63.
4. Индюхин А.Ф. Обработка электроэнцефалографической информации полосовым фильтром с переменными параметрами. Дис. канд. биол. наук. Тула, ТулГУ, 2006.
5. Хабарова М.Ю., Прудникова С.А., Жеребцова В.А., Индюхин А.Ф. Динамическая фильтрация сигнала ЭЭГ в исследовании когнитивных процессов // Медицинские приборы и технологии / Под ред. А.З. Гусейнова и В.В. Савельева. – Тула: Изд-во ТулГУ, 2007. – С. 105 – 108.

Contents

Preface	3
Organization	5

Section 1

Biomedical imaging and signal processing

<i>Marcus Prummer, Joachim Hornegger</i> 3D-Reconstruction in the Presence of Motion	9
<i>J. Schmidt, A. Hapfelmeier, M. Mueller, A. Drzezga, R. Perneczky, A. Kurz, S. Kramer</i> Interpreting PET Scans by Structured Patient Data: A Data Mining Case Study in Dementia Research.....	17
<i>F. Jäger, M. Balda, J. Hornegger</i> Correction of Intensity Inhomogeneities Utilizing Histogram-based Regularization	23
<i>M. Groher, D. Zikic, N. Navab</i> 2D-3D Nonrigid Registration of Vascular Structures for Liver.....	28
<i>K. Höller, M. Petrunina, J. Penne, A. Schneider, D. Wilhelm, H. Feußner, J. Hornegger</i> Taking endoscopy to a higher dimension: Computer Aided 3-D NOTES.....	33
<i>A. Keil, C. Harrer, S. Kirchhoff, C. Kirchhoff, T. Mussack, A. Lienemann, M. Reiser, N. Navab</i> Bolus Detection in Colon MRI.....	38
<i>A. Maistrou</i> Analysis of artificial heart period series for time domain convergence	43
<i>B. Eskofier, J. Kornhuber, J. Hornegger</i> Embedded QRS Detection for Noisy ECG Sensor Data Using a Matched Filter and Directed Graph Search	48
<i>B. Retzlaff, N. Wessel, H. Malberg, G. Brockmann, R. Lange, R. Bauernschmitt</i> Hypertension Causes Lack of Recovery of Baroreflex Function After Heart Surgery	53
<i>T. Girschick, T. Herz, S. Kramer</i> Machine learning based prediction of compound behavior in CYP 3A4, CYP 2D6 and CYP 2C9.....	56
<i>I.N. Spiridonov</i> Structure and form measurement of medical and biologic images.....	61
<i>A.V. Samorodov, M.G. Polyanskaya, I.N. Spiridonov</i> Quantitative Morphometry of Medical and Biologic Preparations.....	66
<i>A.A. Khrulev, E.V. Burlay, I.N. Spiridonov</i> Morphometry of Dermatoglyphic Images.....	71

A.V. Khrustalev, Y.V. Krylov, V.A. Potapov, I.N. Spiridonov Development of Numerical Methods of Iris Integral Parameters Assessment	76
Maria G. Polyanskaya, Andrey V. Samorodov The Developing of Cytological Image Segmentation Method.....	80
Sergei V. Umnyashkin, Dmitri M. Koplovich, Andrei S. Pokrovskiy A Modification of Image Compression Algorithm Based on Encoding of Tree-Arranged Wavelet Coefficients	83
A.S. Pospelov About digital image structure	87
S.A. Bolotov Image compression method using layer decomposition and elementary layer block prediction	93
Sergei V. Umnyashkin, Eugenia A. Koplovich, Andrei A. Alexandrov Layered Motion Compensation for a Low Bit Rate Embedded Wavelet Video Coder.....	97
Y.E. Kirpichenko, D.P. Timohin Tissue modeling for the impedance imaging of the heart	101
Y.E. Kirpichenko, D.P. Timohin Impedance imaging in human's precardiac area	107
Anna G. Mikhaylova Ill-posedness in electric impedance tomography forward problem	112
I.V. Pyanov The experimental setup for obtaining an optical tomograms	116
N.S. Gogulina, I.N. Spiridonov A method for the investigation of psychophysiological status of individuals working under extreme conditions.....	120
A. A. Danilov, Yu. P. Masloboev, D.A.Potapov, S. V. Selishchev and S. A. Tereshchenko Experimental Investigation of Optical Characteristics of Homogeneous High-Scattering Biological Medium.....	124
G.A.Fedorov, S.A.Tereshchenko, M.A.Antakov The Investigation of Tomographical Characteristics of Coded Multi-pinhole Apertures Constructed on the Base of Extended Pseudorandom Sequences.....	131

Section 2

Instrumentation for surgery, implants and artificial organs

Robert Bauernschmitt, Christian Gaertner, Eva U. Braun, Hermann Mayer, Alois Knoll Improving the quality of robotic heart surgery: evaluation in a new experimental system	137
--	-----

S. Demirci, O. Kutter, F. Manstad-Hulaas, N. Navab Towards an Computer Assisted Intervention System for Endovascular Abdominal Aortic Repair	141
A. Schneider, A. Meining, D. Wilhelm, S. v. Delius, S. Can, A. Fiolka, H. Schlicht, E. Wintermantel, H. Feussner A new systems solution to make scarless surgery feasible.....	146
Salman Can, Hermann Mayer, Alois Knoll, Adam Fiolka, Armin Schneider, Johannes Maifeld, Dirk Wilhelm, Hubertus Feussner First cholecystectomy with the new, highly versatile single port system for minimally invasive surgery	152
D. Wilhelm, M. Doundoulakis, M. Burian, H. Friess, H. Feussner Evaluation of CT guided upper GI endoscopy using an electromagnetic navigation system	157
A. Fiolka, M. Polski, S. Can, A. Schneider, H. Feußner An Electromagnetic Camera Control System for Minimally Invasive Surgery.....	162
M. Kranzfelder, A. Schneider, H. Friess, H. Feussner Corpora aliena: Can radio- frequency- identification (RFID) solve the problem?	167
André Adelt, Christian Schaller, Jochen Penne, Florian Höpfl, Peter Nix, Joachim Hornegger Patient Positioning using 3D Surface Registration.....	173
Sonja Gillen, Adam Fiolka, Salman Can, Armin Schneider, Helmut Friess, Hubertus Feussner Rivet application for wound closure with flexible endoscopy in endoluminal endosurgery	178
Guggenbichler JP Incidence, pathogenesis, and clinical diagnosis of implant associated nosocomial infections.....	183
Guggenbichler JP Prevention of implant associated nosocomial infections	190
Björn Schuller, Christoph Scheuermann, Salman Can, Hubertus Feussner, Gerhard Rigoll Robust Speech Recognition for Human-Robot Interaction in Minimal Invasive Surgery.....	197
Jochen Penne, Michael Stürmer, Dirk Wilhelm, Hubertus Feußner Time-of-Flight Based Endoscopy for NOTES Interventions: Challenges and Limitations	202
R.Ghotbi, A. Sotiriou Aortic Aneurysm Therapy: EndoVascular Aortic Repair (EVAR) What do we know and what should we know?	207

M. Burian, M.E. Martignoni, D. Wilhelm, H. Feussner, H. Friess Current status of lymph node mapping in GI-cancer patients and future perspectives: towards application of a miniaturized beta- probe?	209
D.V. Vashurkin, G.I. Itkin, E.V. Konisheva, O.V. Romanov Design and development of axial blood pump for implantable assist circulation system	211
K. Dozorov, G. Itkin, D. Surkov Mathematical model of human cardiovascular system for implantable rotor blood pump research.....	216
N.A. Bazaev, V.M. Grinvald, V.L. Eventov, S.V. Selishchev Hemodialysis with using biological regeneration of dialysis fluid	221
Sudarev A.M., Isaev I.A., Kantor P.S., Korotich E.V., Dvornikov M.V., Buhtiyarov I.V. New approaches to development of means for respiration by multicomponent gas mixtures	226
N.V.Ivakhno An automated complex for respiratory apparatus training.....	229
Sudarev A.M., Isaev I.A., Kantor P.S., Korotich E.V. Technical realization of the external counterpulsation equipment	233
I.I.Leonochev, G.M.Shestopalov Near real-time stereo depth estimation on GPU.....	236
A. M. Antropov, V.A. Bepalov, B. B. Gorbunov, A. N. Gusev, K. A. Mamekin, I. V. Nesterenko, S.V. Selishchev Real-time Control of the Defibrillation Waveform with Digital Signal Processor.....	241

Section 3

Therapeutic and diagnostic systems

A.A. Karyakin (Bio) sensors based on nano-scale arrays and films of novel electrocatalysts.....	249
V.S. Kublanov, V.A. Shmykalov, V.B. Kostousov, Y.E. Kazakov, Kh.Z. Brainina Apparatus-program system for diagnostics and correction of autonomous nervous system dysfunctions.....	253
V.S. Kublanov, V.A. Dorofeev, V.B. Kostousov, A.V. Glazkov Mobile radio-physical system for the functional researches of brain	258
Dmitriy Prilutskiy Polygraphic DC amplifier for biomedical application.	263
I. Chepiga, D. Prilutskiy, A.Ustinov Low power wireless ECG sensor	267

A.V.Kobelev, S.I.Schookin Electrodes' Requirements for Precardiac Measurements	272
Sergey V. Rezvykh, Igor N. Spiridonov, Marina V. Zueva, Irina V. Tsapenko Hardware and software system for single-flash electroretinogram	276
E.V. Sologub, I.N. Spiridonov, A.A. Khrulev Research of Fingerprints Minutiae Position Stability	279
O.V. Vasilevskaya, A.A. Khrulev, J.G. Gorshkov, I.N. Spiridonov Voice-based biometric identification	281
Shchepetov D.S. A multiscale algorithm for P-wave parameters estimation.....	284
L. N. Anischenko, V. B. Parashin Design and Application of the Method for Biolocation DataProcessing.....	289
Kh.Brainina, A.Kositzina, V.Kublanov, Ya.Kazakov, M.Khodos Electrochemical instruments and sensors based on nanocrystalline materials for Bio- , chemical analysis and medical diagnostics.....	294
L.A. Shamkina, P.V.Luzhnov, S.I.Schookin New biofeedback technology for electromagnetic therapy of vascular diseases	299
E.M.Astapenko, P.V.Luzhnov Features of joint brain electric activity and hemodynamics research	304
N.A. Bazaev, A.N. Gusev, A.V. Mikitas Algorithm of automatic fibrillation detection.....	309
Gendel I., Doroshenkov L. EEG segmentation based on Higuchi fractal dimension in automatic sleep stage classification.	313
L.P. Ichkitidze, M.V. Belodedov Comparison characteristics of magnetometers based on ceramic superconductors in biomedical applications	318
O. Merkulova, N. Ivakhno Mathematical model of apnea diagnostics data-measuring system.....	324
D.E. Romanov Mental states BCI	329
D.V. Belilk, K.D. Belik Multifrequency electrical impedance diagnostics of biotissues in oncological surgery.....	334
Zmievskey G.N., Karpukhin V.A., Kosorukov A.E., Galkin M.A., Kostyukov D.V. Corresponding parameters of bio-object response to phototherapy in the task of bio-dosimetry control system development	339
A.A.Danilov The Determination of Optical Characteristics for a High Scattering Medium on the Base of Enhanced Diffusion Model.....	344

A.N.Gusev, I.V.Nesterenko, D.B. Rygalin, D.V. Telyshev Methods of processing, analysis and definition of QRS in ECG	348
L.P. Safonova, V.P. Nevzorov Tissue functional topography and inhomogeneity of metabolic processes observed by the spectrophotometric method	352
Vinokurova M., Solovjeva E., Tarasov R. Estimation of subject emotional state from speech parameters	357
Sidorov V.V., Rogatkin D.A. Multifunctional laser noninvasive diagnostic system for medicine	362
A.F. Indyukhin, M.Y. Khabarova Opportunities of Method of Dynamic Filtration in Allocation of Significant Markers of EEG Activity	367

Труды научной конференции

**Труды 4-й Российско-Баварской конференции
по биомедицинской технике**

Печатается в авторской редакции.

Издательско-полиграфический комплекс МИЭТ.

Подписано в печать с оригинал-макета 17.06.2008. Формат 60×84 1/16. Печать цифровая. Бумага офсетная. Гарнитура Times New Roman. Усл. печ. л. 21,92. Уч.-изд. л. 18,9. Тираж 250 экз. Заказ 66.

Отпечатано в типографии ИПК МИЭТ.

124498, Москва, Зеленоград, проезд 4806, д. 5, МИЭТ.